ELECTROHYDRODYNAMICS AND IONIZATION IN THE ARRAY OF MICROMACHINED ULTRASONIC ELECTROSPRAY (AMUSE) ION SOURCE

A Dissertation
Presented to
The Academic Faculty

By

Thomas P. Forbes

In Partial Fulfillment
of the Requirements for the Degree
Doctor of Philosophy in the
School of Mechanical Engineering

Georgia Institute of Technology

May 2010

ELECTROHYDRODYNAMICS AND IONIZATION IN THE ARRAY OF MICROMACHINED ULTRASONIC ELECTROSPRAY (AMUSE) ION SOURCE

Approved by:

Dr. Andrei G. Fedorov, Advisor
School of Mechanical Engineering
Georgia Institute of Technology

Dr. F. Levent Degertekin, Advisor
School of Mechanical Engineering
Georgia Institute of Technology

Dr. Marc K. Smith
School of Mechanical Engineering
Georgia Institute of Technology

Dr. Thomas M. Orlando
School of Chemistry and Biochemistry
Georgia Institute of Technology

Dr. David C. Muddiman
Department of Chemistry
North Carolina State University

Date Approved: March, 18, 2010

To my parents, Dr. J. Benjamin and Lark Elizabeth Forbes

ACKNOWLEDGEMENTS

I would like to thank my parents, Ben and Lark, whose loving support and unwavering patience have truly provided me the foundation to accomplish any task. Without their constant encouragement I surely would not have accomplished so much. I would also like to thank my brother, Michael, for his close friendship and uncanny talent to make me laugh through even the most difficult times. I am also grateful for the many friendships that I have made during my time at Georgia Tech.

I would like to convey my deepest gratitude to my advisors, Dr. Andrei Fedorov and Dr. Levent Degertekin, for their guidance and encouragement in all aspects of my graduate career. Their continual enthusiasm toward all fields of research has inspired my interest in multidisciplinary sciences.

Financial support for this project was provided by the National Center for Research Resources (NCRR), a component of the National Institutes of Health (NIH), under Grant Number 1 R21 RR021474-01A1.

TABLE OF CONTENTS

ACKNOWLEDGEMENTS ..... **IV**

LIST OF TABLES ..... **IX**

LIST OF FIGURES ..... **X**

SUMMARY ..... **XVI**

CHAPTER 1 INTRODUCTION **1**

1.1 Overview of Mass Spectrometry 1

1.2 Electrospray Ionization (ESI) Ion Sources 2

1.2.1 Assisted Electrospray Ionization 5

1.2.2 Nanoelectrospray Ionization (nanoESI) 7

1.2.3 Micromachined ESI Sources 8

1.3 AMUSE Ion Source 9

1.3.1 Key Ideas 9

1.3.2 Review of Prior Work on Droplet Generator 11

1.3.2.1 Droplet Formation and Ejection Physics 11

1.3.2.2 Mass Spectrometric Characterization 13

1.4 Research Objectives 14

1.5 Thesis Organization and Overview 15

CHAPTER 2 AMUSE ION SOURCE DESIGN **18**

2.1 AMUSE Fabrication and Assembly 19

2.2 Device Configurations and Operating Modes 24

2.2.1 Flow Rate and Total Volume Operation Ranges 24

2.3 Multiplexed Dual-Sample Device 28

2.3.1 Dual-Sample Modeling 29

2.3.1.1 Simulation Domain and Material Properties 30

2.3.1.2 Acoustic Wave Focusing Results 33

2.3.2 Experimental Validation 40

2.3.2.1 Impedance Measurements 41

2.3.2.2 Dual-Sample Ejector 42

CHAPTER 3 AMUSE ANALYTE CHARGING AND IONIZATION 47
3.1 Electrochemically Generated Ions and Analyte Charging.....49
3.2 Protonation and Charge Separation 52
3.3 Electrohydrodynamic Modeling of Charge Transport during Droplet Ejection.....54
3.3.1 Electrohydrodynamic (EHD) Model..... 56
3.3.1.1 Momentum Conservation..... 57
3.3.1.2 Electrodynamics and Charge Transport..... 57
3.3.1.3 Electrohydrodynamic Transport Equations 60
3.3.2 Solution Methodology 62
3.3.2.1 Scalar Transport Equation..... 62
3.3.2.2 Tracking Interface Evolution 63
3.3.2.3 Incorporating Surface Stresses..... 66
3.3.2.4 Numerical Discretization 67
3.3.3 Simulation and Analysis of Special Cases..... 68
3.3.3.1 Electrohydrodynamic Cone-Jet..... 68
3.3.3.2 Perfectly Conducting Fluid – Taylor Cone Electrospray..... 71
3.3.4 Simulation and Analysis of AMUSE Charged Droplet Ejection..... 74
3.3.4.1 DC Charging 78
3.3.4.2 AC Charging 81
3.3.4.3 Alternate Electric Field Waveforms 83

CHAPTER 4 EXPERIMENTAL CHARACTERIZATION AND SCALING: CHARGE MEASUREMENTS AND VISUALIZATION.....86
4.1 Droplet Charge Measurements 86
4.1.1 Experimental Setup..... 87
4.1.1.1 AMUSE Configuration 89
4.1.2 Validation of Charge-per-Droplet Simulated Results..... 90
4.1.2.1 DC Charging 90
4.1.2.2 AC Charging 95
4.1.3 Analysis of Charge Transport 99
4.1.3.1 Bulk Charge Density (Individual Droplet Simulations) 99
4.1.3.2 Charge Transport Time Scale Analysis 102
4.1.3.3 Experimental Characterization..... 107
4.2 Optical Visualization of Ejection Phenomena 114

4.2.1 Device Setup and Electric Field Configuration 115
4.2.2 Representative Visualization Results 118
4.2.3 Scale Analysis: Relevant Time Scales and Dimensionless Numbers 123
4.2.3.1 Conceptual Physics and Scale Analysis of AMUSE 125
4.2.3.2 Ejection Regime Map 129

CHAPTER 5 MASS SPECTROMETRIC CHARACTERIZATION AND APPLICATION 134

5.1 AMUSE Ion Source Demonstration for Mass Spectrometry 134
5.1.1 Peptides and Proteins 135
5.1.2 Pharmaceutical Molecules 138
5.2 Electric Field Induced Charge Separation 140
5.2.1 Mass Spectrometry Setup 141
5.2.2 Electric Field Configurations 143
5.2.3 Signal Abundance and Sensitivity Improvements 145
5.2.4 Comments on the Ionization of Macromolecules for Mass Spectrometry 149
5.3 Potential High-Impact Applications of the AMUSE Ion Source 152
5.3.1 Soft Ionization Capability 152
5.3.1.1 Noncovalent Interactions 152
5.3.1.2 RF-only Mode of Operation 153
5.3.2 Solvent Flexibility 154

CHAPTER 6 CONCLUSIONS AND RECOMMENDATIONS FOR FUTURE WORK 156

APPENDIX A MULTIPLEXED AMUSE ION SOURCE 165

A.1 Modeling of Dual-Sample Configuration 165
A.1.1 Simulation Domain 165
A.1.2 Material Properties 165
A.1.2.1 Piezoelectric Transducer Properties 166
A.1.2.2 Fluid Properties 168
A.1.2.3 Silicon and Spacer Properties 168

APPENDIX B ELECTROCHEMICAL ION GENERATION AND TRANSPORT IN AMUSE 170

B.1 Electrochemically Introduced Ion Transport 170

B.1.1 Time Scale Analysis of Associated Phenomena 170
B.1.2 CFD Simulation of Ion Transport 176
B.1.2.1 Effect of Ejection Duty Cycle 179
B.1.2.2 Effect of Electrode Location 181

APPENDIX C FLUENT CODE IMPLEMENTATION 185
C.1 Electrohydrodynamics Implementation 185
C.1.1 Simulation Domain 190

APPENDIX D ADDITIONAL MASS SPECTRA FROM AMUSE 191
D.1 AMUSE-Air Amplifier-FT-ICR 191
D.2 AMUSE-Air Amplifier-MicrOTOF 192

REFERENCES 195

LIST OF TABLES

Table 2.1 Sample specifications for various liquid chromatography options. 25

Table A.1 PZT-8 properties used in the ANSYS simulations.[188] 167

Table A.2 Fluid (water) properties used in the ANSYS simulations. 168

Table A.3 Silicon nozzle array, spacer, and silicone rubber insert properties used in the ANSYS simulations 169

Table C.1 User-defined scalars (UDSs). 186

Table C.2 User-defined scalar (UDS) implementation. 186

Table C.3 User-defined memory (UDM) variables. 188

LIST OF FIGURES

Figure 1.1 Schematic representation of electrospray ionization as a controlled-current electrolytic cell. 3

Figure 1.2 Schematic representations of the charge residue[7] and ion evaporation[13] mechanisms for dry ion formation. 5

Figure 1.3 Schematic of pneumatically-assisted electrospray ionization, commonly used with higher surface tension solvents and higher flow rate applications. Pneumatically-assisted ESI is often coupled with liquid chromatography or other separation technique. 7

Figure 1.4 AMUSE ion source schematic with representative dimensions of the piezoelectric transducer, sample reservoir, and microfabricated silicon nozzle array for acoustic wave focusing. 10

Figure 1.5 Stroboscopic images of droplet ejection (left) from a 4.5 μm orifice operated at a driving frequency of 0.784 MHz and continuous jet (right) from at 15.7 μm orifice operated at driving frequency of 0.883 MHz. (Adapted from Meacham 2006[67]) 12

Figure 1.6 Mass spectra for cytochrome c in 99.9:0.1 (v/v) water: acetic acid operated in RF-only mode, coupled to a venturi device. (Adapted from Hampton et al. 2007[73]) 13

Figure 2.1 Ejector pyramidal array fabrication process: 1) wafer preparation, 2) PECVD deposition of silicone nitride (Si_3N_4) mask layer for wet etch and membrane for orifice creation, 3) photolithography of nozzle base pattern in positive photoresist, 4) ICP etch of nozzle base pattern in Si_3N_4, 5) potassium hydroxide (KOH) anisotropic wet etch of pyramidal nozzles in (100) oriented silicon, 6) photolithography of orifice pattern in positive photoresist, 7) ICP etch of orifice in Si_3N_4 membrane, 8) DC sputtered tungsten deposition to strengthen membrane. 20

Figure 2.2 Scanning electron microscope (SEM) images of the silicon nitride/tungsten membrane (11 μm on a side) and nozzle orifice (4.5 μm diameter). (Adapted from Meacham 2006[67]) 22

Figure 2.3 AMUSE ion source schematic (inset: exploded view with external counter electrode) of layered assembly consisting of: piezoelectric transducer, Kapton spacer with silicone gasket insert for leak-free fluid reservoir and compression fit fluid inlet, microfabricated silicon nozzle array for acoustic wave focusing, rubber support layer, and external wire electrode for charge separation electric field application. 23

Figure 2.4 Flow rate and sample volume specifications for AMUSE configuration options. 26

Figure 2.5 Schematics displaying various configurations of AMUSE from Figure 2.4 that have been demonstrated, 1 – Full, single sample (online), 2 – Dual-sample multiplexed (online), 4 – Reduced reservoir, single sample (online), 5 – Full, single sample (offline). 27

Figure 2.6 Schematic representation of the multiplexed (dual-sample) droplet ejector array. 29

Figure 2.7 Two-dimensional (2-D) computational domain used to perform simulations of the harmonic response of the system using ANSYS. 31

Figure 2.8 Simulated electrical input impedance as a function of piezoelectric driving signal frequency for the dual-sample multiplexed droplet ejector array. 33

Figure 2.9 Comparison of the simulated electrical input power and power imparted to the fluid as a function of piezoelectric driving signal frequency for the dual-sample multiplexed droplet ejector array. Power imparted to the fluid considers only the active domain. 35

Figure 2.10 Power-transfer efficiency (acoustic power imparted to fluid divided by the electrical input power to the transducer) as a function of piezoelectric driving signal frequency for the dual-sample multiplexed droplet ejector array. 36

Figure 2.11 Real component of the simulated complex acoustic pressure field distribution within the ejector fluid reservoir for operation resulting in efficient wave focusing in the active (right) domain at transducer driving frequencies of (top) 0.88 MHz and (bottom) 1.425 MHz. 37

Figure 2.12 Simulated power imparted to the fluid across a single row of 20 nozzles of the array with and without a cut in the piezoelectric transducer for device operation at 0.88 MHz. 39

Figure 2.13 Simulated power imparted to the fluid across a single row of 20 nozzles of the array with and without a cut in the piezoelectric transducer for device operation at 1.425 MHz. 39

Figure 2.14 Experimentally measured electrical input impedance as a function of piezoelectric driving signal frequency. 41

Figure 2.15 Experimental setup used to demonstrate the multiplexed operation of a dual-sample/domain micromachined ultrasonic droplet ejector array. 43

Figure 2.16 Images of isolated ejection from individual domains of the multiplexed ultrasonic ejector array. Left domain active (left), right domain active (right). 44

Figure 3.1 Schematic representation of computational grid with interface profile, normal vector, and cell volume fraction. 67

Figure 3.2 Left panel: fluid interface profile (liquid volume fraction equal to 0.5) for full electrohydrodynamic simulations of heptane. Right panel: electric potential distribution. Inset: free charge distribution (C/m^3). Simulation parameters: the simulation domain is axisymmetric with capillary radius, r_o = 350 μm, domain radius, R = 1400 μm, capillary length, l_o = 2000 μm, domain length, L = 4500 μm, capillary thickness, t = 50 μm, inlet velocity, u_o = 0.1 m/s, and capillary potential, ϕ_o = 7500V 70

Figure 3.3 Left panel: fluid interface profile (liquid volume fraction equal to 0.5) for electrohydrodynamic simulations considering a perfectly conductive fluid. Right panel: potential gradient magnitude distribution. Inset: velocity field at cone tip. Simulation

parameters: r_o = 350 μm, R = 1400 μm, l_o = 2000 μm, L = 4500 μm, t = 50 μm, u_o = 0.05 m/s, ϕ_o = 7000V 73

Figure 3.4 Simulated droplet evolution during AMUSE ejection through a single pressure wave cycle. Fluid profile results are for a liquid volume fraction of 0.5. 75

Figure 3.5 Axisymmetric simulation domains of droplet ejection in the presence of an electric field for the "full" domain for DC electric field simulations (solid black lines) and the "truncated" domain for AC electric field simulations (dashed blue lines). 77

Figure 3.6 DC charging simulation results for electric potential distribution (left panel), pressure distribution (right panel), and a magnified view of positive charge distribution within an ejected droplet (inset). (Liquid volume fraction equal to 0.5) 80

Figure 3.7 AC charging simulation results for electric potential distribution (left panel), pressure distribution (right panel), and a magnified view of electric potential and net charge distributions for electrical/mechanical signals in-phase (left inset) and 180º out-of-phase (right inset). (Liquid volume fraction equal to 0.5) 82

Figure 4.1 Experimental setup for ejected current and mass measurements for DC charging. 88

Figure 4.2 Experimental setup for ejected current and mass measurements for AC charging with adjustable phase shift. 88

Figure 4.3 Schematic representation of the AMUSE ion source configured for application of an external electric field. The electric field is applied across the AMUSE ion source between the piezoelectric transducer's top electrode and an external wire electrode added to the stack assembly. 90

Figure 4.4 Simulated charge-per-droplet as a function of DC charging electric field magnitude. 91

Figure 4.5 Simulated charge-per-droplet for consecutively ejected droplets with an applied 1 MV/m electric field. 92

Figure 4.6 Dependence of normalized charge-per-droplet on the magnitude of the electric field - comparison between the experimental measurements and simulations. (circles) normalized mass spectrometry signal intensity [obtained for a 3 μM solution of reserpine in an aqueous solvent containing 0.1% (v/v) acetic acid, using a time-of-flight mass spectrometer], (squares) normalized ejection current as measured in charge collection experiments described above [for an aqueous solvent with 0.1% (v/v) acetic acid], and (diamonds) normalized simulated charge-per-droplet. 93

Figure 4.7 Experimentally measured average ejection flow rate (collected mass per collection time) as a function of the charge separating electric field magnitude. 95

Figure 4.8 Simulated charge-per-droplet as a function of the phase-shift between the AC charging electric field and mechanical ejection pressure field. 96

Figure 4.9 Comparison of experimental normalized charge-per-droplet data with theoretical predictions as a function of a relative phase shift between the mechanical and electrical

signals, (diamonds – CFD simulations of charge-per-droplet, squares – experimentally measured charge-per-droplet using ejected current and collected mass measuring techniques described in text). 98

Figure 4.10 Simulated charge-per-droplet as a function of initial bulk charge density for several representative DC electric field magnitudes. 100

Figure 4.11 Simulated charge-per-droplet as a function of applied DC electric field for (a) low (~ 5,000 – 50,000 C/m^3), (b) low-medium (~ 50,000 – 125,000 C/m^3), (c) medium-high (~ 125,000 – 250,000 C/m^3), and (d) high (~ 250,000 – 400,000 C/m^3) bulk charge densities. 101

Figure 4.12 Charge transport time scales for a 1 MHz piezoelectric transducer drive signal, plotted with simulated charge-per-droplet values as a function of the bulk charge density for external electric field strength of 2.5×10^5 V/m. 103

Figure 4.13 Schematic representation of the internal electric field direction and net charge transport in an evolving droplet for each of the regimes of charge transport. 105

Figure 4.14 Experimental charge-per-droplet as a function of the bulk charge density for a 0.905 MHz drive signal. 108

Figure 4.15 Simulated charge-per-droplet for a 1 MHz piezoelectric transducer drive signal, as a function of the initial bulk charge density for the first ejected droplet and the average of consecutively ejected droplets. 109

Figure 4.16 Experimental charge-per-droplet as a function of electric field at higher bulk charge density (200,000 C/m^3). 110

Figure 4.17 Charge transport time scales for a 1 MHz piezoelectric transducer drive signal, plotted with simulated multiple droplet averages of charge-per-droplet as function of the bulk charge density for external electric field strength of 1.0×10^6 V/m. 111

Figure 4.18 Charge transport time scales for a 0.905 MHz piezoelectric transducer drive signal, plotted with experimentally measured charge-per-droplet as function of the bulk charge density for external electric field strength of 3.5×10^5 V/m. 112

Figure 4.19 Experimentally measured average ejection flow rate (collected mass per collection time) as function of the charge separating electric field magnitude. 113

Figure 4.20 Schematic representation of the experimental setup for stroboscopic visualization of the ejection process under the application of an external electric field. 115

Figure 4.21 Timing diagram of the LED pulse and sinusoidal piezoelectric drive signals. 117

Figure 4.22 Simulated droplet profiles (left panels) and axial velocity distributions (right panels) for (a) low, 1.0×10^5 V/m and (b) high, 2.0×10^6 V/m charge separating electric fields (fluid interface is given by a locus of points with a liquid volume fraction of 0.5). 118

Figure 4.23 Sequential stroboscopic images of droplet ejection from a 5 μm orifice device operated at a 0.735 MHz drive frequency with no external electric field applied. There is a 170 ns delay between successive images. 120

Figure 4.24 Sequential stroboscopic images of droplet ejection from a 5 μm orifice device operated at a 0.735 MHz drive frequency under the application of a 1×10^{6} V/m external electric field. There is a 170 ns delay between successive images. 121

Figure 4.25 Images of overall ejection strength and ejection mode with (a) no electric field and (b) a 1×10^{6} V/m external electric field applied. Insets are representative stroboscopic images of droplet ejection under the respective electric field conditions. 122

Figure 4.26 Regime map displaying the relationship between the Strouhal number and the Fenn number for the transition from purely mechanical (abbreviated as "M-spray") to coupled electromechanical atomization (abbreviated "EM-spray"), plotted with experimental results. The insert displays the plot on a log-log scale, resolving the ¼ exponent in the *St* vs. *Fe* relationship. 131

Figure 5.1 Mass spectrum from a FT-ICR mass analyzer for 3.4 μM melittin in 99.9:0.1 (v/v) water/formic acid ionized by AMUSE. 136

Figure 5.2 Mass spectrum from a FT-ICR mass analyzer for 5 μM cytochrome c in 99.9:0.1 (vol/vol) water/formic acid ionized by AMUSE. 136

Figure 5.3 Mass spectrum from a FT-ICR mass analyzer for 10 μM angiotensin I in 99.9:0.1 (vol/vol) water/formic acid ionized by AMUSE. 137

Figure 5.4 Mass spectrum from a FT-ICR mass analyzer for 14 μM chlorpromazine in 99.9:0.1 (vol/vol) water/formic acid ionized by AMUSE. 138

Figure 5.5 Mass spectrum from a FT-ICR mass analyzer for 5 μM caffeine in 99.9:0.1 (vol/vol) water/formic acid ionized by AMUSE. 139

Figure 5.6 Schematic of the experimental system coupling AMUSE to air amplifier to time-of-flight mass spectrometer, including the electrode placement with controlled DC electric bias potentials. 142

Figure 5.7 Schematic representation of electric field configurations: (a) case 1 (squares): $\left(V_{PZT}=+V_{DC},\ V_{ext}=0\right)$, (b) case 2 (diamonds): $\left(V_{PZT}=+V_{DC},\ V_{ext}=removed\right)$, (c) case 3 (circles): $\left(V_{PZT}=0,\ V_{ext}=-V_{DC}\right)$, (d) case 4 (triangles): $\left(V_{PZT}=+V_{DC}=Const,\ V_{ext}=+V_{DC}\right)$, for all cases, $V_{AA}=V_{MS}=0$. 144

Figure 5.8 Extracted ion chromatogram of a base peak (top), and representative mass spectrum (bottom), for 3 μM reserpine in 99.9:0.1 (vol/vol) water/acetic acid ionized by AMUSE. 145

Figure 5.9 Maximum signal intensity obtained with the AMUSE ion source for 3 μM reserpine in 99.9:0.1 (v/v) water/acetic acid for various applied electric field

configurations. Potential configurations: case 1 (squares): $\left(V_{PZT} = +V_{DC},\ V_{ext} = 0\right)$, case 2 (diamonds): $\left(V_{PZT} = +V_{DC},\ V_{ext} = removed\right)$, case 3 (circles): $\left(V_{PZT} = 0,\ V_{ext} = -V_{DC}\right)$, case 4 (triangles): $\left(V_{PZT} = +V_{DC} = Const,\ V_{ext} = +V_{DC}\right)$, for all cases, $V_{AA} = V_{MS} = 0$. 146

Figure 5.10 Signal-to-noise (S/N) ratio obtained with the AMUSE ion source for 3 μM reserpine in 99.9:0.1 (v/v) water/acetic acid for various applied electric field configurations. 148

Figure B.1 AMUSE schematic showing relevant length scales and velocities used in the time scale analysis. 171

Figure B.2 Schematic representation of relevant length scales for electrode location at the pyramidal surfaces of each nozzle. 175

Figure B.3 Simulation domain for electrochemically generated ion transport model. 177

Figure B.4 Simulated results of Zn^{2+} concentration throughout fluid reservoir for 100% (top) and 1% (bottom) duty cycle operation. 180

Figure B.5 Simulated results of Zn^{2+} concentration at each of the 20 nozzle orifices along the nozzle array for changing duty cycle. 181

Figure B.6 Simulated results of Zn^{2+} concentration throughout the fluid reservoir for an electrode at the piezoelectric transducer top surface (top) and at the pyramidal nozzle surfaces (bottom). Both results are for 50% duty cycle operation. 182

Figure B.7 Simulated results of Zn^{2+} concentration at each of the 20 nozzle orifices along the nozzle array for electrode locations at the piezoelectric element and the nozzle surface. 182

Figure B.8 Ionization "efficiency" for all simulated cases as a function of the Peclet number, Eq. B.5. 183

Figure C.1 Two-dimensional (2D), axisymmetric simulation domains of droplet ejection in the presence of an electric field for the "full" domain for DC electric field analysis (solid black lines) and the "truncated" domain for AC electric field analysis (dashed blue lines). 190

Figure D.1 Mass spectrum from a FT-ICR mass analyzer for 4 μM bradykinin in 99.9:0.1 (vol/vol) water/formic acid ionized by AMUSE. 191

Figure D.2 Mass spectrum from a FT-ICR mass analyzer for 2.8 μM BNP-32 in 99.9:0.1 (vol/vol) water/formic acid ionized by AMUSE. 192

Figure D.3 Mass spectrum from a micrOTOF mass analyzer for 50 μM angiotensin III and 400 μM cupric chloride ($CuCl_2$) water ionized by AMUSE with a 1000 V_{DC} applied to the piezoelectric transducer electrode and the external wire electrode grounded. 193

Figure D.4 Mass spectrum from a micrOTOF mass analyzer for 3 μM reserpine in 99.9:0.1 (vol/vol) water/acetic acid ionized by AMUSE. 194

SUMMARY

The focus of this Ph.D. thesis is the theoretical, computational, and experimental analysis of electrohydrodynamics and ionization in the Array of Micromachined UltraSonic Electrospray (AMUSE) ion source. The AMUSE ion source, for mass spectrometry (MS), is a mechanically-driven, droplet-based ion source that can independently control charge separation and droplet formation, thereby conceptually differing from electrospray ionization (ESI). This aspect allows for low voltage soft ionization of a variety of analytes and flexibility in the choice of solvents, providing a multifunctional interface between liquid chromatography and mass spectrometry for bioanalysis. AMUSE is a versatile device that operates in an array format, enabling a wide range of configurations, including high-throughput and multiplexed modes of operation.

This thesis establishes an in-depth understanding of the fundamental physics of analyte charging and electrokinetic charge separation in order to enhance droplet charging and ionization efficiency. A detailed electrohydrodynamic (EHD) computational model of charge transport during the droplet formation cycle in the AMUSE ion source is developed, coupling fluid dynamics, pressure and electric fields, and charge transport in multiphase flow. The developed EHD model presents a powerful tool for optimal design and operation of the AMUSE ion source, providing insight into the microscopic details of physicochemical phenomena, on the microsecond time scale.

Analyte charging and electrohydrodynamics in AMUSE are characterized using dynamic charge generation measurements and high-spatial-resolution stroboscopic

visualization of ejection phenomena. Specific regimes of charge transport, which control the final droplet charging, have been identified through experimental characterization and simulations. A scale analysis of the ejection phenomena provides a parametric regime map for AMUSE ejection modes in the presence of an external electric field. This analysis identifies the transition between inertia-dominated (mechanical) and electrically-dominated (electrospraying) ejection, where inertial and electric forces are comparable, producing coupled electromechanical atomization. The understanding of analyte charging and charge separation developed through complimentary theoretical and experimental investigations is utilized to improve signal abundance, sensitivity, and stability of the AMUSE-MS response. Finally, these tools and fundamental understanding provide a sound groundwork for the optimization of the AMUSE ion source and future MS investigations.

CHAPTER 1

INTRODUCTION

1.1 Overview of Mass Spectrometry

Mass spectrometry is a versatile tool enabling the direct determination of an analyte's nominal mass as well as structural information through analysis of molecular fragments.[1] The last decade of active proteomics research has established mass spectrometry (MS) as the dominant means of obtaining accurate bioanalytical measurements, including protein and other biomolecule identification.[2-4] This tool has not only enabled advances in proteomics, leading to new clinical biomarkers, drug targets and more effective drugs, it is also used to detect explosive residues at airport security, identify elemental composition of molecules, detect/identify steroid use in athletes, and determine authenticity of counterfeit drugs. The main components of MS include (1) the ion source to produce gas phase ions, (2) the mass (m/z) analyzer which separates ions based on a given parameter, e.g. time-of-flight or frequency of oscillation, and (3) the ion detector whose output is converted into a mass spectrum. The first step in the sequence of producing desolvated ions, accomplished by the ion source, is the focus of the present research. The ion source generates and charges droplets/particles of solvent/matrix containing the analyte molecules of interest. The capability of an ion source and its underlying ionization method to effectively disperse and charge analyte are critical aspects that ultimately determine the efficiency of ionization. This, in turn, determines the sensitivity and resolution of the mass spectrometric analysis.

With the development of "soft" ionization methods, electrospray ionization (ESI)[5] and matrix assisted laser desorption ionization (MALDI)[6], the analysis of intact

macromolecules without fragmentation has been achieved. MALDI enables offline gas phase ion introduction of intact molecules by laser-induced desorption. The matrix is used to dilute analyte molecules, preventing analyte-analyte interactions, and absorbs the majority of the laser radiation energy, often ultraviolet or in some cases infrared. This allows for very small increases in internal energy of the analyte during ionization (soft), eliminating fragmentation.[1] The laser bombardment vaporizes the matrix/analyte mixture and the matrix absorbs the laser energy as an analyte is ionized, typically producing singly-charged ions. Alternatively, electrospray ionization provides online (i.e., continuous infusion) ion generation using a strong and focused electric field for fluid dispersion into a fine aerosol containing charged analyte molecules. ESI also has the ability to produce multiply-charged ions, lowering the mass-to-charge (m/z) value for large macromolecules to within the range of most mass spectrometers. MALDI and other offline (i.e., direct injection) laser-based sources will not be discussed further here. The present research focuses on a new droplet-based ion source with independent mechanical and electrical actuation, thus enabling control of droplet formation and analyte charging.

1.2 Electrospray Ionization (ESI) Ion Sources

The development of electrospray ionization (ESI) for efficiently transferring large, dissolved, and neutral biological molecules into the gas phase ions was a breakthrough in structural biology.[5,7-9] ESI enables the generation of intact, low internal energy, gas-phase ions from molecules in solution through the use of electrohydrodynamic focusing of a liquid jet, also known as a Taylor cone (Figure 1.1).[10-12] In this process, the electrically-conducting fluid is delivered through a small bore capillary maintained at relatively high electric potential. The MS inlet typically acts as a

counter electrode, defining the imposed electric field. The strong electric field, focused at the capillary tip, induces free charge migration to the liquid surface. Charge accumulation at the surface creates electrical Maxwell stresses that elongate the emerging fluid interface, producing a conical shape. The highest charge density occurs at the cone apex, where the electrical stresses overcome surface tension, emitting a liquid jet. The jet breaks up into highly charged droplets, eventually leading to desolvated ions via a combination of the ion evaporation[13] and charge residue[7] mechanisms. The introduction of ESI has enabled a drastic growth in the application of mass spectrometry to biomedical research, especially when used in combination with liquid chromatography (LC) separation.[8,14]

Electrospray ion sources utilize Taylor cone formation for *both* droplet formation and selective (positive or negative) charging via charge separation. Electrospray ionization is composed of three main processes: analyte charging, fluid dispersion, and

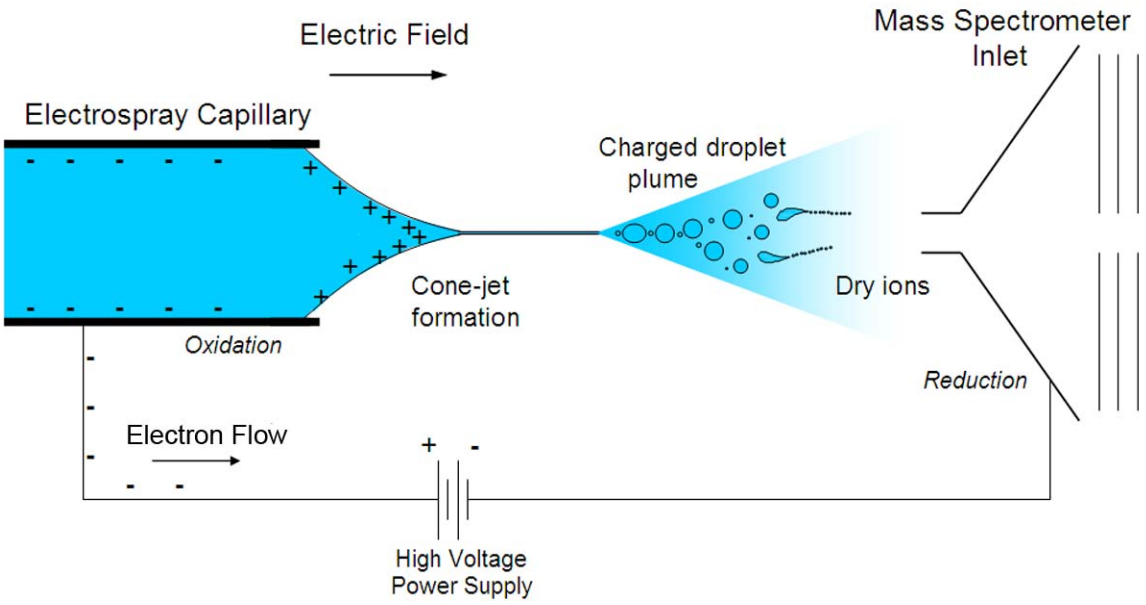

Figure 1.1 Schematic representation of electrospray ionization as a controlled-current electrolytic cell.

ionization (dry ion formation). Analyte charging is a process of attaching a charge to the molecule of interest, typically occurring in solution. It proceeds through adduct formation, often in the form of protonation or adducts formed with various cations from salts in the solution or even electrochemically introduced metal ions.[10,15-18] Electrospray dispersion often shortened to electrospray (ES) is the simultaneous charge separation and fluid dispersion of the solution into charged droplets. This is made possible by applying a large electric field, transporting the positive (or negative in negative mode MS) solvated ions to the fluid interface. The electrokinetic flow at the capillary exit forms the Taylor cone, and once the Coulombic repulsion forces overcome the solution surface tension, spraying is achieved.[10-12,19] Finally, ionization is the transformation of charged solute species in the droplets into free ions in the gas phase, or desolvation. This is believed to occur by either the charge residue mechanism (CRM)[7] or the ion evaporation mechanism (IEM)[13], as shown in Figure 1.2. The charge residue mechanism refers to a process by which the solvent evaporates from the droplet, increasing the charge density until the Rayleigh limit is achieved and the droplet experiences Coulomb fission. The Rayleigh limit provides the charge levels required to overcome surface tension.[20] Similarly, Coulomb fission is the process in which the Coulombic repulsion of same sign charges causes the emission of many smaller offspring droplets. The relative sizes and charge levels of parent and offspring droplets have been investigated in the literature.[21] The fission events continue until only a single charged analyte molecule remains in the gas phase. In the ion evaporation mechanism, charged droplets are also created by Coulomb fission. However, before the Rayleigh limit is reached, the local electric field becomes strong enough for a solvated ion to jump off the droplet into an energetically favorable

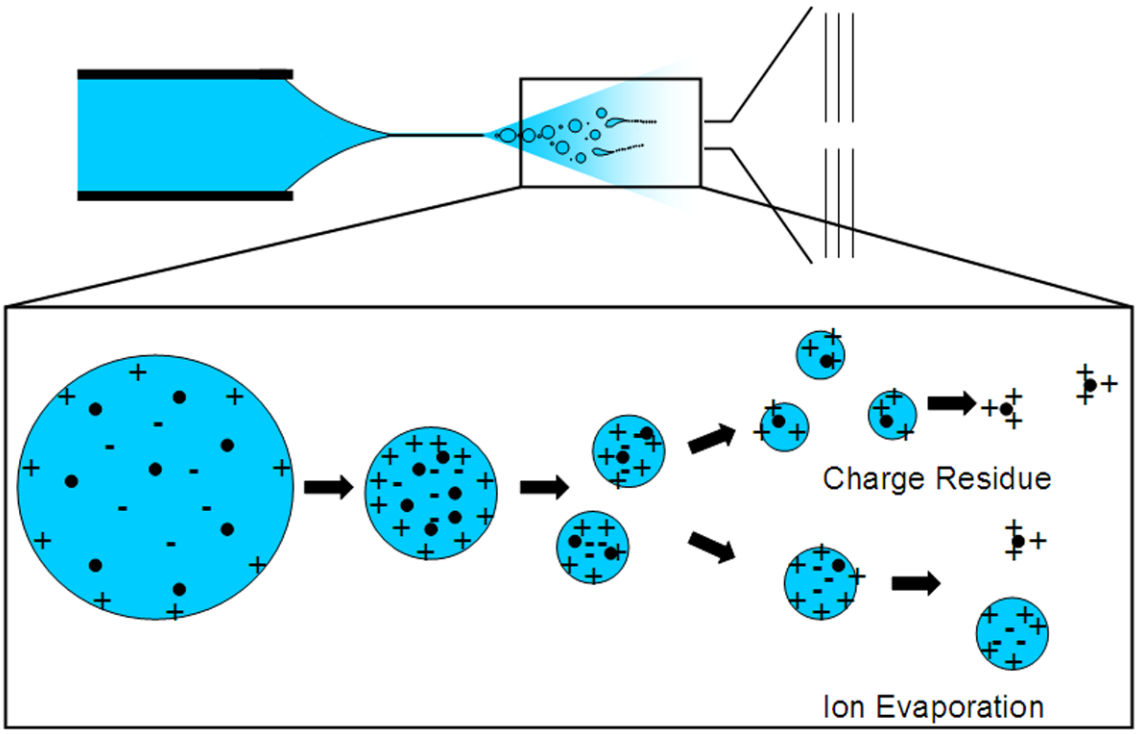

Figure 1.2 Schematic representations of the charge residue[7] and ion evaporation[13] mechanisms for dry ion formation.

gas-phase state.[7,13,15,22] In ESI, all of these processes are interconnected and difficult to investigate independent of one another, thus limiting the current understanding.[10-12,16-17] Analysis of each process independently, uncoupled from the other processes, would therefore be extremely valuable for gaining fundamental insight into the physics of droplet formation and charging under the influence of an electric field.

1.2.1 Assisted Electrospray Ionization

Use of Taylor cone electrospray for liquid atomization and ionization is not without problems and limitations. The large electric potentials required for stable Taylor cone formation, especially at onset of the process, can lead to parasitic electric discharges between the ion source and mass spectrometer inlet, causing sample degradation and

damage to the emitter. This sets a minimum distance between the ion source and mass spectrometer inlet, in effect, limiting droplet collection and ion transmission efficiency to the mass spectrometer. In unassisted ESI sources, the electrohydrodynamically-produced plume of droplets of various sizes results in sample loss due to insufficient droplet desolvation. Taylor cone atomization is also highly dependent on the surface tension of the sprayed solution, making it difficult to achieve a stable spray under conditions of variable solvent composition as typically found in reverse phase LC-MS experiments.[23-24] Organic solvents are often added to reduce solution surface tension; however, these solvents may modify the native conformation of the solutes, resulting in differences between solution-phase and gas-phase conformations of biomolecule ions.[25-26] Clogging and gas bubble formation due to high voltage operation also negatively affect the spray stability and sample throughput.

In an effort to overcome some of these limitations, several ion source designs were developed utilizing pneumatically-assisted and piezo-assisted electrospray. Pneumatically-assisted ESI, Figure 1.3, incorporates a concentric nebulizing gas flow that assists liquid dispersion/droplet formation and droplet desolvation. The nebulizing gas flow enables spraying of high surface tension solutions, e.g. purely aqueous, and at higher solution flow rates. Pneumatically-assisted ESI, with its ability to spray a larger range of solutions at high flow rates, has become popular for coupled liquid chromatography and mass spectrometry analyses (LC-MS).[27-28] Another category of assisted sources utilizes a piezoelectrically-driven (squeeze mode) ultrasonic nebulizer to assist the electrospray ionization process by causing breakup of the liquid jet.[29-32] This ultrasonic nebulizer configuration decouples spray formation from ionization, allowing

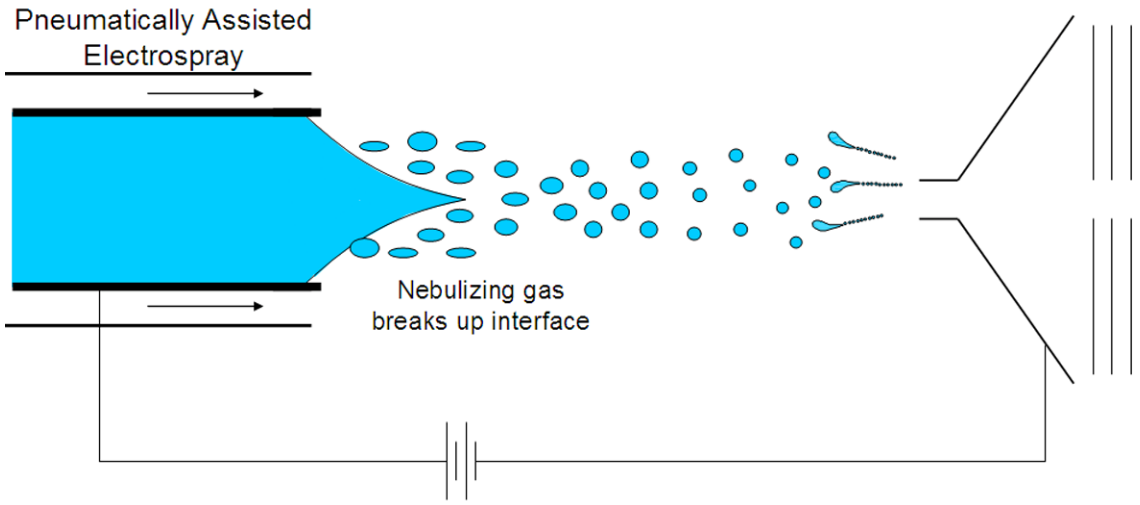

Figure 1.3 Schematic of pneumatically-assisted electrospray ionization, commonly used with higher surface tension solvents and higher flow rate applications. Pneumatically-assisted ESI is often coupled with liquid chromatography or other separation technique.

one to spray high surface tension solvents with throughput up to 100's of μL/min with efficient and stable ionization. While this device produces an improved signal-to-noise ratio (S/N) and flexibility in solvent composition, it suffers from instabilities due to temperature fluctuations, resulting in surface tension variations and thus changes in the wavelength of the acoustically-pumped surface capillary waves. This temperature-dependent fluctuation of capillary waves made it difficult to tune the driving piezoelectric transducer to achieve an efficient resonant operation, which in turn yielded unstable ejection and poor stability of MS measurements.[29-30]

1.2.2 Nanoelectrospray Ionization (nanoESI)

Since this initial breakthrough, numerous improvements upon the basic ESI source have been developed, most notably, the introduction of pressure-assisted microelectrospray and nanoelectrospray ionization (nanoESI).[33-35] A need for increased sensitivity and minimization of sample volume in proteomics has established nanoESI as

the preferred ion source. Nanoelectrospray utilizes capillary tips with diameters as small as 1-3 μm (typically below 10 μm), creating significantly smaller droplets, which results in 10-100 times greater sensitivity of MS analysis as compared to conventional ESI from larger capillaries. A decrease in the capillary size also results in reduction of voltages to the level as low as 900 V_{dc} required for sufficient electric field focusing enabling stable Taylor cone formation.[34] However, capillary nanoelectrospray also has a number of limitations, including low sample throughput, sensitivity to clogging and blocking bubble formation, capillary degradation from electric discharges, and reproducibility difficulties in making such small orifices from pulled capillaries.[36] Several attempts have been made at solving the throughput limitation with multiple capillary sprayers, all operating in parallel.[37-39] These multiple-sprayer systems, however, become too bulky and unpractical in operation, thus promoting a recent trend toward microfabricated devices.

1.2.3 Micromachined ESI Sources

Concurrent with the evolution of ESI techniques, there has been a strong momentum to develop miniaturized sample introduction platforms and lab-on-a-chip ion sources. Microfabricated nanoelectrospray devices enable high-throughput analysis, improved reproducibility, avoid cross contamination between samples, and enable a direct path to coupling with on-chip microfabricated separation columns.[40-41] The microfabrication techniques used for the batch fabrication of electrospray devices can be categorized as follows: (1) ESI devices incorporating fused silica capillary emitters,[42-49] (2) devices that generate ESI from a microchannel exiting the blunt edge of a wafer,[50-57] and (3) monolithic devices incorporating etched ESI tips.[58-65] Within these broad classifications, a number of very interesting device structures have been demonstrated. In

one instance, a 100 nozzle array was fabricated using microfabrication techniques, allowing a 96-well microtiter plate to be processed without reusing a nozzle.[61] Cross contamination is virtually eliminated; however, throughput is still limited. Another device increased throughput with a 3x3 array of Taylor cone emitters.[63] This configuration results in an increased ion current and sensitivity. Although many of these devices lead to enhancements in some aspects of gas phase ion production, they still rely on strongly-electrically-biased nozzles to generate Taylor cone electrospray.

1.3 AMUSE Ion Source

The AMUSE (Array of Micromachined UltraSonic Electrospray) ion source conceptually differs from classical capillary ESI by independently controlling analyte charging/charge separation and droplet/ion formation processes, thus allowing for low voltage soft ionization of a variety of analytes and flexibility in the choice of solvents.[66] This ion source has the potential to eliminate many above described limitations of conventional ESI sources.

1.3.1 Key Ideas

The AMUSE ion source provides a multifunctional interface between liquid chromatography and mass spectrometry for high-throughput and multiplexed bioanalysis. The unique advantage of the AMUSE ion source is its ability to: (1) decouple aerosol/droplet formation from droplet charging, thereby dramatically reducing the ionization potential and flexibility in solvent choice, and (2) adopt a discrete (i.e., drop-on-demand) rather than continuous (i.e., jet-based) approach for controllable generation of charged droplets, thus reducing samples size while maximizing sample utilization. The AMUSE technology can accommodate sample flow rates from 10's of nL/min to 100's of

μL/min and is batch microfabricated in silicon, providing inexpensive and potentially disposable devices, inherently suitable for multiplexed sample analysis.

As shown schematically in Figure 1.4, the AMUSE ion source consists of three main components: 1) a piezoelectric transducer operating in MHz frequency range to generate ultrasonic waves at a resonance frequency of the sample reservoir structure, 2) a micromachined silicon wafer containing an array of pyramidal nozzles that focus the ultrasonic waves, amplifying the pressure gradient at the nozzle apex, and 3) a spacer layer, defining a leak free sample reservoir that allows efficient transfer of ultrasonic energy to the liquid sample. The focused acoustic pressure gradient at the nozzle orifice

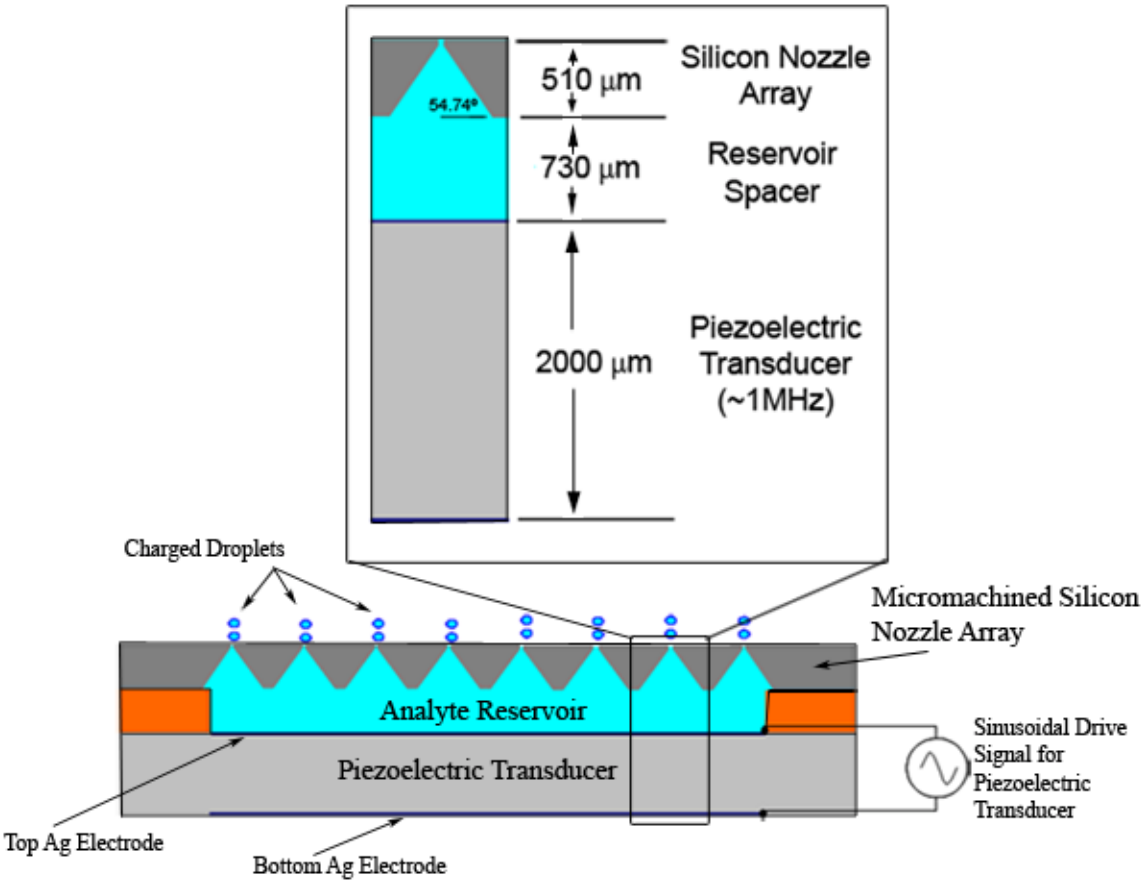

Figure 1.4 AMUSE ion source schematic with representative dimensions of the piezoelectric transducer, sample reservoir, and microfabricated silicon nozzle array for acoustic wave focusing.

accelerates the fluid, ejecting droplets of diameter ~3-5 μm (defined by the nozzle apex size) during every cycle of the sinusoidal drive signal. The AMUSE ion source in its basic form can be run in an RF-only mode, using only the weak electric field of the piezoelectric transducer's drive signal and ion mobility asymmetry for charge separation and droplet charging. Alternatively, an external electric field (DC or AC) can be used to enhance droplet charging via electrokinetic charge separation. In this case, an electric potential is applied to the internal electrode of the piezoelectric transducer relative to an external counter electrode, creating a charge-separating electric field. An in-depth consideration of electric field configurations and electrohydrodynamics of droplet charging is the main focus of this thesis work.

1.3.2 Review of Prior Work on Droplet Generator

The foundation for the AMUSE ion source is a micromachined ultrasonic droplet ejector that utilizes piezoelectric actuation, cavity resonances, and acoustic pressure wave focusing properties of liquid horns to achieve efficient droplet ejection.[67-69] This droplet ejector provides low-power and low-temperature operation with the capacity to scale throughput for the desired application, and is made using a simple, low-cost batch microfabrication process.

1.3.2.1 Droplet Formation and Ejection Physics

As it has been previously established,[68] efficient droplet ejection is achieved at the acoustic cavity resonances of the fluid reservoir, where a standing acoustic wave is formed, drastically elevating the pressure gradient locally at the nozzle orifice, resulting in droplet ejection. The elevated pressure gradient at the nozzle orifice accelerates the fluid, ejecting droplets slightly larger than the nozzle diameter periodically with the

sinusoidal drive signal (droplet size depends on the nozzle orifice and frequency of operation).[67]

Finite element analysis (FEA) of the droplet ejector and associated liquid horn structure using ANSYS[70] confirms the acoustic wave focusing by the nozzle "horn" structures and accurately predicts the resonant frequencies of stable operation.[67-68] The pyramidal horns can be readily fabricated in silicon by exploiting an anisotropic wet etch. The ultrasonic droplet ejector has been shown to successfully atomize a variety of liquids, including water, methanol, kerosene, high viscosity measles vaccine solution (>100 times more viscous than water), glycerol, polyethylene glycol (PEG)/water mixtures, and standard cell media.[71]

The droplet formation and ejection physics of the baseline design of the ultrasonic droplet ejector have previously been characterized, using high-spatial-resolution

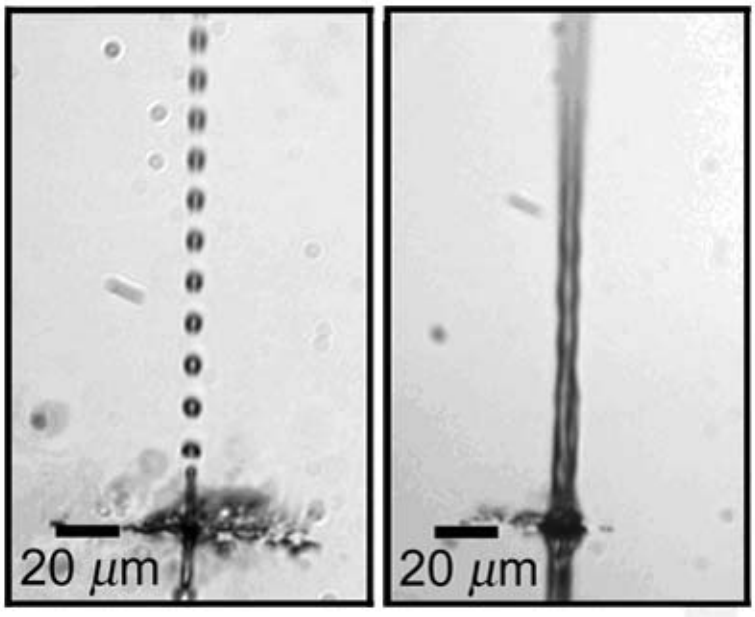

Figure 1.5 Stroboscopic images of droplet ejection (left) from a 4.5 μm orifice operated at a driving frequency of 0.784 MHz and continuous jet (right) from at 15.7 μm orifice operated at driving frequency of 0.883 MHz. (Adapted from Meacham 2006[67])

stroboscopic visualization of fluid ejection, scaling analysis, and computational fluid dynamics (CFD) simulations. A basic understanding of the physics and parameters governing modes of ejection, ranging from individual (discrete) droplets to continuous jet (Figure 1.5), was developed and used to control the ejection regime.[68-69]

1.3.2.2 Mass Spectrometric Characterization

An MS characterization of the AMUSE ion source demonstrated sensitive ionization of peptides/proteins in purely aqueous solutions at micromolar concentrations.[72-73] A number of proteins (e.g., cytochrome c), peptides (e.g., leucine enkephalin), and smaller tuning compounds (e.g., reserpine) were successfully analyzed in both an RF-only mode and with weak DC electric fields (Figure 1.6). The effect of incorporating a Venturi™ device (air amplifier) for droplet collection and desolvation and influence of the nozzle orifice size were also examined.[73-74]

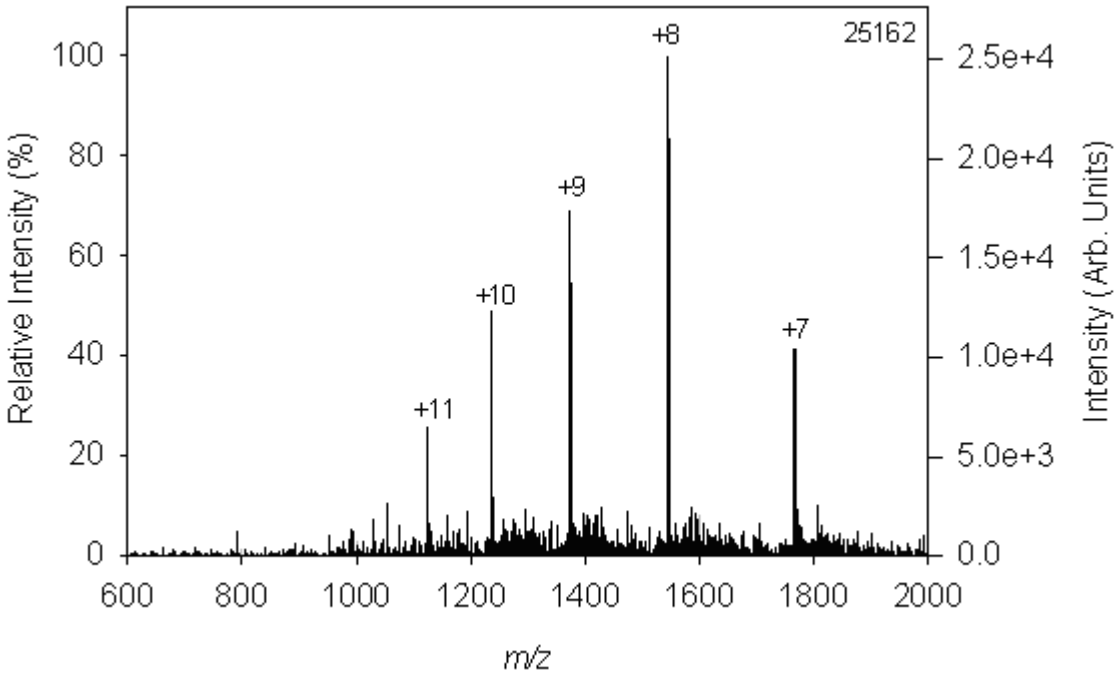

Figure 1.6 Mass spectra for cytochrome c in 99.9:0.1 (v/v) water: acetic acid operated in RF-only mode, coupled to a venturi device. (Adapted from Hampton et al. 2007[73])

More recently, a side-by-side comparison of internal energy deposition between conventional ESI and AMUSE shows that a superior "softness" of analyte ionization can be achieved by AMUSE under certain operation conditions.[75] Internal energy deposition was measured using the "survival yield" method, which correlates the fragmentation extent of a thermometer molecule to the internal energy deposited during ionization (i.e. electrospray ionization or mechanically-driven droplet-based AMUSE ionization). In experiments without an air amplifier, AMUSE demonstrated the capability for softer ionization than ESI, while producing at least a fivefold higher signal-to-noise ratio (sensitivity).[74-75]

1.4 Research Objectives

The modeling and experimental work of this thesis aims to provide an in-depth understanding of ionization in the Array of Micromachined UltraSonic Electrospray (AMUSE) ion source. It is expected that much of the results can be expanded to other mechanically-driven droplet-based ion sources, as well as various application fields beyond mass spectrometry where ultrasonic droplet generation can be used. The major objectives of the present research are as follows:

1. Developing an understanding of analyte charging/charge separation mechanisms and associated transport phenomena in droplet-based ion sources.
2. Developing an understanding of the effect of DC and AC electric fields on droplet ejection and charge separation in droplet-based ion sources.
3. Developing design and operating guidelines for improving the operation of a novel droplet-based micromachined ion source, AMUSE.

4. Demonstration of the AMUSE ion source capabilities for ionization of representative compounds relevant to biomedical research.

1.5 Thesis Organization and Overview

The AMUSE ion source introduces the unique opportunity to independently control charge separation and droplet formation. This thesis research is focused on the underlying physics of charge transport and droplet charging in the AMUSE ion source. It develops a basic understanding of analyte charging, electrohydrodynamics of charge separation, and droplet ejection in the AMUSE ion source through complimentary theoretical and experimental investigations. This analysis is completed through the use of computational electrohydrodynamic simulations in concert with charging measurements and stroboscopic visualization of ejection phenomena under applied DC and AC electric fields. The main goal of the present research is to gain an understanding of the fundamental physics of analyte charging and electrohydrodynamic charge separation in order to develop optimal design and operation guidelines for the AMUSE ion source.

This thesis is organized as follows: Chapter 2 reviews the batch fabrication process and leak-free robust assembly and packaging of the AMUSE ion source developed in this work. Various loading configurations (online and offline loading), sample reservoir volumes (number of nozzle available), and flow rates (operation duty cycle) that AMUSE can cover are presented. A dual-sample multiplexed AMUSE device is developed using the principles of acoustic field isolation. Acoustic response simulations are used to confirm device design methods that isolate pressure wave focusing and identify resonant frequencies for power efficient ejection from individual

domains. Isolated ejection from specified domains of the device is experimentally demonstrated under conditions established in the simulations.

Electrohydrodynamic simulations of analyte charging and ion transport in the AMUSE ion source are described in Chapter 3. Heterogeneous electrochemical ion introduction and homogeneous acid dissociation are considered as the two main origins of adduct ions for analyte charging. A detailed electrohydrodynamic (EHD) computational model of charge transport during droplet formation cycle in the AMUSE ion source is developed. Coupling of the fluid dynamics, pressure and electric fields, and charge transport in a multiphase system is described. The EHD model is validated by simulating the transient cone-jet formation in spraying an electrically-conductive fluid with finite conductivity and the Taylor cone formation of a perfectly electrically-conductive fluid. Charge separation in the AMUSE ion source, under both DC and AC electric fields of varying amplitude and phase relative to the mechanical (actuator) pressure field, is investigated and reported in detail.

In Chapter 4, experimental characterization of charge separation in the AMUSE ion source is presented using dynamic charge collection measurements and optical visualization of ejection phenomena. Experimental measurements of electrical current correlated with ejected mass are used to evaluate a charge-per-droplet for qualitative and quantitative comparison with simulated results. These data, in combination with a charge transport time scale analysis, allow identification of different modes of droplet charging depending on dominant transport process, which is in turn determined by the external electric field, bulk charge density, and frequency of device operation. High-spatial-resolution stroboscopic visualization of droplet ejection under the influence of varying

electric field magnitudes is also presented. A time scale analysis of the ejection phenomena with independently controlled mechanical and electric actuation is developed to establish the relationship between dimensionless parameters that determine ejection regime. This results in a predictive ejection regime map, useful for optimal design and operation of the AMUSE ion source.

Finally, Chapter 5 summarizes the results of AMUSE ion source application for mass spectrometric detection of a number of proteins, peptides, and pharmaceutical molecules. The MS response to a common tuning compound, reserpine, is investigated in detail as a function of the charge separating electric field applied across the AMUSE ion source. Improvements in signal abundance, signal-to-noise ratio, and signal stability are shown to be in agreement with the electrohydrodynamic charge separation framework developed in previous chapters. Several specific examples, in which the AMUSE ion source has the highest potential for breakthrough, are also briefly discussed.

The thesis concludes with Chapter 6, where recommendations are made for interesting venues and remaining open questions for future work on the AMUSE and other mechanically-driven droplet-based ion sources.

CHAPTER 2

AMUSE ION SOURCE DESIGN

Recent developments in microfabrication techniques and a push toward lab-on-a-chip devices have introduced numerous miniaturized electrospray ionization (ESI) sources for mass spectrometry (MS), including some which are available through commercial vendors (e.g., Advion Nanomate™[76]). Microfabrication methods allow for batch fabrication of many identical structures. This introduces an obvious path to high-throughput systems with many parallel ESI streams. Comprehensive reviews are available in the literature covering these microfabricated devices.[40,77]

Multiplexed operation of ion sources allow for numerous samples to be analyzed synchronously, significantly reducing analysis time and expanding MS capabilities for analyzing multiple analyte streams eluted from chromatographic separation. Also, with a multiplexed setup, an internal standard can be continuously and simultaneously ejected into the MS, allowing for quantitative analysis and mass calibration.[78] At present, most demonstrated multiplexed ion sources consist of numerous individually-controlled conventional ESI capillaries operated in parallel. In some cases, dual capillary ESI sources are mounted on a mechanical platform that uses a motor to shift between them.[78-79] In other cases, many parallel capillary ESI sources are mounted on a translational stage and multiplexing is achieved by moving the stage of continuously ejecting devices. Both device types enable, in principle, multiplexed operation, but result in spillover losses of analytes and require the additional burden of an automated system for sample selection.[80-82] Microfabricated two-dimensional arrays of ESI nozzles have been shown to result in

high-throughput MS analysis.[62-63,83] However, transition from high-throughput to multiplexed operation has been elusive, and until now, limited to demonstration of successive spraying of different samples using one-dimensional arrays.[51,57] The AMUSE ion source, which utilizes batch microfabrication techniques to produce an array of identical nozzles, provides a direct path to realizing a multiple-sample ion source for bioanalytical mass spectrometry with easy coupling to up-stream multi-channel liquid chromatography or other sample separation devices. With the introduction of various microfabricated separation systems, the development of a truly lab-on-a-chip multiplexed ion source for MS applications becomes foreseeable.

2.1 AMUSE Fabrication and Assembly

As introduced in Chapter 1, the AMUSE ion source is based on a micromachined ultrasonic droplet ejector array. The micromachined silicon wafer, containing a pyramidal array of nozzles (ejector plate) that focus the ultrasonic waves, is fabricated using a simple two-mask process. The process flow diagram is shown in Figure 2.1. Initially, a (100) oriented silicon wafer is cleaned and prepared for silicon nitride deposition (Figure 2.1(1)). Approximately, 1 μm of silicon nitride (Si_3N_4) is deposited on the back-side of the wafer using plasma enhanced chemical vapor deposition (PECVD), to act as the nozzle base mask for the subsequent wet etch. The etch rate of silicon nitride in potassium hydroxide (KOH) is negligible, making it an excellent wet etch mask material. On the front-side, an approximately 2 μm silicon nitride layer is deposited in the same manner to act as the orifice membrane and wet etch stop (Figure 2.1(2)). The back-side of the wafer is then patterned using a positive photoresist and standard photolithography techniques (Figure 2.1(3)). The nozzle base pattern, consisting of a 20x20 array of

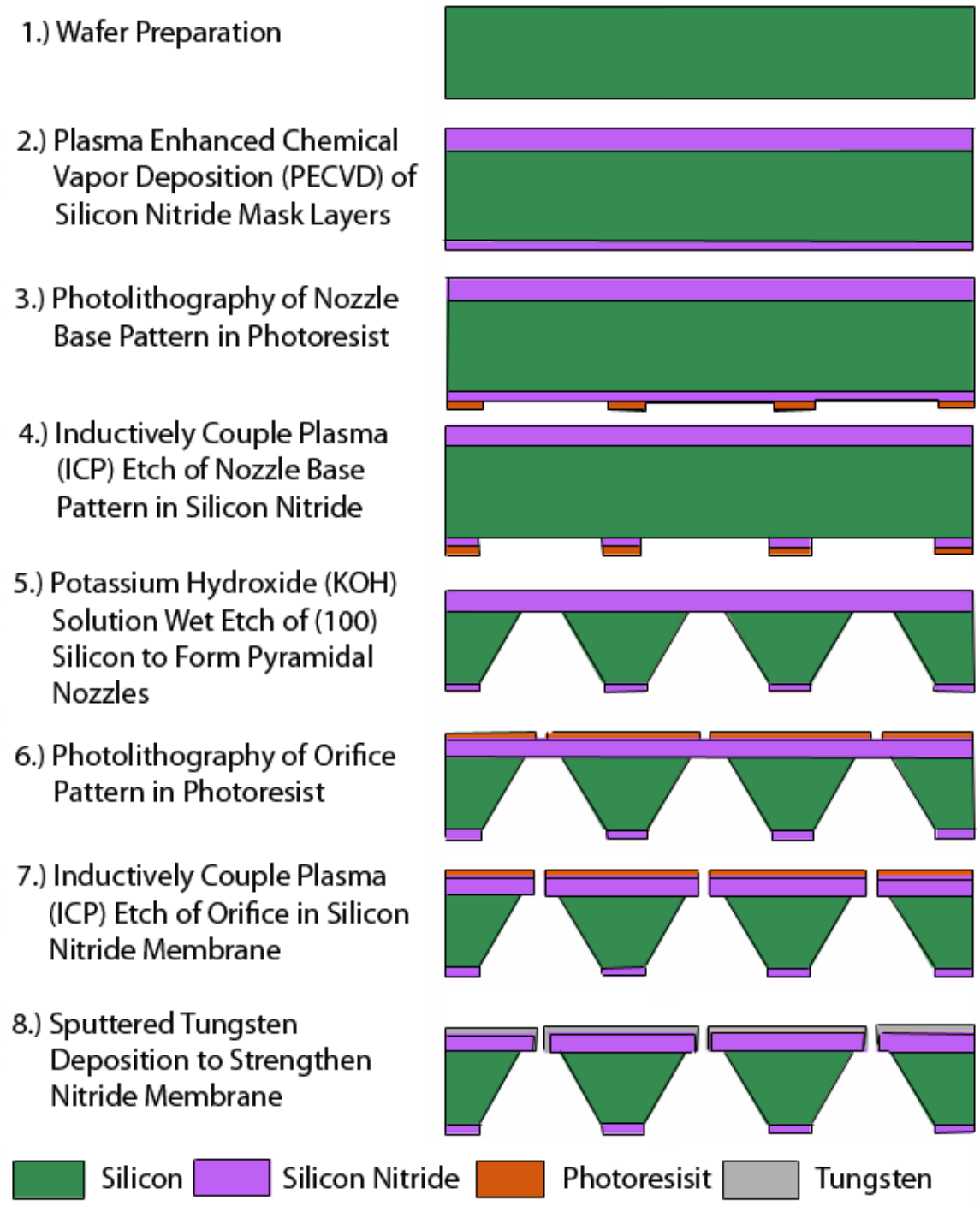

Figure 2.1 Ejector pyramidal array fabrication process: 1) wafer preparation, 2) PECVD deposition of silicone nitride (Si_3N_4) mask layer for wet etch and membrane for orifice creation, 3) photolithography of nozzle base pattern in positive photoresist, 4) ICP etch of nozzle base pattern in Si_3N_4, 5) potassium hydroxide (KOH) anisotropic wet etch of pyramidal nozzles in (100) oriented silicon, 6) photolithography of orifice pattern in positive photoresist, 7) ICP etch of orifice in Si_3N_4 membrane, 8) DC sputtered tungsten deposition to strengthen membrane.

squares, is etched into the silicon nitride mask layer using an inductively coupled plasma (ICP) dry etch (Figure 2.1(4)). The array of squares determines the size of each nozzle base, which in turn determines the membranes size on which the nozzle orifices are etched.

The anisotropic wet etch in potassium hydroxide produces the desired pyramidal structures. The anisotropic etching exposes the (111) plane of the silicon lattice as the nozzle walls at an angle of 54.74º to the surface oriented with the (100) plane (Figure 2.1(5)). The wet etch terminates in small nitride membranes (8-20 μm) on the front-side of the wafer. Upon completion of the wet etch, the nozzle orifices, centered on the nitride membranes, are patterned on the front-side using a photolithography process (Figure 2.1(6)). The nozzle orifices are then etched through the nitride using an ICP dry etch (Figure 2.1(7)). Finally, to strengthen the membranes, a 50 nm titanium seed layer to promote adhesion and a 0.5-0.75 μm thick layer of tungsten is DC sputtered onto the front-side of the array (Figure 2.1(8)). The deposition is conformal and will reduce the diameter of the nozzle orifices produced in the previous step. Additional descriptions of the photomask layout, alignment marks and techniques, and misalignment issues are provided elsewhere.[67] Figure 2.2 provides scanning electron microscope (SEM) images of the silicon nitride and tungsten membrane with the etched nozzle orifice.

The AMUSE ion source is assembled in a simple stack configuration. The three main components at the foundation of the AMUSE ion source (Figure 2.3) are (1) a piezoelectric transducer, generating ultrasonic waves; (2) a micromachined silicon array of pyramidal nozzles, whose fabrication was just covered; and (3) a spacer layer, defining the sample reservoir. The device package was devised to incorporate a leak-free sample

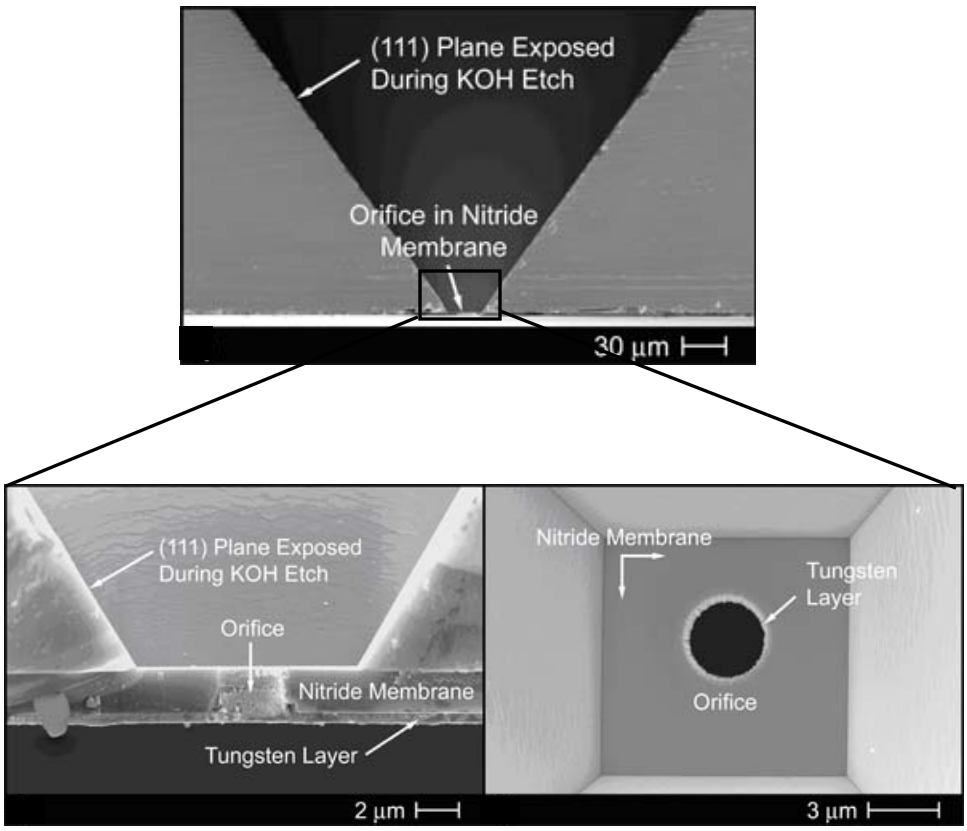

Figure 2.2 Scanning electron microscope (SEM) images of the silicon nitride/tungsten membrane (11 µm on a side) and nozzle orifice (4.5 µm diameter). (Adapted from Meacham 2006[67])

reservoir with simple assembly and packaging. The spacer layer defines the sample reservoir(s) and is composed of numerous sheets of a Kapton™ polyimide tape (manufactured by DuPont) adhered to each other. This allows for easy alterations in the reservoir height, which defines the frequency of cavity resonant modes resulting in efficient droplet ejection. A silicone rubber gasket is inserted to provide a seal for different compartments of the multiplexed fluid reservoir. Polyetheretherketone (PEEK) tubes are inserted through holes in the Kapton spacer and silicone rubber seal, at the side walls, to deliver fluids to the reservoirs. The structure is capped with a nozzle array microfabricated in silicon as described in Figure 2.1. An additional silicone support and

metal frame are used to provide structural integrity to the overall assembly. Finally, the assembled ejector package is held together by a spring-loaded mechanical clamp around the edges which is designed to provide a uniform spatial distribution of the mechanical load.

As mentioned in the introduction of the AMUSE ion source, in its basic form it can be run in an RF-only mode, using only the weak electric field of the piezoelectric transducer's drive signal for charging. To be shown in the later chapters of this thesis,

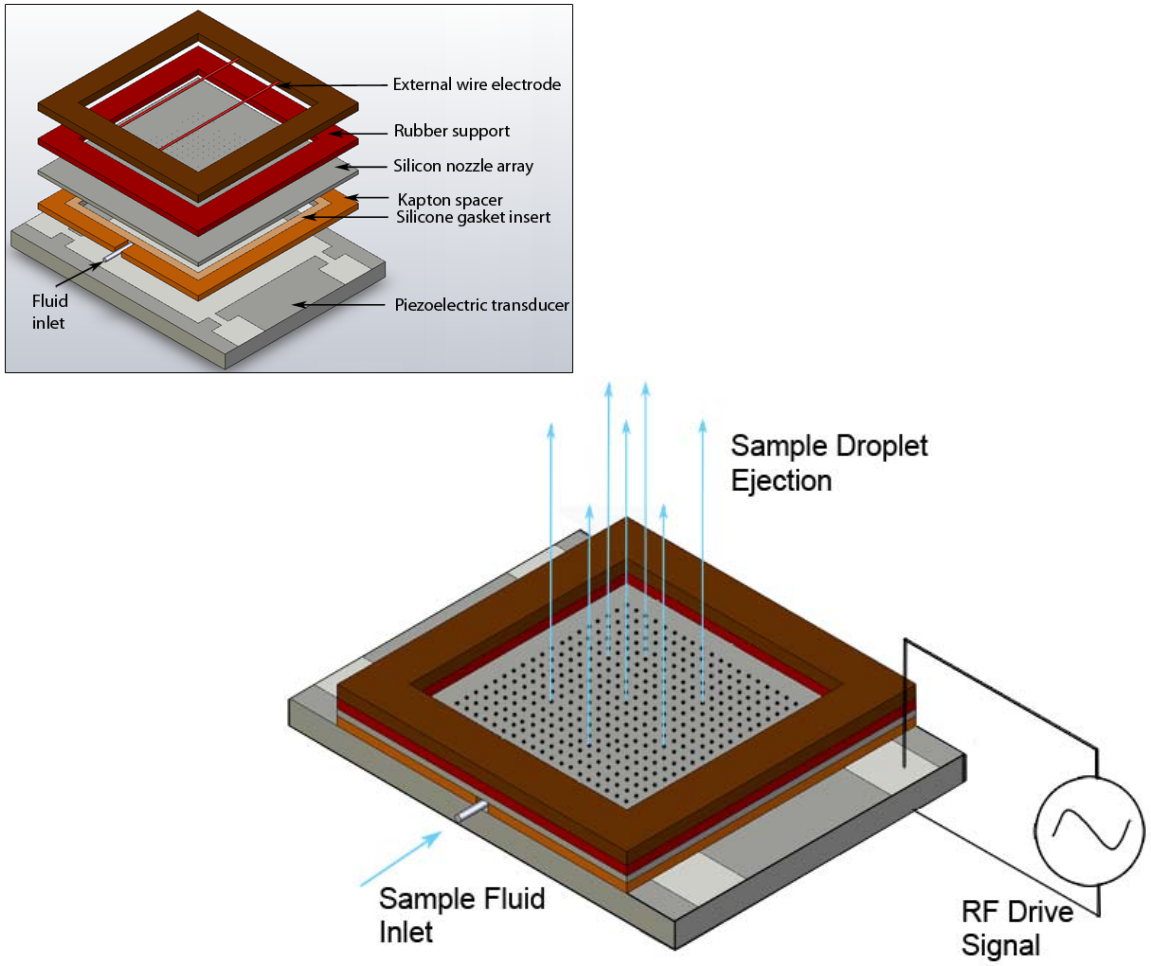

Figure 2.3 AMUSE ion source schematic (inset: exploded view with external counter electrode) of layered assembly consisting of: piezoelectric transducer, Kapton spacer with silicone gasket insert for leak-free fluid reservoir and compression fit fluid inlet, microfabricated silicon nozzle array for acoustic wave focusing, rubber support layer, and external wire electrode for charge separation electric field application.

this provides inefficient droplet charging. On the other hand, static (DC) and dynamic (AC) external electric fields can be used to enhance charge separation and droplet charging. Here, the electric field is applied between the internal electrode of the piezoelectric transducer and an external counter electrode, as shown in Figure 2.3(inset). These aspects will be covered in greater detail in the following chapters.

2.2 Device Configurations and Operating Modes

The versatile AMUSE ion source technology can be configured in numerous ways to meet the desired operating input and output requirements. The array format of the droplet ejector makes AMUSE suitable for both parallel high-throughput and multiplexed multi-sample analysis. Various multiplexed configurations of the AMUSE ion source, along with online and offline operation modes, cover a wide range of total sample volume and flow rate specifications.

2.2.1 Flow Rate and Total Volume Operation Ranges

ESI sources are narrowly limited to a specific sample volume and flow rate for which they were designed. In proteomics research using mass spectrometry (MS), a separation step, such as liquid chromatography (LC), is often completed before MS analysis in order to simplify the biomolecule identification. There are numerous types of liquid chromatography: high performance LC (HPLC), microLC, capillary LC, and nanoLC that are each associated with a range of flow rates and sample capacities.[31-32,84-95] For the wide range of LC flow rates, there is a wide range of ESI and other ion sources available to match analysis requirements. NanoESI sources can create electrospray flow rates down into the nl/min range associated with nanoLC. For high flow rates and high throughput analyses, arrays of parallel ion sources can be used.

Table 2.1 Sample specifications for various liquid chromatography options.

	Column i.d.	***Flow Rate (µl/min)***	***Sample Capacity***	***Post Column Volume***	***Sample in Microcolumn Separations***
HPLC	4.6 mm	100-3000	1-200 µg	100-3000 µl	~ 10000 fmoles
MicroLC	1.0 mm	10-100	0.05-10 µg	1-100 µl	~ 1000 fmoles
CapillaryLC	300 µm	1-10	1-1000 ng	100-1000 nl	~100 fmoles
NanoLC	25-100 µm	0.05-1	0.02-0.05 ng	~100 nl	~ 1 fmole

The AMUSE ion source technology can cover a wide range of the LC and available sample size spectrum for proteomics and protein/biomarker identification. A number of configurations enabling a range of flow rates and sample volumes are realizable. Figure 2.4 shows representative configurations as well as the ranges of device operation, from fully-filled nozzle array with online sample loading to single-nozzle operation with offline sample loading.

The two main curves represent online (1-4) and offline (5-10) sample loading. The online sample loading configurations continuously inject the sample into the fluid reservoir requiring larger volumes. The offline loading fills a subset of nozzles in the array and uses water in the spacer reservoir as the surrogate wave coupling fluid. Figure 2.5 provides a few examples of the device configurations represented in Figure 2.4. Configuration 1 represents the full, high-throughput, single-sample device. The nozzle array and fluid reservoir are filled with the sample continuously supplied from LC separation or alternative external reservoir. This option operates with one sample at a time and is the configuration used in the reported AMUSE-MS analyses to date.[72-73,75,96] Configuration 2 displays a dual-sample, multiplexed device with two isolated domains, allowing for individual ejection from one domain or the other. This configuration can hold two sample fluids and eject them successively or simultaneously. To reduce the

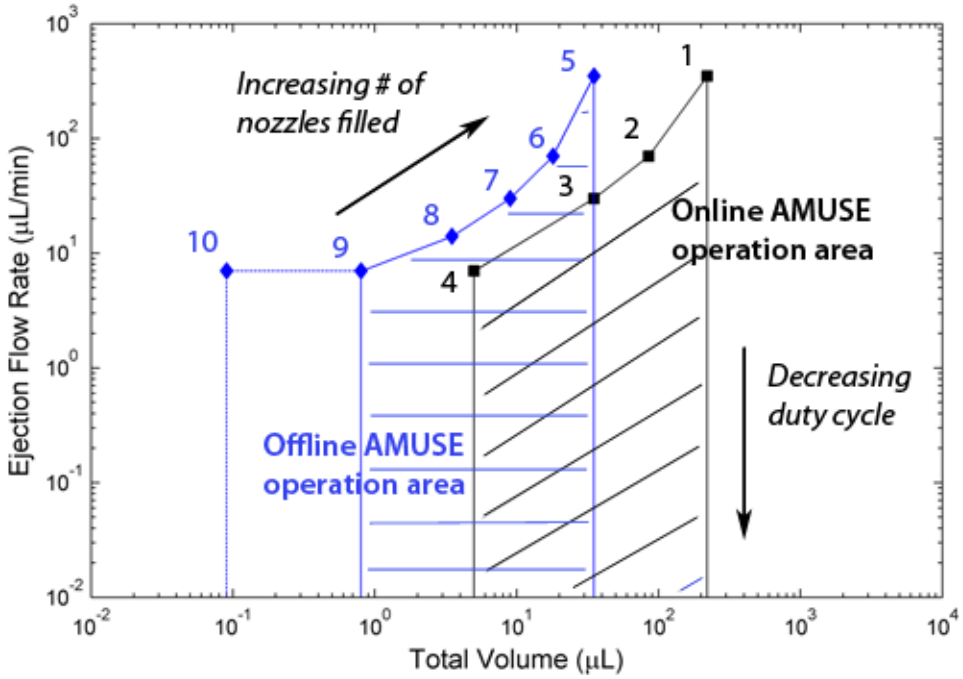

Figure 2.4 Flow rate and sample volume specifications for AMUSE configuration options.

required sample volume, configuration 4 sacrifices the multiplexed operation for a decrease in fluid reservoir size. The fluid reservoir is replaced with a silicone rubber insert that covers all of the nozzles except a 3x3 (or other reduced size) array in the center of the original 20x20 array. This device design maintains online continuous operation of a single-sample stream at a time. Configurations 5-10 eliminate the large amount of sample required to fill the fluid reservoir for wave transmission, by incorporating an offline loading approach. Here, the fluid reservoir is filled with water or other wave transmitting fluid and sample is loaded, offline, into each of the 400 individual nozzles. The two fluids are separated by a thin diaphragm, composed of a wave transmitting rubber. The sample is loaded and placed onto the device and ejected until depleted. The offline configuration can be combined with the various multiplexed online configurations to match the available sample volume.

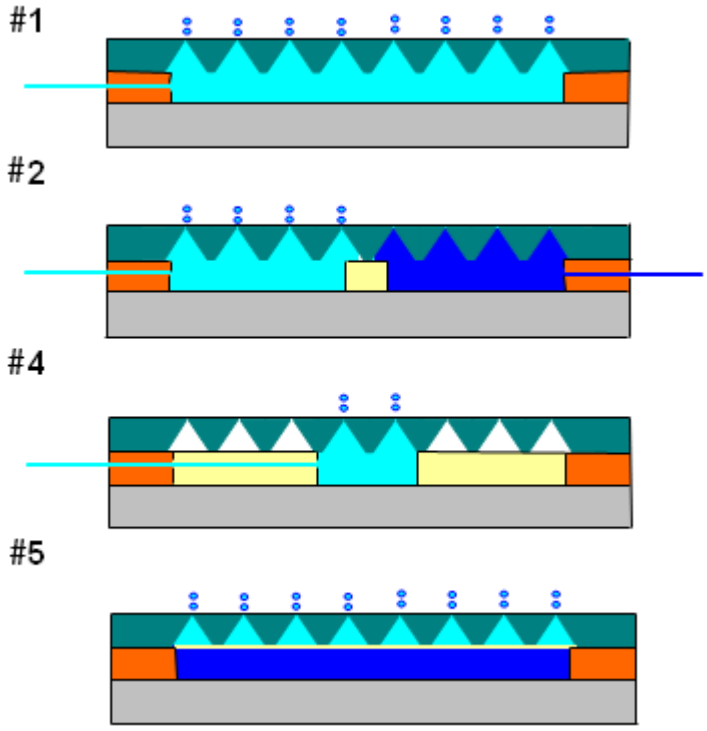

Figure 2.5 Schematics displaying various configurations of AMUSE from Figure 2.4 that have been demonstrated, 1 – Full, single sample (online), 2 – Dual-sample multiplexed (online), 4 – Reduced reservoir, single sample (online), 5 – Full, single sample (offline).

The areas below each curve are included in the device's operational range because the device allows for complete control over flow rate and ejection. Flow rates can be decreased by control of the operation duty cycle (percentage of a time period that the RF signal is applied to the piezoelectric transducer). This allows the online configurations to accommodate the full range of LC flow rates. The offline configurations do not require matching LC flow rates. In these devices, the sample fractions would be initially separated and collected, and then loaded into the desired number of wells of the microarray and ejected/ionized for MS analysis. The data point 10 in Figure 2.4 is left with dotted lines because it has proven difficult to eject from a single nozzle

independently with the baseline device design utilizing a bulk piezoelectric transducer. Using alternative transducers, such as capacitive micromachined ultrasonic transducers (CMUTs),[97-98] should allow one to overcome the challenge of single nozzle ejection.

2.3 Multiplexed Dual-Sample Device

To demonstrate the concept of the multiplexed device, a dual-sample configuration with two sub-domains is used.[99] Multiplexing of the micromachined ultrasonic droplet ejector is approached by partitioning the fluid reservoir and the nozzle array of the monolithic device into sub-domains with individual control of ejection. Figure 2.6 shows a schematic representation of the implemented multiplexed device. The fluid reservoir is partitioned into two chambers, providing separate sub-reservoirs for each sub-domain, to decouple the fluid streams introduced into the device. A compliant material, silicone rubber, is used as the reservoir separation layer so that the motion of the piezoelectric transducer is not restricted in the middle when this layer is compressed to provide a leak-free seal. Silicone rubber also has low acoustic impedance, close to the fluid samples in the reservoirs. Hence, the domain separating gasket does not significantly disturb the quasi-1D acoustic field in the separated fluid domains, as compared to that in a single reservoir of a monolithic device. The hot RF and ground electrodes of the piezoelectric transducer are also partitioned to provide independent control of the electric signals driving the segments of the piezoelectric transducer. This allows one to apply electrical signals with different amplitude, frequency, and phase to control multiplexed operation using the same or different resonant modes of each separate fluid reservoir successively or simultaneously. As discussed in the next section, there are several routes for mechanical energy coupling between the domains, including

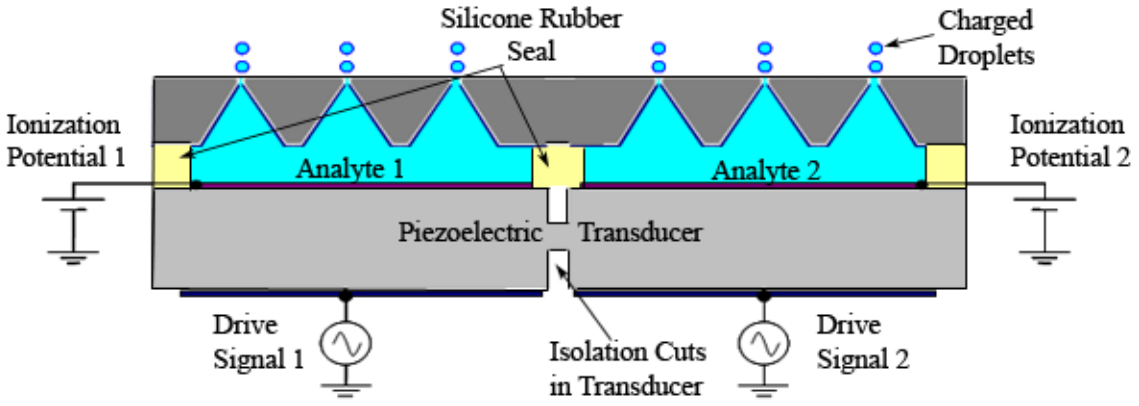

Figure 2.6 Schematic representation of the multiplexed (dual-sample) droplet ejector array.

the piezoelectric transducer itself. To reduce the latter effect, the piezoelectric transducer is diced to a certain depth on both sides, a procedure commonly used to form transducer arrays for medical ultrasound imaging.[100] Although some minor alterations have been made to the original three-component design of the high-throughput, single domain version of the device, the multiplexed device is still simple and easily assembled in a stack configuration.

2.3.1 Dual-Sample Modeling

In order to gain a better understanding of multiplexed operation of the ultrasonic droplet ejector and to aid the design process, the device is modeled using ANSYS[70] finite element software, according to the concepts and operating principles outlined in the previous section. A two-dimensional harmonic response analysis, across the ejector's operational frequency range, is used to simulate a single row of 20 nozzles from the 20x20 nozzle array in the square shaped silicon cover plate. The simulations are used to predict the fluid cavity resonant frequencies and which of the resonance modes result in pressure wave focusing at the nozzle orifice. The simulations provide information on

electrical input impedance of the device, which is then used to predict the electrical input power to the piezoelectric transducer. Also predicted is the acoustic pressure distribution in the sample reservoirs and nozzle cavities. This pressure distribution yields an estimate for the power imparted to the "ejected" fluid volume near the nozzle orifice, whose size is equivalent to that of an ejected droplet. Such a calculation of the imparted acoustic energy (power), when compared to the minimum energy required to produce a droplet (product of the fluid surface tension and surface area of the droplet), allows one to establish a simple criterion for ejection to occur.[68] Although approximate, the results of such an analysis have been shown to agree well with experimental measurements on the single domain ejector.[68-69]

2.3.1.1 Simulation Domain and Material Properties

The simulation domain dimensions, seen in Figure 2.7, of the modeled device closely represent the experimental configuration shown in Figure 2.6. The PZT-8 piezoelectric transducer thickness, t_{piezo}, and width, w_{piezo}, are 2 mm and 24 mm, respectively. The thickness of Kapton and silicone rubber spacer layer, t_{spacer}, determines the fluid cavity height, h_c, and resonant frequencies of operation, while providing a liquid-tight seal. The simulations consider a single 720 μm thick spacer layer, corresponding to the first two cavity resonances in the range of 0.5-1.5 MHz. This will allow the cavity resonance to fall around the piezoelectric transducer's first longitudinal resonance, ~1.12 MHz. The silicon nozzle array thickness, t_{si}, is 510 μm, and the width of the silicone rubber insert dividing the two chambers, w_{insert}, is 2 mm. The cuts in the piezoelectric element are 250 μm wide (w_{cut}), equal to the standard thickness of a dicing

saw blade, and 1.75 mm deep (d_{cut}). In this model as well as the proof-of-concept experiments, water is used as the sample fluid in both reservoirs.

The two-dimensional (2D) variable density mesh is shown in Figure 2.7. The high mesh density in the nozzles allows for adequate resolution of the pressure wave focusing. Previous studies of the baseline droplet ejector array have thoroughly investigated the simulation domain. Convergence studies were conducted to ensure the simulation results

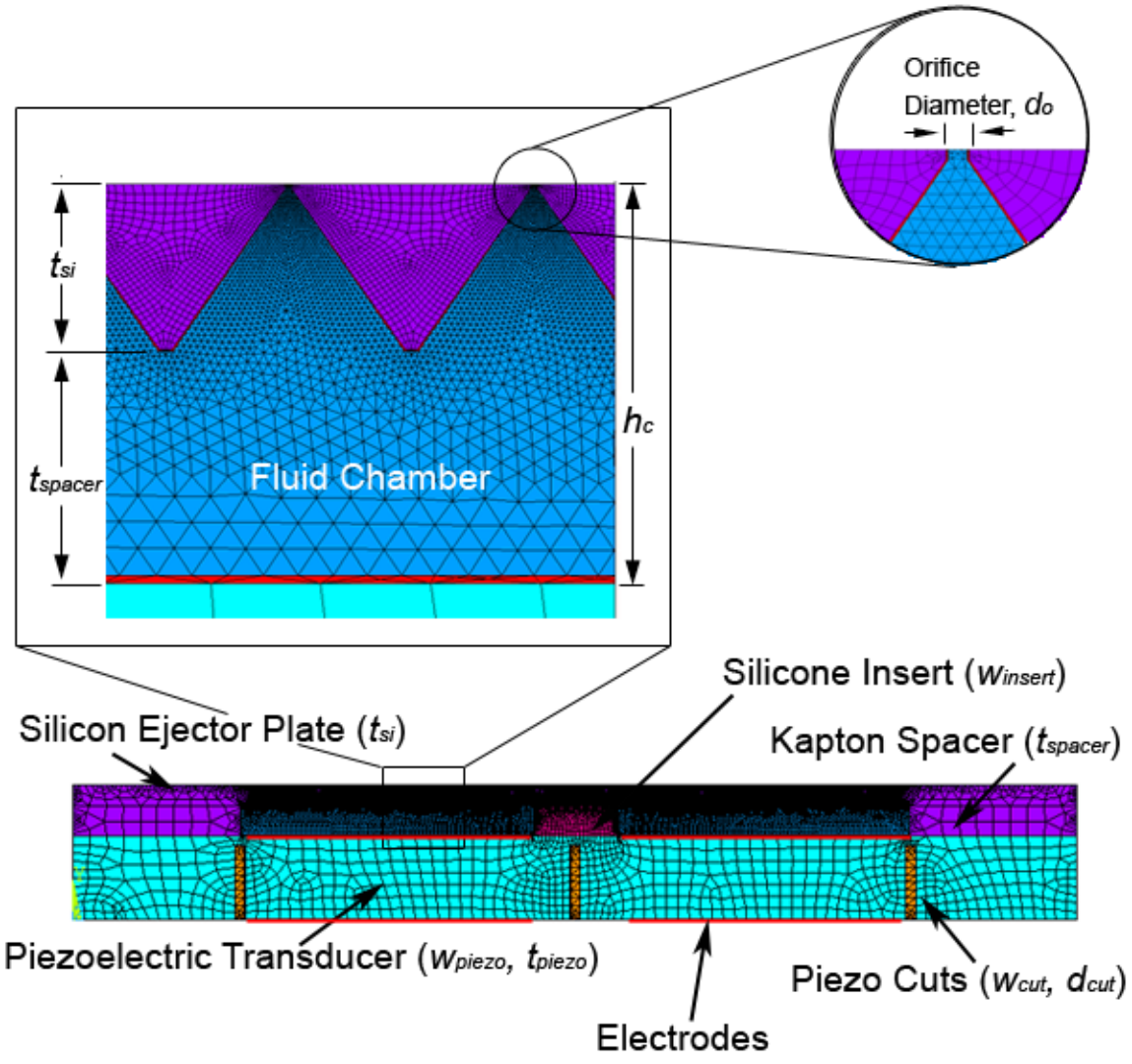

Figure 2.7 Two-dimensional (2-D) computational domain used to perform simulations of the harmonic response of the system using ANSYS.

are independent of mesh size and a three-dimensional (3-D) investigation of a single nozzle geometry has verified that the 2-D simulations accurately capture the acoustic wave focusing of the actual device. A previously completed convergence study found the simulation results to be independent of mesh size.[67] Additional details of the ANSYS model as well as material properties for the solid and fluid domains can be found in Appendix A.

The boundary conditions for the simulation domain consist of the applied voltages and fixed displacement conditions. In the multiplexed dual-sample domain, the representative case considered is for the applied electric signal localized to the right "active" domain and the left domain is electrically grounded, i.e. both the ground and hot electrode are connected to 0V potential. The electrode in the right-hand side active domain is driven with a 30V peak-to-peak AC electric signal. The top surface of the silicon ejector plate is constrained with a zero vertical displacement boundary condition and the pressure (gage) at each nozzle orifice exit is set to zero. All loads and displacements vary sinusoidally at the same known frequency and consist of real and imaginary components.

An extensive validation of the fundamental model methodology and its ability to accurately simulate the acoustic wave focusing of the actual device has been covered elsewhere for the baseline micromachined droplet ejector array.[67] Comparison of the simulated (ANSYS) and experimentally measured (network analyzer: Agilent Technologies, Inc. Model 8753 ES) electrical input impedance of unloaded and water-loaded devices, for a variety of piezoelectric transducer and spacer thicknesses,

demonstrates the ability of the model to accurately simulate the acoustic response with only minor discrepancies.[67]

2.3.1.2 Acoustic Wave Focusing Results

In simulations, the piezoelectric transducer is partially cut in the middle and has two sets of electrodes to allow the application of independent signals to each ejection domain, and also to reduce the cross-coupling of the acoustical and electrical fields. The simulations predict a number of resonance modes in the active domain for the investigated frequency range of 0.5 to 1.5 MHz as well as the piezoelectric transducer's first longitudinal resonance. Figure 2.8 shows the simulated electrical input impedance for the described dual-sample configuration as a function of frequency. The electrical input impedance is calculated as, $Z = V/i_{piezo}$, where V and i_{piezo} are the voltage applied and current through the piezoelectric transducer, respectively. The piezoelectric

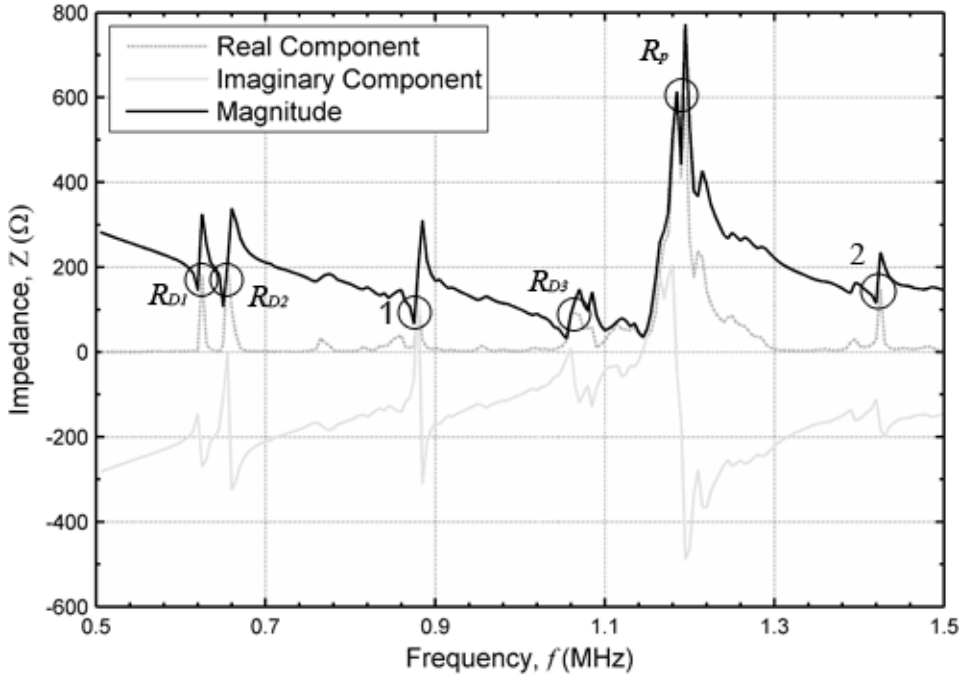

Figure 2.8 Simulated electrical input impedance as a function of piezoelectric driving signal frequency for the dual-sample multiplexed droplet ejector array.

transducer current is calculated from the displacement current, i_{ANSYS}, provided by the ANSYS 2-D harmonic response analysis.[70] These currents are related by $i_{piezo} = j\omega d_{piezo} i_{ANSYS}$, where $j = \sqrt{-1}$, ω is the angular frequency, and d_{piezo} is the depth of the piezoelectric transducer. The piezoelectric transducer's first longitudinal open-circuit resonance, R_p (~1.2 MHz), falls slightly higher than the expected ~1.12 MHz resonance for a 2mm thick element. However, the isolation cuts made to the piezoelectric transducer are expected to cause slight variations in the electrical impedance. Figure 2.8 also identifies a number of other resonance modes at 0.63, 0.66, 0.88, 1.05, and 1.425 MHz that may or may not correspond to cavity resonances and acoustic wave focusing.

In order to identify those resonance modes which result in efficient acoustic wave focusing, electrical input power and power transfer to the fluid are investigated. Figure 2.9 displays the electrical input power to the piezoelectric transducer and the power imparted to the ejected fluid. Power imparted to the fluid is calculated with the approximate kinetic energy imparted to a single droplet. The kinetic energy imparted to a droplet is estimated using the average acoustic velocity of the fluid at the nozzle orifice, $KE_d = \frac{1}{2}\rho \forall_d u_d^2$. Here, ρ is the fluid density, $\forall_d$ is the droplet volume (assuming droplet of radius equal to the orifice radius[67]), and u_d is the estimated droplet velocity. Therefore, assuming a droplet is ejected from every nozzle, *N*, for each cycle at driving frequency, f, the total imparted to the fluid is, $P_F = fN\left(KE_d\right)$. Again, this is an approximation, neglecting losses and assuming all nozzles are ejecting. The electrical input power to the piezoelectric transducer is calculated by, $P_E = V\,\mathrm{Re}\left(i_{piezo}\right)$.

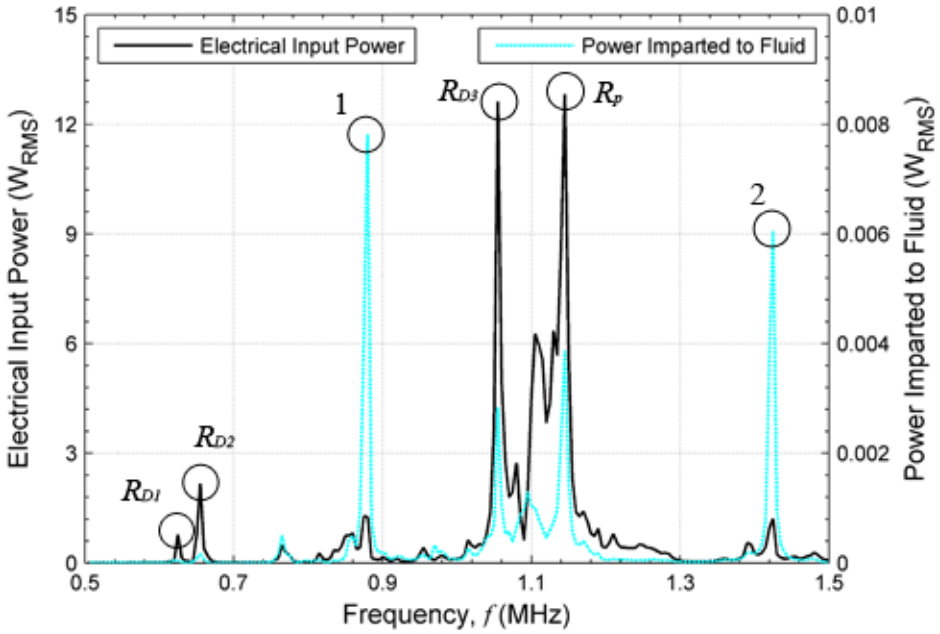

Figure 2.9 Comparison of the simulated electrical input power and power imparted to the fluid as a function of piezoelectric driving signal frequency for the dual-sample multiplexed droplet ejector array. Power imparted to the fluid considers only the active domain.

As shown in Figure 2.9, the resonance modes of high electrical input power and power imparted to the fluid do not coincide. The resonance modes at 0.63 and 0.66 MHz, R_{D1} and R_{D2}, impart very little power to the fluid and do not correspond to cavity resonances. These frequencies do not result in wave focusing at the nozzle aperture and instead are likely resonance modes of the device structure. The resonance mode at 1.05 MHz, R_{D3}, and the piezoelectric transducer's longitudinal resonance (1.2 MHz) both impart significant power to the ejected fluid; however, they also have a high electrical input power. High electrical input power results in elevated resistive and frictional losses without the acoustic wave focusing of cavity resonances. The increase in frictional losses also leads to excessive device heating which will lead to denaturing of large biomolecules being considered for MS analysis. This is generally undesired and operation at these

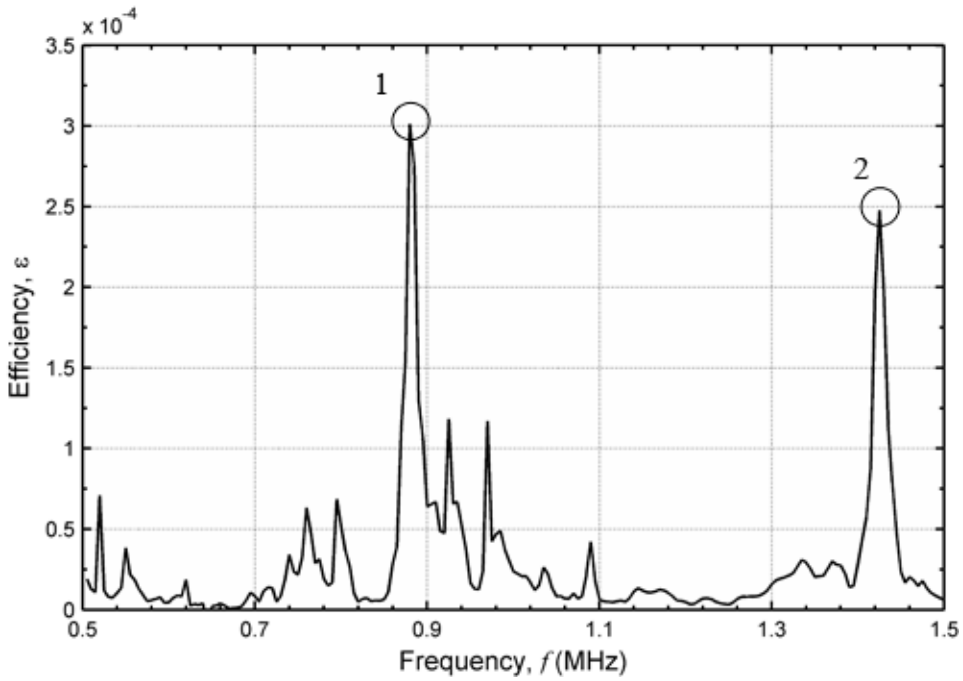

Figure 2.10 Power-transfer efficiency (acoustic power imparted to fluid divided by the electrical input power to the transducer) as a function of piezoelectric driving signal frequency for the dual-sample multiplexed droplet ejector array.

frequencies is avoided. This leaves the resonance frequencies at 0.88 and 1.425 MHz, which are imparting a significant level of power to the fluid relative to the electrical input power. To visualize this better, Figure 2.10 displays the power-transfer efficiency, ε, as defined by the acoustic power imparted to the fluid (the active domain) divided by the electrical input power to the transducer. This bolsters the above conclusions, identifying maximum ejection efficiencies at 0.88 and 1.425 MHz.

The first and second fluid cavity resonance modes at 0.88 and 1.425 MHz display efficient power transfer to the fluid as well as acoustic wave focusing as shown in Figure 2.11. Figure 2.11 depicts the real component of the simulated complex acoustic pressure field distribution. The pressure field within the active domain is not entirely one-dimensional at either of the cavity resonance frequencies, similar to the results from the

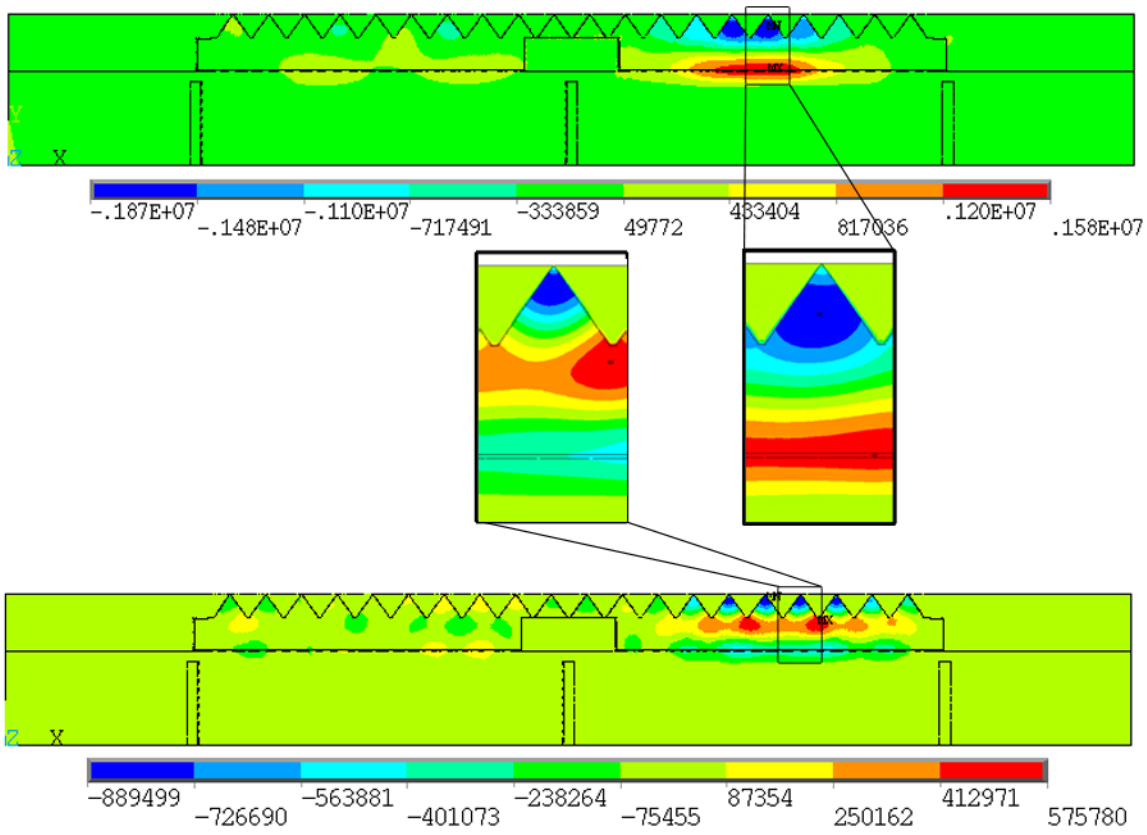

Figure 2.11 Real component of the simulated complex acoustic pressure field distribution within the ejector fluid reservoir for operation resulting in efficient wave focusing in the active (right) domain at transducer driving frequencies of (top) 0.88 MHz and (bottom) 1.425 MHz.

full array baseline simulations.[67] Constructive interference of the acoustic waves within the nozzles causes the nozzles near the center of the active domain to exhibit higher pressure gradients and better wave focusing. During experimental operation, it is found that those nozzles near the center of the active domain provide stronger and more stable ejection. The results clearly show efficient and localized wave focusing by only the nozzles located within an electromechanically isolated "active" domain of the device, which makes the device suitable for multiplexed, selective ejection of analyte from this reservoir.

Figures 2.12-2.13 demonstrate the isolation of the acoustic energy to a single domain in the device by plotting the power imparted to the equivalent "ejected" volume of fluid at the nozzle orifice across the row of 20 nozzles. The figure provides the power levels for two different cases: with and without cuts in the piezoelectric transducer intended for acoustical cross-coupling reduction. To provide a baseline for comparison, also shown is the ejection threshold, defining the minimum (capillary) power required to eject a droplet (red horizontal line). The ejection threshold approximation is based on an estimate of the free surface energy associated with droplet formation at each frequency of operation.[68] The level of parasitic acoustic coupling between the active and inactive domains and the effect of introducing a cut in the piezoelectric transducer can be quantified using a cross-talk figure of merit (CT) for the device, defined as $\mathrm{CT\ (dB)} = 10\log_{10}\left(P_{off}/P_{on}\right)$. Here, P_{on} and P_{off} are the average power (per nozzle) imparted to the fluid for the nozzles located in the active (ON) and inactive (OFF) domains of the multiplexed device, respectively. The simulated CT for the uncut piezoelectric transducer is -9.6 and -9.7 dB for the two identified cavity resonance modes, 0.88 and 1.425 MHz, respectively. With the introduction of a cut to isolate the two domains, CT is decreased considerably, to -14.2 and -19.6 dB for the two resonance modes, respectively. Note that ejection from a nozzle occurs when an energy (power) threshold exceeds the capillary and viscous forces at the orifice. Therefore, when sufficient power is applied to the selected domain, for example greater than the minimum (capillary only) power threshold shown in Figure 2.12 droplets will be ejected from most of the nozzles in the active domain, whereas in the inactive domain the power imparted to the fluid will be below the ejection threshold. In that sense, the CT figures for an uncut

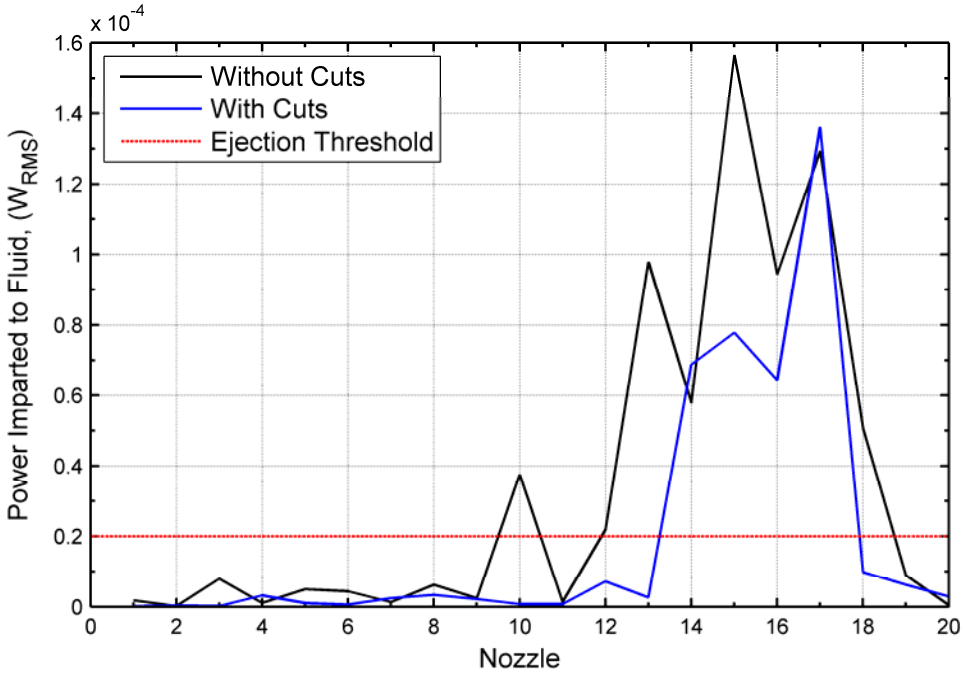

Figure 2.12 Simulated power imparted to the fluid across a single row of 20 nozzles of the array with and without a cut in the piezoelectric transducer for device operation at 0.88 MHz.

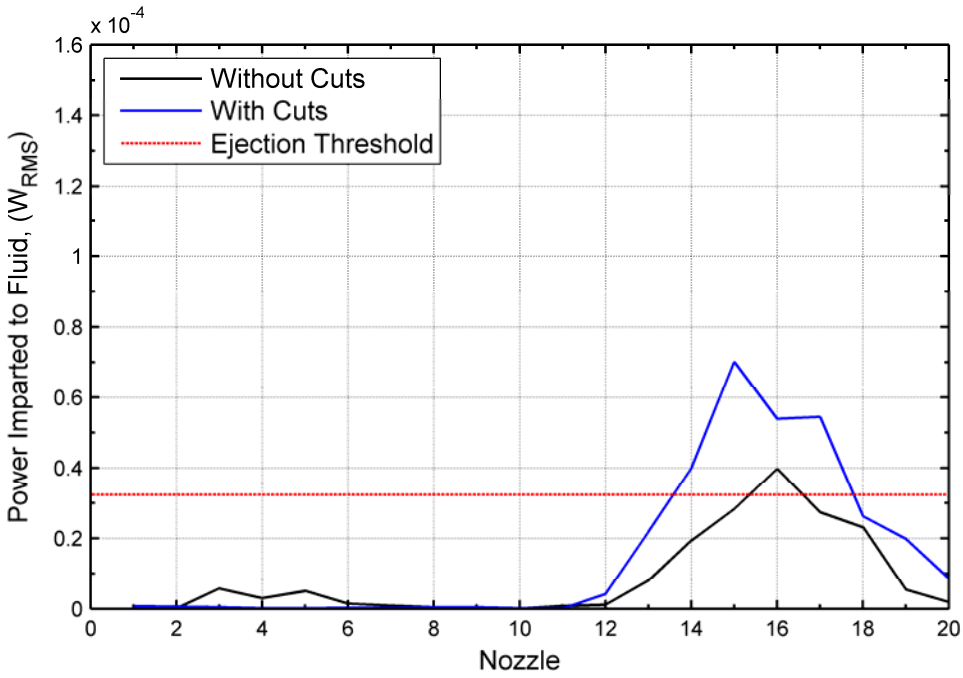

Figure 2.13 Simulated power imparted to the fluid across a single row of 20 nozzles of the array with and without a cut in the piezoelectric transducer for device operation at 1.425 MHz.

transducer, or for a shallower cut as used in the experiments described in the next section, should be sufficient to achieve isolated or multiplexed ejection. Nevertheless, the lower CT levels enabled by the combination of the piezoelectric electrode partitioning, sub-division of the fluid reservoir into independent sub-domains, and introducing cuts in the transducer ensure that there is a larger margin for selective ejection, leading to more robust multiplexed operation at the device level.

In summary, the finite element model simulations identify a clear possibility for localized acoustic wave focusing isolated to the active sub-domain of the sample reservoir, where the RF electric signal is applied to the segmented piezoelectric transducer. Since the wave focusing is well correlated with ejection, this result supports the feasibility of achieving multiplexed operation of the ultrasonic ejector array at the device level. Next, the methods developed from the simulations for isolating pressure wave focusing are incorporated into the actual device, which is experimentally characterized.

2.3.2 Experimental Validation

For experimental validation, a dual-sample multiplexed ultrasonic droplet ejector is assembled according to the schematic shown in Figure 2.6. The silicon nozzle array is 510 μm thick with 5 μm diameter nozzle orifices. The 2 mm thick piezoelectric transducer is partially diced 500 μm deep on either side using a 250 μm wide blade in a Direct Automatic Wafer Saw DAD321, separating the electrodes into two independently controlled parts. This depth reduces mechanical coupling between the fragments of the segmented transducer without compromising its structural integrity. The materials of all other components of the ejector used in the experiments are the same as those described

above. The fluid streams are introduced via capillary tubes fed through, with compression-fit, the silicone insert to enable leak-free fluid filling into two separated sample reservoirs. The silicone divider, separating two sample reservoirs, is also used to seal the cut in the piezoelectric element. The fluidic package has been shown to effectively isolate the separate sample fluids to their respective sub-domains.

2.3.2.1 Impedance Measurements

The electrical impedance is experimentally measured using a network analyzer (Agilent Technologies, Inc. Model 8753 ES). The measured electrical impedance, Figure 2.14, identifies many of the device's structural resonances found in the simulation, but only weakly identifies the cavity resonances. The longitudinal resonance of the piezoelectric transducer is ~1.14 MHz, slightly shifted to a lower frequency from the simulated impedances. Upon closer inspection, the other simulated resonances that are

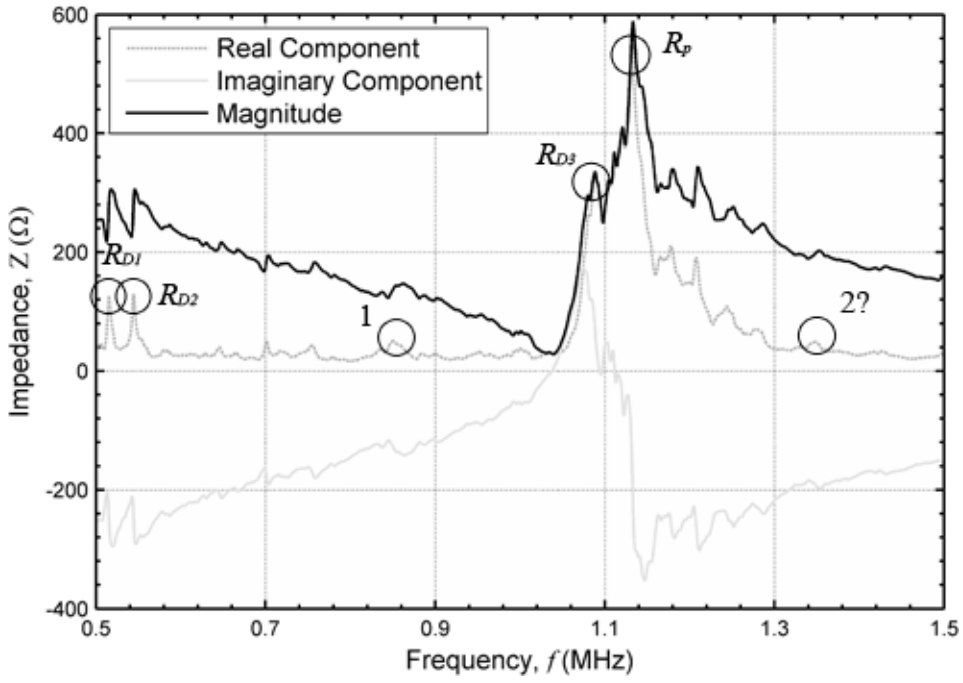

Figure 2.14 Experimentally measured electrical input impedance as a function of piezoelectric driving signal frequency.

attributed to the multiplexed structure at 0.63 and 0.66 MHz are experimentally measured at 0.52 and 0.55 MHz, again a shift to lower frequencies. This overall shift in the structural resonances can be due to a number of factors, most apparent being three-dimensional effects and coupling of mechanical energy. A small but broad resonance peak can be identified at ~0.86 MHz that represents the first resonance mode. However, it is difficult to identify the 2^{nd} resonance mode in the 1.425 MHz range, found in the simulations. Shifts in the cavity resonances can be attributed to slight variations in fluid temperature which result in changes in the speed of sound within the fluid. A 10ºC change in temperature can cause a 10 kHz shift in cavity resonances. Also the accuracy with which the spacer thickness is measured effects comparison between predicted and measured resonances. A 10 μm difference in spacer height can result in ~8 kHz shift in frequency.

Next, experimental ejection of an active domain is completed to easily identify those resonances which produce adequate acoustic wave focusing.

2.3.2.2 Dual-Sample Ejector

To demonstrate multiplexed operation of the device, experiments are conducted to show on-demand ejection, isolated to a specified "active" domain occupied with the sample of interest. Figure 2.15 shows the schematic of the setup used in the experiments: a single function generator supplies the RF electric signal to drive fragments of the piezoelectric transducer for both domains of the device; the signal is amplified using an RF power amplifier and selectively applied to the electrode of the piezoelectric transducer in the "active" domain where ejection is desired, whereas the other electrodes

are grounded; an on-line, gravity-feed sample delivery system is used to fill the fluid reservoir.

The multiplexed device successfully achieves isolated ejection from an "active" sub-domain of the fluid reservoir with no ejection from the "inactive" domain. In the demonstration experiments (Figure 2.16), the RF signal was applied to each sub-domain successively and multiple times to ensure repeatable switching of ejection from one sub-domain to another. The strongest ejection was achieved at the frequencies around 890 kHz. This ejection frequency corresponds relatively well to the most power-transfer efficient, wave-focusing mode identified in the device simulations (Figure 2.10). The discrepancy in operating frequency is minimal and can be due to a number of factors previously mentioned as well as three-dimensional effects which are not captured in the simplified 2-D simulations under idealized conditions. A 2nd cavity resonance mode was unsuccessfully identified as expected from the network analyzer electrical impedance

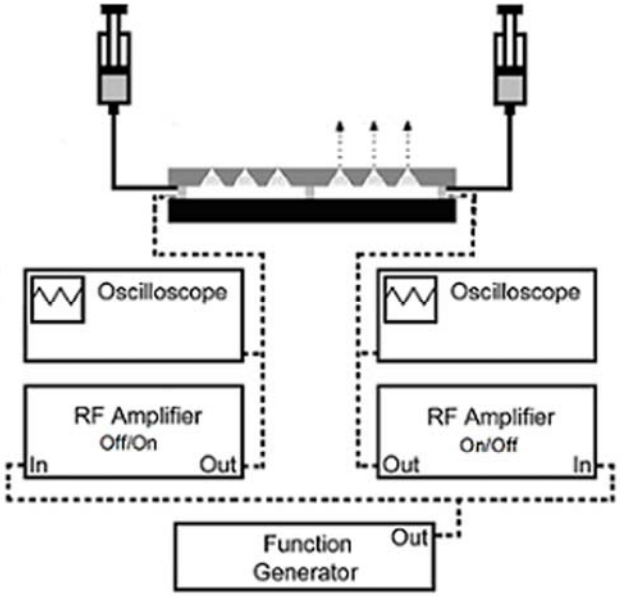

Figure 2.15 Experimental setup used to demonstrate the multiplexed operation of a dual-sample/domain micromachined ultrasonic droplet ejector array.

measurements (Figure 2.14).

The device demonstrates some cross-coupling from one domain to the other, but the divisions in the device introduce a significant (and desired) asymmetry that allows for cleanly isolated ejection from the "active" domain as suggested by the simulations. This cross-coupling is expected, as to eject the desired fluid, the active domain is driven with an electric input power above a required threshold for ejection, while the electromechanical coupling transfers some of this power to the inactive domain as well. The ejection is cleanly isolated to the active domain only if the power leaked to the inactive domain is below the threshold value. However, if the electric signal amplitude applied to the transducer is steadily increased, eventually the amplitude of the coupled signal will also exceed the threshold. Therefore, this approach allows the use of a single driving signal applied to one (active) electrode of the device to eject fluid from one or both domains. For the demonstrated arrangement, the experimentally observed ejection threshold for isolated ejection only from the active domain is ~25 V_{pp} and the threshold

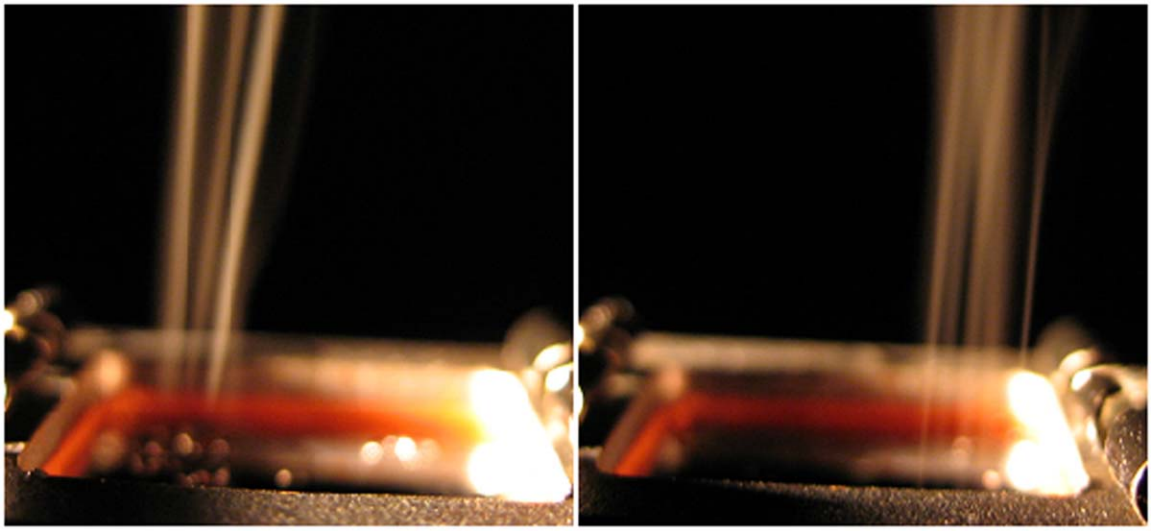

Figure 2.16 Images of isolated ejection from individual domains of the multiplexed ultrasonic ejector array. Left domain active (left), right domain active (right).

for coupled ejection from both the active and inactive domains is ~40 V_{pp} (CT = -4.1 dB). Switching of the active domains (from left to right in Figure 2.16) yields the corresponding threshold values for isolated and coupled ejection as ~22 V_{pp} and ~48 V_{pp} (CT = -6.7 dB), respectively. Thus, multiplexed ejection is achieved even with moderately high CT values when the ejection threshold phenomenon is exploited. The differences observed in switching from domain to domain are fairly small, and it is mainly due to a lack of mirror image symmetry between domains in the device production and assembly. This includes asymmetries in the piezoelectric transducer cuts, placement of the silicone divider, relative position of the piezoelectric transducer and fluid reservoirs, uneven mechanical clamping of the package, and non-uniformity in fluid filling of the sample reservoirs. These variations and the three-dimensional nature of the actual device are all possible causes for the difference observed between the measured and simulated CT values.

In summary, the nozzle array component of the AMUSE ion source is fabricated in a simple batch microfabrication process, requiring only two masks. The simple stack configuration allows for a leak-free easily assembled device. AMUSE's array format is inherently suitable for numerous variations of the basic device configuration, including disposable offline and multiplexed online configurations. Successful multiplexed fluid ejection by a micromachined ultrasonic droplet ejector has been demonstrated. Isolated ejection from specified domains of the device was achieved experimentally under conditions established in the simulations. In conjunction with previously demonstrated utility of the ultrasonic ejector array as an ion source,[72-73,75] these results suggest a path to device application as a parallel, multiple-sample ion source for bioanalytical mass

spectrometry. Simulations and experiments indicate a potential for further multiplexing of the ejector array (ion source), for example, into individually-actuated quadrants. Division of the nozzle array into individually controlled ejection/ionization sub-domains and their coupling to the up-stream multi-channel liquid chromatography or other sample separation devices would be a major step towards development of a truly lab-on-a-chip ion source for MS applications.

In the following chapters, a basic understanding of analyte charging and charge separation during droplet ejection in the AMUSE ion source is developed through complimentary theoretical and experimental investigations. An in-depth analysis of charge separation due to the application of both DC and AC electric fields or varying amplitude and phase is undertaken. A thorough understanding of ultrasonic droplet ejection and droplet charging in the presence of an electric field is obtained through the use of computational simulations, experimental charge collection measurements, stroboscopic visualization of ejection phenomena, and MS characterization.

CHAPTER 3

AMUSE ANALYTE CHARGING AND IONIZATION

As discussed in Chapter 1, electrospray ionization is composed of analyte charging, charge separation, and dry ion formation. In ESI and AMUSE ion sources, analyte charging takes place in solution through adduct formation with available ions. Adduct formation typically occurs in the form of protonation and/or adducts formed with various ions from salts in the solution or even electrochemically introduced metal ions.[10,15-18] Electrospray ion sources utilize Taylor cone electric field focusing for both droplet formation and placing net charge on droplets. The application of a large electric field in ESI ion sources induces electrokinetic flow accomplished by charge separation in the course of Taylor cone formation, leading to charged fluid dispersion. Taylor cone formation, discussed in detail in Chapter 1, describes the phenomena by which increasing charge density at the fluid interface creates Coulombic forces that overcome surface tension, resulting in a jet of highly charge droplets.[10-12,19] Once the highly charged droplets are created, the transformation of solute species into free ions in the gas phase (desolvation) occurs by either the charge residue mechanism or the ion evaporation mechanism (Figure 1.2).[7,13,15,22] These processes are interconnected and difficult to investigate individually in conventional ESI sources.[10-12,16-17] The AMUSE ion source allows for analysis of each process independently, uncoupled from the other processes, which is extremely valuable for gaining fundamental insight.

In order to fully understand the operation of the AMUSE ion source and other droplet-based ion sources an investigation into analyte ionization is conducted. The basic

idea of the AMUSE ion source is to decouple analyte charging and droplet/ion formation, thus providing independent control of these processes which are precursors to gas phase ion formation. Understanding the mechanisms of analyte charging and charge separation will allow one to identify the optimum conditions for efficient ionization and MS sensitivity and stability. Analyte charging occurs through adduct formation between the analyte and ions present in solution. The ions used for charging can be introduced in a number of ways. One typical method for bioanalytical MS is the addition of a weak acid (acetic, formic, etc.), reducing solution pH by introducing hydrogen ions resulting in protonation of the analyte molecule. In the case of protonation, the adduct formation is a homogenous reaction which occurs essentially instantaneously and analyte charging is trivial. In other cases, the adducts are formed by the addition of a variety of cations (positive mode), for example, M^+ (metal ions), such as Na^+, Li^+, etc. For the case of adducts formed by ions that are obtained from dissociating salts (typically added as a supporting electrolyte), the reactions are homogeneous. When adducts are formed with metal ions obtained from corrosion of the electrode material, the adduct formation is again occurring as a fast homogeneous reaction; however, the cations are introduced to the sample solution through heterogeneous electrochemical reactions occurring at electrode surfaces. For the case of electrochemical reactions occurring at the electrodes, transport processes become important to deliver the ions from the surface to the bulk reservoir where adducts are formed. A number of investigations into the importance of electrochemistry in ESI have been presented in the literature.[10,15-18,101-102] Figure 1.1 demonstrates electrospray ionization as a controlled-current electrolytic cell. The AMUSE ion source behaves in a very similar manner.

Adduct ion introduction via heterogeneous electrochemistry at the electrode and homogeneous acid dissociation are considered as the two main origins of adduct ions for analyte charging. This chapter first provides a brief overview of electrochemically driven ion generation and transport in the AMUSE ion source. Additional details and discussion of this mode of charging can be found in Appendix B. The investigation then turns to protonation and electrokinetic charge separation, the typical method for analyte charging in ESI and the AMUSE ion sources. A detailed electrohydrodynamic (EHD) computational model of charge transport during the droplet formation cycle in the AMUSE ion source is developed, coupling of the fluid dynamics, pressure and electric fields, and charge transport in multiphase flow. Additional details and implementation of this model can be found in Appendix C. Charge separation in the AMUSE ion source, under both static and dynamic electric fields of varying amplitude and phase relative to the mechanical pressure field, is investigated and discussed in detail.

3.1 Electrochemically Generated Ions and Analyte Charging

In electrospray ionization, the analyte charging process can be viewed as a controlled-current electrochemical flow cell.[17-18,21,103] An investigation into analyte charging in AMUSE by means of heterogeneous electrochemical reactions is completed through time scale analysis and computational fluid dynamics modeling. For positive-mode ESI, the metallic capillary acts as the oxidizing/corroding anode. In a similar manner, ions are generated and transported to and from the piezoelectric transducer electrode of the AMUSE ion source. The analysis of these processes needs to consider the interplay between advective and diffusive ion transport of electrochemically generated ions due to anodic corrosion of a metal electrode, as a function of the source

duty cycle (percent of each droplet ejection cycle that the piezoelectric transducer is active) and electrode location. The model formulation, detailed results, and figures of this investigation can be found in Appendix B. The results demonstrate that for 100% duty cycle operation with the electrochemically "hot" electrode on top of the piezoelectric transducer, the majority of the analyte solution is ejected prior to coming into contact with the cations produced at the electrode surface. In other words, the majority of AMUSE nozzles are ejecting droplets lacking the analyte-charging ions, which will lead to very poor ionization efficiency.

While reducing the duty cycle allows for improved ion transport from the electrode to the bulk by diffusion, it greatly reduces throughput which may be undesirable in some applications. Also, operation of the device in multiplexed format with a smaller sample reservoir would impose an even more stringent requirement on the sample residence time (and, thus, will put a severe limit on device throughput) if the change of the duty cycle was the only way to improve analyte charging. To circumnavigate this challenge, the electrode location is moved from the surface of the piezoelectric element to the walls of each nozzle, making the diffusion length scale the ions must travel from the electrode surface to the bulk greatly reduced. This results in much faster diffusion, occurring on a time scale smaller than the residence time of the analyte within the AMUSE chamber prior to its ejection. Indeed, moving the electrode to the nozzle surface shows a dramatic increase in the concentration of ejected cations. This in turn provides a greater opportunity for adduct formation with the analyte (typically a very fast process) and improved charging and ionization.

In order to compare the ion production for each case, an ionization "efficiency" parameter is defined as the rate of cations exiting the device (encompassed into ejected droplets) normalized by the total mass flow rate. This value is compared for various duty cycles, as well as for both electrode locations. The ionization "efficiency" is computed as a function of a single dimensionless parameter, the Peclet number, which expresses the effects of both the duty cycle reduction and charging electrode location in a generalized fashion. The Peclet number used here is defined in terms of relevant diffusion and advection time scales, $Pe = \frac{t_{diff}}{t_{adv}} = \frac{\delta^2 / D}{L/u} = \frac{u\delta^2}{DL}$, where all properties and length scales are defined in Appendix B.

The Peclet number is a dimensionless measure of the relative dominance of advection versus diffusion in transport of ions. All cases with variable duty cycle and the charging electrode placed on the piezoelectric transducer yield $Pe > 1$ (the lower the duty cycle is, the smaller the Peclet number is). These flow conditions are therefore characterized by longer diffusion times relative to advection, $t_{diff} > t_{adv}$. As the duty cycle (and throughput) is decreased and the advection time approaches the diffusion time, the ionization "efficiency" increases steadily. On the other hand, for the electrode placed on the nozzle surface, analyte advection is slower than ion diffusion, $Pe < 1$. This leads to an increase in the ionization "efficiency" without a sacrifice in the device throughput. Moving the charging electrode from the piezoelectric transducer to the nozzle surface improves the ionization "efficiency" by more than 40%, which is significantly greater than what is achievable even with greatly reduced (down to 1%) duty cycles. It is

important to emphasize that this gain in ionization efficiency, enabled by moving the electrode, comes with no sacrifice of the device throughput.

3.2 Protonation and Charge Separation

With a basic understanding of the analyte charging through electrochemically generated ions and adduct formation, focus is now shifted to mechanisms of charge separation and charged droplet formation in the AMUSE ion source. As introduced at the beginning of this chapter, analyte charging is most commonly accomplished by the addition of a weak acid (acetic, formic, etc.). This method of analyte charging is typical for bioanalysis with predominately aqueous solvents. In this case, the weak acid dissociates, introducing hydrogen ions which reduce solution pH and result in protonation of the analyte molecule. Unlike electrochemically driven analyte charging, in the case of protonation, the adduct formation is a homogenous reaction occurring very fast, as compared to the ejection time scale, allowing macroscale ion transport to be neglected. However, charge separation is still necessary to improve charge availability within individual droplets as they are ejected. Analysis of electrokinetic transport underlying charge separation is performed next to identify the optimum conditions for efficient ionization and improved MS sensitivity and stability.

In the case of ESI, a large electric field causes charge separation by forming a Taylor cone-jet, resulting in the dispersion of highly charged droplets. Alternatively, the AMUSE ion source utilizes mechanical pressure waves for droplet generation, separating solution dispersion from charge separation. Although the mechanical and electric fields are largely independent, they are not completely decoupled. As previously discussed in Chapter 1, in RF-only mode the weak electric field of the piezoelectric transducer's

driving voltage signal and ionic mobility asymmetry of the dissociated acid ions are sufficient for a limited degree of charge separation and droplet charging without using any additional means for charge separation. Therefore, the drive signal that controls the mechanical droplet formation does have an effect, albeit small, on the analyte charging. While, this has been shown to be sufficient for analyte charging and obtaining mass spectra,[72-73,75] the effect on MS sensitivity and signal stability is limited due to relatively low fields produced by the piezoelectric drive signal.

In order to maximize the net charge on individual droplets and hence improve ionization efficiency and sensitivity, a greater degree of charge separation must be achieved. In a couple of classical studies, it was shown that an external electrode successfully polarized a neutral spray from a pneumatic nebulizer.[104-105] Similarly, an external electric field can be used to enhance droplet charging in the AMUSE ion source. In this case, an electric potential difference is applied between the internal electrode of the piezoelectric transducer and an external counter electrode, creating a charge separating electric field. The induced electric field will draw positive charges (positive mode MS) toward the fluid-air interface and the negative charges will be repelled away from the surface. In this scenario, droplets with a much greater positive charge will be ejected. This imbalance in charge ejection will result in an overall negative charge being accumulated in the fluid reservoir. The electrochemical oxidation of relevant anions, for example the acetate anion from acetic acid, at the piezoelectric transducer's top electrode surface will eliminate the accumulating negative charge, thus completing the electrochemical cell. This electrochemical oxidation of excess negative charge is also present in ESI, as shown in Figure 1.1.

3.3 Electrohydrodynamic Modeling of Charge Transport during Droplet Ejection

Electrohydrodynamic atomization and tip streaming have been studied experimentally, analytically, and more recently computationally. Pioneering experimental work by Zeleny[106] and analysis by Taylor[107] considered the interface deformation experienced by an electrically-conducting fluid subjected to an electric field. Over the years, numerous reports of experimental characterization and visualization of various electrospraying modes under a variety of conditions appeared in the literature.[106-112] In parallel, analytical and computational models of varying complexity and implementation techniques have been developed.[19,108-109,113-121] Taylor's initial electrostatic solution of an equilibrium liquid cone formed under application of an electric field considers a limiting case of perfectly conductive fluid. This resulted in what is now known as the classical "Taylor cone" with the jet apex angle of 98.6º.[107] Similar results with perfectly conducting liquids have been demonstrated in the area of liquid metal ion sources (LMIS).[122-125] While providing an important qualitative insight into the physics of electrospray, a perfectly-conducting fluid approximation is, however, unable to capture the cone-jet formation, commonly seen experimentally with typical MS solvents. To address this challenge, several improved models have been developed that incorporate a simplified set of electrohydrodynamic equations for a "leaky dielectric fluid," first introduced by Melcher and Taylor[117] and reviewed by Saville.[119] In a leaky dielectric model, the free charge within the bulk liquid is assumed to be zero (electro-neutrality condition) and all charges are concentrated at the fluid-air interface. The free charge accumulated at the surface modifies the electric field and exerts normal and tangential Maxwell stresses at the interface, resulting in formation of the experimentally-observed

cone-jet profiles.[113,115,119-121] The most comprehensive models solve a complete set of coupled equations for the fluid flow field, electric field and charge transport,[116,119,126] which is often required for a wide range of applications, besides electrospray ionization.

Mechanically-driven ion sources, such as AMUSE, allow for decoupling of the charge separation and droplet formation processes. In contrast to conventional Taylor-cone-based ESI, in which fluid dispersion and droplet charging are intimately coupled, the AMUSE ion source allows one to utilize mechanical actuation for droplet generation and independently-controlled electrical actuation for droplet charging. Computational modeling enables insight into the microscopic details of physicochemical phenomena, underlying analyte ionization in AMUSE, on the microsecond time scale. Further, the simulations allow one to evaluate ion source design modifications instrumental to developing an improved design and optimal operation.

In the remainder of this chapter, a computational model is developed, employing the full set of electrohydrodynamic and charge transport equations.[127] The model is applied to investigate charge transport in atmospheric pressure ion sources based on electrospray and mechanically-driven droplet ejection. The chapter starts by presenting the electrohydrodynamic (EHD)-charge transport model formulation, including governing transport equations and interface conditions coupling electric and hydrodynamic fields. Then, the model implementation is covered, including the simulation platform (FLUENT CFD software) and numerical algorithms that are used for incorporating the EHD boundary conditions into the FLUENT simulation framework. This is followed by discussion of the EHD model application to several special cases relevant to MS ionization, including the electrospray from a thin capillary and

mechanically-driven droplet-based analyte charging by AMUSE. For the former case (ESI), both the cone-jet formation for a fluid with finite electrical conductivity as well as the Taylor cone formation for a perfectly-conducting fluid are demonstrated and compared to models and experimental results from the literature. For the latter case (AMUSE), the EHD model is coupled to the fluid mechanics model of mechanically-driven droplet generation. Simulation results are compared to experiments with both DC and AC-electric fields used for droplet charging in Chapter 4.

3.3.1 Electrohydrodynamic (EHD) Model

A comprehensive electrohydrodynamic model is utilized to thoroughly investigate charge separation phenomena in various ion sources. Currently, there is no commercial code that is capable of fully modeling the electrohydrodynamic atomization process and includes all relevant physics. The computational fluid dynamics (CFD) package FLUENT[128] provides a sound framework for modeling hydrodynamics of complex flows, including free surface flows and fluid interface evolution, but is unfortunately not equipped to solve the electric field or charge transport equations. FLUENT does, however, allow for the incorporation of additional equations and boundary conditions through the built-in heuristic of generalized transient advective-diffusive type equations for user-defined scalars (UDS) and user-defined functions (UDF), which must be hand-coded by a user using C/C++ language. These user-defined capabilities are taken advantage of to develop and implement a set of UDSs for the electric potential evolution and charge transport, as well as UDFs for the charge and electric (Maxwell) stress boundary conditions at all interfaces. The UDSs and UDFs for each scalar field are then solved along with the basic hydrodynamic equations.

First, the basic formulation of the hydrodynamic and electric field equations and boundary conditions are reviewed. This is followed by a description of the methodology for tacking interfaces and coupling the hydrodynamic and electric fields, which completes the electrohydrodynamic model.

3.3.1.1 Momentum Conservation

The incompressible fluid flow in the ion source is governed by a set of transient, three-dimensional Navier-Stokes equations of motion for a two-phase (liquid-gas) fluid,

$$\frac{\partial}{\partial t}\left(\rho\vec{u}\right)+\nabla\cdot\left(\rho\vec{u}\vec{u}\right)=-\nabla p+\rho\left[\nu\left(\nabla\vec{u}+\nabla\vec{u}^{T}\right)\right]+\rho\vec{g}+\vec{F} \tag{3.1}$$

$$\nabla\cdot\vec{u}=0 \tag{3.2}$$

where $\vec{u}$ is the velocity vector, p is pressure, $\vec{F}$ is a net body force vector, and ρ and ν are the density the kinematic viscosity of the liquid, respectively. In the solution methodology employed by the FLUENT software the body force term is used to both describe the bulk point-like forces acting on the fluid, as well for incorporating the surface stress (e.g., surface tension) at the interfaces located within the simulation domain using the volume-of-fluid algorithm. Therefore, the electric field forces acting on a charged fluid are incorporated as body forces within the liquid domain. Interfacial effects, such as Maxwell stresses and surface tension, are also accounted for through the equivalent body force terms.

3.3.1.2 Electrodynamics and Charge Transport

The governing equations for the electric field (potential) are derived from the Maxwell's equations of general electromagnetism, using typical simplifications defined by the relative magnitude of the characteristic timescales for electric phenomena,

$\tau_e = \varepsilon\varepsilon_o/\sigma$, and magnetic phenomena, $\tau_m = \mu\mu_o\sigma l^2$. (Here, ε is dielectric permittivity, σ is the electric conductivity, μ is the magnetic permeability, l is a characteristic length scale). For the cases considered here, the characteristic magnetic timescale is much smaller than that for the electric field, thus simplifying Maxwell's equations to the quasi-electrostatic limit of electrohydrodynamics.[119,126] This yields the Poisson equation for the electric potential within the fluid domain with the source term resulting from the presence of free unbound charges.

$$\nabla^2\phi = -\frac{q}{\varepsilon_o\varepsilon_r}, \tag{3.3}$$

where ϕ is the electric potential$\left(\vec{E} = -\nabla\phi\right)$, ε_o is the permittivity of free space, ε_r is the relative permittivity of the material, and q is the local net free charge density.

In the consideration of electrochemical ion introduction, a macroscale approach is taken. Transport to and from the piezoelectric transducer is relevant. Here, ion introduction and adduct formation is homogenous and uniform in the fluid bulk, and charge separation is considered at the length and time scales of the individual nozzle orifice and single droplet evolution, respectively. Initial charge densities are determined by the concentration of an added weak acid, e.g. acetic acid. The ionic current through the solution consists of transport by ionic drift, diffusion, and advection. This can be separated into the relative motion of ions, $\vec{J}'$, and the bulk advection of ions with the fluid, $q\vec{u}$.

$$\vec{J} = \vec{J}' + q\vec{u} = q\mu_{em}\vec{E} - D\nabla q + q\vec{u} \tag{3.4}$$

For the cases considered here, proton transport in an aqueous solvent, it can be shown from the time scale analysis below, that for electric fields greater than approximately

0.025 V/m, diffusion can be neglected. For the applications at hand, the electric fields required for electrospray and also relevant to AMUSE are fairly strong, and therefore the diffusion time scale for charge transport is much longer than the other transport processes (e.g., charge migration). Thus, only advection, $q\vec{u}$, and migration, $\mu_{em} q\vec{E}$, of charged fluid particles under the application of an electric field need to be considered (here, μ_{em}, is the electrical mobility of the respective ion and $\vec{E} = -\nabla\phi$ is the electric field vector). The governing equations for charge transport are as follows:

$$\frac{\partial q}{\partial t} + \nabla \cdot \vec{J} = 0 \quad \rightarrow \quad \frac{\partial q}{\partial t} + \nabla \cdot \left(q\mu_{em}\vec{E} + q\vec{u} \right) = 0 \tag{3.5}$$

Expanding the divergence of the current produces individual terms, which can be used to evaluate the associated time scales.

$$\frac{\partial q}{\partial t} + \underbrace{\mu_{em}\vec{E} \cdot \nabla q}_{\text{Ion Transit}} + \underbrace{\mu_{em} q \nabla \cdot \vec{E}}_{\text{Charge Relaxation}} + \underbrace{\vec{u} \cdot \nabla q}_{\text{Advection}} + \cancel{q\nabla \cdot \vec{u}} = 0 \tag{3.6}$$

Ion transport is only considered in the liquid, and the last term on the left hand side is dropped by the assumption of incompressibility. The advection time scale is similar to that obtained previously (Appendix B), but evaluated using different characteristic scales for length and velocity. The other two terms, found from ionic drift, represent the ionic transit time and the charge relaxation time, respectively.[126] The ionic transit time represents a global migration of charge:

$$t_i \sim \frac{l}{\mu_{em} E}$$

Here, l is the characteristic length scale, μ_{em} is the ion mobility, and E is the characteristic electric field. The charge relaxation time represents the Coulombic repulsion and a local migration of charge:

$$t_{relax} \sim \frac{\varepsilon_o \varepsilon_r}{\mu_{em} q} = \frac{\varepsilon_o \varepsilon_r}{\sigma}$$

Here, ε_o and ε_r are the free space and relative permittivity, respectively, q is a characteristic charge density, and σ is the solution conductivity.[126] The conductivity is a function of the charge density and is typically considered to be a constant for macroscale fluidics; however, here the charge densities vary widely, as will the liquid conductivity.

3.3.1.3 Electrohydrodynamic Transport Equations

In the presence of the electrohydrodynamic body forces the momentum conservation equation (Eq. 3.1) becomes,

$$\rho\left(\frac{\partial \vec{u}}{\partial t} + \vec{u} \cdot \nabla \vec{u}\right) = \nabla \cdot \left(\boldsymbol{T}^{\mu} + \boldsymbol{T}^{e}\right) + \rho \vec{g} \tag{3.7}$$

The left-hand side represents the typical unsteady and inertial terms, and the right hand side represents the mechanical (pressure and viscous stress) and electrical (Maxwell stress) stress tensors, respectively, given by:

$$\boldsymbol{T}^{\mu} = -p + \rho\nu\left(\nabla \vec{u} + \left(\nabla \vec{u}\right)^{T}\right) \qquad \nabla \cdot \boldsymbol{T}^{\mu} = -\nabla p + \rho\nu\nabla^2 \vec{u} \tag{3.8}$$

$$\boldsymbol{T}^{e} = \varepsilon\varepsilon_o\left(\vec{E}\vec{E} - \tfrac{1}{2}\left|E^2\right|\vec{I}\right) \qquad \nabla \cdot \boldsymbol{T}^{e} = q\vec{E} - \tfrac{1}{2}E^2\varepsilon_o\nabla\varepsilon + \nabla p_{st} \tag{3.9}$$

All parameters have been previously defined above, except $\nabla p_{st} = \frac{1}{2}\nabla\left(\rho\,\partial\varepsilon/\partial\rho\right)E^2$, defined as the electrostrictive pressure.[126] For the problem at hand, the gravity and electrostrictive pressure terms are neglected (as being much smaller than the surface tension and the electrostatic body force), giving the final form of the momentum balance:

$$\rho\left(\frac{\partial \vec{u}}{\partial t} + \vec{u} \cdot \nabla \vec{u}\right) = -\nabla p + \rho\nu\nabla^2 \vec{u} + q\vec{E} - \tfrac{1}{2}E^2\nabla\varepsilon \tag{3.10}$$

The electric body force terms, the Coulombic force $\left(q\vec{E}\right)$ and the dielectric force $\left(-\frac{1}{2}E^2\nabla\varepsilon\right)$, are incorporated into the hydrodynamic momentum equation as source terms driving the fluid flow. The Coulombic force, generally dominant in the presence of DC electric fields, is typically the strongest electrohydrodynamic force. The dielectric force, on the other hand, is usually dominant in the presence of AC electric fields, specifically when the electric field period is much shorter than the charge relaxation time.[126] This force is included because of the gradient in permittivity that arises in the interface region of the volume of fluid (VOF) solver, to be discussed later.

The general electric field boundary/interface conditions are Dirichlet and/or Neumann conditions, depending on the nature of the boundary/interface.[129]

Interface between two dielectrics, *i* and *j*:

$$\phi_i = \phi_j \qquad E_{t,i} = E_{t,j} \qquad D_{n,i} = D_{n,j}\left(\varepsilon_i E_{n,i} = \varepsilon_j E_{n,j} \rightarrow \varepsilon_i \nabla_n \phi_i = \varepsilon_j \nabla_n \phi_j\right) \tag{3.11}$$

Interface between a dielectric, *i*, and conductor, *k*:

$$\phi_i = \phi_k \qquad E_t = 0 \qquad D_{n,i} = q_{s,k}\left(\varepsilon_i \varepsilon_o E_{n,i} = q_{s,k} \rightarrow -\varepsilon_i \varepsilon_o \nabla_n \phi_i = q_{s,k}\right) \tag{3.12}$$

Symmetry and far-field boundaries for all domains:

$$\nabla_n \phi = 0 \tag{3.13}$$

Here, D_n is the normal component of the electric flux density vector, q_s is the surface charge density, and $\nabla_n = \vec{n}\cdot\nabla = \partial/\partial n$ is a projection of the gradient operator on the outer normal to the boundary. As it follows from Equations 3.11 and 3.12, the boundary conditions for electric flux density can be described in terms of a normal gradient of an electric potential, which is related to the surface charge density at the interface between a dielectric and conductor.

In all simulations the counter electrode is placed at the (top) boundary of the domain and is assigned a specified (reference) potential, $\phi = \phi_{CE}$. The electric field driving the electrospray process is then set by specifying a bias electric potential (relative to the reference potential) at the boundary in contact with the charging electrode of the ion source, whose location depends on a specific case being analyzed. For quantitative predictions, the applied bias potential is scaled appropriately to match the electric field strength used in simulations to those measured in experiments. Finally, either a far-field or a symmetry boundary condition (zero normal gradient of the potential, Equation 3.13) is applied at the other outer boundaries defining the simulation domain. For the internal boundaries/interfaces between sub-domains of different nature (e.g., liquid-gas interface) the potential must be continuous across the material boundaries, as seen in Equations 3.11-3.13. Specifically, at the interface between a dielectric and conductor, the permittivity and normal potential gradient of the dielectric determine the surface charge density in the conductor, Equation 3.12.[126,129] In the case of two dielectrics, no charge can be stored at the interface and most of the potential drop will occur in the matter with lowest dielectric constant, Equation 3.11 (e.g., in the air as compared to the sprayed fluid).

3.3.2 Solution Methodology

3.3.2.1 Scalar Transport Equation

FLUENT is a general CFD software package which has a built-in solver, based on the SIMPLE (semi-implicit method for pressure-linked equations) algorithm, for solving the pressure-linked momentum and mass conservation equations. For the problem at

hand, the transient advection-diffusion equations for user-defined scalars (UDS) of interest (electric field potential and charge density) are added to the solution algorithm via FLUENT-defined linkage and solved simultaneously with the Navier-Stokes equations of motion, augmented for the electric body forces. For an arbitrary scalar θ_k, the general transient advection-diffusion transport equation with the source terms is cast in FLUENT as:

$$\frac{\partial}{\partial t}\left(\rho\theta_k\right)+\nabla\cdot\left(\rho\vec{u}\theta_k-\Gamma_{\theta_k}\nabla\theta_k\right)=S_{\theta_k} \tag{3.14}$$

where Γ_k is the diffusion coefficient and S_{θ_k} is the source term. Clearly, the electric field potential (Equation 3.3) and the charge transport equations (Equation 3.5) can be readily cast in the form of Equation 3.14 for incorporation into FLUENT software. It is worth noting that in the UDS equation for the charge transport, the velocity component in the advection (second) term in Equation 3.14, $\vec{u}$, is replaced with an overall charge velocity, $\vec{V}=\vec{u}+\mu_{em}\vec{E}$, representing the fluid velocity and charge migration. Appendix C provides additional details of the user-defined scalars and code implementation.

3.3.2.2 Tracking Interface Evolution

The model employs the volume-of-fluid (VOF) technique[130-135] for tracking interface evolution due to its applicability to free surface flows where interface breakup and coalescence are important. The basic idea of VOF is to retain the phase (volume of each phase) data in each cell of a fixed computational domain as a volume fraction of the i^{th} fluid, α_i. Thereby mixed cells that define the interface between the i^{th} fluid and one of more other fluids will have a volume fraction between zero and one $\left(0<\alpha_i<1\right)$, and

cells away from the interface will be either empty, with zero volume fraction of the i^{th} fluid $(\alpha_i = 0)$, or full, with unity volume fraction of the i^{th} fluid $(\alpha_i = 1)$. The interface between two fluids is then tracked by advancing fluid volumes forward in time through the solution of an advection equation in the following form:

$$\frac{1}{\rho_i}\left[\frac{\partial}{\partial t}(\alpha_i \rho_i) + \nabla \cdot (\alpha_i \rho_i \vec{u}_i) = S_{\alpha_i} + \sum_{j=1}^{n}(\dot{m}_{ji} - \dot{m}_{ij})\right] \tag{3.15}$$

Here, ρ_i and $\vec{u}_i$ are the density and velocity vector of the i^{th} fluid, respectively, $\dot{m}_{ij}$ is the mass transfer from phase *i* to phase *j*, and S_{α_i} is the source term due to chemical reactions leading to production or destruction of the phase, α_i (zero by default). In the case of electrospray problems, there are two phases (liquid and gas) without mass transfer (evaporation is neglected) between phases, no source term (no new phase nucleation), and the density is constant within each fluid, reducing Equation 3.15 to:

$$\frac{\partial \alpha_i}{\partial t} + \nabla \cdot (\alpha_i \vec{u}_i) = 0 \quad i=1,2 \tag{3.16}$$

The fluid properties for the computational cells defining the interface between phases $(0 < \alpha_i < 1)$ are calculated as the volume-fraction-weighted average of the two fluids. For example, the interface density is,

$$\rho = \alpha_2 \rho_2 + (1 - \alpha_2)\rho_1 \tag{3.17}$$

It should be noted that one drawback of the VOF technique for interface tracking is that it produces a "diffuse" (i.e., consisting of several computational cells) interface instead of a sharp inter-phase boundary. The main difference in various VOF implementations is the method of discretization of the volume fraction advection equation and interface reconstruction.

The simplest reconstruction scheme is the simplified line interface calculation (SLIC),[136] which defines the interface within each cell using a straight line parallel to one of the coordinate directions. The Donor-Acceptor Scheme is an improved version of SLIC, but still results in an interface parallel to one of the coordinate directions.[132] Higher-resolution differencing schemes, such as compressive interface capturing scheme for arbitrary meshes (CICSAM)[137] and inter-gamma differencing scheme,[138] have also been developed to compress the interface broadening. Youngs' VOF method[139] is an accurate scheme in which the interface is approximated by a straight line at some linear slope such that the fractional fluid volume is conserved. Since the interface is no longer parallel to one of the coordinate directions, improved accuracy is achieved. The geometric reconstruction scheme, based on Youngs' method, is used by FLUENT in these simulations to represent the interface between liquid and gas phases. The geometric reconstruction scheme uses a piecewise-linear approach to determine the face fluxes for the partially filled cells at the interface.

The resolution of the interface reconstruction is limited by the mesh size. Regions of fluid comparable to the mesh size cannot be accurately resolved.[134] The areas of coarse meshing, specifically those with radii of curvature on the scale of the mesh, are unresolvable by these methods. The piecewise-linear approach for interface reconstruction flattens high curvature regions, resulting in numerical artificial surface tension.[133] Interface reconstruction in thin filament regions where the interface normal approximations are inaccurate, are also subject to an error due to artificial surface tension. In these instances, artificial surface tension can be reduced and the accuracy of the solution improved by decreasing the mesh size. In the limit of an infinitely refined

mesh, the exact solution is reconstructed.[133] In this work, for accurate results a fine quadrilateral element mesh is used in all areas of the simulated domains where surface tension effects are thought to be important.

3.3.2.3 Incorporating Surface Stresses

The effect of interfacial tension is accounted for through the use of an equivalent virtual body force derived from the continuum surface force (CSF) method.[140] An expression for the body force due to surface tension is given by Rudman[135] as

$$\vec{F} = \kappa\delta\left(r_I\right)\hat{n} \tag{3.18}$$

where κ is the radius of curvature of the interface at a location r_I, $\delta(r_I)$ is a one-dimensional indicator function that is zero everywhere except at the interface, and $\hat{n}$ is the unit normal to the interface. The unit normal, $\hat{n} = \vec{n}/|\vec{n}|$, is constructed from the interface normal, $\vec{n} = \nabla\alpha_i$ (Figure 3.1). The curvature κ is defined in terms of the divergence of the unit normal, $\kappa = \nabla\cdot\hat{n}$. The virtual body force term is inserted into the momentum equation for all interfacial cells with volume fraction greater than 0 and less than 1, between phases *i* and *j*.

$$F = \gamma\frac{\rho\kappa_i\nabla\alpha_i}{\frac{1}{2}\left(\rho_i+\rho_j\right)} \tag{3.19}$$

where ρ is the volume-averaged density computed using Equation 3.17. When simulating a perfectly conducting fluid in which all charges are located at the liquid-gas interface, the Maxwell stresses, Equation 3.9, are expressed in terms of an equivalent virtual body force acting at the interface and incorporated into the FLUENT using a custom-coded user-defined function (UDF) in a similar manner as the surface tension.

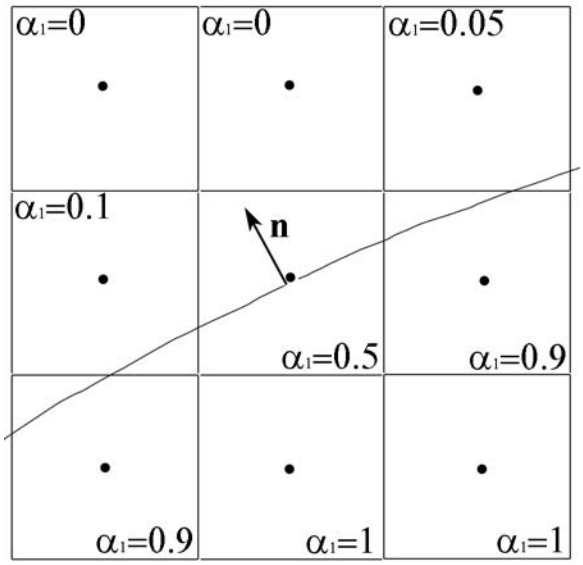

Figure 3.1 Schematic representation of computational grid with interface profile, normal vector, and cell volume fraction.

3.3.2.4 Numerical Discretization

A control-volume-based scheme is used to numerically solve the governing transport equations. Each equation is integrated about each control volume (individual cell), producing a set of discrete algebraic equations for the entire computational domain.[128] The numerical schemes for spatial and temporal terms of the standard Navier-Stokes equations with additional body forces are well established and described elsewhere.[141-143] The additional Maxwell and charge transport equations are all discretized in a similar manner. The pressure-velocity coupling of the Navier-Stokes Equations is solved using a semi-implicit method for pressure-linked equations (SIMPLE) algorithm. Finally, as discussed above, a geometric reconstruction scheme, based on Youngs'[139] VOF method, is used to represent the interface between fluids. The geometric reconstruction scheme uses a piecewise-linear approach to determine the face

fluxes for the partially filled cells at the interface. For more information on the numerical schemes employed by FLUENT, methods of equation solving, incorporation of user-defined scalars and memory, and other features, the interested reader is referred to FLUENT's extensive documentation.[128]

3.3.3 Simulation and Analysis of Special Cases

First, two classical cases of electrospray, the cone-jet formation in a finite electrical conductivity fluid and Taylor cone formation in a perfectly conductive fluid, are considered. These cases are used to validate the developed EHD model and solution methodology by comparison with experiments and simulation results from the literature. Once the predictive capabilities of the EHD model are established, it is applied to the AMUSE ion source to demonstrate the model's capability for simulation of mechanically-driven, droplet-based ion sources, with independently-controlled DC and AC-electric bias used for drop charging.[127]

3.3.3.1 Electrohydrodynamic Cone-Jet

In this case, the fluid-gas interface evolution during the electrospray of a finite electrical conductivity liquid from a capillary is considered, which is representative of a typical ESI scenario described in the literature. In these axisymmetric simulations, a small flow rate is provided at the capillary inlet to prime the flow. Initial cone-jet simulations only contain the Coulombic body force in the momentum equation. Figure 3.2 shows the forming cone-jet fluid profile as well as free charge and electric potential distributions. The fluid considered is heptane for comparison with other available simulation results from the literature. As shown in Figure 3.2(inset), the charge concentrates at the liquid-gas interface and along the capillary walls, which is expected

for the interface between the bulk dielectric (air) and conductor (fluid). Charge density is greatest in the streaming jet emanating from the cone apex. The increasing charge density at the interface creates the electric forces that elongate the emerging fluid interface. This leads to an eventual break-up of the jet when the liquid surface tension is overcome. The ultimate outcome of this electrospray mode is a well-known and experimentally-observed tip streaming phenomenon, which is clearly seen in Figure 3.2. A number of scaling laws for jet breakup have been developed to determine the droplet size, typically based on fluid properties and relevant length scales.[108,113] Note that essentially the entire drop in electric potential across the interface occurs within the air (dielectric) domain and the liquid (conductor) domain is locally almost equipotential, as one would expect from Equations 3.11-3.12.

The simulation results are qualitatively similar to many previously experimentally visualized and computationally simulated cone-jet profiles for a fluid of finite electrical conductivity.[109,114-116,120-121] At this point, validation of the simulation's accuracy is based on the qualitative cone-jet "shape" comparison to other published results. The cone-jet profiles closely represent the experimental visualization and analytical model obtained by Hartman et al.[109] A side-by-side comparison with the simulated results produced by Lastow and Balachandran[116] using the CFX 4.4 (ANSYS Inc.) CFD package for heptane also demonstrate qualitatively similar profiles. The simulated results are validated by comparison with experimentally obtained jet profiles by Ganan-Calvo, et al.[108] While qualitatively similar, discrepancies arise due to differences in simulated domain, capillary geometry, and applied electric field. Lastow and Balachandram use an infinitely thin cylindrical wall producing an infinitely high potential gradient, causing the cone to retract

into the capillary. The cone in these simulations also retracts slightly, but no infinite potential gradients can be supported realistically by the present capillary geometry. The simulations also produce jet breakup as seen in the Figure 3.2. Altering any of a number of parameters such as flow rate, surface tension, applied potential, etc. allow for slightly different results, such as cone-jet formation without breakup.

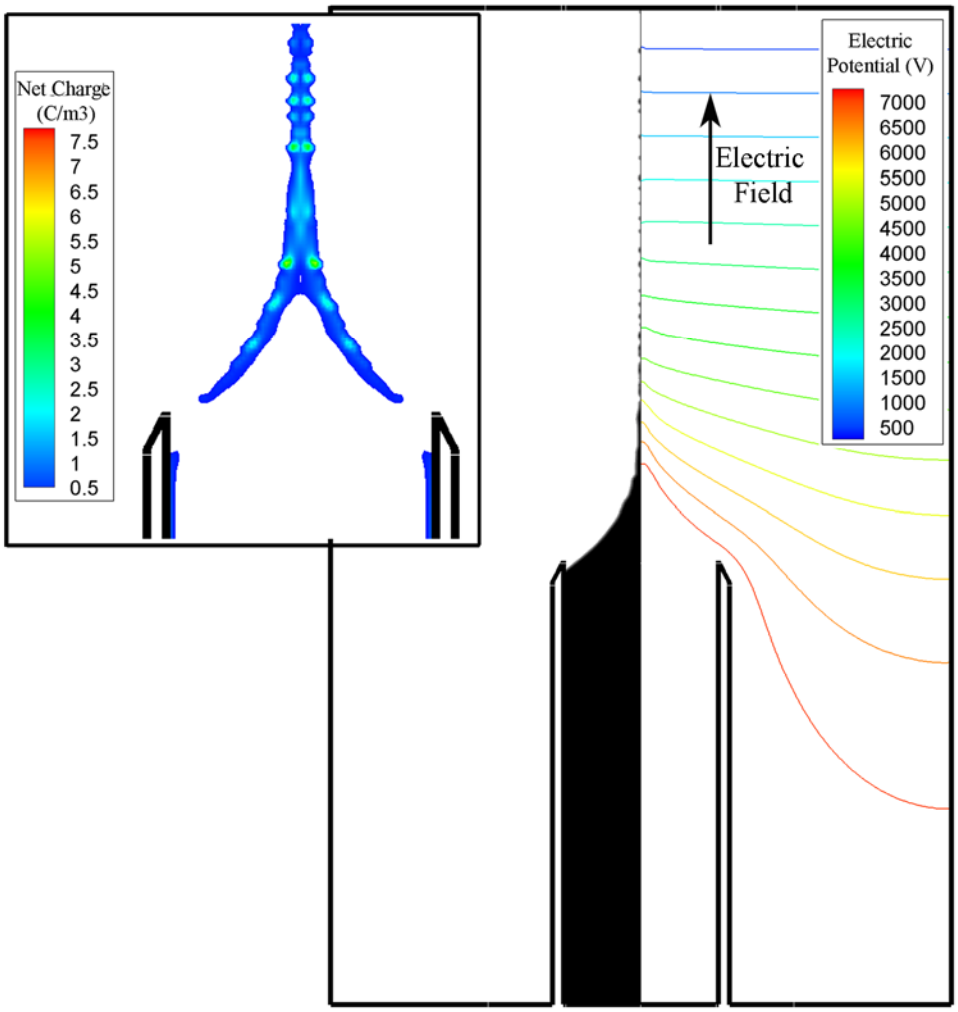

Figure 3.2 Left panel: fluid interface profile (liquid volume fraction equal to 0.5) for full electrohydrodynamic simulations of heptane. Right panel: electric potential distribution. Inset: free charge distribution (C/m^3). Simulation parameters: the simulation domain is axisymmetric with capillary radius, r_o = 350 μm, domain radius, R = 1400 μm, capillary length, l_o = 2000 μm, domain length, L = 4500 μm, capillary thickness, t = 50 μm, inlet velocity, u_o = 0.1 m/s, and capillary potential, ϕ_o = 7500V.

3.3.3.2 Perfectly Conducting Fluid – Taylor Cone Electrospray

To display the versatility of the electrohydrodynamic model implementation, the limiting case of electrospraying a perfectly conducting fluid is simulated. In an infinitely-conducting liquid domain, the free charges redistribute themselves along the domain boundaries essentially instantaneously (on time scale $t_{electric} = \varepsilon\varepsilon_o / \sigma$) relative to all other time scales. As the free charges move to the boundary (charge density within the bulk domain is now zero), they also realign themselves to exactly cancel the internal electric field within the bulk fluid. The electric potential, governed by Poisson's equation (Eq. 3.3), reduces to a Laplace equation $\left(\nabla^2 \phi = 0\right)$ within all domains considered. The electric field within a perfectly conducting fluid domain must be zero, therefore the gradient of the potential is also zero, $\vec{E} = -\nabla\phi = 0$. In order for both this condition and the Laplace equation to be satisfied, the potential within a conductor must be a constant. Therefore, the liquid fluid domain for these simulations is set to be equipotential.[144-145]

The boundary conditions from the previous section are still valid here. However, now the fluid becomes a conductor so that the surface charge density can be found from the normal component of the electric field in the adjacent dielectric domain (Equation 3.12).[129] This accumulated charge along the surface introduces electric Maxwell stresses at the interface which act to reduce the effective liquid-gas surface tension.

In the VOF model, surface tension is incorporated by representing it as a virtual body force term in the momentum equation, which is inserted for all cells along the interface between phases. The force term is defined as the stress due to surface tension, $\gamma\nabla\cdot\vec{n}$, taken from a basic static interface stress balance multiplied by a factor that is a

function of densities and volume fraction gradient at the interface. Starting with a general stress balance at the liquid-gas interface,

$$\left[\boldsymbol{T}^{\mu}+\boldsymbol{T}^{e}\right]\cdot\vec{n}=\gamma\vec{n}\nabla\cdot\vec{n} \tag{3.20}$$

Here, $\boldsymbol{T}^{\mu}$ and $\boldsymbol{T}^{e}$ are the mechanical (pressure and viscous) and Maxwell electrical stress tensors, respectively, as defined in Equations 3.8-3.9. The right hand side represents the stress due to the interfacial tension. The mechanical stress tensor includes the normal stress due to the hydrostatic pressure drop across the interface and viscous shear stresses. Since the Ohnesorge number, $Oh=\mu/\sqrt{\rho r_o\gamma}$, defining relative importance of viscous forces as compared to surface tension, is much less than unity, the viscous stress terms can be neglected. The tangential electric field is continuous across a boundary and since the fluid is assumed highly conducting, there is no internal electric field (Equation 3.12). Therefore, no useful information can be gained from the tangential component of the stress balance and it is not shown here. Only the normal component of the stress balance is of concern.

$$\Delta p=\gamma\nabla\cdot\vec{n}-\tfrac{1}{2}\varepsilon\varepsilon_o\left(\nabla\phi\cdot\vec{n}\right)^2 \tag{3.21}$$

The surface tension (first) term in this stress balance is an exact component of the body force that is used by FLUENT in conventional free surface problems. In EHD problems involving perfectly-conducting fluids, the last term in Equation 3.21 is expressed in a similar manner to the surface tension and added to the momentum equation as a virtual volumetric body force term for the Maxwell stresses.

$$\vec{F}=-\tfrac{1}{2}\varepsilon\varepsilon_o\left(\frac{\partial\phi}{\partial n}\right)^2\left[\frac{\rho\nabla\alpha}{\frac{1}{2}\left(\rho_1+\rho_2\right)}\right] \tag{3.22}$$

In order to demonstrate this implementation of the Maxwell stresses, a VOF simulation of Taylor cone formation is reported here. The initial interface profile at the start of the simulation is a hemisphere (an equilibrium shape) with radius equal to that of the capillary. The gradient of the potential field (electric field) is highest at the tip of the developing interface (Figure 3.3b), causing the highest level of electric stresses to occur. As shown in Figure 3.3, the evolving cone forms a 98.6º angle, as analytically predicted in Taylor's seminal work for a perfectly conducting fluid.[107] The Figure 3.3 inset displays the velocity field at the Taylor cone's tip, demonstrating the vortex as described by

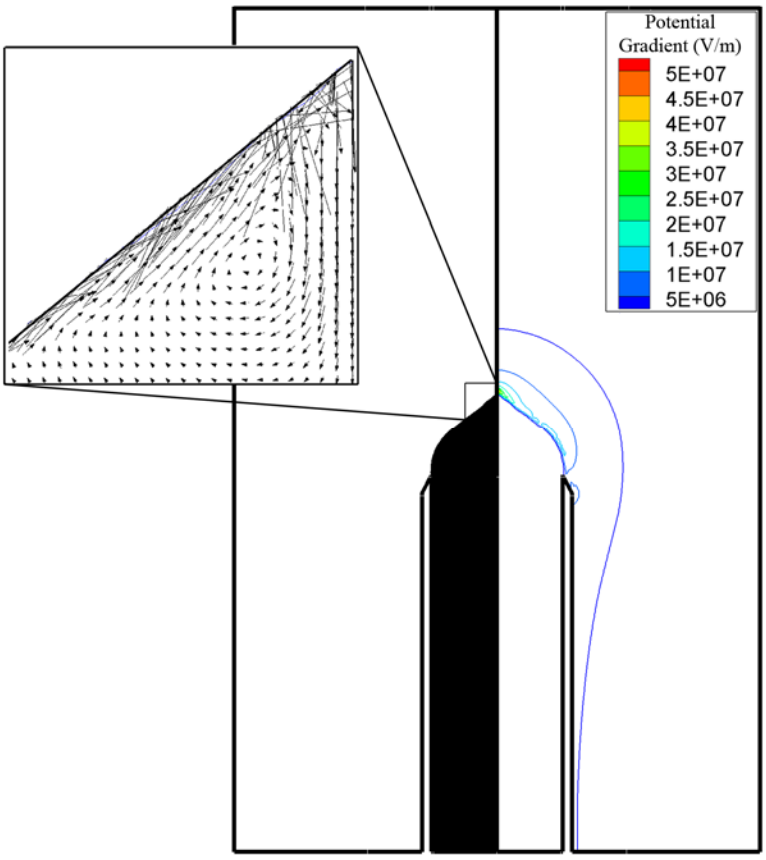

Figure 3.3 Left panel: fluid interface profile (liquid volume fraction equal to 0.5) for electrohydrodynamic simulations considering a perfectly conductive fluid. Right panel: potential gradient magnitude distribution. Inset: velocity field at cone tip. Simulation parameters: r_o = 350 µm, R = 1400 µm, l_o = 2000 µm, L = 4500 µm, t = 50 µm, u_o = 0.05 m/s, ϕ_o = 7000V.

Shtern et al.[146] and experimentally observed by Hayati et al.[114] The cone formation is also favorably compared to previous experimental results and numerical simulations of perfectly conducting liquids,[107,113,118] specifically in the area of liquid metal ion sources (LMIS)[122-125] further validating the modeling approach.

3.3.4 Simulation and Analysis of AMUSE Charged Droplet Ejection

With the predictive capabilities of the EHD model validated, it is applied to the case of a mechanically-driven, droplet-based ion source, such as AMUSE, with independently-controlled DC and AC-electric bias for charging the analyte. The results of the simulations are compared to integral measurements of the AMUSE ion source from the mass spectrometric and charging experiments (electric current and charge-per-droplet vs. applied electric field), reported in the next two chapters of this thesis.

This device conceptually differs from classical electrospray ionization by decoupling analyte charging and droplet/ion formation. ESI ion sources leave little room for control of the charging process because the electric field drives fluid dispersion as well as charge transport/separation. In contrast, the AMUSE ion source enables independent control of the charge separating electric field by utilizing mechanical means (focused ultrasonic waves) for droplet ejection. This results in control over both ejection regime (i.e., discrete droplet to continuous jet) and droplet charging through localized charge separation. Obviously, this independence of mechanical and electrical stimuli control is not absolute, as the droplet-charging electric field also locally influences the mechanical aspects of the droplet ejection process due to the Maxwell stresses. Also, the electrical field applied to the piezoelectric transducer for its actuation has some effect on the charging electric field. Yet, since the electric and mechanical signals can be spatially

localized in AMUSE (e.g., by using charging electrodes placed in the immediate vicinity of the ejection nozzles) the degree of their independent control is substantial for all practical purposes.

Figure 3.4 demonstrates the droplet evolution during the ejection process within an individual nozzle of the AMUSE array. Ejection is driven by the pumping action of a sinusoidal standing pressure wave (1MHz) generated by the piezoelectric transducer. Visualization and scaling of the ejection process, specific to AMUSE, has been described elsewhere as a balance between the periodic pressure forces, surface tension, and viscous stresses.[67,69] Comprehensive accounts of physics governing droplet formation, including the effect of an electric field are available.[118,130] The complex interface evolution dynamics (Figure 3.4) induce electromechanical, which in turn result in coupled charge transport and electric field gradients at the interface. The processes occur on temporal (~microsecond) and spatial (~micrometer) scales that are not readily accessible experimentally. However, with the help of a carefully validated EHD model, the

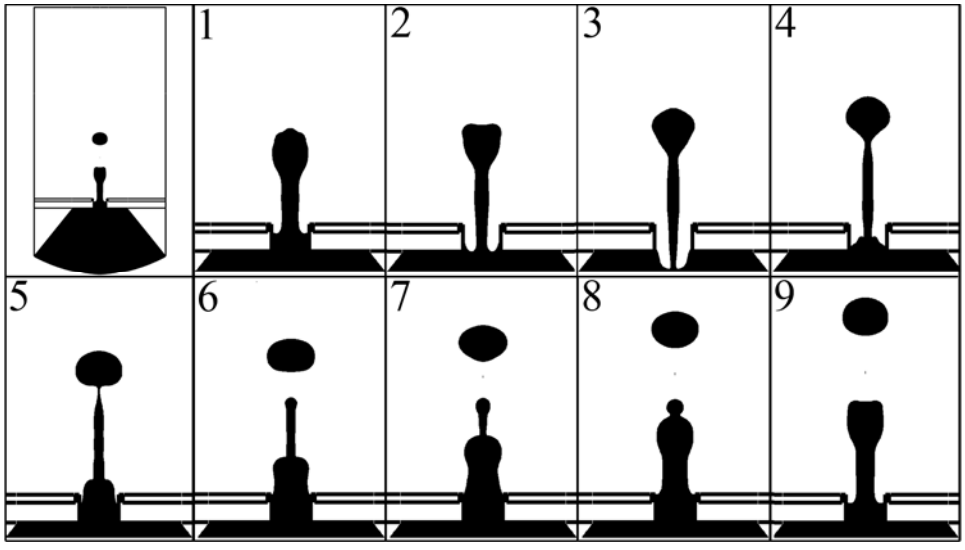

Figure 3.4 Simulated droplet evolution during AMUSE ejection through a single pressure wave cycle. Fluid profile results are for a liquid volume fraction of 0.5.

microscopic details of fluid flow, charge transport, and electric field can be computationally investigated during the droplet ejection, even within the nozzle orifice on the microsecond time scale.

An axisymmetric domain is used for simulations that include the apex portion of a single nozzle (Figure 3.5). Two sizes of the simulation domains are considered: (1) a "full" domain that includes solid dielectric domains for the silicon nozzle and silicon nitride membrane, and the strengthening tungsten layer, all of which are present in the AMUSE microfabricated nozzle array[67] (Figure 3.5(solid)), and (2) a "truncated" domain that eliminates the excess solid domains and reduces the overall extent of the domain (Figure 3.5(dashed)). The "full" domain is used in the DC electric field simulations, however, once an AC electric field is introduced, the computational time required for the continuously changing electric field to diffuse through the domain becomes prohibitively long to carry out parametric calculations. Therefore, for the AC electric field simulations, a "truncated" domain is used to reduce the computational burden and time. A DC electric field simulation of the "truncated" domain is used to verify that no significant loss of information is introduced by reducing the size of the domain.

A representative 2.5 micron radius of the nozzle orifice is considered for all simulations. Figure 3.5 is an example of the axisymmetric simulation domain. A harmonic response acoustic simulation, using the finite element analysis (FEA) software ANSYS,[70] is used to predict the oscillating pressure field within a nozzle. These simulations indicate that the amplitude of the oscillating pressure field is approximately uniform about a hemispherical section centered around the orifice. The hydrodynamic boundary condition at the hemispherical "inlet" to the simulated nozzle (Figure 3.5) is

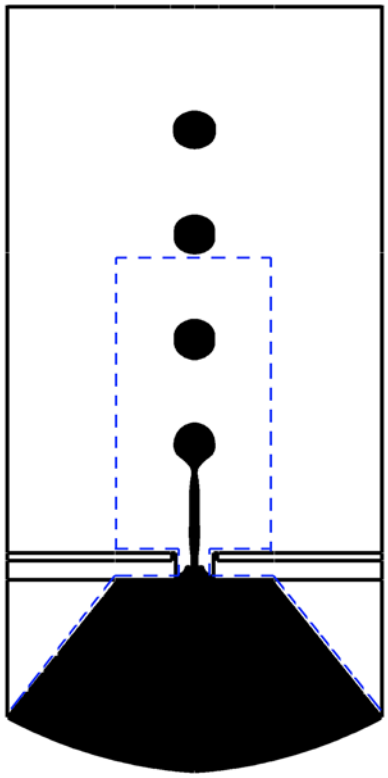

Figure 3.5 Axisymmetric simulation domains of droplet ejection in the presence of an electric field for the "full" domain for DC electric field simulations (solid black lines) and the "truncated" domain for AC electric field simulations (dashed blue lines).

therefore represented as an oscillating pressure boundary. The electric boundary condition at the inlet is a bias (charging) potential, chosen to represent the specified electric field strength. The "outlet" boundary at the top of the computational domain is specified as a pressure-outlet boundary condition for the hydrodynamics, and a fixed reference potential, representing the counter electrode. A no-slip condition is implemented at all solid-liquid interfaces. All other electrohydrodynamic boundary conditions are as specified in the previous sections, Equations 3.11-3.13.

Prior to final simulations, sensitivity studies have been performed to investigate sensitivity of numerical results on the mesh density, computational cell shape, and domain size.[67] The mesh density has been selected to minimize the numerical errors and

artificial effects due to VOF interface tracking, as discussed in section 3.3.2.2 "*Tracking Interface Evolution*", in order to accurately capture the advancing fluid interface during an ejection cycle. In the bulk domain, the radial and axial mesh density of 10 quadrilateral elements per μm in the vicinity of the nozzle orifice is employed. This mesh density decreases to 5 elements per μm in the axial direction approaching the outlet of the computational domain (Figure 3.5). Sensitivity studies of the simulation domain size indicates that its radial extent greater than three orifice diameters and its axial length capturing two wavelengths (droplet-to-droplet) of the ejection cycle are sufficient to yield no observable differences in results.

Charge transport equations are solved for both positive and negative charge carriers. The charge carriers considered are ions introduced throughout the fluid domain in a spatially uniform (isotropic analyte charging) manner. Specifically, these are considered to be the ions introduced by adding a small amount, 0.1% (v/v), of acetic acid to an aqueous solvent (hydrogen cations and acetate anions). Relative to the timescales of relevant phenomena considered here, dissociation of the acid molecules is essentially instantaneous and the recombination of ions is neglected. Unipolar ion injection is not considered, but reduction of ions is accounted for to maintain an electro-neutral condition within the bulk fluid. (As consecutive droplets are ejected, thus removing net charge from the bulk, an electrochemical "reduction" condition is incorporated into simulations to maintain electroneutrality in the bulk reservoir.)

3.3.4.1 DC Charging

Simulating charge transport under the application of a DC electric field induces charge separation throughout the fluid domain. Positive hydrogen cations migrate toward

the evolving droplet interface, increasing the net positive charge on ejected droplets (Figure 3.6). Hydrogen cations, having an electrical mobility approximately an order-of-magnitude larger than the acetate anions, for the most part experience transport dominated by migration. Through parametric investigations, it is determined that at low bulk charge density levels (~10 C/m^3), those associated with purely aqueous solutions, and the electric field magnitudes utilized here, the mechanical ejection process (i.e., fluid transport) is much faster than charge transport. This results in weak droplet charging because droplets are ejected before sufficient charge separation can occur. However, for high bulk charge levels (~10^4 C/m^3), the mechanical ejection and charge transport processes take place on comparable timescales, thereby coupling the associated phenomena. All simulation results shown hereafter are for the high bulk charge levels, which are the most interesting for bioanalytical MS. Initial charge densities are determined by a 0.1% (v/v) acetic acid addition to an aqueous liquid. This is also the solvent used in the AMUSE-MS charge separation experiments,[96] as well as the electric current and droplet charging measurements reported in the following chapters of this thesis, thus allowing for direct comparisons between the model predictions and experimental measurements.

Figure 3.6 shows the interface profile and pressure distribution for a time instant during the ejection cycle at which a single droplet has pinched off and a second droplet is evolving. The simulations show that the electric potential distribution is approximately linear within the air bulk except in the droplet region. Here, the electric field magnitudes are elevated above the driving electric field between the bias (charging) and counter electrodes due to the highly-charged, elongated fluid interface. As expected, the highest

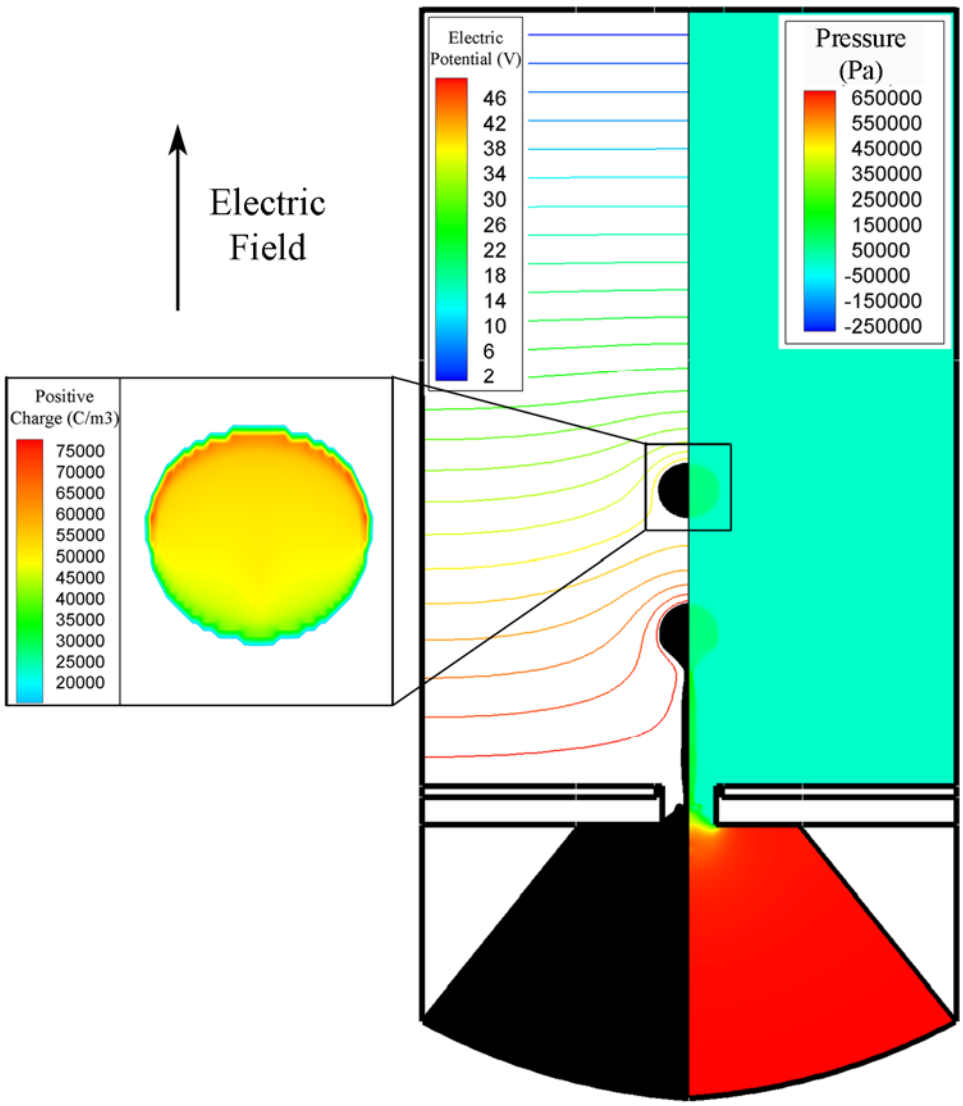

Figure 3.6 DC charging simulation results for electric potential distribution (left panel), pressure distribution (right panel), and a magnified view of positive charge distribution within an ejected droplet (inset). (Liquid volume fraction equal to 0.5)

levels of charge accumulation are in the areas of the highest electric field strength, at the poles of the droplet and within the evolving interface. For the case of applying a DC electric field, after a relatively quick transient, the bulk fluid maintains an approximately uniform potential (Figure 3.6). This reduces the electric field strength, and therefore the charge migration, in the necking region of the evolving interface (Figure 3.4(1-4)). This

phenomena will be discussed again when AC charging is described. However, as the droplet pinches off (Figure 3.4(5-6)), there is sufficient charge migration into the nozzle apex (orifice) region to produce increasingly charged droplets (Figure 3.6 inset).

3.3.4.2 AC Charging

Under the application of a DC electric field, described in the preceding section, charge separation occurs much as expected. Next, charge separation under a time-varying charging electric potential (field), specifically using a sinusoidal AC electric charging signal at the same frequency as the mechanical drive signal that generates the pressure field is investigated. As previously mentioned, the AC charging simulations use a "truncated" domain in order to improve the speed of calculations required for parametric analysis. All other aspects of the model implementation are identical to the "full" domain simulations for the DC charging case presented above. The initial simulation of droplet charging with an AC electric field, in-phase with the oscillating mechanical (pressure) field driving droplet ejection, yields net positive charge in ejected droplets (Figure 3.7). For the most part, the charge transport characteristics under the application of an AC electric field are similar to those discussed for the DC electric field simulations. However, with a continuously changing electric field, the bulk fluid never achieves a steady uniform potential. Comparing the electric potential distributions for DC (Figure 3.6) and AC (Figure 3.7) charging cases, there are obvious differences in the neck region of the evolving interface. Unlike the DC electric field, the applied AC electric field maintains an electric field presence in the necking region, allowing for increased migration of charge. This interesting theoretical result can be exploited in practice for

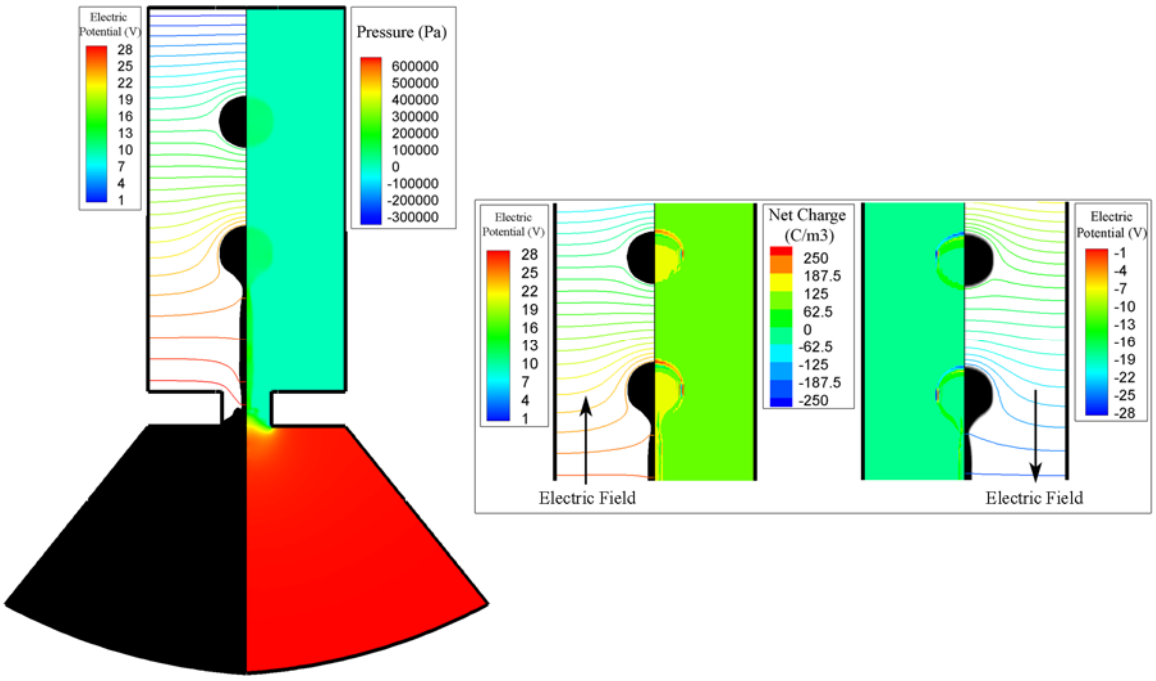

Figure 3.7 AC charging simulation results for electric potential distribution (left panel), pressure distribution (right panel), and a magnified view of electric potential and net charge distributions for electrical/mechanical signals in-phase (left inset) and 180º out-of-phase (right inset). (Liquid volume fraction equal to 0.5)

improved droplet charging in mechanically-driven droplet-based ion sources, and this point is revisited in following chapters.

With nearly-independent control of the mechanical (pressure) and electric fields, the phase shift between the ejection (mechanical) and charging (electrical) signals can be varied to achieve either net positive or negative droplets. The Figure 3.7 inset demonstrates the differences in the electric potential and net charge distributions for the pressure and electric fields in-phase (left) and 180º out-of-phase (right). The electric field drives net charge to the far surface (north or south pole) of the ejected droplet, depending on the direction of the applied electric field. For the pressure and electric fields in-phase, as the electric field is positive (pointing toward the outflow from the nozzle), positive charges are also driven from the fluid bulk toward the orifice. The opposite is true for

out-of-phase signals. The direction of the electric field during the time leading up to a droplet pinch-off determines the final net charge of ejected droplets. These unexpected trends in the case of AC charging are intriguing, and an experimental validation of the predictions on the effect of the phase shift between pressure and electric fields on droplet charging is presented in the next chapter.

3.3.4.3 Alternate Electric Field Waveforms

Through the investigation of both static (DC) and dynamic (AC) charge separating electric fields, a number of useful aspects were identified. For example, in the AC charging case, the electric field is continuously changing, hindering the bulk fluid from achieving a steady uniform potential. From Figures 3.6-3.7 it is apparent that the continuously changing AC electric field maintains an electric field presence in the necking region and the DC-charging does not. This induces charge migration that is not present in the DC charging cases, where the electric field is essentially zero within the fluid after an initial transient. These results can be utilized with alternative waveforms and time dependent electric fields to optimize droplet charging in mechanically-driven droplet-based ion sources.

Also, during experimental validation of these simulations (described in Chapter 4), it is observed that for high electric fields ($>7.0\times10^5$ V/m) the mode of ejection changes drastically. While droplet charging continues to increase with increases in electric field magnitude, the robustness and mode of ejection change towards becoming inferior. Based on the results presented here, another solution to sidestep the detrimental effects of high electric fields on interface evolution and discrete droplet ejection is the use of alternate charge separating electric field waveforms. For example, a step- or pulse-

function electric field could be used to enhance charge separation just before droplet pinch-off without detrimentally affecting the rest of the ejection cycle. Such waveforms would not only reduce or eliminate any electric effects on the ejection process, but also enhance charging by creating a transient electric field within the fluid just before pinch-off, transporting more charge to the interface as discussed during the comparison of DC and AC electric potential distributions. The bulk fluid would have no time to reach a steady uniform potential, and therefore as the pulse-signal is applied, the internal electric field enhances charge migration into droplets. An exploratory simulation comparing DC and step-function electric fields has shown the expected increase in charge per ejected droplet.

In Chapter 3, the development and validation of a complete electrohydrodynamic computational model for atmospheric pressure ion sources with minimal simplifications was reported. The model solves a coupled electrohydrodynamic problem for fluid flow, pressure and electrical potential fields, and charge transport in a multiphase fluidic system with evolving interfaces. The model is implemented using the FLUENT CFD platform and allows one to study a variety of complex phenomena involving interactions between the electrical and fluid mechanical fields. Demonstration of the predictive capabilities of the model by successfully simulating the multiphysics processes for three exemplary cases relevant to analyte ionization in bioanalytical mass spectrometry is accomplished. This includes, prediction of the cone-jet structure in electrospraying a fluid with finite electrical conductivity, the quasi-equilibrium Taylor-cone formation in electrospraying an infinitely-conducting fluid, and effects of the DC and AC-charging electric fields on charge separation and droplet charging in a mechanically-driven,

droplet-based AMUSE ion source. The next chapter discusses in depth the experimental validation of the EHD model as well as static and dynamic droplet charging in the AMUSE ion source. Optical visualization and scaling analysis are also used to gain insight into the physics determining the mode of ejection.

CHAPTER 4

EXPERIMENTAL CHARACTERIZATION AND SCALING: CHARGE MEASUREMENTS AND VISUALIZATION

Charge separation in the AMUSE ion source is experimentally characterized using charge collection measurements and optical visualization of ejection phenomena. Experimental charge-per-droplet values are evaluated from electrical current measurements correlated with ejected mass. These data are utilized for qualitative and quantitative comparison with simulated results using the EHD model presented in Chapter 3. Droplet charging analysis is performed for both static (DC) and dynamic (AC) charge separating electric fields, as well as a function of the bulk charge density. Through complementary computational and experimental investigations, distinct regimes of charge transport, which determine the extent of droplet charging, are identified. Additionally, high-resolution stroboscopic visualization of droplet ejection under the influence of varying electric fields is combined with a scale analysis of the ejection phenomena to develop an ejection regime map for the AMUSE ion source.

4.1 Droplet Charge Measurements

In the previous chapter, the predictive capabilities of the developed EHD model are demonstrated by considering three special cases: the electrohydrodynamics of a cone-jet, Taylor cone, and a mechanically-driven, droplet-based ion source (AMUSE). The computational predictions open up a window into the microscale physics of droplet charging in field-coupled electrohydrodynamic ion sources. They also suggest a new way

of using judiciously chosen AC electric fields for improved charge separation in the AMUSE ion source with independent control of electrical and mechanical actuation. In this section, the results of theoretical predictions are compared qualitatively and quantitatively with experimental measurements on the AMUSE ion source subject to DC and AC charging.

4.1.1 Experimental Setup

To validate the trends and results obtained with the electrohydrodynamic simulations, a number of experiments, measuring current and ejected mass (i.e., charge-per-droplet), have been carried out.[127] Experiments were conducted using aqueous (deionized water, Ricca Chemical Company, Arlington, Texas, USA) solutions containing 0.001% – 5.7% (v/v) glacial acetic acid (BDH Aristar, Westchester, PA, USA) (pH 4.26 – 2.38). Schematics of the experimental setup used for DC and AC charging experiments are shown in Figures 4.1-4.2. In both cases, the piezoelectric transducer is driven by an amplified (T&C Power Conversion RF Amplifier) RF signal at a resonant frequency of the fluid reservoir, generated by a Stanford Research Systems DS345 function generator labeled "RF Signal Generator (1)".[67,72-73] All respective signals were monitored with the use of a Tektronix TDS 2014 oscilloscope. The AMUSE ion source, operating under the specified electric field, ejected droplets into a small enclosed aluminum foil electrode box, collecting all ejected mass and charge. The current produced by the ejection of charged droplets was measured using a picoammeter (Keithley Instruments, Inc., Model 6485 Picoammeter, Cleveland, OH, USA) as the droplets deposit their charge upon impingement on the metallic receptor. The typical environmental radio-frequency-induced noise picked up by the sensitive picoammeter

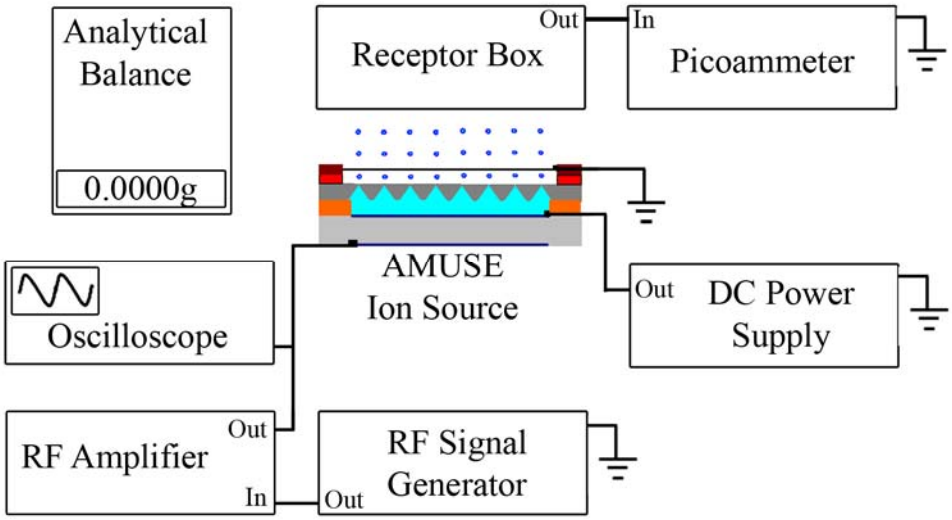

Figure 4.1 Experimental setup for ejected current and mass measurements for DC charging.

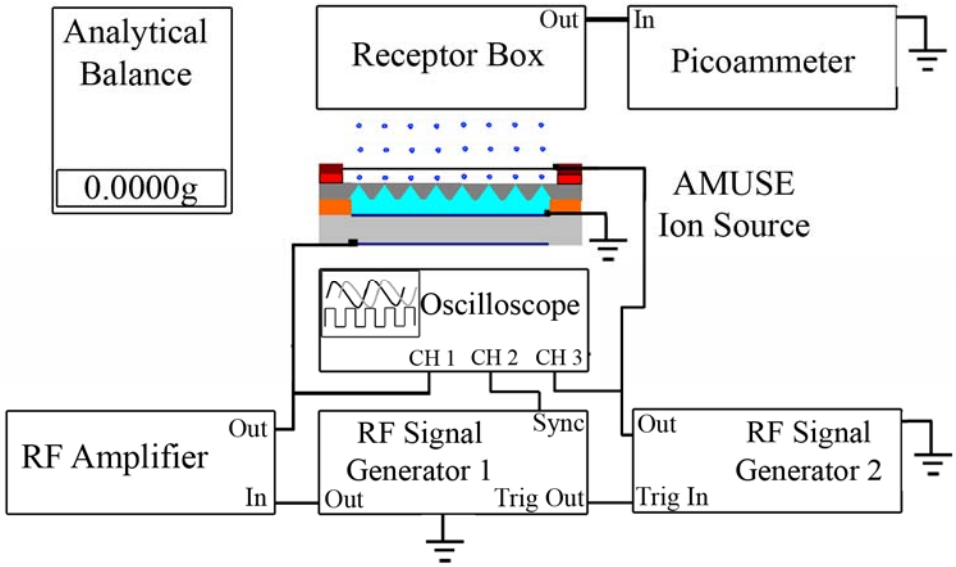

Figure 4.2 Experimental setup for ejected current and mass measurements for AC charging with adjustable phase shift.

was i_{RMS} ~ 0.05 nA. After a 60 second ejection period, the change in mass of the aluminum box was measured using an analytical scale (Mettler-Toledo Inc., AE 200 Analytical Balance, Columbus, OH, USA) with ±0.1 mg accuracy. An estimate of the

charge-per-droplet was obtained by assuming uniform droplet size, with diameter approximately equal to that of the nozzle orifice.[67] Specific to the AC electric field experiments (Figure 4.2), a second function generator, "RF Signal Generator 2" replaces the "DC Power Supply." The second function generator was triggered externally by "RF Signal Generator 1" to lock the phase of its signal to the signal from "RF Signal Generator 1" at the same frequency. All signals were monitored by the oscilloscope. The SRS DS345 function generators have phase shift adjusting capabilities to be used when considering AC charging mode of operation.

4.1.1.1 AMUSE Configuration

The mechanically-driven, droplet-based ion source AMUSE (Array of Micromachined UltraSonic Electrospray) allows for nearly-independent control of analyte charging and droplet formation, by decoupling the droplet-producing pressure field and the charge-separating electric field. The AMUSE ion source fabrication, assembly, and characterization have been described in Chapters 1-2, with further details available elsewhere.[66-69,72-73,75,96,99] The configuration equipped to apply a desired charging (bias) electrical potential, DC and AC, is used in these experiments. For the charge separation investigations, a brass support containing a transformer wire (electrically shielded) electrode is added to the standard assembly (Figure 4.3). This electrode acts as a "counter" electrode in the charge separation experiments, defining the electric field between inner electrode of the piezoelectric transducer, V_{PZT}, and the external wire counter electrode, V_{ext}. Control of these potentials provides accurate control of the induced electric field strength.

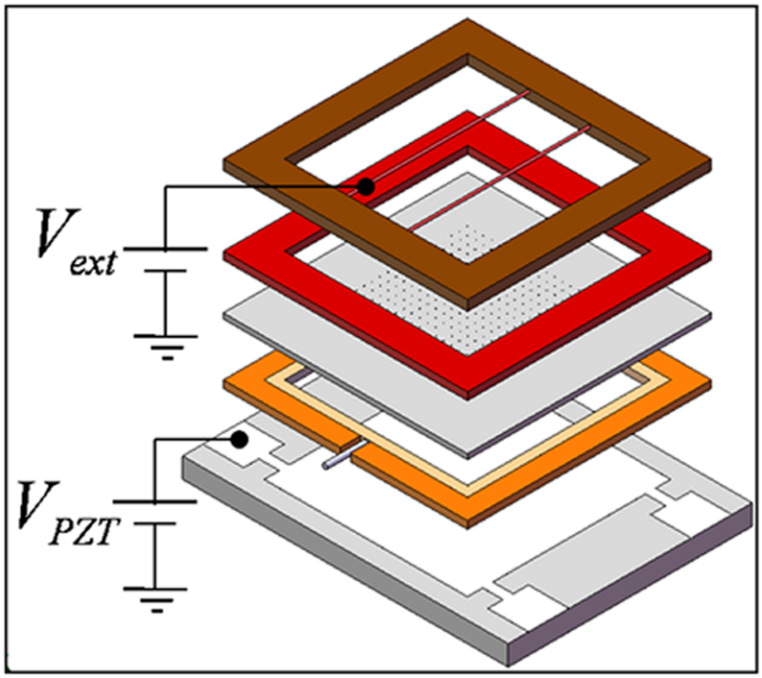

Figure 4.3 Schematic representation of the AMUSE ion source configured for application of an external electric field. The electric field is applied across the AMUSE ion source between the piezoelectric transducer's top electrode and an external wire electrode added to the stack assembly.

4.1.2 Validation of Charge-per-Droplet Simulated Results

The experimental validation of theoretical predictions obtained with the EHD model (Chapter 3) for both DC and AC electric charging in the AMUSE ion source is reported in this section. The key trends, defining the effects of DC/AC signal amplitude and phase-shift on charge-per-droplet, are qualitatively compared between simulations and experiments. These specific sets of experiments are conducted using aqueous solutions containing 0.1% (v/v) acetic acid (~50,000 C/m^3, pH 3.25).

4.1.2.1 DC Charging

Figure 4.4 depicts the simulated charge-per-droplet as a function of applied DC electric field strength. As expected, a linear relationship is obtained, demonstrating the

increase in charge-per-droplet with magnitude of external electric field. This is in agreement with the results of MS-AMUSE droplet charging measurements as a function of external electric field discussed in Chapter 5.[96] Figure 4.5 displays the charge-per-droplet for four consecutively ejected droplets, indicating a reduction in the "effective" charge-separating electric field acting on each consecutive droplet. This reduction is due to electric field shielding caused by previously ejected highly-charged droplets. However, the linear relationship of the charge-per-droplet with the far-field electric field magnitude is maintained even for consecutive droplets. The detrimental effect of shielding on droplet charging is unlikely to be an issue in typical mass spectrometry investigations using the AMUSE ion source, because of its coupling to a droplet transmission/evaporation interface (e.g., in-line air amplifier). The air amplifier immediately draws the droplets away, focusing the droplet plume and improving desolvation prior to the mass spectrometer inlet.[147]

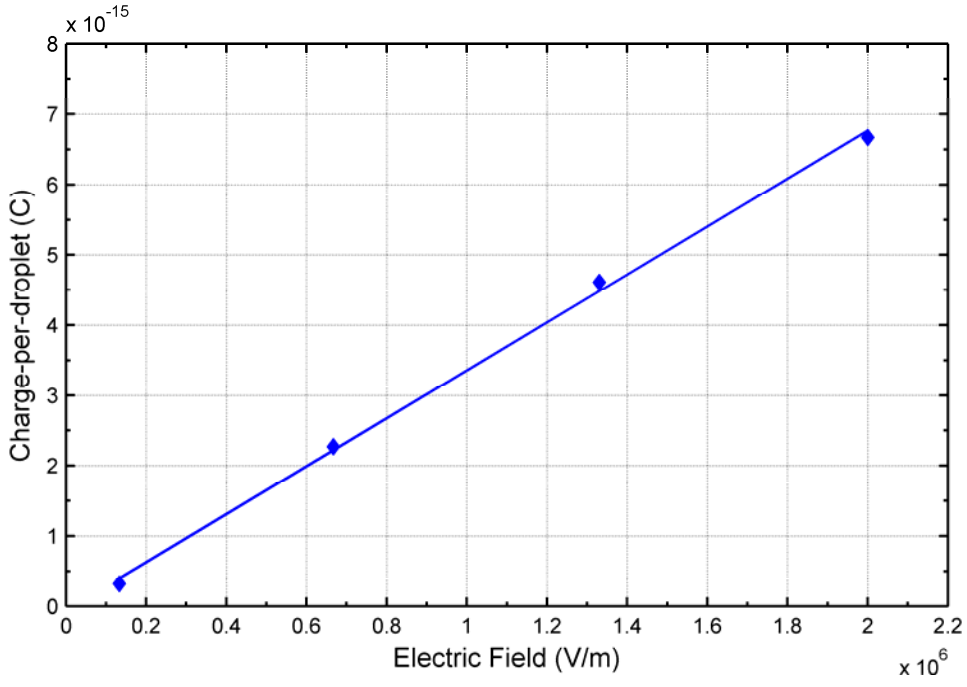

Figure 4.4 Simulated charge-per-droplet as a function of DC charging electric field magnitude.

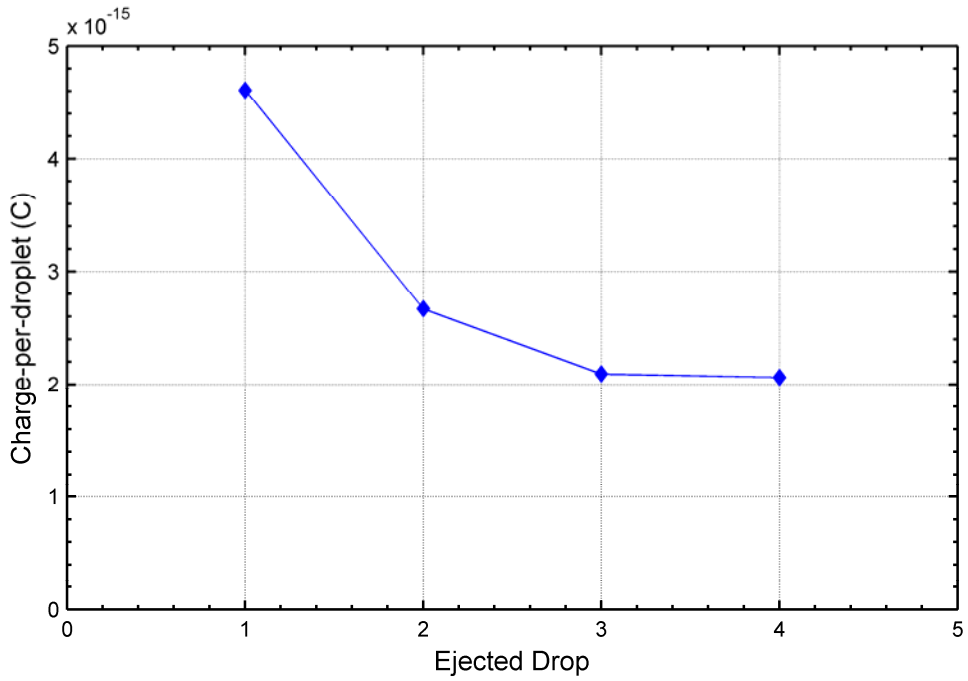

Figure 4.5 Simulated charge-per-droplet for consecutively ejected droplets with an applied 1 MV/m electric field.

For the range of electric field magnitudes analyzed in simulations (0 – 2×10^6 V/m), as well as employed in the experiments, the Maxwell stresses are not sufficient to produce significant interface deformation as seen in ESI. (In electrohydrodynamic cone-jet atomization, much higher electric fields are utilized (1×10^6 V/m – 3×10^6 V/m), which are further amplified at the capillary tip by the elongated capillary geometry ($\sim1\times10^7$ V/m).) Despite its relatively low strength, the electric field used in the AMUSE ion source is sufficient to increase the velocity of ejected highly-charged droplets by approximately 50% across the range of electric field magnitudes considered in Figure 4.4.

To validate these simulated trends, a number of experimental measurements were completed. Electric current data, in the range of nanoamperes to tens of nanoamperes,

were taken for DC charging electric field magnitudes in the range 1.0×10^5 V/m – 1.5×10^6 V/m, which were also used in the mass spectrometry measurements[96] (Chapter 5) and simulations. Figure 4.6 presents the results of experimental measurements and simulations, normalized for direct comparison. The circles represent the MS signal intensity data (reported in Chapter 5),[96] the squares represent ejection current, and the diamonds represent the simulated charge-per-droplet as shown in Figure 4.4. With linear fits to each set of data, remarkably similar results in slope between experimental measurements and simulated results are obtained, providing validation of the trends produced by the EHD model for the DC charging electric field.

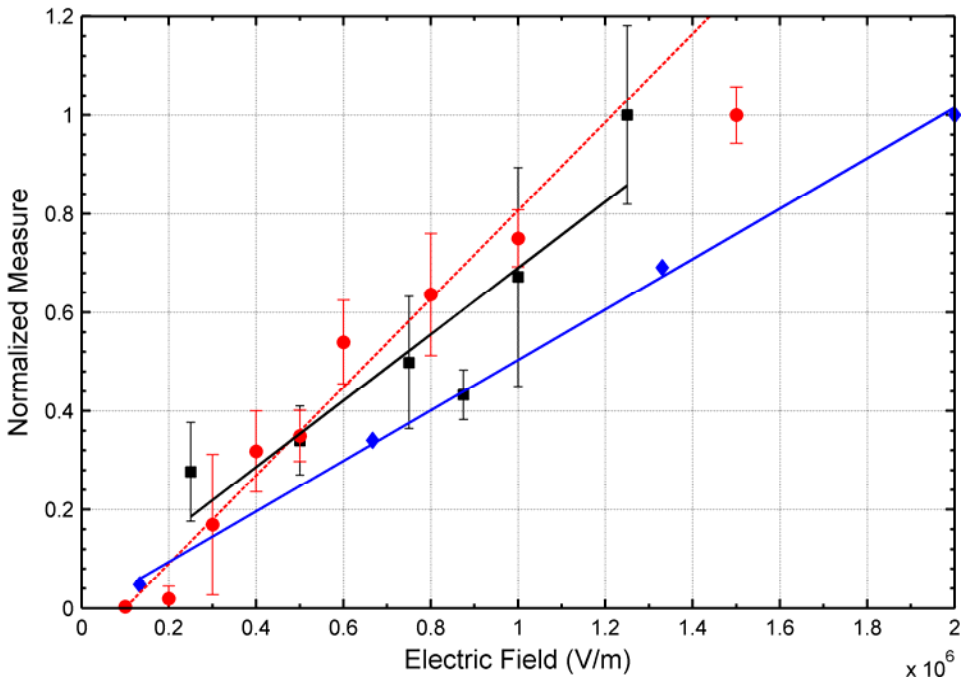

Figure 4.6 Dependence of normalized charge-per-droplet on the magnitude of the electric field - comparison between the experimental measurements and simulations. (circles) normalized mass spectrometry signal intensity [obtained for a 3 μM solution of reserpine in an aqueous solvent containing 0.1% (v/v) acetic acid, using a time-of-flight mass spectrometer], (squares) normalized ejection current as measured in charge collection experiments described above [for an aqueous solvent with 0.1% (v/v) acetic acid], and (diamonds) normalized simulated charge-per-droplet.

To provide an approximate experimental measure of the charge-per-droplet, the electric current and ejected mass measurements are coupled. Ejected droplets are assumed to be monodisperse, with diameter approximately equal to the orifice diameter (dependent on frequency of operation).[67] This provides a direct relationship between the mass of a single droplet and total mass collected during the experiment (~10-50 milligrams per 60 seconds). Experimental data on collected current and ejected mass yield estimates for charge-per-droplet to be in the range of $2\times10^{-15}-1\times10^{-14}$ C across the range of DC electric field magnitudes considered here. Remarkably, these charge-per-droplet measurements are of the same order-of-magnitude as the simulated results (Figure 4.4) for equivalent electric fields. Also, at the highest electric field considered ($\sim 2\times10^{6}$ V/m), both experimentally and computationally, the charge-per-droplet is an order-of-magnitude less than the Rayleigh limit for a water drop of similar size ($\sim 1\times10^{-13}$ C). The maximum local charge density at the droplet pole approaches the local Rayleigh limit, i.e., ~800 C/m^3 versus ~980 C/m^3, respectively.

During the experimental validation of the EHD model, it is observed that for high electric fields ($>7.0\times10^{5}$ V/m) the mode of ejection changes drastically. The ejection strength (droplet velocities/ejection height) and level of ejection (number of active nozzles) noticeably decrease. This is demonstrated in Figure 4.7 by the decrease in flow rate, i.e. collected mass per ejection period, as the charge separating electric field increases. The deviation in collected data at individual electric field magnitudes simply demonstrates the variability in ejection across a number of tests. There appears to be a transition in ejection regime around 7×10^{5} V/m, from higher flow rates at low electric field to lower flow rates at high electric field. It is interesting to note that although

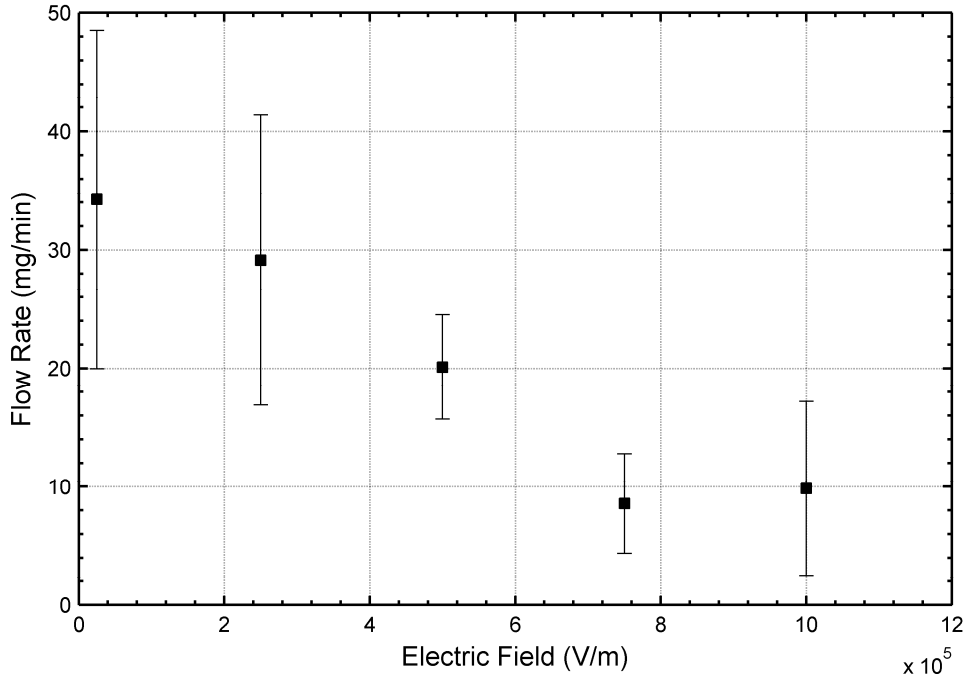

Figure 4.7 Experimentally measured average ejection flow rate (collected mass per collection time) as a function of the charge separating electric field magnitude.

ejection levels decrease, droplet charging continues to increase linearly with increasing electric field magnitude (Figure 4.6), showing no considerable effect on charge transport.

4.1.2.2 AC Charging

With the use of a time-varying electric field, a great deal of control over charge separation and ultimately droplet charging is gained. In this section, a special case of AC charging at the same frequency as the acoustic pressure field is considered to illustrate the power of judiciously-implemented interplay between the separately controlled mechanical and electrical fields, as a means to dramatically enhance the charging efficiency. The coupling between interface evolution, specifically pinch-off, and a dynamic electric field is a complex relationship which, if well understood, can be exploited to optimize device operation and ionization efficiency.

Figure 4.8 shows simulated charge-per-droplet as a function of the relative phase-shift between the electric signal, which charges the droplets, and the acoustic pressure signal, which mechanically drives droplet ejection. As expected, a periodic sinusoidal relationship between ejected charge-per-droplet and the relative phase shift between acoustic pressure and electric charging signals is obtained. The simulated data points are plotted with a line to guide the underlying sinusoidal function. From the simulated net charge distributions shown in Figure 3.7, positive charging is expected when the acoustic pressure field at the nozzle and electric charging signal are in-phase, and negative charging should occur when the fields are 180º out-of-phase, exactly as shown in Figure 4.8. Next, experimental charge measurements for an AC charge separating electric field are qualitatively compared to the simulation results.

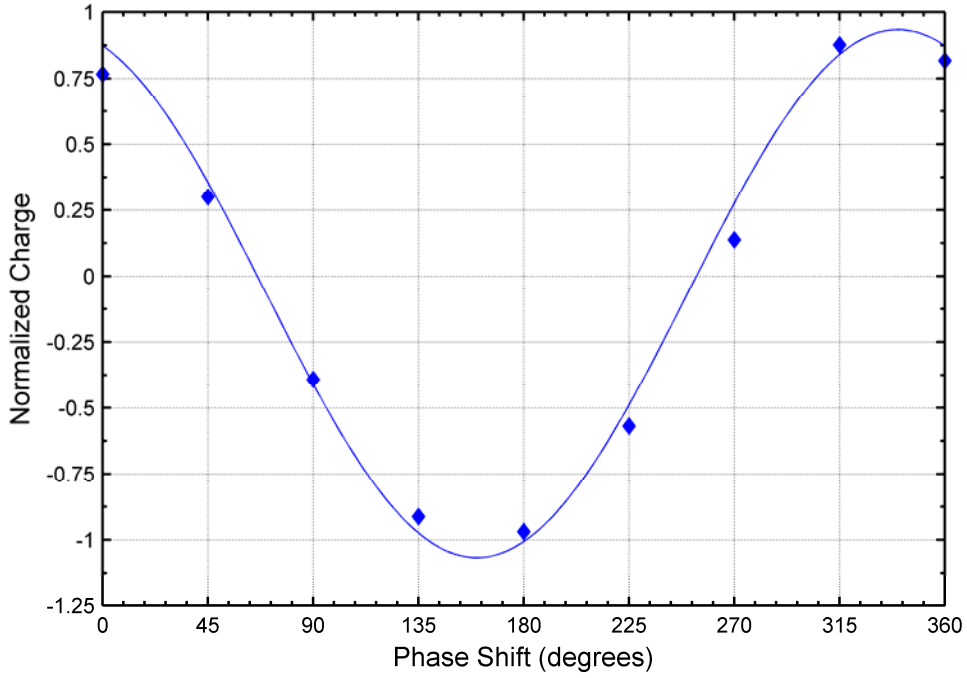

Figure 4.8 Simulated charge-per-droplet as a function of the phase-shift between the AC charging electric field and mechanical ejection pressure field.

Note that the AC electrical field applied to the piezoelectric transducer to generate the acoustic pressure field also generates an electrical field with a *fixed* phase difference with respect to the pressure field. That *fixed* phase difference determines the polarity and amount of charge-per-droplet as simulated in Figure 4.8, which can be called RF-only charging since there is no DC bias involved.[73,75,96] This can be considered as a constant, baseline charging level. In order to show that a separate AC electrical field can be used to control the droplet charging, a secondary AC signal at the same frequency is used. The secondary AC signal induces a charge-separating electric field in the proximity of the nozzle at a desired phase shift with respect to the driving pressure signal. In such an arrangement, the secondary AC signal should introduce a modulation on the droplet charge over the baseline as this secondary electric field interferes with the electric field generated by the piezoelectric transducer drive signal (RF Signal Generators 1 and 2 in Figure 4.2, respectively). Figure 4.9 shows the experimental data and prediction of the charge-per-droplet as a function of a relative phase-shift, normalized for comparison. The experimental values are obtained from measurements of current and ejected mass, as a function of the phase-shift between the piezoelectric drive and secondary AC signals. The *fixed* phase-shift between pressure and electric signals generated by the piezoelectric transducers results in the net negative charge baseline, and the secondary electric field creates the expected sinusoidal relationship with maxima and minima in the measured charge-per-droplet. The secondary electric field interferes constructively and destructively with the *fixed* phase signal as the relative phase is varied between 0º and 360º.

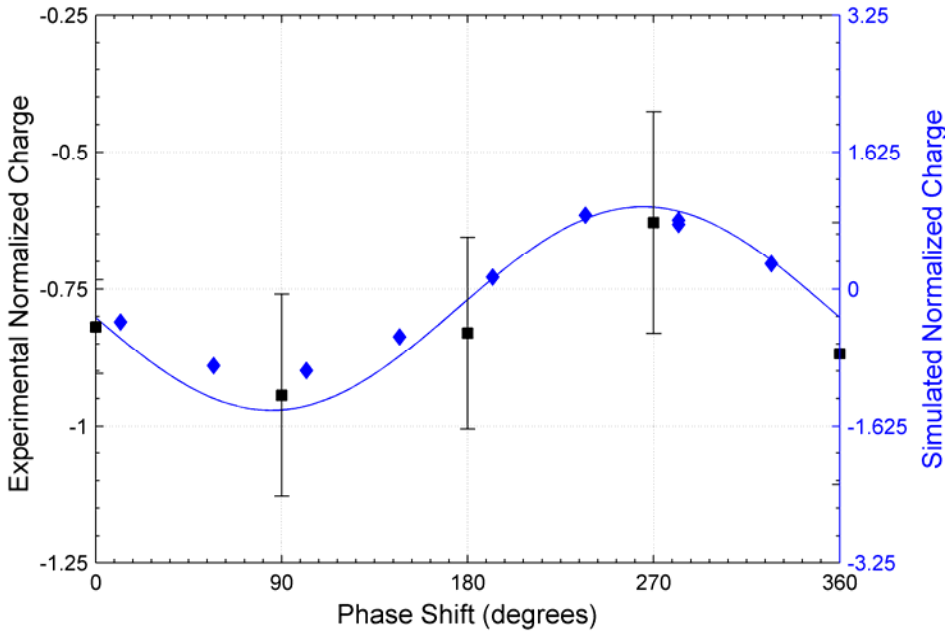

Figure 4.9 Comparison of experimental normalized charge-per-droplet data with theoretical predictions as a function of a relative phase shift between the mechanical and electrical signals, (diamonds – CFD simulations of charge-per-droplet, squares – experimentally measured charge-per-droplet using ejected current and collected mass measuring techniques described in text).

This result shows that a significant increase or a decrease in charge separation and droplet charging can be achieved by judicious combination of external DC and AC-charging electric signals of appropriate waveform and phase-shift relative to the mechanical drive signal. This idea could be further extended to preferential pre-concentration of selected charged analyte molecules within an ejected droplet by exploiting the differences in ionic mobility in conjunction with the appropriately-chosen frequency, waveform, and phase-shift of the AC-charging electric field. The EHD model developed in this thesis becomes a powerful tool that makes such design exploration studies possible.

4.1.3 Analysis of Charge Transport

In Chapter 3, droplet charging in the presence of both static (DC) and dynamic (AC) electric fields was investigated computationally. This was followed by experimental validation using ejected current and collected mass measurements, discussed above. In all the cases discussed in the previous sections, droplet charging is considered as a function of the electric field for a common bulk charge density for MS analyses, i.e. 0.1% (v/v) acetic acid in water (~50,000 C/m^3). Now, an investigation of charge separation and droplet charging as a function of bulk charge density is considered.

4.1.3.1 Bulk Charge Density (Individual Droplet Simulations)

Utilizing the computational model developed in Chapter 3, a numerical investigation of droplet charging as a function of bulk charge density is completed. The simulated results are reported for an individually ejected droplet, neglecting any "shielding" effects produced by previously ejected droplets. Figure 4.10 depicts the simulated charge-per-droplet as a function of the bulk charge density for several representative electric field strengths. Quite unexpectedly, the charge-per-droplet does not monotonically increase with increasing bulk charge density, as it did for increasing external electric field strength (see discussion in the previous section). In fact, negatively charged droplets are obtained upon application of a positive DC electric field for bulk charge densities in the range of around 125,000-300,000 C/m^3. To take a closer look, Figure 4.11 displays the droplet charging trends as a function of electric field strength for a range of different bulk charge densities. In Figure 4.11(a), at lower bulk charge densities, the linear trend between charge increase and electric field is observed in agreement with both computational (Figure 4.4) and experimental (Figure 4.6) results

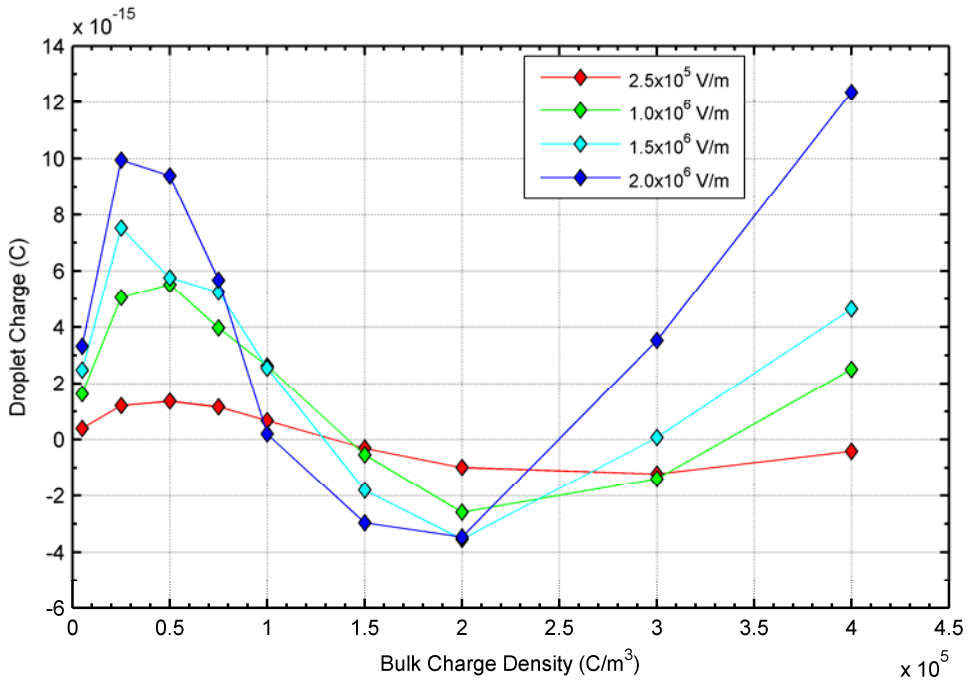

Figure 4.10 Simulated charge-per-droplet as a function of initial bulk charge density for several representative DC electric field magnitudes.

demonstrated in the previous section. However, with increasing bulk charge density, the charge-per-droplet trends as a function of electric field start to deviate from monotonically increasing, to having a local maximum, and then even decreasing (Figure 4.11(b)). As the bulk charge density is increased further, a monotonically decreasing droplet charging trend is obtained (Figure 4.11(c)). In this range, negatively charged droplets are produced under the application of a positive electric field. Increasing the bulk charge density even further, reverses this trend and results again in monotonically increasing positive charge-per-droplet, although in a nonlinear fashion (Figure 4.11(d)). In general, at these high charge densities, the ejected droplets are consistently negative at low electric field strengths and transition to positive charging at high electric fields (Figure 4.10).

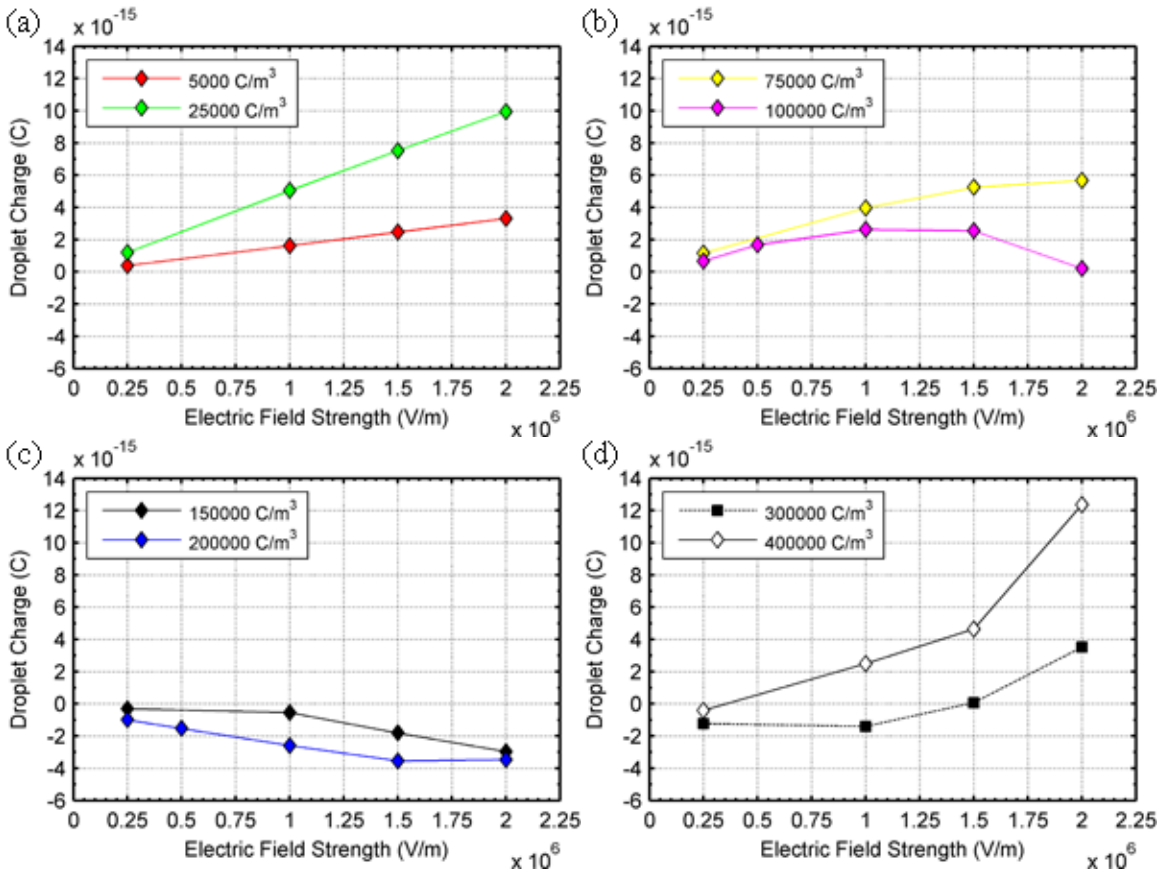

Figure 4.11 Simulated charge-per-droplet as a function of applied DC electric field for (a) low (~ 5,000 – 50,000 C/m^3), (b) low-medium (~ 50,000 – 125,000 C/m^3), (c) medium-high (~ 125,000 – 250,000 C/m^3), and (d) high (~ 250,000 – 400,000 C/m^3) bulk charge densities.

The transient nature of the droplet ejection in the AMUSE ion source is a root-cause of complex interplay between charge transport by fluid motion, bulk charge density, and external electric field. Thus, the physics of interacting charge and fluid transport under periodic ejection must be investigated to expand the present understanding of droplet charging. To this end, a scale analysis is used to develop an insight and predictive relationships that determine droplet charging mechanism(s) for a range of electric field and bulk charge densities.

4.1.3.2 Charge Transport Time Scale Analysis

A simple scaling analysis is used to gain insight into the dominant physics of the charge transport as a function of the bulk charge density. It is important to note that by its nature, the scaling analysis is an approximate technique and the results are strictly valid for an "on-the-order-of" basis. Considering the charge transport equation, Equation 3.5, the relevant transport time scales can be identified as (1) the process time scale $\left(t_p \sim 1/f\right)$, (2) the advection time scale $\left(t_u \sim l/u_o\right)$, and (3) the charge relaxation time scale $\left(t_{relax} \sim \varepsilon_o \varepsilon_r / \mu_{em} q_o\right)$. The ionic transit (ion migration) time scale $\left(t_i \sim l/\mu_{em} E_o\right)$ is more than an order of magnitude greater than all other time scales and therefore is not going to influence the process under investigation. Figure 4.12 depicts the charge transport time scales for a 1 MHz drive signal as a function of the bulk charge density, overlaid with the charge-per-droplet curve for a 2.5×10^5 V/m electric field, from Figure 4.10. The periodic nature of the pressure field at the nozzle orifice driving ejection determines the inverse of the driving frequency as the characteristic time scale on which dynamics of all processes must be compared. For a given set of operating conditions, the process time scale is only a function of the drive signal (pressure field) frequency, and therefore constant (note that it may not be constant if a more complex waveform is employed to drive ejection). The advection time scale is a function of the characteristic length (radius of the nozzle orifice) and characteristic velocity, both constant for a given drive signal frequency and amplitude. The charge relaxation time scale is a function of the characteristic charge density, q_o, which depends on the bulk charge density, the liquid permittivity, and the ionic mobility of the relevant charge carrier (H^+ ions for the

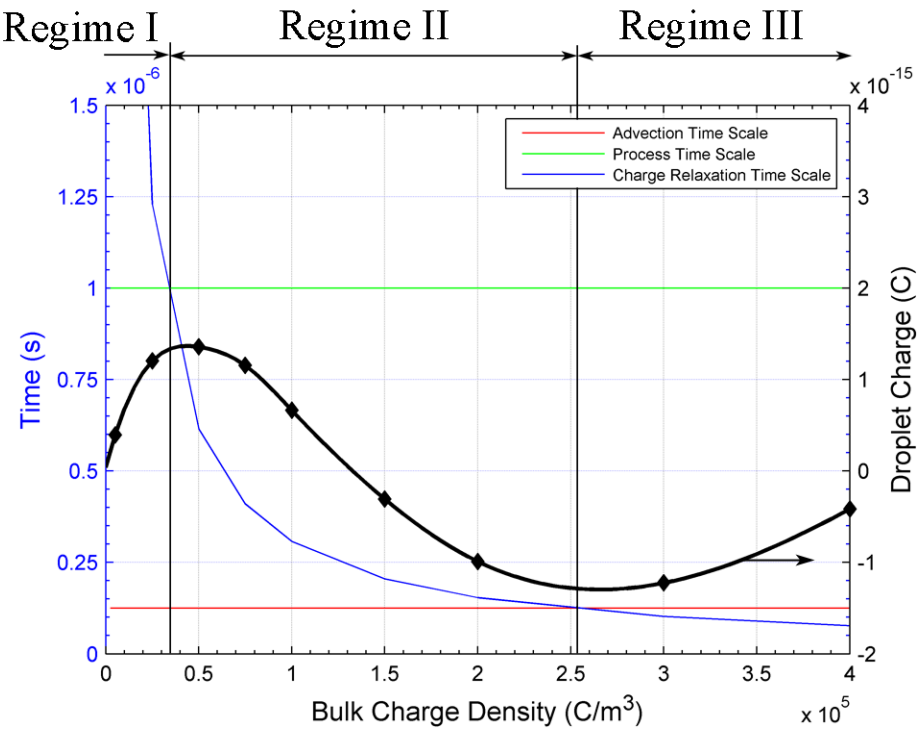

Figure 4.12 Charge transport time scales for a 1 MHz piezoelectric transducer drive signal, plotted with simulated charge-per-droplet values as a function of the bulk charge density for external electric field strength of 2.5×10^5 V/m.

analysis here). In Figure 4.12 the inverse relationship between the charge relaxation time scale and characteristic charge density separates the parameter space into three regimes, as the points where the charge relaxation time scale crosses with the process and advection time scales.

Regime I: At low bulk charge densities, the charge relaxation time is longer than both the process and advection time scales, $t_u < t_p < t_{relax}$. As long as charge relaxation, due to the application of an external disturbance (i.e., external electric field), is slower than droplet formation (process time), any increase in bulk charge density results in a decreased charge relaxation time, thus allowing more time for charge separation. This in turn leads to an increase in charge-per-droplet levels as more charge makes it into the ejected

droplets. This is clearly displayed in Figure 4.11(a) by the noticeable increase in charge-per-droplet levels as the bulk charge density increases from 5,000 to 25,000 C/m^3. It is in this regime of low bulk charge densities that the linear relationship between droplet charging and applied electric field is found, as discussed in Chapter 3. It must be emphasized that this behavior is only observed when the charge relaxation time scale is the longest of all relevant time scales.

Regime II: For intermediate bulk charge densities, the charge relaxation time decreases past the process time, but is not yet smaller than the advection time scale, $t_u < t_{relax} < t_p$. In this case, the charge within a forming droplet has sufficient time to fully relax before the droplet is ejected (on the process time scale), redistributing to cancel any internal electric field induced by the application of an external electric field. However, since the advection time is still faster, dominating charge transport, already separated charge is "pushed" (advected) into the evolving droplet. From the Poisson equation (Eq. 3.3), this excess charge, beyond equilibrium, causes an increase in the local electric potential in the ejecting droplet region above the applied external potential in the bulk reservoir (all potentials are relative to the ground at the external electrode above the ejector surface). As schematically shown in Figure 4.13, this induces an adverse internal electric field that actually enhances migration of negative charge into the droplet region, therefore, decreasing the net positive charge-per-droplet. As the bulk charge density increases, the time for charge relaxation continues to decrease, allowing more time for the adverse electric field to transport negative charges into the droplet before droplet pinch-off. The overall effect of the preferential transport of negative charge carriers (acetate anions, CH_3COO^-) toward the evolving droplet interface causes the steady decrease in net

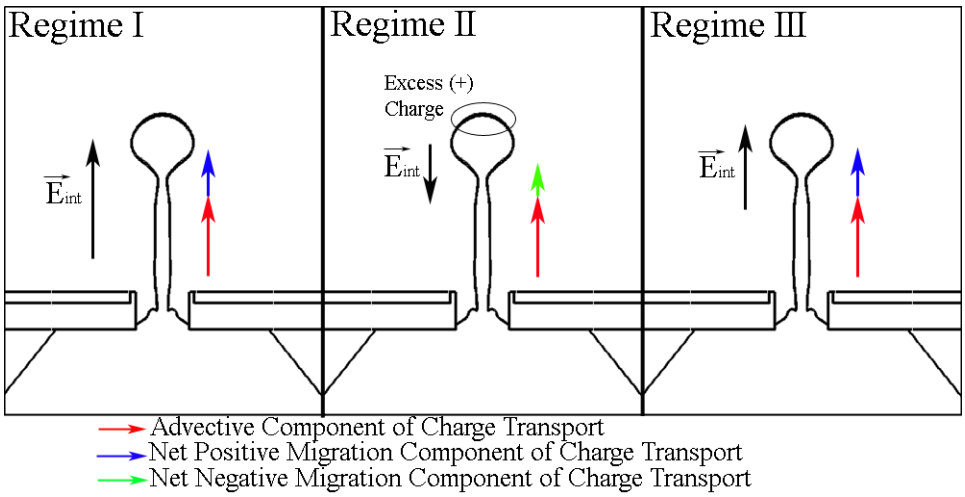

Figure 4.13 Schematic representation of the internal electric field direction and net charge transport in an evolving droplet for each of the regimes of charge transport.

positive charge-per-droplet seen in Figures 4.10 and 4.11(b-c), even producing negative droplets in the presence of a positive external electric field at the higher end of bulk charge densities in this regime. In essence, Regime II is composed of two sub-regimes: the first (Regime IIa), in which droplet charging starts about a local maximum and then rapidly decreases with bulk charge density (Figure 4.12, negative second derivative of charge-per-droplet vs. bulk charge density), and the second (Regime IIb), in which droplet charging decreases slowly with bulk charge density as the charge relaxation time scale approaches the advection time scale (Figure 4.12, positive second derivative of charge-per-droplet vs. bulk charge density). This inter-regime transition occurs around the inflection point of the droplet charging curve in Figure 4.12. In Regime IIa, droplet charge begins to increase as a function of electric field, experiences a local maximum and then decreases (Figure 4.11(b)), and in Regime IIb droplet charging decreases slowly with external electric field (Figure 4.11(c)).

The simulations have confirmed that the decrease in charging, to the point of producing negative droplets, is due an increase in selective transport of negative charges into the droplet region and not due to the removal of positive charges when an adverse internal electric field is induced (Figure 4.13). This is conceptually better understood by noting that when the advection time scale is still the fastest, it is the advection that dominates transport of both positive and negative charges into the evolving droplet region. And it is the direction of the internal electric field that enhances the relative transport of positive versus negative charge carriers through ionic migration. From the simulations, it is found that during the ejection process (before pinch-off), the net electric field direction (sum of local/internal and external electric fields) matches the sign of the slope of the charge-per-droplet curve (Figures 4.12-4.13), providing solid support to the arguments on the interplay of different processes when charging occurs in regime II.

Regime III: Finally, as the charge relaxation time becomes faster than all other time scales, $t_{relax} < t_u < t_p$, a steady increase in charge-per-droplet is observed, as in the case of Regime I. Now, the charge relaxes sufficiently fast to dominate the effects of all other transport processes. Therefore, as the charge relaxes to cancel the external electric field, advection still pushes separated charge into the evolving droplet, inducing an adverse electric field. However, the charge moves fast enough to redistribute within a droplet and cancel the induced adverse electric field. As shown in Figures 4.10 and 4.11(d), increasing charge density in this regime leads to an increase in charge-per-droplet.

Understanding of droplet charging mechanisms, as determined by the relative magnitudes of the charge transport time scales, has direct implications for the use of alternate waveforms, e.g. pulsed-function electric fields for charge separation, as

introduced in Chapter 3. If the goal is to achieve maximum droplet charging, the device needs to be operated at the boundary of Regimes I and II, where the charge relaxation time and process time scales are comparable. For bulk charge densities in Regime I, a linear increase in droplet charging with electric field is observed, and reduction in the duration of the applied electric field will reduce overall droplet charging. Therefore, for bulk charge densities in this regime, DC-charging yields optimal results. However, for bulk charge densities in Regime IIa, the charge has sufficient time to induce an adverse electric field, thus reducing droplet charging. In this region, it is beneficial to reduce the duration over which the electric field is applied (e.g., using a reduced electric pulse width). Specifically, using an electric field pulse right before droplet pinch-off will provide the desired charge separation without leaving time for an adverse electric field to inject negative charging into a droplet that would lead to a net reduction of positive charge in the ejected droplet.

4.1.3.3 Experimental Characterization

To experimentally investigate the charge-per-droplet trends as a function of bulk charge density, the same setup is used as the one employed in measuring the charge-per-droplet as a function of electric field (Figure 4.1). Figure 4.14 displays the charge-per-droplet measurements as a function of the bulk charge density, taken at a constant external electric field of 3.5×10^{5} V/m with the AMUSE operated at 0.905 MHz. The experimental results demonstrate a more gradual increase and decrease about the local maximum in droplet charging than found computationally in Figure 4.10. Additionally, for the same range of bulk charge densities as considered in simulations, the local minimum from Figure 4.10 is absent. Because the experimental trends demonstrate

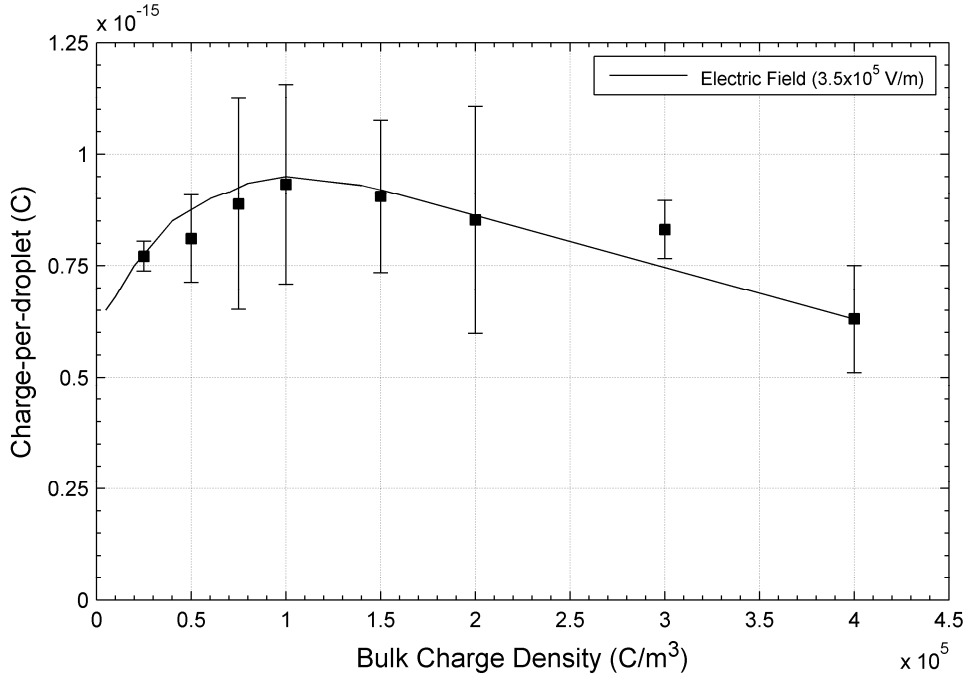

Figure 4.14 Experimental charge-per-droplet as a function of the bulk charge density for a 0.905 MHz drive signal.

similarities to the individual droplet simulations, it can be hypothesized that the local electric field distortion due to previously ejected droplets (i.e., electric field shielding) is in fact relevant and causing the discrepancy.

Therefore, simulations of droplet charging as function of the bulk charge density that consider the average charging of consecutively ejected droplets (~8-10) are completed to check the hypothesis of the local electric field shielding. Indeed, for this case, previously ejected droplets are shown to play an important role on the charging of successive droplets. Figure 4.15 compares the charge-per-droplet simulation results for both individual droplet and multiple droplet averages for electric field strength of 1.0×10^{6} V/m. In agreement with the experimentally observed trend, the computed

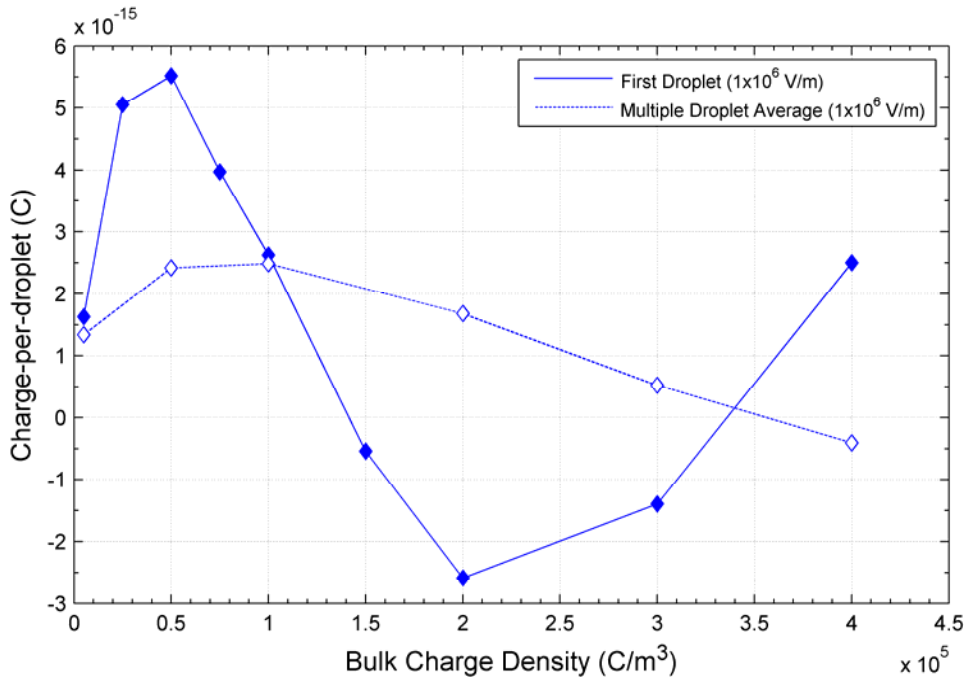

Figure 4.15 Simulated charge-per-droplet for a 1 MHz piezoelectric transducer drive signal, as a function of the initial bulk charge density for the first ejected droplet and the average of consecutively ejected droplets.

multiple-droplet-charge-averages show a more gradual increase and then a decrease about a reduced-magnitude local maximum as the bulk charge density increases.

The first set of experiments, discussed in the previous section, considered droplet charging as a function of electric field for a relatively "low" charge density (~50,000 C/m^3) that belongs to Regime I, in the range where a linear relationship between the charge and electric field was identified (Figure 4.6). Now, a higher charge density is considered. Figure 4.16 displays the charge-per-droplet behavior for a bulk charge density of 200,000 C/m^3 as function of an external DC electric field. Measurements past 7.5×10^5 V/m were not possible due to the increased frequency of the ejection surface flooding with electrolyte, leading to dielectric breakdown between the liquid and counter electrode (wires), tripping the power supply. At this elevated bulk charge density, the

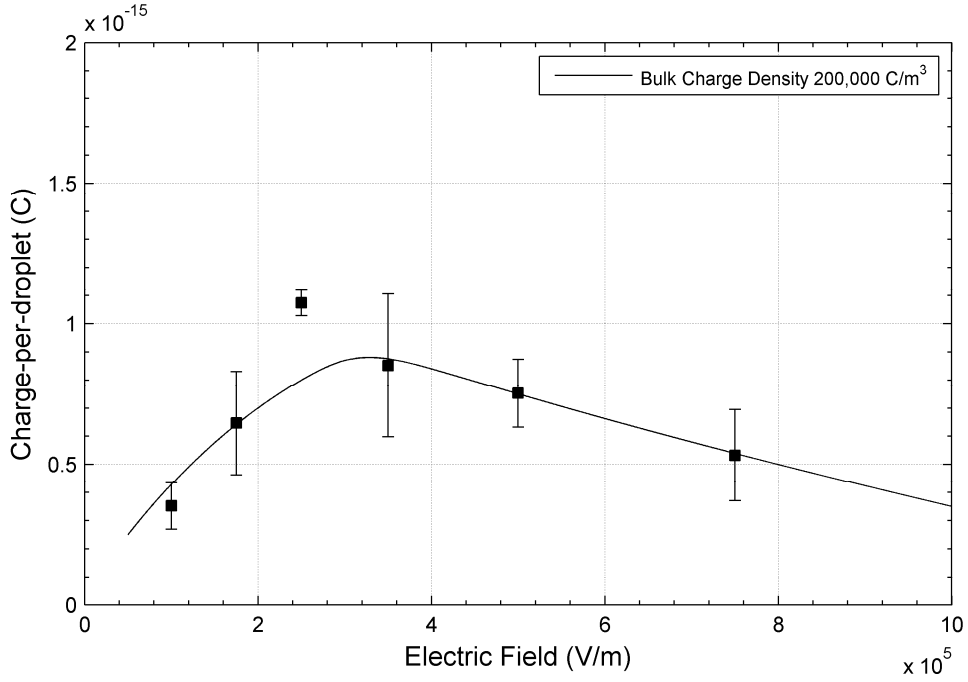

Figure 4.16 Experimental charge-per-droplet as a function of electric field at higher bulk charge density (200,000 C/m^3).

charge-per-droplet initially increases with increasing electric field. However, upon reaching a strong enough electric field ($\sim 3.0\times10^5$ V/m) the droplet charging begins to decrease.

Comparing the droplet charging trends between experimental measurements and simulations for both individual droplet and multiple droplet averages, there are obvious similarities. Similar to the way in which successive droplets "shield" the external electric field in the DC simulations at low bulk charge density (Figure 4.5), the presence of successive droplets also attenuate the charge transport into each ejected droplet. To substantiate this point, Figure 4.17 shows the time scales and droplet charging for the multiple droplet average charging simulations. As in the case of individual droplet analysis, the charge relaxation time scale again separates the regimes of droplet charging.

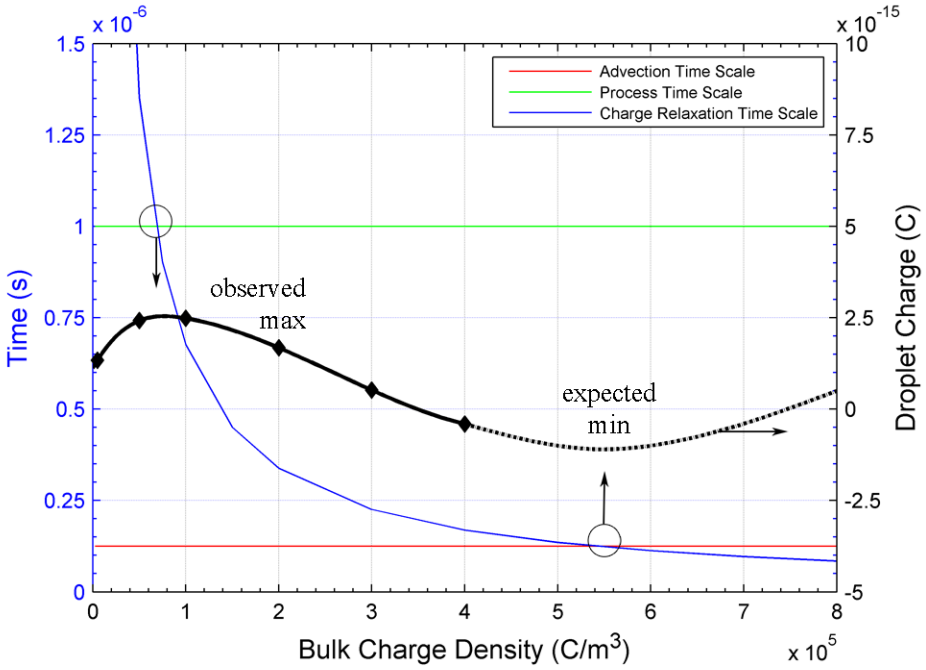

Figure 4.17 Charge transport time scales for a 1 MHz piezoelectric transducer drive signal, plotted with simulated multiple droplet averages of charge-per-droplet as function of the bulk charge density for external electric field strength of 1.0×10^{6} V/m.

Unfortunately, the model is incapable of providing data at charge densities much greater than 400,000 C/m^3 as the VOF computational algorithm cannot resolve the increasing levels of charge within the liquid-gas interface region, leading to simulation divergence. From comparisons to the individual droplet data, it can be expected that the droplet charge curve for multiple droplets will also experience a local minimum around 550,000 C/m^3 where the charge relaxation time scale becomes faster than the advection time scale and begin to dominate all other transport processes (Figure 4.17). This expected transition is shown schematically in Figure 4.17 by a dashed line.

Theoretical arguments and simulation results discussed in the previous paragraph provide a framework for interpreting the results of experimental measurements. Figure 4.18 displays the relevant time scales overlaid with experimentally measured droplet

charging. As in the case of excessive electric field, experiments are not possible to conduct for bulk charge densities beyond 400,000 C/m^3 due to the drastic increase of ejector surface flooding and associated with it dielectric breakdown, tripping the power supply. However, extrapolation of presented experimental trends past this bulk charge density limit is possible using theoretical arguments from the scaling analysis and simulations, which suggests that the droplet charge curve should experience a local minimum around 600,000 C/m^3 as shown in Figure 4.18. This fact has not been experimentally verified due to the above-stated difficulties in conducting experiments at high charge densities, but it is strongly supported by the time scale analysis, which was validated using single droplet charging simulations. By using the map of the charge transport regimes as introduced in Figure 4.12, it can be determined that a bulk charge density in the range of 100,000 – 400,000 C/m^3 falls into Regime IIa (Figure 4.18).

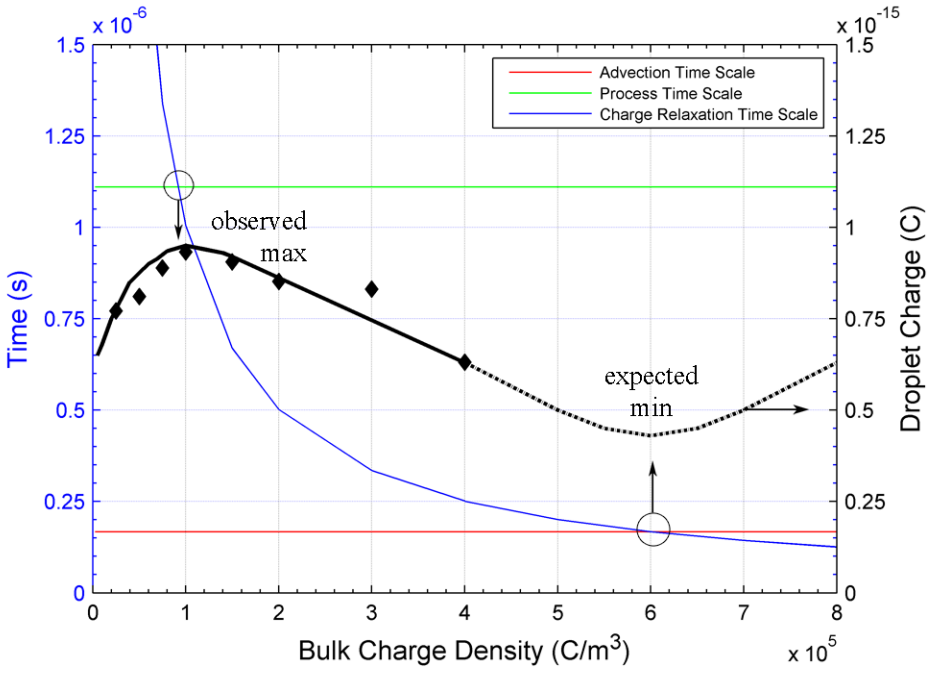

Figure 4.18 Charge transport time scales for a 0.905 MHz piezoelectric transducer drive signal, plotted with experimentally measured charge-per-droplet as function of the bulk charge density for external electric field strength of 3.5×10^5 V/m.

Consistent with the expected trends in Regime IIa, a representative case of bulk charge density of 200,000 C/m^3 (Figure 4.16) shows droplet charging that increases with electric field, reaches a local maximum, and then decreases, just as experimentally demonstrated in Figure 4.16.

As an additional note, similarly to the drastic decrease in the level of ejection identified in the DC-charging experiments with an increase in applied electric field at low bulk charge density (Figure 4.7), the mode of ejection was observed to change similarly for the case of bulk charge of 200,000 C/m^3 as well. This is demonstrated in Figure 4.19 by the decrease in ejected flow rate as the charge separating electric field increases past around 2.0×10^5 V/m. Comparing these flow rates to the droplet charging data (Figure 4.16) there appears to be little correlation, suggesting that droplet charging is dominated by charge transport and the flow rate is *independently* determined by the ejection

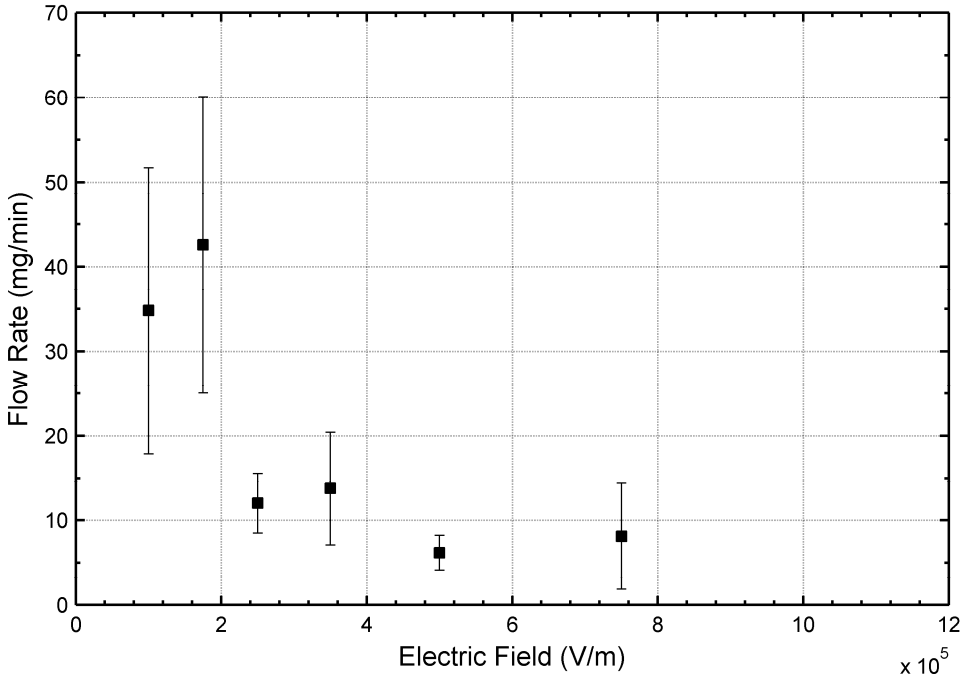

Figure 4.19 Experimentally measured average ejection flow rate (collected mass per collection time) as function of the charge separating electric field magnitude.

mode, which depends on the magnitude of applied electric field and bulk charge density of ejected fluid.

The experiments of droplet charging under a number of conditions presented in this section validate the model and demonstrate its utility to investigate coupled electrohydrodynamic processes at the micrometer length and microsecond time scales. The conditions necessary for optimal droplet charging have been identified as a function of the bulk charge density, external electric field (magnitude and duration), and frequency of operation. During these investigations, elevated electric fields and high bulk charge densities have been observed to detrimentally effect droplet ejection. In the next section, optical visualization and a scaling analysis are used to gain insight into the physics determining the mode of ejection.

4.2 Optical Visualization of Ejection Phenomena

Complimentary to computational and experimental investigations of optimal charging in the AMUSE ion source, a study into the effects of electric field on droplet ejection is also completed. The effects of an external electric field on ultrasonic droplet ejection are considered in a broader context to obtain general conclusions that are applicable not only to droplet-based ion sources for mass spectrometry, but also to other applications of charged droplets subjected to electric fields. Through simulations and optical visualization of droplet generation, a regime map for ultrasonic ejection in the presence of an electric field is completed. This regime map identifies the parametric regions where purely mechanical or coupled electromechanical ejection is expected to occur.

4.2.1 Device Setup and Electric Field Configuration

Droplet ejection in the presence of an electric field is visualized using a stroboscopic optical technique, previously developed for determining the mode of droplet ejection from the ultrasonic droplet generator.[67,69] A high-spatial-resolution stroboscopic imaging technique is employed, focusing on ejection from a single nozzle orifice which is illuminated with high intensity light (using a light-emitting diode LED), pulsed at the same frequency as that driving the piezoelectric transducer. The short exposure time due to pulsed LED operation, synchronized with ejection, enables capturing and recording of still images of multiple, overlaying on top-of-each-other, droplets by a charge-coupled device (CCD) camera, linked to a computer and image processor (Figure 4.20).[130,148] This

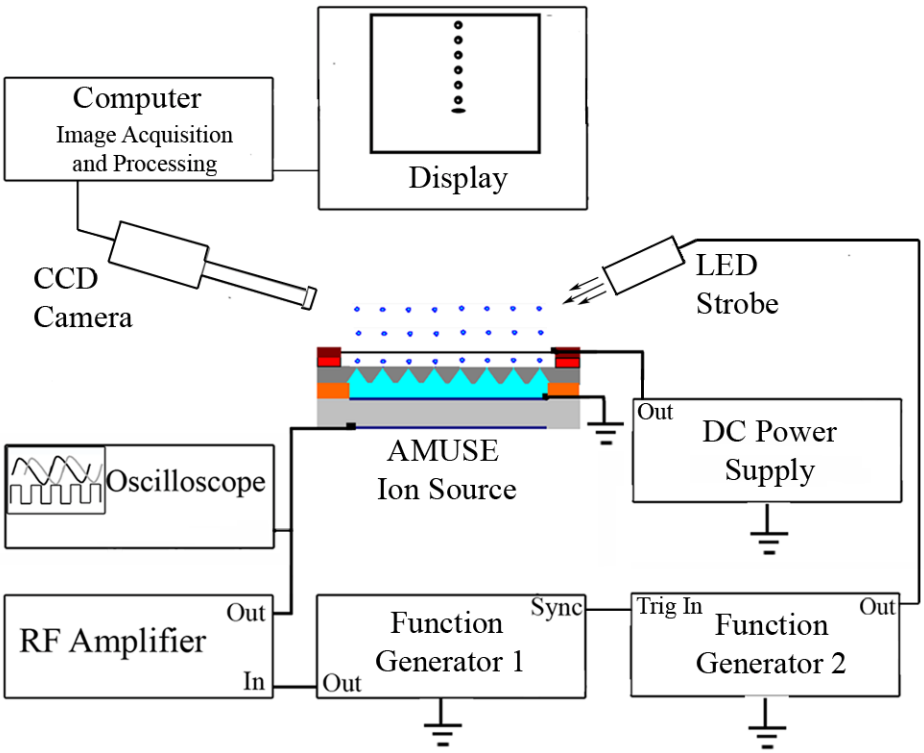

Figure 4.20 Schematic representation of the experimental setup for stroboscopic visualization of the ejection process under the application of an external electric field.

technique, which can be traced back to Lord Rayleigh's original work,[149-151] provides still images of any periodic ejection process, "frozen" in space/time.

Experiments are conducted using aqueous (deionized water, Ricca Chemical Company, Arlington, Texas, USA) solutions containing 0.1% and 1% (v/v) glacial acetic acid (BDH Aristar, Westchester, PA, USA) (pH 3.25 and 2.76, respectively). A schematic of the experimental setup used for the stroboscopic visualization experiments is shown in Figure 4.20. The piezoelectric transducer is driven at a resonant frequency of the fluid reservoir by an amplified (T&C Power Conversion RF Amplifier) RF signal, generated by a Stanford Research Systems DS345 30MHz (or Agilent 33250A) function generator labeled "Function Generator 1".[67,72-73] All respective signals are monitored with the use of a Tektronix TDS 2014 oscilloscope. An LED, operated at the same frequency as the piezoelectric drive signal, is used to illuminate droplet ejection from a single nozzle. The LED is driven using an Agilent 33250A function generator (Agilent Technologies, Inc., Model 33250A 80MHz) labeled "Function Generator 2", which is externally triggered by Function Generator 1 so that both piezoelectric drive signal and the LED pulse are at the same frequency (Figure 4.20). Function Generator 2 produces a pulsed signal, whose width and delay are controlled by the user. For the frequencies of operation considered here (~ 0.5–1.5 MHz), the LED is pulsed with a 100 nanosecond pulse width. This method illuminates the same time instant in each cycle of ejection (Figure 4.21), effectively "freezing" the image. Each captured image is the superposition of thousands of images, all captured at the same point in each ejection cycle while the camera shutter is open (32 ms).

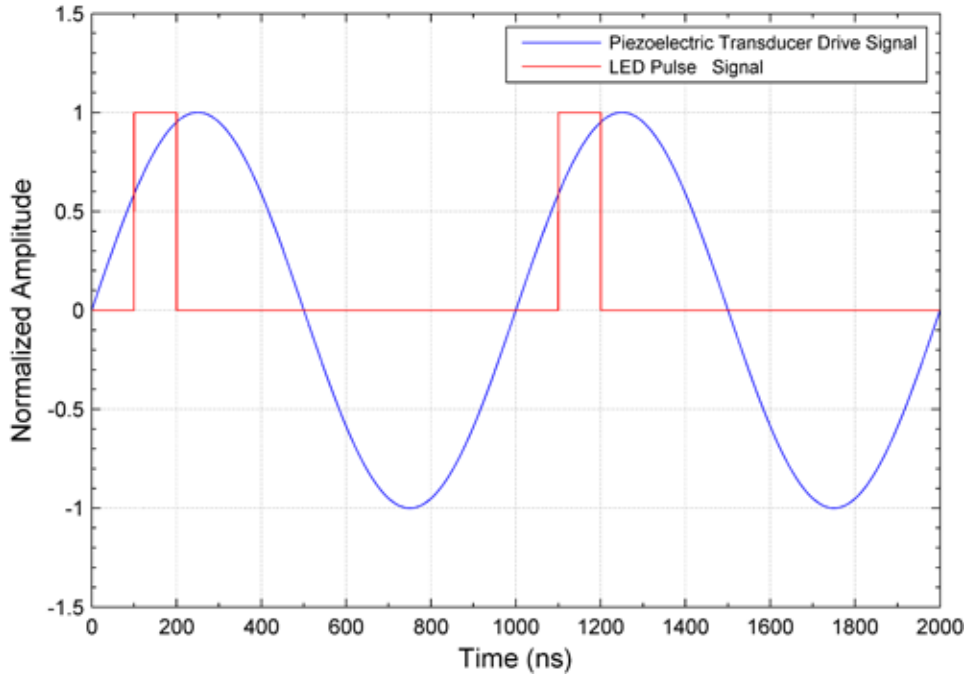

Figure 4.21 Timing diagram of the LED pulse and sinusoidal piezoelectric drive signals.

In order to visualize the interface evolution during the ejection cycle, similar to the simulated results in Figure 3.4, the LED pulse can be delayed from the beginning of each cycle. Initially, the LED pulse is set at the beginning of every ejection cycle, triggered by Function Generator 1 (Figure 4.20). Marching through successively longer pulse delays from the beginning of each cycle enables acquisition of consecutive images spanning a complete cycle of droplet evolution and ejection. The image collection and control over the LED pulse delay is managed through a National Instruments LabVIEW[152] virtual instrument. The LED is best positioned providing backlighting to the droplet stream. The ejector is located on a three-axis stage to move the field of view of the camera. The CCD camera (Redlake MASD, Inc., Model MegaPlus ES 1.0) with adjustable magnification lenses (200-1400X) has a focal length of ~1-1.5 inches and is maintained at a 30º inclination angle with respect to the nozzle array surface. The CCD

camera output is directly connected to a computer with a National Instruments image acquisition module (National Instruments, Model 1422 Digital IMAQ).

4.2.2 Representative Visualization Results

As shown before (Figure 4.6), the linear relationship between charge-per-droplet and external electric field strength is demonstrated with both the electrohydrodynamics model and experimental measurements at sufficiently low bulk charge density. For the electric field strengths considered ($0–2.0\times10^{6}$ V/m), the model shows little effect of the electric field on the evolving droplet profile as a function of electric field. Figure 4.22 displays the simulated droplet profiles and axial velocity distributions for the application

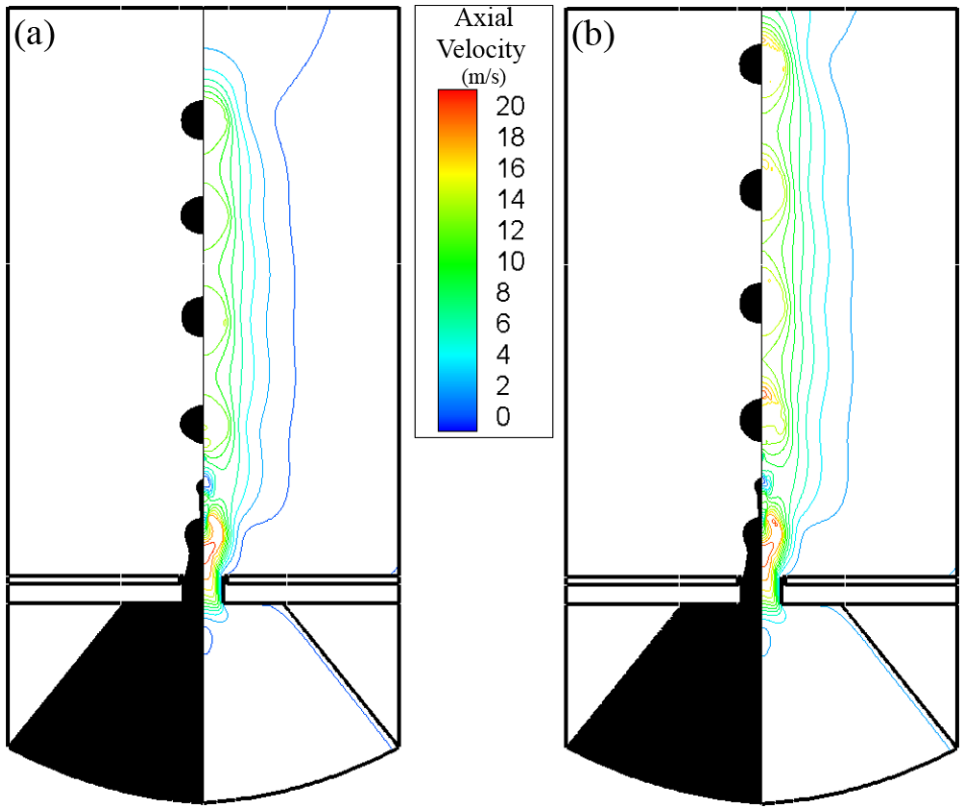

Figure 4.22 Simulated droplet profiles (left panels) and axial velocity distributions (right panels) for (a) low, 1.0×10^{5} V/m and (b) high, 2.0×10^{6} V/m charge separating electric fields (fluid interface is given by a locus of points with a liquid volume fraction of 0.5).

of low (1.0×10^5 V/m) and high (2.0×10^6 V/m) external electric fields. While the interface evolution remains essentially unaltered, the higher electric field induces a greater droplet velocity due to the Coulombic body force.

Yet, as discussed in the previous section, ejection strength is visually observed to change drastically under the application of strong electric fields. To investigate physical mechanisms responsible for such a behavior, the high-spatial-resolution stroboscopic imaging technique, introduced above, is used to image ejection from a single nozzle. From the simulations and using the ejection regime maps of the ultrasonic ejector developed in References 67 and 69, for the operating conditions considered here (5 μm orifice, ~0.5–1.5 MHz drive frequency, and aqueous solvent), AMUSE must operate in the discrete droplet ejection mode with and without an applied external electric field.[67,69]

Figure 4.23 displays a series of sequential images (400X magnification) of ejection of individual droplets from a 5 μm orifice at 0.735 MHz with no external electric field, which are in agreement with theoretical predictions. Next, images are taken for ejection under the application of a 1×10^6 V/m external electric field. This electric field strength is well within in the range for which ejection has been experimentally observed to transition. Figure 4.24 displays a series of sequential images (400X magnification) of ejection from the same device under equivalent electric field conditions. As predicted by the EHD simulations, the mode of ejection (discrete droplets) is largely unaffected by the electric field. Unfortunately, this does not immediately explain the observable deterioration of ejection quality under the application of strong electric fields. Complementary observations may, however, provide an answer to this dilemma.

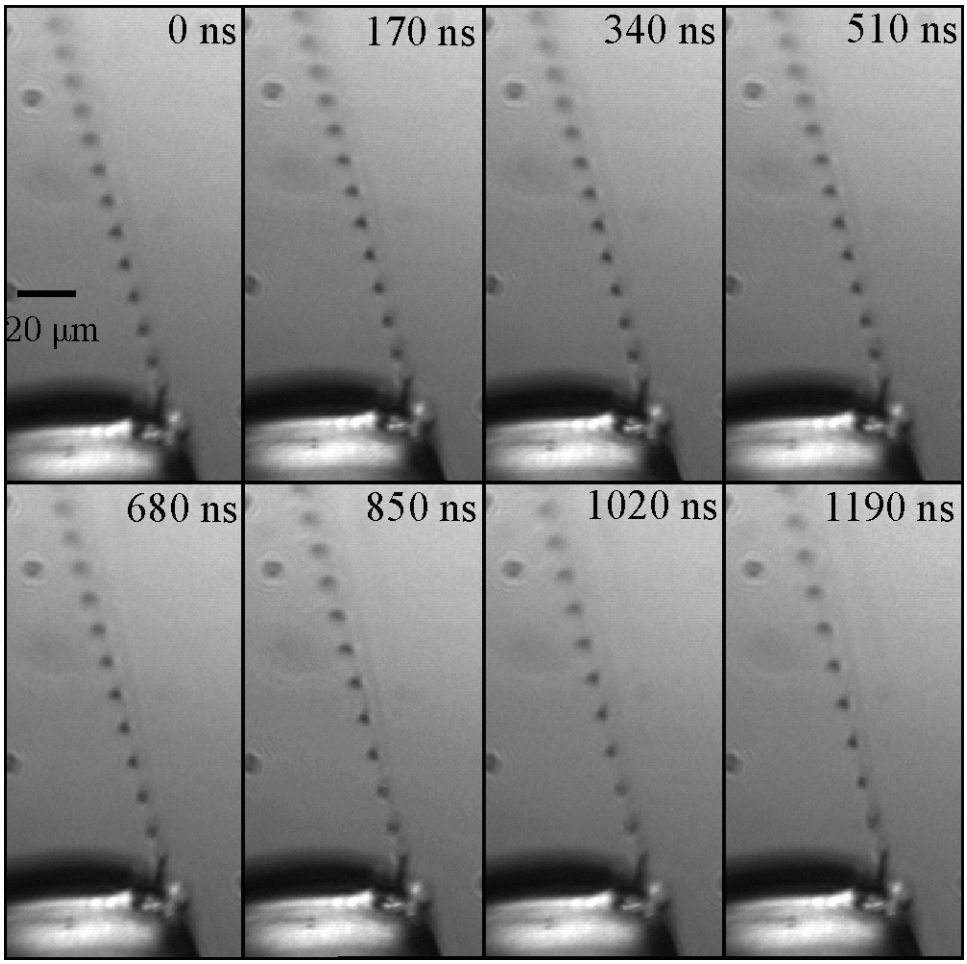

Figure 4.23 Sequential stroboscopic images of droplet ejection from a 5 μm orifice device operated at a 0.735 MHz drive frequency with no external electric field applied. There is a 170 ns delay between successive images.

For example, during experimental characterization of droplet charging, it is found that as the electric field and bulk charge density increase, the extent and frequency of occurrence of surface flooding increases, ceasing ejection. Flooding has been shown to cause problems for across-the-array ejection levels, even for the baseline ultrasonic ejector with no electric field or bulk charge in the fluid. However, this is typically an issue only when the flow rate provided by the syringe pump exceeds the flow rate being ejected. Excessive flooding reduces ejection levels (number of nozzles ejecting in the array)

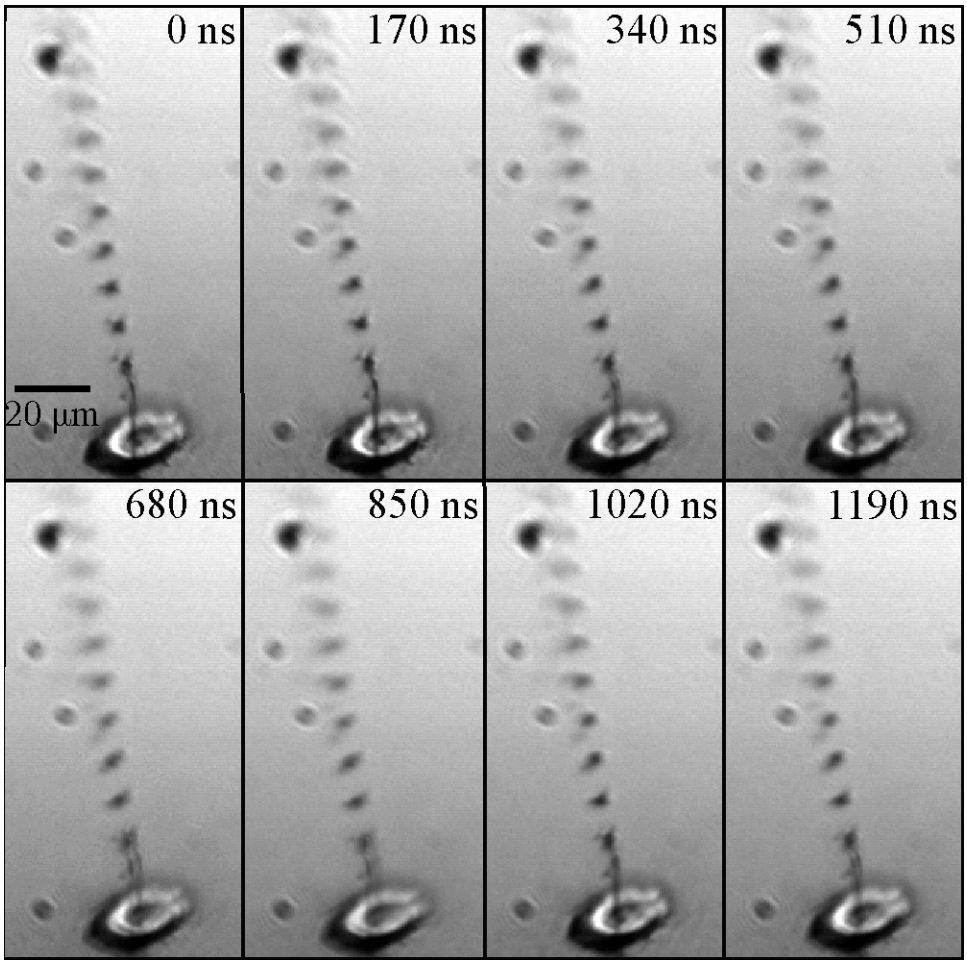

Figure 4.24 Sequential stroboscopic images of droplet ejection from a 5 μm orifice device operated at a 0.735 MHz drive frequency under the application of a 1×10^{6} V/m external electric field. There is a 170 ns delay between successive images.

and may provide an explanation for the reduction in ejected flow rate observed in Figures 4.7 and 4.19, but not necessarily the change in ejection strength.

As shown in Figure 4.25, the strength of droplet streams (defined as the height of an ejected plume above array surface) also decreases in the case of reduced ejection levels. A number of causes are likely at work here. While an electric field high enough to achieve electrospraying from the AMUSE ion source is not realizable due to earlier onset of dielectric breakdown, ejection of highly charged droplets with local charge densities at

the droplet pole approaching the Rayleigh limit[20] is possible. Once ejected, these highly charged droplets repel each other and interact with the external counter electrode. What are isolated streams of droplets without the application of an electric field, display a plume-like behavior at high electric fields, suggesting the importance of in-flight electrostatic repulsion. It is possible that a combination of these interactions results in a significant increase in electric field magnitudes *locally* around the external electrodes, which in conjunction with droplet evaporation promote fission of highly charged droplets upon ejection (Figure 4.25 (b inset)). This is why ejection at the surface still maintains

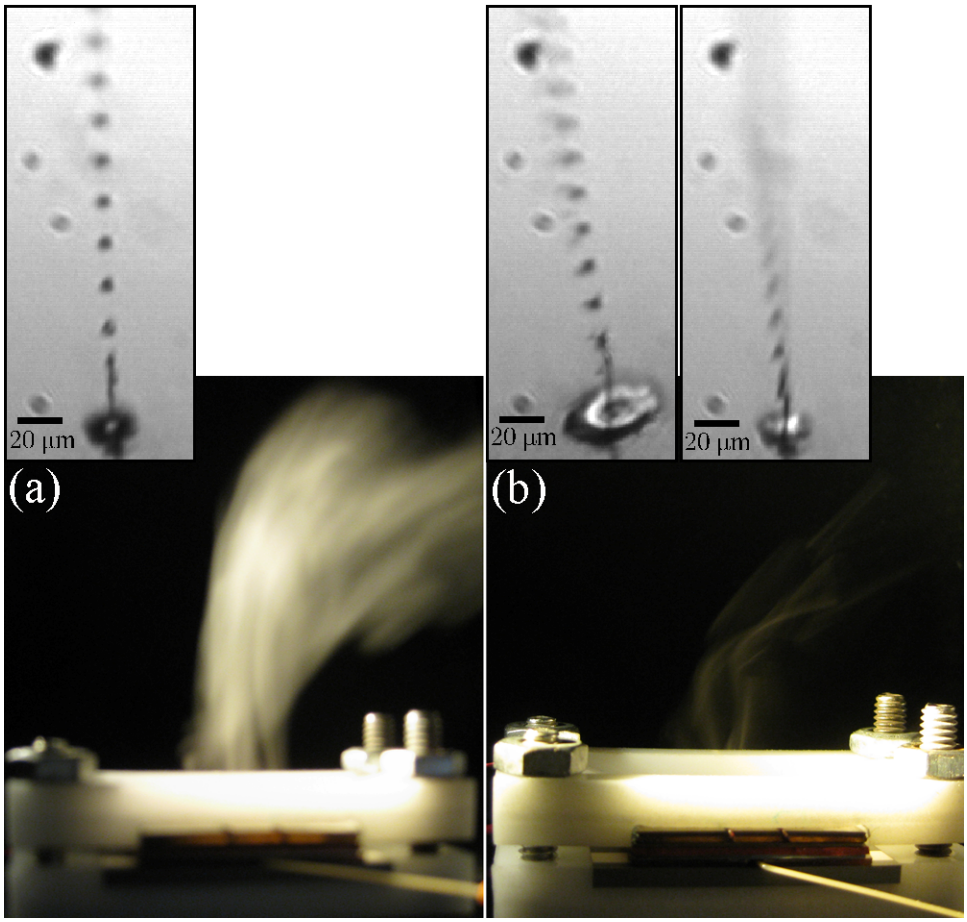

Figure 4.25 Images of overall ejection strength and ejection mode with (a) no electric field and (b) a 1×10^{6} V/m external electric field applied. Insets are representative stroboscopic images of droplet ejection under the respective electric field conditions.

coherent droplet streams, typical of mechanically driven ejection, which then quickly deteriorates into a fissioning mist. In addition, under these ejection conditions, the highly charged droplets are attracted to the external counter electrode wires and condense on their surfaces, further effecting the electric field distribution in unpredictable ways. Unfortunately, due to these interactions, random location of ejecting nozzles, and a breakdown in periodicity, stroboscopic visualization more than a few hundred microns above the ejector surface is not possible. However, as already stated, ejection behavior right near the ejection point was successfully captured even for coupled electromechanical ejection (Figure 4.24-4.25) and shows the periodic discrete-droplet mode as predicted in simulations.

Visualization of ejection under various electric field strengths (e.g. Figure 4.23-4.25) and bulk charge densities has revealed distinct ejection mode regions. To investigate the underlying physics of this transition in ejection mode, a scaling analysis is used, similar to that used in the previous section to determine the regimes of charge transport. The developed relationships should help identify the dominate physics and allow for development of a predictive ejection regime map, enabling an improved AMUSE design and operation.

4.2.3 Scale Analysis: Relevant Time Scales and Dimensionless Numbers

A scaling analysis, supported by experimental results, is used to gain insight into the dominant physics of the ejection process in the presence of an electric field. The scaling analysis developed here is an approximate technique and results are only valid within an order-of-magnitude. Therefore, including numerical factors on the order of '1' is beyond the accuracy of this analysis. The ejection process is governed by the

momentum equations of bulk fluid flow (Navier-Stokes equations of motion, Eq. 3.10) completed with the boundary conditions of surface stress balances. The nondimensionalization of the governing equations yields:

$$\frac{\rho u_o}{\tau}\left[\frac{\partial \vec{u}}{\partial t}\right]+\frac{\rho u_o^2}{l}\left[\vec{u}\cdot\nabla\vec{u}\right]=-\frac{p_o}{l}\left[\nabla p\right]+\frac{\mu u_o}{l^2}\left[\nabla^2\vec{u}\right]+q_oE_o\left[q\vec{E}\right]-\frac{\varepsilon E_o^2}{l}\left[\tfrac{1}{2}E^2\nabla\varepsilon\right] \qquad (4.1)$$

All bracketed terms are now dimensionless and on the order of '1'. The respective parameters multiplying each dimensionless term are the characteristic scales, which are specific to the problem being investigated. Rearranging these characteristic scales, the time scales of each process can be determined in a manner similar to that performed for the electrochemical ion transport analysis (Appendix B) and charge transport analysis (Chapter 3), by balancing each process term with the transient term.

$$\frac{1}{\tau}\left[\frac{\partial \vec{u}}{\partial t}\right]+\frac{u_o}{l}\left[\vec{u}\cdot\nabla\vec{u}\right]=-\frac{p_o}{\rho u_o l}\left[\nabla p\right]+\frac{\mu}{\rho l^2}\left[\nabla^2\vec{u}\right]+\frac{q_oE_o}{\rho u_o}\left[q\vec{E}\right]-\frac{\varepsilon E_o^2}{\rho u_o l}\left[\tfrac{1}{2}E^2\nabla\varepsilon\right] \qquad (4.2)$$

For the AMUSE ion source, the fluid inertia is driven by the time-varying sinusoidal pressure field, therefore the dynamic pressure is the appropriate characteristic scale for the pressure, $p_o \sim \rho u_o^2$. Equation 4.2 yields the following time scales: process time scale $\left(t_p \sim 1/f\right)$, inertia time scale $\left(t_u \sim l/u_o\right)$, viscous time scale $\left(t_\mu \sim \rho l^2/\mu\right)$, Coulombic time scale $\left(t_c \sim \sqrt{\rho l/q_oE_o}\right)$, and dielectric time scale $\left(t_d \sim \sqrt{\rho l^2/\varepsilon E_o^2}\right)$. The characteristic length scale is defined as the radius of the nozzle orifice and the process time scale is again dictated by the periodicity of the ejection process, or the inverse of the frequency.

4.2.3.1 Conceptual Physics and Scale Analysis of AMUSE

From the non-dimensional momentum equation (Equation 4.2), it is found that the viscous and dielectric force terms are more than an order-of-magnitude smaller (time scales are much longer) than the remaining terms. Also, as already mentioned, the pressure and inertia terms are coupled and described by the same time scale. Therefore, for the ejection process under an applied electric field, there is a balance between the unsteady periodicity of ejection, and the inertia and Coulombic force terms. The relative magnitudes of these terms will determine the mode of ejection. By forming balances among these three terms, three distinct regimes of ejection can be identified.

Regime I. Purely Mechanical Ejection

In the first regime, the Coulombic force is negligible, resulting in a balance between the unsteady process and inertia terms. In this limiting regime, the electric field has little or no effect, resulting in purely mechanical ejection. That is, mechanical ejection occurs when (1) the process and inertia time scales are of the same order, $t_p \sim t_u$, and (2) the Coulombic time scale is much longer, $t_c >> t_p, t_u$. From the first condition, comparing the process and inertial time scales, $\frac{1}{f} \sim \frac{l}{u_o}$, provides a scale for the *minimum* characteristic velocity of the stable ejected jet/droplets as, $u_o \sim fl$. Further, it has been shown in visualization of the baseline ultrasonic droplet ejector that an increase in the amplitude of the driving signal of the piezoelectric transducer beyond the minimum threshold for ejection will increase the number of active ejectors and also increase the velocity of the jet/droplets.[67,69] Therefore, the "characteristic velocity" is a function of the amplitude of the driving signal, which can be estimated from experimentally

(stroboscopic visualization) obtained values of droplet velocities. From the second condition on the Coulombic time scale, the parameter region for purely mechanical ejection is determined as:

$$\sqrt{\frac{\rho l}{q_o E_o}} >> \frac{l}{u_o} \qquad \boxed{q_o E_o << \rho l f^2} \tag{4.3}$$

Equations 4.3 isolates and compares the electric parameters (electric field and charge density) to the mechanical parameters (orifice size and driving frequency) and fluid properties (fluid density). This relationship demonstrates that the mode of ejection is not only determined by the external electric field, but by the product of the characteristic charge density and electric field.

While the balance of bulk forces within the fluid is used to determine the onset and transition of ejection modes, the type of ejection (discrete drops, transition, or continuous jet) is determined by a balance of forces occurring at the boundary, i.e., whether the surface tension acts faster (droplets) or slower (jets) than the change in the pressure gradient at the orifice occurring on the process time scale. The types of ejection for the ultrasonic droplet ejector in the absence of electric effects has been previously investigated in depth,[67,69] and its conclusions apply to the AMUSE ion source operation both without the application of an external electric field and for relatively low external electric fields (determined by condition 4.3).

Regime II. Electrospraying

In the opposite limit, the electric field dominates and drives all flow processes, resulting in steady-state electrospraying on the ejection time scale. The necessary

condition for this regime is that the Coulombic time scale is much faster than all other relevant processes, $t_c << t_p, t_u$.

$$\sqrt{\frac{\rho l}{q_o E_o}} << \frac{l}{u_o} \qquad \boxed{q_o E_o >> \frac{\rho u_o^2}{l}} \tag{4.4}$$

For this condition, the determination of the appropriate characteristic velocity and length scale is less straight-forward. Electrospraying can be achieved from a wide range of capillary sizes and flow rates, and occurs in a number of different regimes, including the dripping regime,[153] burst regime,[154] pulsating regime,[19,110] astable regime,[155] and the cone-jet regime.[156] A number of parametric relationships and scaling laws have been developed for spray current, minimum flow rate, electric field for the onset of spraying, and droplet/jet diameter. For example, Fernandez de la Mora and Loscertales have developed the following relationship for the minimum volumetric flow rate, Q, of electrospray:[157]

$$Q_{\min} \sim \frac{\varepsilon_{r,gas}\varepsilon_o \gamma}{\rho\sigma} \qquad \rightarrow \qquad u_o \sim Q/d^2 \tag{4.5}$$

The minimum flow rate required for stable electrospraying can be used to obtain a characteristic velocity, as given above. However, the determination of an appropriate jet/droplet diameter to derive the velocity scale from Equation 4.5 is ambiguous. Various relationships exist in the literature for the diameter of electrospraying jet/droplets, based on empirically chosen parameters to fit experimental data.[108,113,157-158] For example, Gavan-Calvo et al.[108] developed the following expression for an electrospraying jet diameter,

$$d_j \sim 3.78\pi^{-2/3} 0.6 Q^{1/2} \left(\frac{\rho\varepsilon_o}{\gamma\sigma} \right)^{1/6} \tag{4.6}$$

From relationships 4.4–4.6, an order-of-magnitude estimate for the electric field magnitude necessary for Coulombic-force-dominated mode of ejection of an aqueous solvent containing 0.1% (v/v) acetic acid (~50,000 C/m^3) is estimated to be ~10^7 V/m. This is in close agreement with the electric field magnitude necessary for the onset of electrospraying as developed by Smith.[159]

$$E_{onset} \sim \sqrt{\frac{2\gamma \cos\theta}{\varepsilon_{r,gas}\varepsilon_o r_{capillary}}} \tag{4.7}$$

In typical capillary electrospray, the high aspect ratio capillary produces a local amplification of the electric field magnitude. This enables electric field magnitudes at the capillary tip to be greater than the dielectric breakdown of the surrounding gas. However, in the AMUSE ion source, no such enhancement of the external electric field exists due to the conical geometry of ejection nozzles, and therefore the electric field magnitude necessary for the electrospraying regime cannot be achieved with the current device configuration before dielectric breakdown occurs.

Regime III. Coupled Electromechanical Atomization (Transition)

An important regime lies at the transition between purely mechanical ejection and electrospraying. In this case, the process, inertia, and Coulombic time scales are all of the same order, $t_p \sim t_u \sim t_c$, and play competing roles in ejection. This should occur when:

$$\sqrt{\frac{\rho l}{q_o E_o}} \sim \frac{l}{u_o} \qquad \boxed{(q_o E_o)_{trans} \sim \rho l f^2} \tag{4.8}$$

From visual observations, this regime still results in mechanically-driven discrete droplet ejection (Figure 4.24), however, ejection is adversely affected by the increasing electric field (shielding) and ejected droplets (fission). This results in both reduced ejection level and ejection strength (Figure 4.25). However, it is important to note that even in this

coupled electromechanical regime, droplet charging still follows the same physical description defined by the dominant charge transport process, as given in the previous section. For example, with a bulk charge density of 50,000 C/m3, under an increasing electric field, droplet charging continues to increase linearly (as determined by the charge transport analysis in the previous section) even though the ejection mode has transitioned.

4.2.3.2 Ejection Regime Map

The transition from purely mechanical to coupled electromechanical ejection, due to electrohydrodynamic effects, can be expressed as a relationship between dimensionless numbers obtained from the Navier-Stokes equations of motion generalized to include electric effects:

$$St\left[\frac{\partial \vec{u}}{\partial t}\right]+\left[\vec{u}\cdot\nabla\vec{u}\right]=-Eu\left[\nabla p\right]+\frac{1}{\mathrm{Re}}\left[\nabla^2\vec{u}\right]+\frac{E_{HD}}{\mathrm{Re}^2}\left[q\vec{E}\right]-\frac{Md}{\mathrm{Re}^2}\left[\tfrac{1}{2}E^2\nabla\varepsilon\right] \qquad (4.9)$$

The dimensionless parameters in Equation 4.9 are the Strouhal number, $St = fl/u_o$, the Euler number, $Eu = p_o/\rho u_o^2$, the Reynolds number, $\mathrm{Re} = \rho u_o l/\mu$, the EHD number, $E_{HD} = q_o E_o l^3 \rho/\mu^2$, and the Masuda number, $Md = \varepsilon_o E_o^2 l^2 \rho/\mu^2$. The EHD number (or the Conductive Electric Rayleigh Number) and Masuda number (or the Dielectric Electric Rayleigh Number) have been defined for use in electrohydrodynamics by the Institute of Electrical and Electronics-Dielectric and Electrical Insulation Society-Electrohydrodynamics (IEEE-DEIS-EHD) Technical Committee.[160] Interestingly, these parameters are more commonly used in applications involving electric-field-enhanced heat transfer. However, the problem at hand calls for a combination of the EHD and Reynolds numbers to describe the interplay between the inertia and Coulombic forces, resulting in a new dimensionless parameter. It is proposed that this parameter be named

the Fenn number, $Fe = E_{HD}/\mathrm{Re}^2 = q_o E_o l/\rho u_o^2$, which will be used to identify the transition between mechanically-dominated and electrically-dominated regimes of electromechanical ejection. The dimensionless Fenn number conveys the relative importance of the Coulombic force versus inertia and is named in honor of John Fenn, who shared the 2002 Nobel Prize in Chemistry for his invention of electrospray ionization of biomolecules. John Fenn has made seminal contributions not only to electrospraying,[5,8,161] but also ultrasonically-assisted[30] and pneumatically-assisted[9] modes of electrospraying. Thus, the Fenn number is very much appropriate to define the transition between purely mechanical ejection and electrospraying of electrically charged liquids.

From the regimes identified above, the transition away from purely mechanical ejection to coupled electromechanical ejection to electrospraying is expected to occur when $t_u \sim t_c$, or when the Strouhal number, *St*, is on the order of the reciprocal of the fourth root of the Fenn number, $1/Fe^{0.25}$. To validate this prediction of scaling analysis, a series of experiments were performed to populate the regime map in Figure 4.26. All data are taken for a 5μm diameter orifice device at two different charge densities, 5×10^4 C/m^3 and 1.7×10^5 C/m^3. Under each frequency of operation considered, the electric field magnitude is steadily increased across the range reported, identifying the onset of coupled electromechanical ejection. As shown in Figure 4.26, the experimental data clearly support the scaling analysis relationship where regime transition should occur. The specific value of the power exponent "1/4" in the relationship between the Strouhal and Fenn numbers is apparent in plotting the data on the log-log scale, as shown in the inset of Figure 4.26. As discussed in the previous section, data points in the regime map

where electrospraying should occur are far beyond the onset of coupled electromechanical atomization and cannot be recorded due to frequent power supply tripping owing to dielectric breakdown between the liquid and external electrodes. It should be kept in mind that this relationship for the onset of coupled electromechanical ejection is contingent on the conditions of the scaling analysis, i.e. the viscous and dielectric time scales are much longer than the inertia, process, and Coulombic time scales, $t_\mu, t_d \gg t_u, t_p, t_c$.

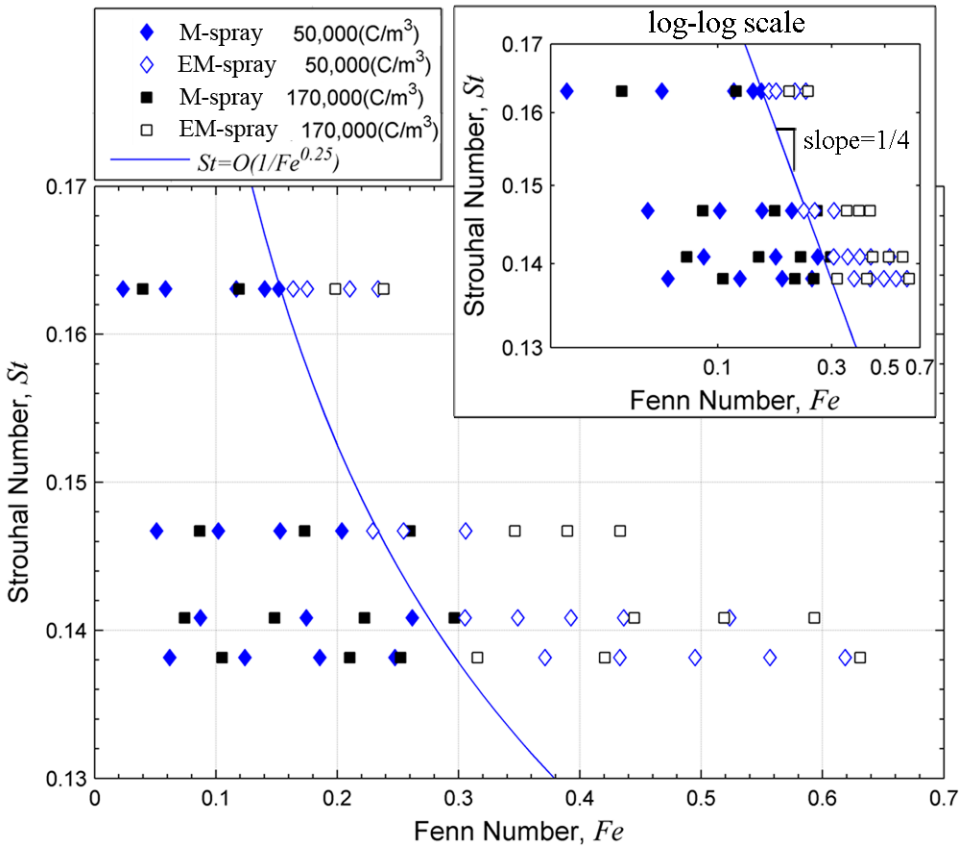

Figure 4.26 Regime map displaying the relationship between the Strouhal number and the Fenn number for the transition from purely mechanical (abbreviated as "M-spray") to coupled electromechanical atomization (abbreviated "EM-spray"), plotted with experimental results. The insert displays the plot on a log-log scale, resolving the ¼ exponent in the *St* vs. *Fe* relationship.

In summary, experimental droplet charge, deduced from the measured electrical current correlated with the collected mass, allow for both qualitative and quantitative comparisons with simulations using the EHD model developed in Chapter 3. Excellent agreement between predictions and measurements have been demonstrated for electrohydrodynamic behavior of ultrasonically-driven, droplet-based ion sources, including charge separation as function of both static (DC-charging) and dynamic (AC-charging) electric fields, as well as its dependence on the bulk charge density for a constant DC electric field. Through these investigations and a fundamental time scale analysis of charge transport processes, specific regimes of droplet charging are identified, as defined by the dominant transport process. These regimes not only predict the final charge placed on an ejected droplet, but also how droplet charging is effected by increasing electric field strength. Lastly, high-spatial-resolution stroboscopic visualization has been used to investigate the mode of droplet ejection under the application of an external electric field. Through optical visualization and a scale analysis of the ejection phenomena, a predictive regime map has been developed for determining the electromechanical mode of ultrasonic ejection. The transition criterion between purely mechanical and coupled electromechanical ejection has been identified, as a relationship between the dimensionless Strouhal number and a newly introduced Fenn number.

Development of the comprehensive computational model, experimental characterization, optical visualization, and scale analysis of charge transport and ejection phenomena enabled an in-depth understanding of the physics of droplet charging subjected to individually-controlled mechanical and electric fields. The results provide

fundamental information on droplet charging as function of electric field, static and dynamic, and bulk charge density, which are relevant to many practical applications. In the next chapter, this understanding is adopted and expanded to the realm of mass spectrometry (MS), specifically for an investigation of the MS response to an AMUSE-ionized small tuning compound, reserpine, as a function of applied DC-charging electric field.

CHAPTER 5

MASS SPECTROMETRIC CHARACTERIZATION AND APPLICATION

The application of the AMUSE ion source to mass spectrometry has been demonstrated by analyzing a number of proteins, peptides, and pharmaceutical molecules relevant to bioanalytical research. Charge separation using locally-controlled DC electric fields is discussed in this chapter in evaluating its effect on MS sensitivity and stability, as a method to improve droplet charging and analyte ionization (see Chapters 3 and 4).

5.1 AMUSE Ion Source Demonstration for Mass Spectrometry

The AMUSE ion source has been successfully demonstrated for molecular ionization with a number of mass spectrometers, including time-of-flight MS (AccuTOF MS, JEOL, Inc.[72] and micrOTOF, Bruker Daltonics[96]), linear ion trap (LiT) (LTQ, ThermoFinnigan),[73] quadrupolar ion trap (QiT) (LCQ Deca XP+, ThermoFinnigan),[73,75] and a hybrid linear ion trap (LTQ) Fourier transform ion cyclotron resonance (FT-ICR) (IonSpec FTMS Systems, Varian, Inc.). Application of the AMUSE ion source showed its capability for soft ionization of peptides/proteins in purely aqueous solutions at micromolar concentrations in both an RF-only mode and with weak DC electric fields.[72-73] Parametric investigations into the effect of incorporating a Venturi™ device (air amplifier) for droplet collection and desolvation,[73-74] the influence of the nozzle orifice size,[73-74] extrapolated detection limits,[74] and internal energy deposition comparisons with conventional ESI[75] have been reported in the literature.

In this work, the focus is on reporting the MS results for peptide/proteins (e.g., melittin, angiotensin I, bradykinin, cytochrome c, and BNP-32) and small molecules (e.g., caffeine and chlorpromazine) as function of charging electrode configuration and DC voltage applied at the AMUSE ion source. This allows the linking of the fundamental theoretical (Chapter 3) and experimental (Chapter 4) studies on droplet charging in AMUSE to their resulting effect on the analyte ionization, which is ultimately relevant to MS. All analytes are added in micromolar concentrations to an aqueous solvent containing 0.1% (v/v) formic acid (pH 2.66).

5.1.1 Peptides and Proteins

Several representative peptides and proteins have been identified with the AMUSE ion source coupled, via an air amplifier, to a hybrid linear ion trap (LTQ) Fourier transform ion cyclotron resonance (FT-ICR) mass spectrometer. Sensitivity of MS analysis is enhanced by applying a small (~100-250 V_{DC}) potential to the inner piezoelectric transducer electrode.

Figure 5.1 displays the mass spectrum of a 3.4 μM sample of melittin (2846.5 Daltons). Melittin is a peptide consisting of 26 amino acids and is the main component of honeybee venom. Melittin has also been used in a number of biomedical applications, specifically as a toxin against cancer. Antibody-melittin conjugates have been used to slow the growth of tumors in mice.[162] Figure 5.1 demonstrates the +2, +3, and +4 peaks produced by the AMUSE ion source, as well as their isotopic distributions.

The AMUSE ion source can also successfully ionize proteins, for example cytochrome c (~12 kDa). Figure 5.2 displays the mass spectrum of a 5 μM sample of cytochrome c. Cytochrome c is a water soluble protein with a primary structure

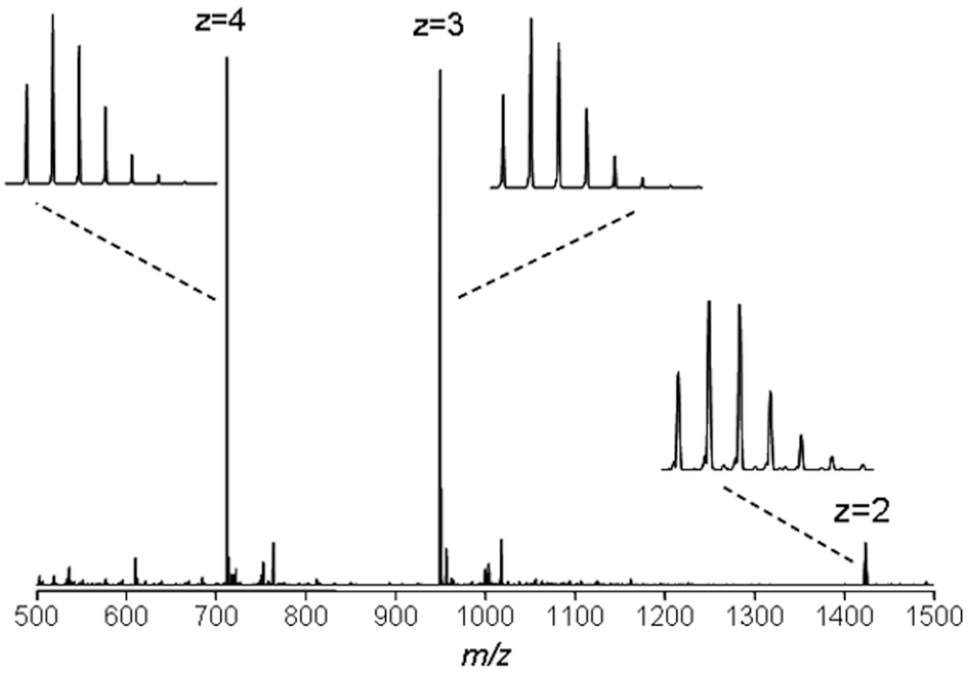

Figure 5.1 Mass spectrum from a FT-ICR mass analyzer for 3.4 μM melittin in 99.9:0.1 (v/v) water/formic acid ionized by AMUSE.

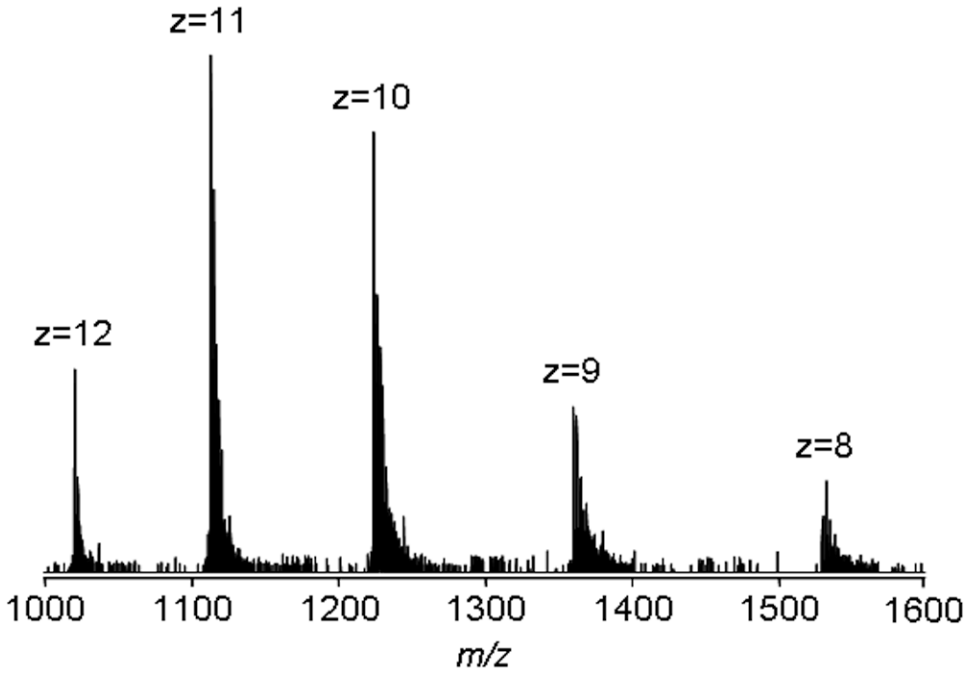

Figure 5.2 Mass spectrum from a FT-ICR mass analyzer for 5 μM cytochrome c in 99.9:0.1 (vol/vol) water/formic acid ionized by AMUSE.

consisting of a single 104 amino acid peptide. Due to its presence across species and sequence homology, cytochrome c is often used in studies of evolutionary molecular biology.[163] Similar to ESI, AMUSE has the ability to produce multiply charged ions, bringing the m/z value of large mass molecules to within the detection range of most mass spectrometers. The +8 through +12 charged states are identifiable in Figure 5.2, distributed around the base peak at the +11 charge state.

Figure 5.3 displays the mass spectrum of a 10 μM sample of angiotensin I (1296.5 Da). Angiotensin I is a physiologically inactive peptide in blood that is the precursor to angiotensin II. Angiotensin II has a number of effects throughout the body, including, cardiovascular, neural, adrenal, and renal.[164] The relatively simple spectrum presented in Figure 5.3 clearly shows the singly charged ion and its isotopic distribution. Additional

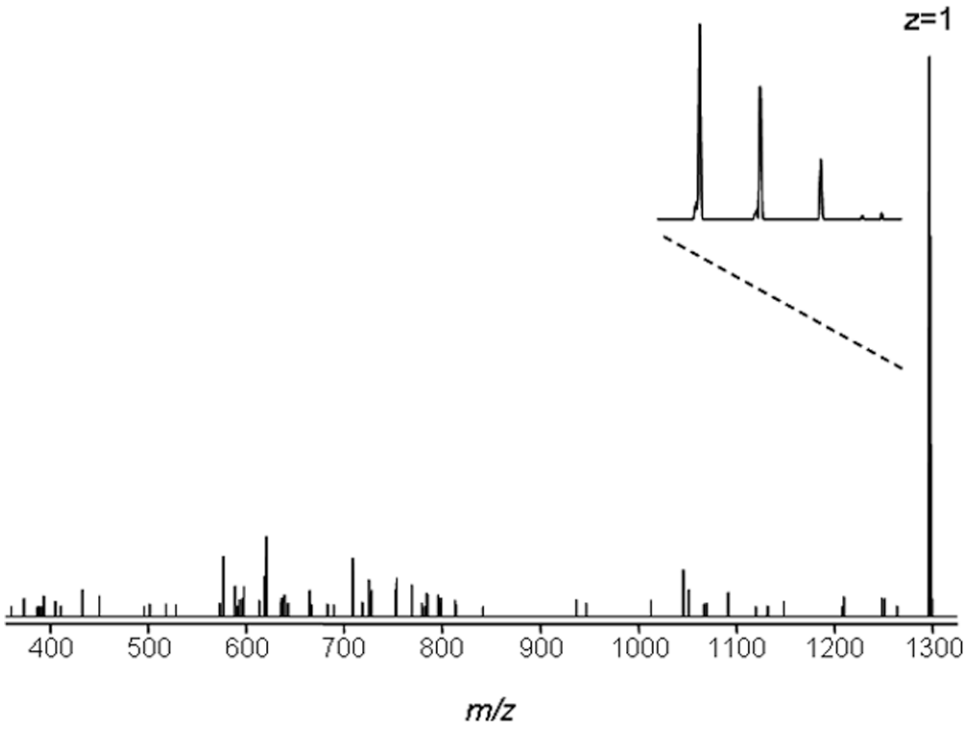

Figure 5.3 Mass spectrum from a FT-ICR mass analyzer for 10 μM angiotensin I in 99.9:0.1 (vol/vol) water/formic acid ionized by AMUSE.

mass spectra of proteins/peptides ionized using the AMUSE ion source, including bradykinin, BNP-32, and angiotensin III can be can be found in Appendix D.

5.1.2 Pharmaceutical Molecules

A couple of smaller pharmaceutical molecules are also demonstrated using the AMUSE ion source coupled with an air amplifier to a hybrid linear ion trap (LTQ) Fourier transform ion cyclotron resonance (FT-ICR) mass spectrometer.

Figure 5.4 displays the mass spectrum of a 14 μM sample of chlorpromazine (318.86 Da). Chlorpromazine is a drug in the class of conventional antipsychotics, used for treating a wide range of psychotic disorders. The +1 base peak charge state is clearly seen in Figure 5.4 with its isotopic distribution representative of the presence of chlorine. The other peak is likely due to the common chlorpromazine hydrochloride complex that has lost a chloride ion.

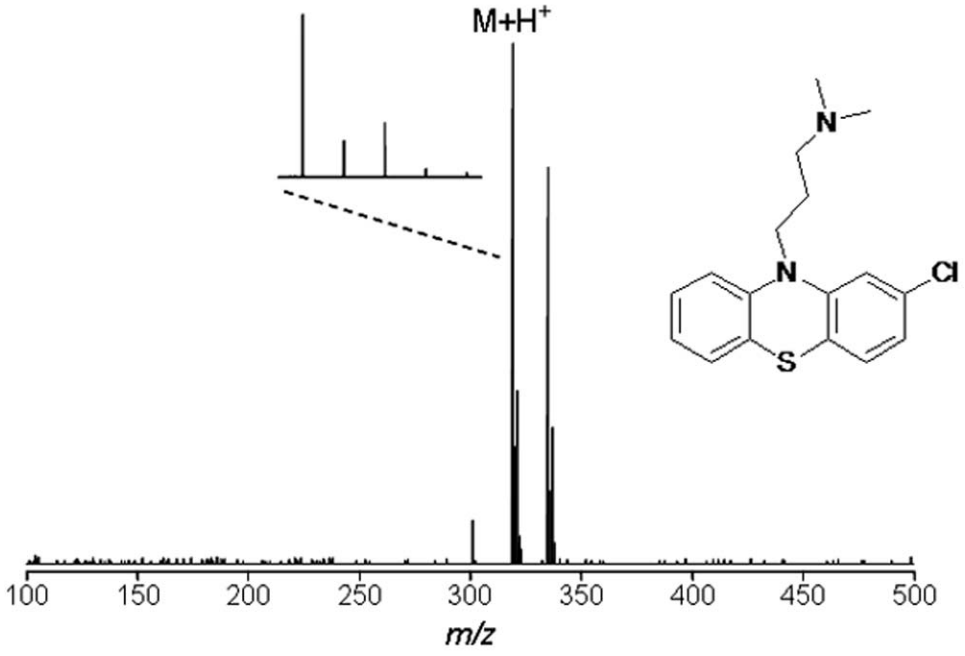

Figure 5.4 Mass spectrum from a FT-ICR mass analyzer for 14 μM chlorpromazine in 99.9:0.1 (vol/vol) water/formic acid ionized by AMUSE.

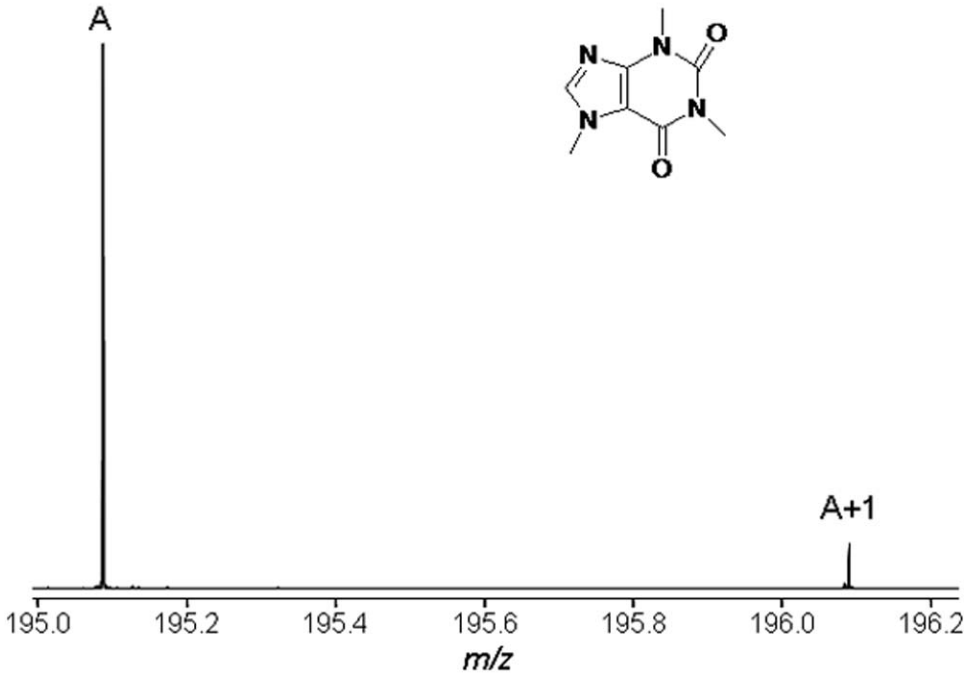

Figure 5.5 Mass spectrum from a FT-ICR mass analyzer for 5 μM caffeine in 99.9:0.1 (vol/vol) water/formic acid ionized by AMUSE.

The mass spectrum of another familiar and common pharmaceutical molecule, caffeine (194.19 Da), is displayed in Figure 5.5. Caffeine is a widely known psychoactive drug that affects the body metabolism and stimulates the central nervous system. Figure 5.5 clearly demonstrates the isotopic distribution of caffeine caused by the presence of carbon-13 (^{13}C) atoms.

Next, the charge separation methods developed in Chapters 3 and 4 to improve droplet charging are evaluated in respect to their effectiveness for improving analyte ionization for MS analysis of a common tuning compound, reserpine. The MS sensitivity and signal stability are investigated as a function of the charge separating electric field (magnitude and configuration) in the AMUSE ion source.

5.2 Electric Field Induced Charge Separation

In the case of ESI, application of a large electric field causes charge separation and electrokinetic flow, which yields a Taylor cone that ejects charged droplets when the electrostatic repulsion force overcomes surface tension.[17] As previously discussed, one of the main benefits of the AMUSE ion source is its ability to separate droplet formation from charge separation via individually controlled mechanical (piezo-driven) and electrical actuation. When operating the AMUSE in an RF-only mode, without any external electric field, only weak charge separation occurs. While the weak RF electric field, induced by the drive signal of the piezoelectric transducer, and the ionic mobility asymmetry between ions are sufficient to achieve analyte ionization at higher analyte concentrations, such a mode of operation is not optimal.[73-74] In order to maximize the net charge placed on individual droplets upon ejection and hence improve ionization efficiency and sensitivity, an enhanced charge separation is desirable. It has been shown in literature that a DC-potential-biased external electrode could be successfully used to polarize a neutral spray from a pneumatic nebulizer.[104-105] When a similar idea is applied to the AMUSE ion source, as discussed in Chapters 3-4, the induced electric field forces the positive charges (positive mode of operation) toward the fluid-air interface where a droplet is formed, while the negative charges are left behind in the bulk solution. The electrochemical oxidation of relevant anions at the piezoelectric transducer's top electrode facing the solution neutralizes these negative charges, similarly to the ESI, resulting in continuous device operation as a closed circuit electrochemical cell. Under these conditions, droplets with a much greater net (positive) charge are ejected, resulting in an improved ionization efficiency, stability, and sensitivity of MS detection.

Electrohydrodynamic simulations, validated by experimental measurements, have provided a basic understanding of charge separation in the AMUSE ion source. This section completes that analysis by demonstrating the effects of charge separation on the MS signal. DC-charging is considered for the AMUSE ion source coupled to, via an air amplifier, a micrOTOF mass spectrometer.

5.2.1 Mass Spectrometry Setup

As compared to the standard AMUSE assembly, new to these experiments is the addition of a brass support, containing a transformer wire (electrically shielded) electrode. As seen in Figure 5.6, this electrode acts as a "counter" electrode in the charge separation experiments. Bias DC potentials are applied to the inner electrode of the piezoelectric transducer, V_{PZT}, and the external counter electrode, V_{ext}, allowing a precise control of the induced electric field strength. An exploded view of the AMUSE ion source, identifying the specific location of the electrodes used to induce the external electric field can be seen in Figure 4.3.

For mass spectrometry operation, the AMUSE ion source is coupled to an air amplifier (EXAIR Corporation, Cincinnati, OH) to improve collection and transport of droplets/ions to the mass spectrometer inlet (Figure 5.6). The air amplifier is also used to assist in droplet desolvation, by heating the assisting nitrogen gas flow with a coil heater (Omega, Stamford, CT). In experiments, the AMUSE is set in an orthogonal orientation, relative to the inlet of the air amplifier and the assisting air flow, for visual inspection of device operation under various conditions.

A time-of-flight mass spectrometer (Bruker Daltonics micrOTOF^{TM}, Billerica, MA) is used as the mass analyzer. All experiments are conducted in positive ionization

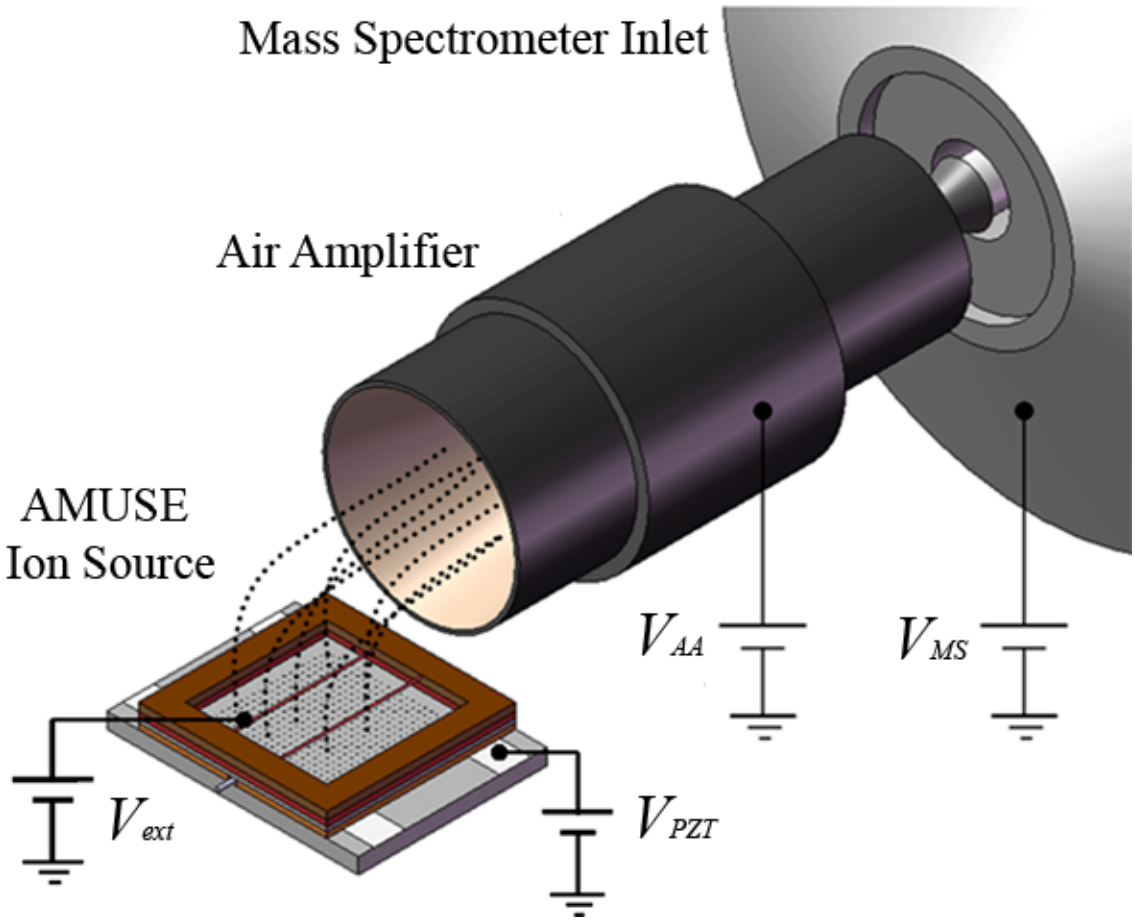

Figure 5.6 Schematic of the experimental system coupling AMUSE to air amplifier to time-of-flight mass spectrometer, including the electrode placement with controlled DC electric bias potentials.

mode with the air amplifier, V_{AA}, and mass spectrometer inlet, V_{MS}, grounded (zero DC potential relative to a common electric ground). The TOF capillary is maintained at 180°C with a dry gas counter-flow rate of 3 L/min and spectra collected are a rolling average at a scan rate of 3 Hz.

Reserpine, purchased from Sigma-Aldrich (St. Louis, MO, USA) is used as received. Micromolar solutions of the compound are prepared in deionized water (Ricca Chemical Company, Arlington, Texas, USA) containing 0.1% (v/v) glacial acetic acid (BDH Aristar, Westchester, PA, USA). No organic solvents are used in the working

solutions. The experiments are completed for a 3 μM solution of reserpine delivered to the AMUSE fluid reservoir at 30 to 50 μL/min using a syringe pump.

5.2.2 Electric Field Configurations

Figure 5.7 displays the different electric field configurations considered in this investigation. The electric field lines induced between the external wire electrode of the AMUSE ion source and the grounded (zero electric potential relative to common ground) air amplifier are also displayed.

Figure 5.7(a) represents the first dataset (squares), in which a positive DC potential is applied to the piezoelectric transducer electrode, $V_{PZT} = +V_{DC}$, and the wire counter electrode is grounded, $V_{ext} = 0$. The resulting electric field induces charge separation by moving positive charges toward the nozzle orifice. The second dataset (diamonds), shown in Figure 5.7(b), is for the case when the wire counter electrode is removed, while leaving the remainder of the setup the same. The relevant potential difference that defines the electric field strength now becomes $\Delta\phi_{\Diamond} = V_{PZT} - V_{AA}$. This configuration is similar to that used in other investigations of the AMUSE ion source.[72-73,75] Figure 5.7(c) displays the third dataset (circles), which describes experiments in which all applied DC potentials are altered, relative to a common electric ground, but proportionally; therefore, no effect is expected on the strength of the electric field. In particular, the piezoelectric electrode is grounded, $V_{PZT} = 0$, and a negative DC bias is applied to the wire electrode, $V_{ext} = -V_{DC}$, with potential difference defined as $\Delta\phi_o = V_{PZT} - V_{ext}$. This configuration is intended to isolate the signal improvement due to charge separation by eliminating any signal increase/decrease that may be due to

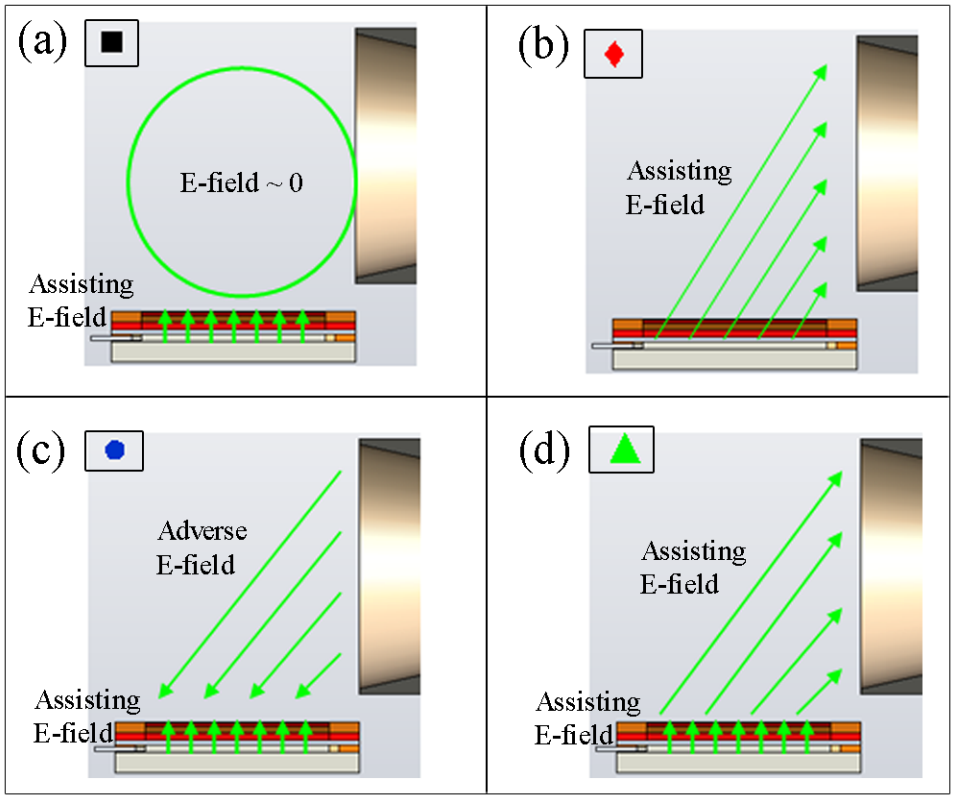

Figure 5.7 Schematic representation of electric field configurations: (a) case 1 (squares): $\left(V_{PZT} = +V_{DC},\ V_{ext} = 0\right)$, (b) case 2 (diamonds): $\left(V_{PZT} = +V_{DC},\ V_{ext} = removed\right)$, (c) case 3 (circles): $\left(V_{PZT} = 0,\ V_{ext} = -V_{DC}\right)$, (d) case 4 (triangles): $\left(V_{PZT} = +V_{DC} = Const,\ V_{ext} = +V_{DC}\right)$, for all cases, $V_{AA} = V_{MS} = 0$.

increased/decreased charge levels due to electrochemical processes at the piezoelectric transducer electrode. The final dataset (triangles), presented in Figure 5.7(d), further aims to eliminate the effects of solvent oxidation by applying a constant (positive) potential to the piezoelectric electrode, $V_{PZT} = +V_{DC} = Const$, while positively biasing the wire electrode, $V_{ext} = +V_{DC}$, $\left(\Delta\phi_{\Delta} = V_{PZT} - V_{ext}\right)$.

5.2.3 Signal Abundance and Sensitivity Improvements

The investigation into the effect of electrical field configuration and strength on the signal intensity and stability is completed with the use of a micrOTOF mass spectrometer (Figure 5.6). Two crossing wires are used as a counter electrode providing an electric field in the direction normal to the nozzle array, while minimizing ejection blockage due to the wires. MS intensity values are taken from the extracted ion chromatogram as shown in Figure 5.8 (top) and a representative mass spectrum (bottom) for reserpine.

Figure 5.9 shows the maximum signal intensity of the base peak and Figure 5.10 shows the signal-to-noise ratio (sensitivity) as a function of the DC electric field applied in the device. As the first dataset (squares, electric field configuration Figure 5.7(a)) shows, increasing the potential drop, $\Delta\phi_{\square} = V_{PZT} - V_{ext}$, and therefore the charge separating electric field magnitude, increases the signal intensity (Figure 5.9) and

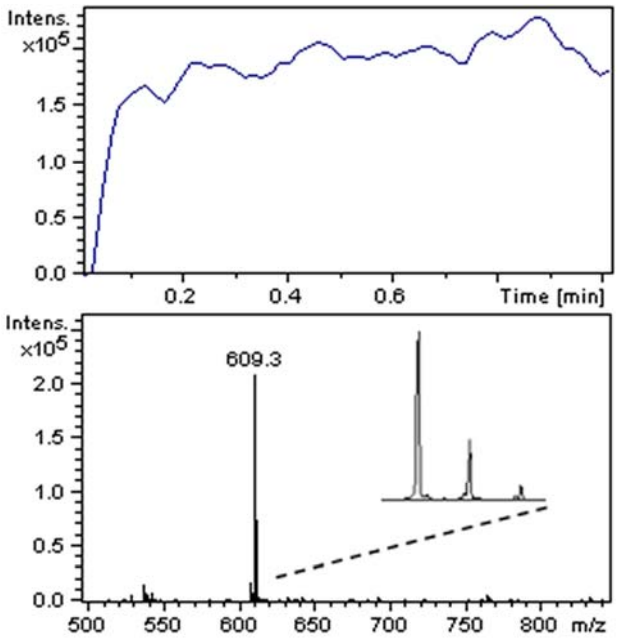

Figure 5.8 Extracted ion chromatogram of a base peak (top), and representative mass spectrum (bottom), for 3 μM reserpine in 99.9:0.1 (vol/vol) water/acetic acid ionized by AMUSE.

improves signal-to-noise ratio (S/N) (Figure 5.10) from ~60 up to values greater than 2000. An order of magnitude increase in the electric field strength results in two orders of magnitude increase in S/N ratio. As mentioned above, the second dataset (diamonds, electric field configuration Figure 5.7(b)), is similar to that used in other analytical characterization reports of the AMUSE ion source.[72-73,75] In this configuration, the air amplifier acts as the counter electrode, and moving it further away results in a decreased electric field strength. This, in turn, yields a reduced charge separation and less efficient analyte ionization. As the potential is increased, $V_{PZT} >$ 1000V, the electric field eventually becomes sufficiently strong to promote charge separation at the point of droplet ejection and the signal intensity experiences a modest gain. It is apparent and

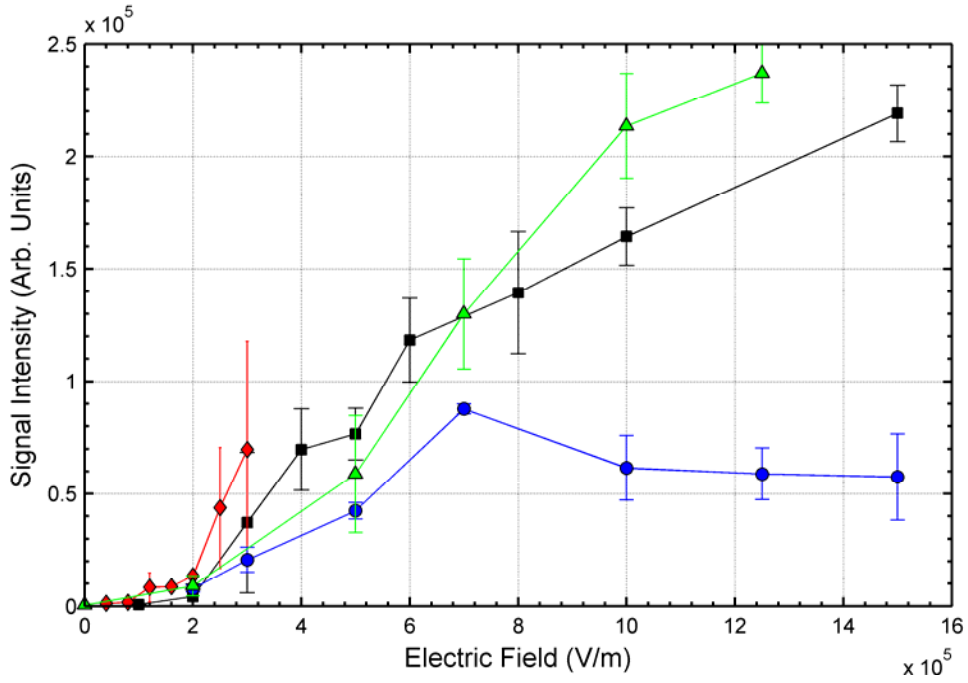

Figure 5.9 Maximum signal intensity obtained with the AMUSE ion source for 3 µM reserpine in 99.9:0.1 (v/v) water/acetic acid for various applied electric field configurations. Potential configurations: case 1 (squares): $\left(V_{PZT} = +V_{DC},\ V_{ext} = 0\right)$, case 2 (diamonds): $\left(V_{PZT} = +V_{DC},\ V_{ext} = removed\right)$, case 3 (circles): $\left(V_{PZT} = 0,\ V_{ext} = -V_{DC}\right)$, case 4 (triangles): $\left(V_{PZT} = +V_{DC} = Const,\ V_{ext} = +V_{DC}\right)$, for all cases, $V_{AA} = V_{MS} = 0$.

hardly surprising that the electric field strength, and not just the potential drop, is determining the charge separation and therefore the extent of the signal improvement.

As discussed in the pervious section, the third dataset (circles, electric field configuration Figure 5.7(c)) is meant to isolate the effects of charge separation by eliminating any signal differences that may be due to differences in charge levels from electrochemical processes at the piezoelectric transducer electrode. As shown in Figure 5.9, the signal intensity begins to increase with an increase in the applied electric field in line with the measurements obtained for the first dataset. However, upon reaching a certain electric field magnitude, the signal intensity begins to drop and level off with further increase in the electric field. The source for discrepancy between the first (squares) and third (circles) datasets at higher electric fields becomes apparent if one considers not only the magnitude, but also the direction of the electric field along the entire ion/charged droplet transmission path from the ejection point to the mass spectrometer inlet (Figure 5.6). In the first (squares) set of experiments, the wires were grounded so no external electric field existed between the wire counter electrode and air amplifier. In contrast, for the third dataset (circles), although the local electric field between the AMUSE ejection surface and the wire electrode is the same, there is now an adverse electric field between the negatively biased wires $\left(V_{ext} = -V_{DC}\right)$ and the grounded air amplifier $\left(V_{AA} = 0\right)$ that hinders positive ion transport to the MS inlet. Thus, while the charge separation remains equally effective in the latter (third) set of experiments, the measured MS signal intensity decreases at higher piezo-to-wire potential differences due to diminishing the charged droplet/ion transmission between the wire electrode and the air amplifier/MS inlet when the droplets contain high levels of charge. This conclusion is

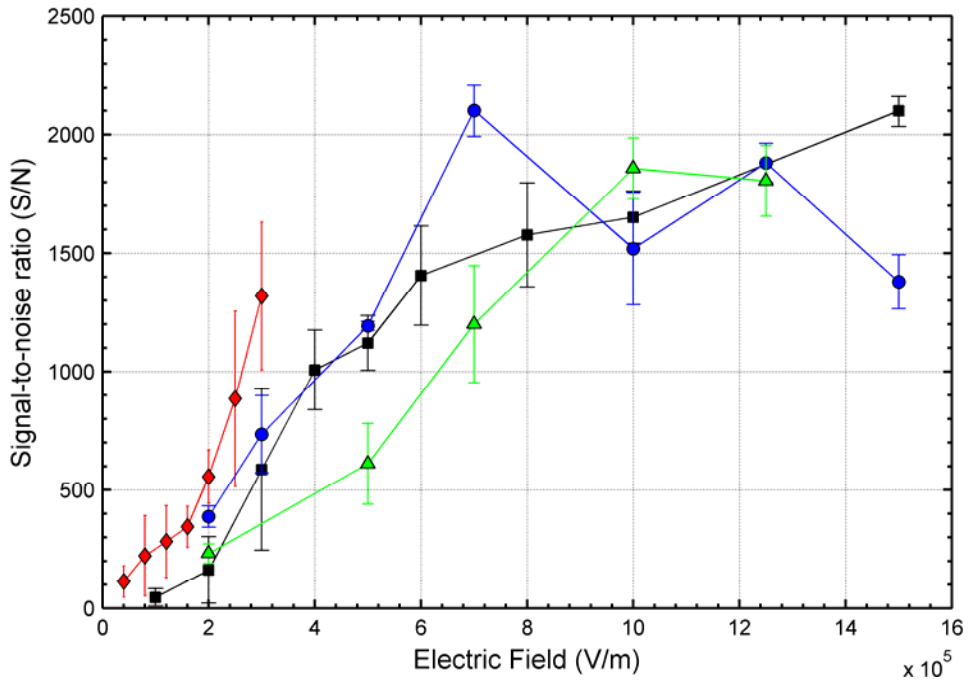

Figure 5.10 Signal-to-noise (S/N) ratio obtained with the AMUSE ion source for 3 µM reserpine in 99.9:0.1 (v/v) water/acetic acid for various applied electric field configurations.

further supported, in Figure 5.10, by the fact that while the signal intensity is depressed at stronger electric field operation, the S/N ratio is not, maintaining ~1500. To summarize, while charge separation helps increase the charge density in ejected droplets, ion transport remains a vital process in MS operation with the AMUSE ion source.

In the final dataset (triangles, electric field configuration Figure 5.7(d)) the electric field across the AMUSE is the same as for the first case and, as expected, the data follows each other very closely (Figure 5.9). The slight increase in an MS signal at high electric fields can be attributed to the small ion-transport-assisting electric field produced between the wire counter electrodes and air amplifier as shown in Figure 5.7(d). The experimental data from these tests clearly show that an increase in the external charge separating electric field strength at the point of droplet ejection improves the signal

intensity and S/N ratio, as long as the electric field distribution is optimized between the ion source and the mass spectrometer inlet. A direct correlation between increasing the local electric field and experiment repeatability is also found.

In summary, MS characterization of various electrode configurations in the AMUSE ion source indicates that an external electric field localized and focused at the ejection interface near the nozzle orifice induces efficient charge separation, resulting in the ejection of increasingly charged droplets. An increased charge density within droplets improves both the signal-to-noise ratio (sensitivity) and signal stability, allowing for more efficient analyte ionization. Improvements in signal abundance, signal-to-noise ratio, and signal stability support the validity of the electrohydrodynamic charge separation analysis developed in previous chapters.

5.2.4 Comments on the Ionization of Macromolecules for Mass Spectrometry

It is important to note right away that the conclusions drawn in this section may well be dependent on the method by which dry ions are formed, and therefore must be used in a context of the specific application. The two competing methods for dry ion formation, as discussed in Chapter 1 and displayed in Figure 1.2, are the charge residue mechanism (CRM)[7] and the ion evaporation mechanism (IEM).[13] For relatively small molecules, such as reserpine, the IEM dominates. The small molecules reside on the surface of charged droplets, along with the majority of the free charge carriers, and upon charge fluctuation they get transferred into an energetically favorable state in a gas phase.[7,13,15,22] It is under these conditions that increasing the available charge carriers on individual droplets results in improvements in signal abundance and sensitivity, as demonstrated in the previous section. However, for much larger macromolecules or

highly hydrophilic molecules, the CRM is more common. These molecules reside in the interior of charged droplets and require sufficient solvent evaporation and numerous Coulombic fission events before the macromolecule is completely desolvated and ionized by condensed residual charge carriers. In this case, improvements in signal abundance and sensitivity are *unlikely* to continue linearly with increasing charge separating electric field. It has been demonstrated that at ~80% of the Rayleigh limit, highly charged droplets fission approximately 20 satellite droplets. These satellite droplets carry away disproportionately large amount (~15%) of the charge and only ~2% of the mass from the parent droplet.[21] Therefore, it is possible that increasingly charged droplets will simply lose most of their excess charge during fission events before the macromolecule completely desolvates. This would be detrimental to ionization of high molecular weight and hydrophilic molecules.

Furthermore, there are additional aspects of droplet charging that must also be considered for AMUSE application in mass spectrometry. While the charge-per-droplet measurements obtained in Chapter 4 are very useful defining how the greatest amount of charge can be transferred into an ejected droplet, these maximum charging conditions may not be optimal for producing "dry" ions for mass spectrometry, especially in the case of macromolecules. Indeed, if macromolecules are ionized by the CRM, then the solvent in which the molecules reside plays an important role in charging. Excluding the effects of molecule denaturing, it has been demonstrated that the extent of charging of large molecules is correlated to the Rayleigh limit $\left(q^2 = 64\pi^2\varepsilon_o\gamma r^3\right)$ of a droplet of solvent approximately the same size (diameter) as the macromolecule.[165-168] Therefore, not only the solvent composition, but the vapor pressures and surface tension of each component

play a role in the effective molecule charging. For example, so called "supercharging" has been demonstrated for water/methanol mixtures by adding m-nitrobenzyl alcohol (m-NBA) or glycerol.[165-168] m-NBA and glycerol have very low vapor pressures and higher surface tensions than the base water/methanol mixture. Therefore, as the water and methanol more readily vaporize from the droplet surface, the solvent that remains at the time of CRM charging is predominantly the m-NBA or glycerol. This in effect increases the surface tension of the solvent at the time of CRM charging, compared to a water/methanol mixture. An increase in surface tension results in an increase in the Rayleigh limit $\left(q^2 = 64\pi^2\varepsilon_o\gamma r^3\right)$, which results in more available charge at the time of complete desolvation. However, it should be noted that such additives would decrease the overall surface tension of a purely aqueous solvent (high surface tension), thus reducing the Rayleigh limit and available charge upon complete desolvation.

This method for macromolecule charging becomes relevant in the AMUSE ion source as the percentage of acetic acid (or alternative weak acid, e.g. formic acid) is increased to enhance droplet charging. Experimental measurements have demonstrated that droplet charging does not increase monotonically with increasing bulk charge density (percent of acetic acid) due to competing charge transport processes (Figure 4.14). But, for mass spectrometry ionization, an additional consideration should be taken into account. As the level of acetic acid ($\gamma_{AA} = 0.027\,\text{N/m}$, $p_{vap,AA} = 2.64\,\text{kPa}$ at 35ºC) in the aqueous solvent ($\gamma_{H_2O} = 0.072\,\text{N/m}$, $p_{vap,H_2O} = 5.63\,\text{kPa}$ at 35ºC) increases, the solution surface tension will decrease. Since water has a higher vapor pressure than acetic acid, this effect will become amplified as the water preferentially evaporates from the droplet, increasing the percent of acetic acid further.[168] The reduced surface tension of the droplet

immediately before CRM ionization will reduce molecule charging, due to a reduction in the Rayleigh limit and therefore available excess charge. For mass spectrometry applications that require maximum charging for efficient ionization, the competing charge transport, solution composition, and ionization method (i.e. IEM or CRM) must all be considered.

5.3 Potential High-Impact Applications of the AMUSE Ion Source

Several specific examples where the AMUSE ion source has the highest potential for improving the mass spectrometry analysis are briefly discussed in the following sections.

5.3.1 Soft Ionization Capability

Computational and experimental analyses discussed in the previous chapters demonstrated the AMUSE capability for nearly independent control over droplet charging and ejection. This aspect becomes increasingly useful in achieving the soft ionization of fragile macromolecules.

5.3.1.1 Noncovalent Interactions

In the field of mass spectrometry, analyses of noncovalent interactions and biological species, such as deoxyribonucleic acid (DNA) and protein complexes, are less prominent than proteomic analyses. This is likely due to the difficulties that arise during the ionization process of noncovalent biological species and the presence of alternative technologies such as capillary electrophoresis (CE). Thermally labile macromolecules, such as oligonucleotides, will easily fragment with increases in their internal energy.[169] Within the area of noncovalent interactions, protein complexes have been studied much

more frequently than interactions between proteins and nucleic acids. Difficulties in studying these interactions are again due to a need for soft ionization, as well as the need for high salt concentration solutions and the heterogeneity of oligonucleotides.[170] An additional difficulty in the investigation of noncovalent complexes is the unknown degree to which the observed complexes are due to nonspecific interactions. It is still unclear to what extent the gas-phase complexes detected by the mass spectrometer reflect the solution equilibrium conditions before ionization.[1,171]

Like electrospray ionization, AMUSE has the capability to produce multiply charge ions, which is imperative to mass spectrometric analysis of such large macromolecules with masses in the 10s-100s kDa range. Multiple charging to high charge states brings the mass-to-charge (m/z) ratio to within the limits of typical mass spectrometers. The AMUSE ion source uniquely allows for soft ionization of compounds formed through weak non-covalent interactions, as well as reduced sensitivity to the salts and detergents (due to mechanical droplet ejection) often present in non-covalent interaction solvents.

5.3.1.2 RF-only Mode of Operation

Studies by Fernandez's Research Group at Georgia Tech demonstrated that the AMUSE ion source has a superior softness of analyte ionization as compared to conventional ESI under certain operation conditions.[75] Ionization softness was determined by a comparison of internal energy deposition, measured using the "survival yield" method. This method correlates the fragmentation extent of a specific thermometer molecule, para-substituted benzylpyridinium salts, to the internal energy deposited during ionization. Upon surpassing an inherent dissociation energy threshold, the thermometer

molecule cleaves to form a benzyl cation and pyridine.[172] The internal energy deposition during ionization was compared for operation of AMUSE and ESI with and without the assistance of an air amplifier for droplet desolvation and focusing. AMUSE demonstrated the capability for softer ionization than ESI, while also producing superior MS sensitivity.[75] Complete results and detailed description of the analysis can be found in Reference 75.

5.3.2 Solvent Flexibility

The AMUSE ion source has many benefits that are derived from its intrinsic decoupling of droplet formation and analyte charging processes. This mechanically-driven ion source is capable of atomizing many liquids with a wide range of properties. The main method of solution-based ionization, electrospray ionization, relies on the application of a strong electric field for fluid dispersion. Numerous modes of electrospraying exist, dripping,[153] burst,[154] pulsating,[19,110] astable,[155] and the stable cone-jet,[156] dependent on the fluid conductivity, applied potential, and flow rate. Therefore, the fluid properties play a significant role in maintaining a strong and stable spray required for MS analysis. Electrospray ionization suffers from ionization suppression due to charge competition between analytes or the analyte and solvent, differences in droplet surface affinities between analytes, and stability of spraying.[23,173-174] The spray stability of electrospray ionization is very much dependent on the solvent conductivity. The presence of salts and other charged species that influence the liquid conductivity affect the spray stability. The increase in liquid conductivity affects the Maxwell stresses at the cone-jet surface and disrupts the balance of forces producing the steady jet. As the spraying becomes erratic, the droplets sizes produced become unpredictable, leading to

irregular analyte ionization and signal suppression.[23] The AMUSE ion source produces monodisperse droplets using mechanical actuation, which is thus independent of the electric field used for analyte/droplet charging. This results in insensitivity to liquid conductivity and salts, present in the solvent, which is very beneficial in the field of LC-MS, where solvent gradients and additives are common in the mobile phase.

This chapter presented the MS characterization and applications of the AMUSE ion source. AMUSE has been successfully demonstrated for a range of mass spectrometers (TOF, LiT, QiT, FT-ICR), operation conditions (RF-only, DC-charging), and biologically (proteins/peptides) and pharmaceutically (drug molecules) relevant analytes. Parametric studies have been performed to yield an increased understanding of AMUSE-MS operation and directions toward optimal performance. Applying the charge separation framework developed computationally in Chapter 3, and verified experimentally in Chapter 4, the MS response was analyzed as function of a DC-charging electric field. The charge-separating electric field applied in the AMUSE ion source generated increasingly charged droplets, improving ionization efficiency. The amplified free charge availability in ejected droplets led to enhancements in the MS signal abundance, sensitivity, and stability. The chapter concluded with a discussion of applications, notably soft ionization and solvent insensitivity, for which the AMUSE ion source has potential for the most impact in the field of bioanalytical mass spectrometry.

CHAPTER 6

CONCLUSIONS AND RECOMMENDATIONS FOR FUTURE WORK

This thesis presents the theoretical, computational, and experimental analysis of electrohydrodynamics and ionization in the Array of Micromachined UltraSonic Electrospray (AMUSE) ion source. The AMUSE ion source is a mechanically-driven droplet-based ion source that can independently control charge separation and droplet formation, which conceptually differs from electrospray ionization (ESI) in this aspect. AMUSE is a versatile device that operates in an array format, which enables a wide range of configurations, including high-throughput and multiplexed modes of operation. This thesis establishes an in-depth understanding of the fundamental physics of analyte charging and electrohydrodynamic (EHD) charge separation. The EHD model developed presents a powerful tool for optimal design and operation of the AMUSE ion source. Analyte charging and electrohydrodynamics in AMUSE are characterized using dynamic charge collection measurements and optical visualization of ejection phenomena. The scale analysis of the ejection phenomena provides guidelines for AMUSE ejection mode in the presence of an external electric field. Finally, an understanding of analyte charging and charge separation developed through complimentary theoretical and experimental investigations is utilized to improve signal abundance, sensitivity, and stability of the AMUSE-MS response.

In Chapter 2, the AMUSE design, fabrication, and a number of device configurations are discussed. Specifically, the design and analysis of a dual-sample

multiplexed configuration is presented. The acoustic wave isolation techniques developed using FEA simulations are experimentally validated, resulting in successful independent ejection from individual domains. Multiplexed configuration of the AMUSE ion source has many potential used in MS analysis. Therefore, analytical characterization of a multiplexed AMUSE ion source is recommended, as a natural extension of this work, to demonstrate quantitative MS analysis and mass calibration by simultaneously spraying an internal standard and molecule of interest. Sequential analysis of multiple molecules should also be investigated, considering the time response of switching between samples.

In Chapter 3, the development of an electrohydrodynamic (EHD) model coupling the electric and hydrodynamic fields is presented. The EHD model can serve as a versatile design tool in future investigations, leading to the exploration of new operating modalities for existing ion sources, especially those with a significant degree of independent control of fluid dispersion and charge transport processes, such as AMUSE. The model also enables development of new types of ion sources, which allow for even greater control of the interacting fluid flow and charge transport phenomena. The following studies are recommended for future research:

1. An in-depth investigation into various aspects of electrospray ionization should be conducted. The model provides the framework necessary to examine the conditions and specific parameters affecting the onset of spraying from various capillary geometries and configurations. Parametric studies can also be completed to study the conditions necessary for transitions between spraying modes, i.e. dripping, burst, pulsating, astable, and cone-jet. Other studies might identify parametric relationships between input/output variables, e.g. droplet size as a

function of capillary geometry, flow rate, electric field, and fluid conductivity. The model also enables investigation of the transport phenomena out of reach for experimental visualization, for example, the physics of transition from conventional ESI to nanoESI.

2. The generality of the model also enables the investigation of charge transport and electrohydrodynamics in various other ESI-based and droplet-based ion sources. Specifically, both piezoelectrically-assisted and pneumatically-assisted ESI sources can be modeled. As reviewed in Chapter 1, piezoelectrically-driven (squeeze mode) ultrasonic nebulizers assist the interface breakup during the electrospraying process. In this case, a cylindrical piezoelectric element concentrically covers the capillary, applying squeezing pressure at high frequency (MHz) to assist interface breakup. Pneumatically-assisted ESI can also be modeled with the addition of a concentric nebulizing gas flow (Figure 1.3). These ion sources, as well as many others, can be analyzed and improved with the use of the developed EHD model.
3. One aspect yet to be incorporated into the model is Joule heating of a conducting fluid upon current flow. In cases with high electric fields, Joule heating may cause a considerable temperature increase. Therefore, energy conservation, including Joule heating, should be added to the current EHD model. The inclusion of energy conservation may help estimate the internal energy deposition under various AMUSE operating modes, i.e. RF-only, DC-charging, AC-charging. These trends can be compared to the established experimental internal energy deposition data using the "survival yield" method.[75] Such a comparison would enable further

investigations into waveforms (e.g., pulsed vs. continuous) driving ejection/charge separation that would maximize analyte charging while minimizing internal energy deposition.

4. In the present thesis, the model has been validated by simulating cone-jet and Taylor cone profiles, as well as matching droplet charge levels and trends measured experimentally with the AMUSE ion source. However, the general limits of the model validity have yet to be quantitatively determined. It is believed that the accuracy of charge conservation will deteriorate as bulk charge densities increase. As electric fields are applied, charges migrate to the fluid-gas interface. At the interface, mass is conserved by the volume-of-fluid technique, however, charge is conserved using far simpler discretization methods. Expanding the current code to incorporate volume-of-fluid discretization for the advective terms of the charge transport equation should improve accuracy and expand the limits of validity, and is recommended for future work.
5. Superior softness was achieved by the AMUSE ion source when run in an RF-only mode. The application of a DC-charging electric field will undoubtedly increase the internal energy deposition levels. While the charge separation investigation conducted here provides a method for improving droplet charging and in turn the MS response, the applied electric fields may reduce or even eliminate the superior softness that AMUSE demonstrates over ESI. As a result, to simultaneously produce both superior softness and improved ionization efficiency with the AMUSE ion source, a new modality of operation may be required. The theoretical model and simulation tools developed here provide a

versatile and general analytical framework for fundamental investigations of coupled electrohydrodynamics and charge transport. This tool specifically enables the exploration of different configurations and operating modes which not only optimize charge separation but would also minimize internal energy deposition to the analyte. For example, a short-pulse-width charge-separating electric field would enable charge separation for improved MS response, yet minimize the internal energy increase caused by the application of an electric field.

The validity of the electrohydrodynamics model developed in Chapter 3 is demonstrated in Chapter 4 by comparison to experimental measurements of droplet charge as function of electric field magnitude and bulk charge density. Both DC and AC-charging dependence is measured by correlating the electrical current with ejected mass using an AMUSE configuration with an external wire counter electrode. A time scale analysis of the competing charge transport processes produces a regime map, which identifies the extent of droplet charging based on the dominant transport processes. In addition, high-spatial-resolution stroboscopic visualization of droplet ejection and a scale analysis of the ejection phenomena yield the parameters defining a transition between inertia-dominated and electrically-dominated ejection. The transition region, where inertial and electric forces are comparable, produces coupled electromechanical ejection. Further recommended investigations include the following:

1. The charge transport analysis provides a framework for the relevant time scales at which each transport process dominates and under what conditions a certain level of charging is expected. Through this framework, an analysis of alternative

waveforms, e.g. pulsed charge-separating electric fields, can be parametrically investigated to find an optimal waveform and pulse strength, width, and delay.

2. In order to eliminate condensation of droplets on the external wire counter electrodes resulting in signal suppression in the current AMUSE arrangement (Figure 4.3), alternative configurations should be considered. One option is to sputter or evaporate specific electrode patterns directly onto the AMUSE nozzle array surface. The EHD model developed in Chapter 3 could be used for optimizing these electrode patterns before fabrication.
3. The extent of the experimental investigation of electric field magnitude and bulk charge density have been limited by the elevated frequency of dielectric breakdown between the pooling liquid and external electrodes. New strategies to reduce pooling, leading to dielectric breakdown should be considered. Some promising alternatives to eliminate these issues include (1) moving the counter electrode further away and using a more powerful voltage source, and/or (2) utilizing a configuration that quickly removes the pooling liquid from the ejector surface, e.g., a hydrophobic surface coating and vertical device orientation.

Much of the work completed in this thesis focuses on the development of computational tools and investigations into electrohydrodynamics and charge separation in the AMUSE ion source. These tools and fundamental understanding provide a sound groundwork for the optimization of the AMUSE ion source and future studies of AMUSE-MS applications. Among important extensions of this work to be considered in the future are (1) development of the actuation technology (e.g., the capacitive micromachined ultrasonic transducers) for robust ejection from a single nozzle, (2)

coupling of an AMUSE ion source to liquid chromatography separation (LC-AMUSE-MS), and (3) optimized droplet desolvation and transmission interface development to effectively couple AMUSE to MS. Specifically, the following studies are recommended for future research:

1. In the initial characterization of LC-AMUSE-MS coupling using calpain inhibitors, it has been found that the large volume of the sample reservoir in the baseline AMUSE ion source causes chromatographic peak broadening and loss of fidelity.[74] While LC-AMUSE-MS coupling was demonstrated, reduction in the sample reservoir is required to improve chromatographic fidelity. From Chapter 2, it has been discussed that in its current configuration, utilizing a bulk piezoelectric element for actuation, the AMUSE ion source cannot be operated using a single nozzle. Therefore, it is recommended that an in-depth investigation into utilizing alternative transducers, such as capacitive micromachined ultrasonic transducers (CMUTs),[97-98] is completed in an effort to provide a robust method for ejection from a single nozzle. Such a configuration would drastically increase the AMUSE ion source's multiplexing capabilities.
2. With the development of a CMUT-AMUSE ion source as described above, all components of the AMUSE ion source can be fabricated "on-chip" and bulk elements, such as the original piezoelectric transducer, are no longer needed. Following the current trend toward lab-on-a-chip devices, this technology provides a direct path toward development of a monolithic LC-CMUT-AMUSE micro total analysis system (μTAS). A number of monolithic LC-ESI chips have been demonstrated, incorporating both chromatographic separation columns and

electrospray tips. On-chip chromatographic columns have been fabricated using a wide range of well documented techniques, including surface micromachining,[175-178] bulk silicon[179] and glass[180-181] micromachining, and polymer micro-fabrication.[182-185] A multiplexed monolithic LC-CMUT-AMUSE device would be an important addition to a toolbox for high-throughput MS analysis.

3. In the AMUSE-MS investigations covered here (Chapter 5) and in the literature,[73-75,96] AMUSE has been coupled to MS via an air amplifier to enhance droplet collection, desolvation, and transmission. However, the air amplifier is a commercial product not designed with this application in mind. Recently, the new concept of DRy Ion Localization and Locomotion (DRILL) interface between the ion source and mass spectrometer was introduced.[186] The DRILL interface utilizes a combination of converging vortex flow and electrode arrays to guide and focus droplets/ions from the ion source plume to the MS inlet. Since AMUSE generates relatively large initial droplets, the DRILL embodies a direct approach to improving desolvation by increasing droplet flow path and residence time. This method of enhanced desolvation can be performed at ambient temperature and provides an important alternative to increasing the assist gas temperature, which would undoubtedly increase the internal energy deposition that is undesired in many emerging MS applications of highly unstable molecules and complexes.
4. The correlation between an enhanced droplet charging and an improved MS response, as established in this work, has been validated for a relatively small molecule that are ionized by the IEM. Chapter 5 introduced a discussion on the differences that might arise between the maximum droplet charging and MS

response for large macromolecules, ionized through the CRM. It is recommended that comprehensive MS characterization experiments be conducted for larger molecules, e.g. cytochrome c or myoglobin, as a function of charge separating electric field and solvent composition, i.e., bulk charge density (acetic acid percentage).

APPENDIX A

MULTIPLEXED AMUSE ION SOURCE

A.1 Modeling of Dual-Sample Configuration

The ANSYS acoustic simulation utilizes the default solver options for a harmonic response analysis. Specifically, it solves the 2nd order (in time) equations of motion governing the structural response of the silicon nozzle array and the acoustic response of the fluid reservoir. The harmonic response analysis also solves the mixed order (electrical and structural) governing equations of the piezoelectric transducer dynamics.[70] The accuracy of this approach is founded on the small amount of energy transferred to the ejected fluid, which leaves the linear acoustic field undisturbed.[67]

A.1.1 Simulation Domain

Element types for the various domains considered in the simulation are, coupled-field solid (PLANE13) for the piezoelectric transducer, bulk fluid (FLUID29 (KEYOPT (2)=1) for the fluid domains, structural interface fluid (FLUID29 (KEYOPT (2)=0) for the thin domain between solid and fluid elements, and structural solid (PLANE82) for the silicon nozzle array, silicone rubber insert, and Kapton spacer.

A.1.2 Material Properties

The material properties for modeling the lead zirconate titanate piezoelectric transducer, ejected water, silicone spacer, and silicon nozzle array are summarized next.

A.1.2.1 Piezoelectric Transducer Properties

The lead zirconate titanate (PZT-8) piezoelectric transducer material is characterized by a coupled structural and electric field. Piezoelectric materials deform in the presence of an applied voltage and generate a potential under an applied displacement. The most common formulation for the piezoelectric equations provide the electric field and stress as independent variables.[187]

$$\in_I = \sum_J S_{IJ}^E \sigma_J + \sum_j E_j d_{jI} \tag{A.1}$$

$$D_i = \sum_J d_{iJ} \sigma_J + \sum_j \varepsilon_{ij}^\sigma E_j \tag{A.2}$$

Here, $\in$ is the strain, σ is the stress, ε is the dielectric permittivity, S_{IJ} is the compliance coefficient, d is the piezoelectric stress coefficient, E is the electric field, and D is the electric displacement. The compliance matrix is a required input for the ANSYS code and is given here for the PZT-8 material.

$$S = \begin{vmatrix} \frac{1}{E_p} & \frac{-\nu_p}{E_p} & \frac{-\nu_{zp}}{E_z} & 0 & 0 & 0 \\ \frac{-\nu_p}{E_p} & \frac{1}{E_p} & \frac{-\nu_{zp}}{E_z} & 0 & 0 & 0 \\ \frac{-\nu_{pz}}{E_p} & \frac{-\nu_p}{E_p} & \frac{1}{E_z} & 0 & 0 & 0 \\ 0 & 0 & 0 & \frac{1}{2G_{zp}} & 0 & 0 \\ 0 & 0 & 0 & 0 & \frac{1}{2G_{zp}} & 0 \\ 0 & 0 & 0 & 0 & 0 & \frac{(1+\nu_p)}{E_p} \end{vmatrix} \tag{A.3}$$

where, $\frac{\nu_{pz}}{E_p} = \frac{\nu_{zp}}{E_z}$

PZT-8 is a transversely isotropic material, whose properties are constant in one plane (e.g., the x-y plane or unpolarized direction) and vary in the direction normal to that plane (e.g., the z-axis or polarized direction). In Equation A.3, E_p and ν_p are the Young's modulus and Poisson's ratio in the unpolarized x-y symmetry plane, respectively, E_z and ν_{zp} are the Young's modulus and Poisson's ratio in the polarized z-direction, respectively, and G_{zp} is the shear modulus in the z-direction. The elastic and piezoelectric constants for the PZT-8 material (Table A.1) were provided by the manufacturer APC International, Ltd.[188]

Table A.1 PZT-8 properties used in the ANSYS simulations.[188]

Property	**Value**
Youngs' modulus in the unpolarized direction, E_p	$9.00\times10^{10}\ N/m^2$
Youngs' modulus in the polarized direction, E_z	$8.64\times10^{10}\ N/m^2$
Shear modulus in the polarized direction, G_{zp}	$1.57\times10^{10}\ N/m^2$
Poisson's ratio (unpolarized/polarized), ν_p	0.333
Poisson's ratio (polarized/unpolarized), ν_{zp}	0.345
Piezoelectric constant relating voltage applied in the polarized direction to strain in the polarized direction, d_{33}	$215\times10^{-12}\ m/V$
Piezoelectric constant relating voltage applied in the polarized direction to strain in the unpolarized direction, d_{31}	$-95\times10^{-12}\ m/V$
Piezoelectric constant relating voltage applied in the unpolarized direction to generated shear stress, d_{15}	$330\times10^{-12}\ m/V$
Relative permittivity in the unpolarized direction, $\varepsilon_{r,p}$	1290
Relative permittivity in the polarized direction, $\varepsilon_{r,z}$	1000
Mass density, ρ	$7600\,kg/m^3$
Damping coefficient, γ	1×10^{-9}

A.1.2.2 Fluid Properties

The properties of water in Table A.2 are used in all acoustic response simulations. In MS applications, the AMUSE ion source ejected aqueous solutions containing a small amount of acetic or formic acid for charging. Any variations in fluid properties due to the acid is assumed to be minimal and ignored.

Table A.2 Fluid (water) properties used in the ANSYS simulations.

Property	**Value**
Mass density, ρ_{water}	$1000\,kg/m^3$
Speed of sound, c_{water}	$1500\,m/s$
Dynamic viscosity, μ_{water}	$1.00\times10^{-3}\,kg/ms$

A.1.2.3 Silicon and Spacer Properties

The remaining domains consist of either silicon (nozzle array and spacer) or silicone rubber (domain separating spacer), both treated as linear isotropic materials. For these materials, the stress-strain relationship is defined by Hooke's law, given by:

$$\in = S_E \cdot \sigma \tag{A.4}$$

For isotropic materials, the compliance matrix is defined by the bulk Young's modulus, E, and major Poisson's ratio, ν.

$$S = \frac{1}{E} = \begin{vmatrix} 1 & -\nu & -\nu & 0 & 0 & 0 \\ -\nu & 1 & -\nu & 0 & 0 & 0 \\ -\nu & -\nu & 1 & 0 & 0 & 0 \\ 0 & 0 & 0 & 1+\nu & 0 & 0 \\ 0 & 0 & 0 & 0 & 1+\nu & 0 \\ 0 & 0 & 0 & 0 & 0 & 1+\nu \end{vmatrix} \tag{A.5}$$

The relevant properties for silicon and silicone are given in Table A.3.

Table A.3 Silicon nozzle array, spacer, and silicone rubber insert properties used in the ANSYS simulations.

Material	**Property**	**Value**
Silicon	Young's Modulus, E_{Si}	$150\times10^{9}\ N/m^{2}$
	Poisson's ratio, ν_{Si}	0.21
	Mass density, ρ_{Si}	$2330\,kg/m^{3}$
	Damping coefficient, γ_{Si}	6×10^{-9}
Silicone	Young's Modulus, E_{insert}	$2.5\times10^{6}\ N/m^{2}$
	Poisson's ratio, ν_{insert}	0.45
	Mass density, ρ_{insert}	$1510\,kg/m^{3}$

APPENDIX B

ELECTROCHEMICAL ION GENERATION AND TRANSPORT IN AMUSE

B.1 Electrochemically Introduced Ion Transport

Ion transport to and from the charging piezoelectric transducer electrode in AMUSE is analyzed. The analysis focuses on the ion transport of electrochemically generated ions from anodic corrosion of a metal electrode. These results can be generalized to the case of solvent oxidation. With fundamental modes of ion transport processes being the same in both cases, results for ion ejection into a fluid represent the *removal* of ions in solution as well.

B.1.1 Time Scale Analysis of Associated Phenomena

In evaluation of the electrochemical ion generation and transport, a time scale analysis for associated transport modes is conducted first. The case being considered is for a purely aqueous solution in which the concentration of free charge carriers is low. A schematic of the arrangement considered, the electrode location and associated length and velocity scales, is shown in Figure B.1. The top electrode of the piezoelectric element is the place where the electrochemical reaction for production of ions occurs. The relevant length scales for this analysis are the length of the electrode and the height of the fluid reservoir. Order of magnitude approximations for the necessary length scales and other parameters used in the scaling analysis are given as:

$L \sim 1\times10^{-2}\,m$: Maximum horizontal distance fluid must travel to exit the device;

$\delta \sim 1\times10^{-3} m$: Maximum distance the analyte species must vertically diffuse to reach the electrode for electrochemical charging or the generated adduct ions must diffuse to reach analyte in the sample as it travels from the electrode to the droplet ejection point;

$u_o \sim 2\times10^{-3}\, m/min$: Mean longitudinal flow velocity in the sample reservoir for 100% duty cycle operation;

$D \sim 10^{-5}\, cm^2/s$: Typical diffusivity of an analyte in liquid solvent (order of magnitude value).

For the present analysis, migration effects are neglected (i.e., assuming negligibly small Debye layer and an excess of supporting electrolyte).

The two main cases considered are (1) the anodic corrosion (oxidation) of a metal electrode (M), e.g., $M \rightarrow M^+ + e^-$, producing the metal ions diffusing into the solution to form adducts with the analyte molecules, and (2) solute/solvent oxidation, e.g. $2H_2O \rightarrow 4H^+ + O_2 + 4e^-$, in which water or other solvents (methanol, buffer (salt), etc) are oxidized removing electrons through the electrode and leaving positive charges in the solution to form adducts with analyte molecules. The results for these two cases are qualitatively similar, which is expected due to the linearity of the governing equations

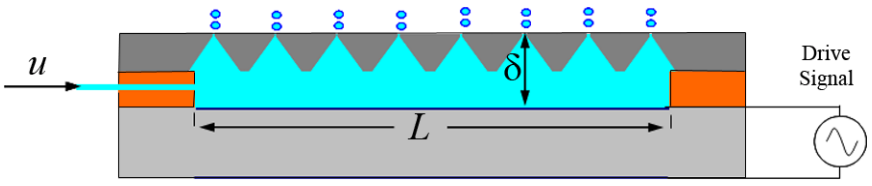

Figure B.1 AMUSE schematic showing relevant length scales and velocities used in the time scale analysis.

and boundary condition, and the analysis and discussion presented here apply equally to both cases.

The time scale analysis considers the advection, diffusion, and reaction processes. Efficient electrochemical analyte charging is expected if the following relationship holds for the associated time scales: $t_{rxn} \leq t_{diff} << t_{adv}$. For the example of solvent oxidation, if the time scales observed in AMUSE operation fall in this order then, 1) the ion precursor species (e.g., water for protons) are oxidized sufficiently fast as they reach the electrode surface, 2) the electrochemically generated ions have adequate time to reach all/most of the analyte molecules in the bulk solution by diffusion, and 3) the sample has a sufficiently long residence time for the former two processes to be completed. Under these conditions, increased sample ionization is expected by virtue of having an adequate number of generated adduct ions and sufficient time for those ions and analyte to associate in solution (leading to analyte charging) before droplets containing the analyte molecules are ejected from the device. Next, the relevant time scales for the operating conditions which are typically used in AMUSE-MS experiments are analyzed.

The electrode reaction time scale depends on the value of the applied potential with respect to the redox potential (ϕ_{redox}) for the given reaction and electrode material. Thermodynamically, for an applied potential greater than the redox potential, $\phi > \phi_{redox}$, oxidation of the cation-donor species (and cation generation) occurs and electrons, e^-, flow from the solution to electrode. On the other hand, if the applied potential is less than the redox potential, $\phi < \phi_{redox}$, species reduction (and anion generation) occurs and electrons, e^-, flow from the electrode into solution. The redox potential(s) for most redox couples is in the 100s mV range vs. SHE, so the potentials typically applied to the

AMUSE electrode (1-100V) is significantly greater than the redox potential. Thus, kinetic limitations are removed and the electrode reaction can be treated as infinitely fast $\left(t_{rxn} \to 0\right)$. For a more accurate estimate of the reaction time scale, exact mechanisms and relevant rate constants describing chemical kinetics of relevant redox reactions would be required. The analysis of "negative" mode operation involving the respective anion production by reduction of appropriate carrier species is fundamentally identical to the discussed case of "positive" mode ionization.

The remaining time scales are derived from the transient advection-diffusion equation for a representative species of interest [e.g., cations (Zn^{2+}, H^{+}), which are being generated or cation-precursor species, which are being oxidized as a result of electrochemical reaction on the electrode].

$$\frac{\partial C_i}{\partial t} = -\nabla \cdot \left(-D_i \nabla C_i + \vec{u} C_i - \frac{z_i F}{RT} D_i C_i \nabla \phi \right) \quad \to \quad \frac{\partial C_i}{\partial t} = D_i \nabla^2 C - \vec{u} \cdot \nabla C_i \qquad \text{(B.1)}$$

The left-hand side of Equation B.1 is the transient change in the concentration of species *i* (i.e., mass storage term) which is balanced by either/both diffusion or/and advection of species *i* (the first and the second terms, respectively, in the right hand side). As mentioned, migration effects have been neglected in this analysis in the limit of sufficiently strong buffer electrolyte. Expressing the governing transport equation (Eq. B.1) in dimensionless form with the appropriate characteristic scales, enables the analysis of balances between dominant transport mechanisms.

- *Diffusion Time Scale* $\left(t_{diff}\right)$

$$\frac{\partial C}{\partial t} \sim D\nabla^2 C \to \frac{C_o}{\tau}\left(\frac{\partial C}{\partial t}\right) \sim D\frac{C_o}{l_{char}}\left(\nabla^2 C\right) \to \frac{1}{t_{diff}} \sim D\frac{1}{\delta^2} \to \boxed{t_{diff} \sim \frac{\delta^2}{D}} \sim 1000\,\text{sec}$$

- *Advection Time Scale* $\left(t_{adv}\right)$

$$\frac{\partial C}{\partial t} \sim \vec{u} \cdot \nabla C \;\rightarrow\; \frac{C_o}{\tau}\left(\frac{\partial C}{\partial t}\right) \sim \frac{C_o u_o}{l_{char}}\left(\vec{u} \cdot \nabla C\right) \;\rightarrow\; \frac{1}{t_{adv}} \sim u\frac{1}{L} \;\rightarrow\; \boxed{t_{adv} \sim \frac{L}{u}} \sim 300\,\text{sec}$$

It is now apparent from this approximate examination that one of desired conditions, $t_{diff} < t_{adv}$, is not satisfied for the baseline AMUSE ion source operating with the piezoelectric transducer acting as a charging electrode and operated at 100% duty cycle. Therefore, the sample may be advected (transported) through the device too fast, resulting in insufficient residence time required for efficient diffusion of electrode-generated adduct-forming ions and charging of the analyte before it is being ejected out of the device. One solution to this problem would be to increase the sample residence time by reducing the duty cycle of the device. This would, however, reduce the device throughput. Alternatively, the electrode location (and therefore diffusion length scale) can be easily modified in the realized AMUSE ion source. An additional motivation for considering alternative placement of the charging electrode comes from the "disposable" AMUSE embodiment,[66] in which the piezoelectric transducer (electrode surface) is completely isolated from the sample. This configuration was discussed in Chapter 2.

One alternate location for the charging electrode is along the pyramidal walls of each individual nozzle in the array of the AMUSE nozzle plate. This can be realized by sputtering or evaporation of thin film metal electrodes onto the AMUSE nozzles. With the electrodes placed on the surface of converging nozzles, the characteristic length scale for diffusion is drastically reduced (from $\delta \sim 1\times10^{-3} m$ for the baseline AMUSE design down to $\delta_2 \sim 2\times10^{-6} m$ for the electrodes at the nozzle aperture). This length scale reduction results in significantly faster ion transport from the electrode to the analyte in

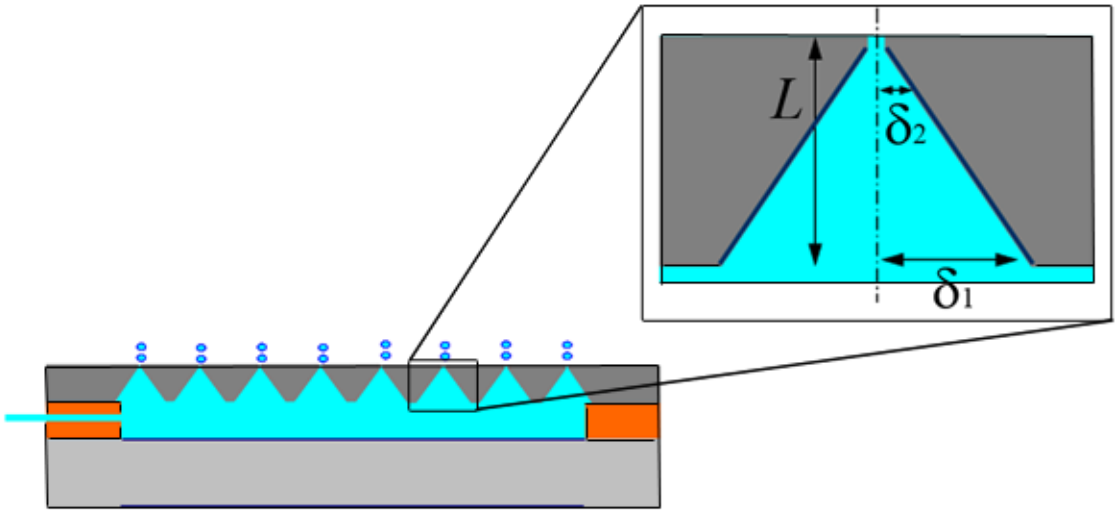

Figure B.2 Schematic representation of relevant length scales for electrode location at the pyramidal surfaces of each nozzle.

solution and therefore more efficient ionization. To quantify these advantages, the time scale analysis is repeated for a single AMUSE nozzle with integrated electrode as shown in Figure B.2. Estimates of relevant length scales and parameters are summarized below:

$L \sim 5\times10^{-4}\,m$: Maximum distance fluid must travel (be advected) past electrodes to exit nozzle as ejected droplets;

$\delta_1 \sim 3.5\times10^{-4}\,m$: Maximum distance the species must diffuse to reach the electrode or the generated ions must diffuse to reach analyte in the sample;

$\delta_2 \sim 2\times10^{-6}\,m$: Minimum distance the species must diffuse to reach the electrode or the generated ions must diffuse to reach analyte in the sample;

$D \sim 10^{-5}\,cm^2/s$: Typical diffusivity of an analyte in liquid solvent (order of magnitude value).

For the new length scales given above and the velocity scale obtained for a single nozzle in the array (based on the total volumetric flow rate and operating frequency), the following value of the time scales are obtained:

- *Diffusion Time Scale*, $t_{diff,\max} \sim \frac{\delta_1^2}{D} \sim 100\,\text{sec}$ $\qquad$ $t_{diff,\min} \sim \frac{\delta_2^2}{D} \sim 2\times10^{-3}\,\text{sec}$
- *Advection Time Scale*, $t_{adv} \sim \frac{L}{u} = \frac{L}{V_d f / A} = \frac{V_{nozzle}}{V_d f} \sim 1\,\text{sec}$
- *Reaction Time Scale*, $t_{rxn} \to 0$

Here, f is the AMUSE operating frequency. Comparing the relevant time scales indicates that, although at the base (large area) of the pyramidal nozzle the diffusion time is still longer than the advection time, as the sample approaches the nozzle orifice, diffusion becomes very fast and a sufficient number of adduct ions are able to reach and charge the analyte before it is ejected from the device. Thus, the time scale analysis clearly suggests that using the nozzle surface as an electrode should enable much more efficient charging/ionization of the analyte as compared to the baseline case, where the piezoelectric transducer is used for analyte charging in the case of electrochemical charging mode. To further investigate the conclusions reached from an approximate time scale analysis, detailed computational fluid dynamics (CFD) simulations are performed with representative results discussed next.

B.1.2 CFD Simulation of Ion Transport

An investigation into analyte charging by means of heterogeneous electrochemical reactions has been performed using time scale analysis and computational simulations. The commercial computational fluid dynamics (CFD)

package, Fluent[128], is used for model implementation. As introduced above, the two main cases considered are (1) the anodic corrosion of a metal electrode (M), e.g. $M \rightarrow M^+ + e^-$, and (2) solute/solvent oxidation, e.g. $2H_2O \rightarrow 4H^+ + O_2 + 4e^-$. Since the results for these two cases are qualitatively similar, only those for the case of anodic corrosion of a zinc electrode are reported as a representative example.

The two-dimensional simulations are performed for a domain consisting of the fluid reservoir and an array of 20 nozzles, with the fluid inlet on the left hand side and the piezoelectric transducer electrode along the bottom (Figure B.3). Since the ejection time scale, $t_{eject} \sim 1/f$, based on the frequency of operation (~1MHz), is much faster than the diffusion and advection time scales, a time-averaged, quasi-steady-state advection-diffusion equation can be used to describe the time-averaged concentration field of electrochemically generated ions.

$$\vec{u} \cdot \nabla C_i = D_i \nabla^2 C_i \qquad\qquad i = \left\{ Zn^{2+} \right\} \qquad\qquad \text{(B.2)}$$

No homogeneous reactions are considered in the analysis, limiting consideration to only the heterogeneous electrochemical reactions taking place at the electrode surface.

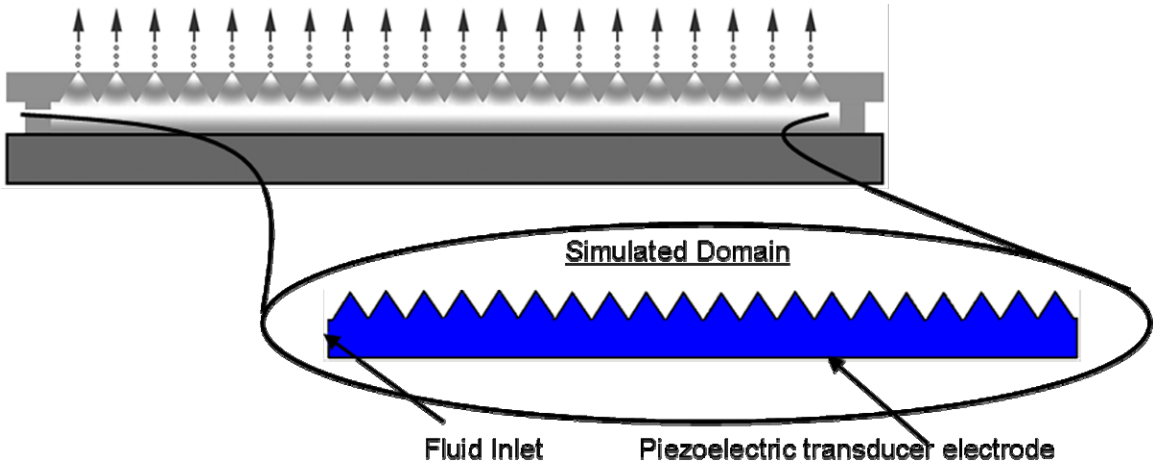

Figure B.3 Simulation domain for electrochemically generated ion transport model.

The bulk velocity, $\vec{u}$, is calculated from momentum conservation by solving the full set of incompressible Navier-Stokes equations of motion. The heterogeneous electrochemical reaction considered is the anodic corrosion of a zinc electrode; however, this could be generalized to represent corrosion of other electrode materials or solute/solvent oxidation of a cation-precursor species.

Equation (B.2) is numerically solved for concentration of zinc cations produced as a result of the electrochemical reduction reaction at the transducer electrode. The following boundary conditions are used to complete the model formulation.

All Solid Surfaces: $\nabla_n C_{Zn^{2+}} = 0$ and $\vec{u} = 0$

Nozzle Exits: $\nabla_n C_{Zn^{2+}} = 0$ and $p = p_{atm}$

where, $\nabla_n = \vec{n} \cdot \nabla = \partial / \partial n$, is a projection of the gradient operator on the outer normal to the boundary. The model considers ejection of droplets of radius equal to the nozzle aperture radius from each nozzle, corresponding to the ejection cycle, resulting in the following boundary conditions.

Inlet: $C_{Zn^{2+}} = 0$ and $\vec{u} = u_{in} = NV_d f A_{in}$

Here N is the total number of nozzles in the array, f is the frequency of the drive signal, V_d is the volume of a single ejected droplet, and A_{in} is the inlet cross sectional area. The concentration of zinc cations is set to zero at the inlet. The fluid velocity at the inlet is an input parameter, which is varied depending on the sample flow rate based on the operational duty cycle. Assuming infinitely fast kinetics of the electrochemical reaction results in instantaneous production of Zn^{2+} at the electrode surface, yielding the following (scaled) boundary condition for concentration.

Electrode Surface: $C_{Zn^{2+}} = 1$ and $\vec{u} = 0$

The concentration of Zn^{2+} throughout the domain is scaled by the equilibrium value at the electrode surface for a given electrode potential determined by the Nernst equation.[189] For a generic redox reaction, $R \leftrightarrow O + ze^-$, the Nernst equation relates the electrode potential to the equilibrium concentrations of the oxidized (O) and reduced (R) species at the electrode surface:

$$E = E^o + \left(\frac{RT}{zF}\right)\ln\left(\frac{C_O}{C_R}\right) \qquad \rightarrow \qquad C_O = C_R \exp\left(\frac{zF\left(E - E^o\right)}{RT}\right) \tag{B.3}$$

Here, E^o is the standard potential and depends on the reaction pair and electrode material, R is the universal gas constant, T is the absolute temperature, F is the Faraday constant (the charge on one mole of electrons), and z is the number of electrons transferred in the reaction. This equation can be used to find the concentration of zinc cations produced at the surface of the electrode under equilibrium conditions for a given electrode potential. It is this value that is used to scale the metal ion concentration throughout the simulation domain, resulting in a dimensionless value of 1 at the electrode surface and 0 at the fluid reservoir inlet.

B.1.2.1 Effect of Ejection Duty Cycle

First, a base case simulation is run for operation at 100% duty cycle considering the ion generating electrode as the piezoelectric transducer's top electrode in contact with the solution. From Figure B.3, the solution flows into the domain from the fluid inlet, on the left hand side of the reservoir, and out through the 20 nozzles. As clearly seen in Figure B.4(top) showing the zinc ion concentration within the fluid reservoir at 100% duty cycle, the incoming solution and analyte are ejected prior to coming into contact

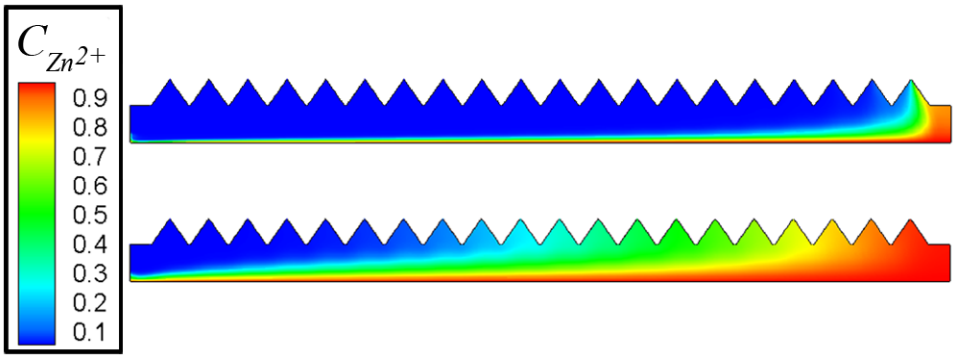

Figure B.4 Simulated results of Zn^{2+} concentration throughout fluid reservoir for 100% (top) and 1% (bottom) duty cycle operation.

with the cations produced at the electrode surface. This result was also predicted by the time scale analysis, showing the diffusion time to be much longer than the advection time. From a charging standpoint, very little of the bulk solution and analyte experience contact with the generated adduct ions before being ejected. Figure B.4(bottom) also shows the concentration contours for a 1% duty cycle. By decreasing the duty cycle, the advection and residence times are increased allowing for improved ionization of the analyte due to a greater penetration zone of electrochemically generated adduct ions.

Figure B.5 is another representation of the concentration of zinc cations at the exit of each individual nozzle. Again, it is apparent that for 100% duty cycle, the majority of nozzles are ejecting droplets without the presence of any zinc ions. Reducing the duty cycle does improve adduct ion penetration in the nozzles further downstream from the inlet, but still leaves insufficient time for ion diffusion in the upstream nozzles, resulting in inefficient ionization. An alternate electrode location, instead of reduced duty cycle, is considered next as a means to improving analyte charging via heterogeneously produced adduct ions.

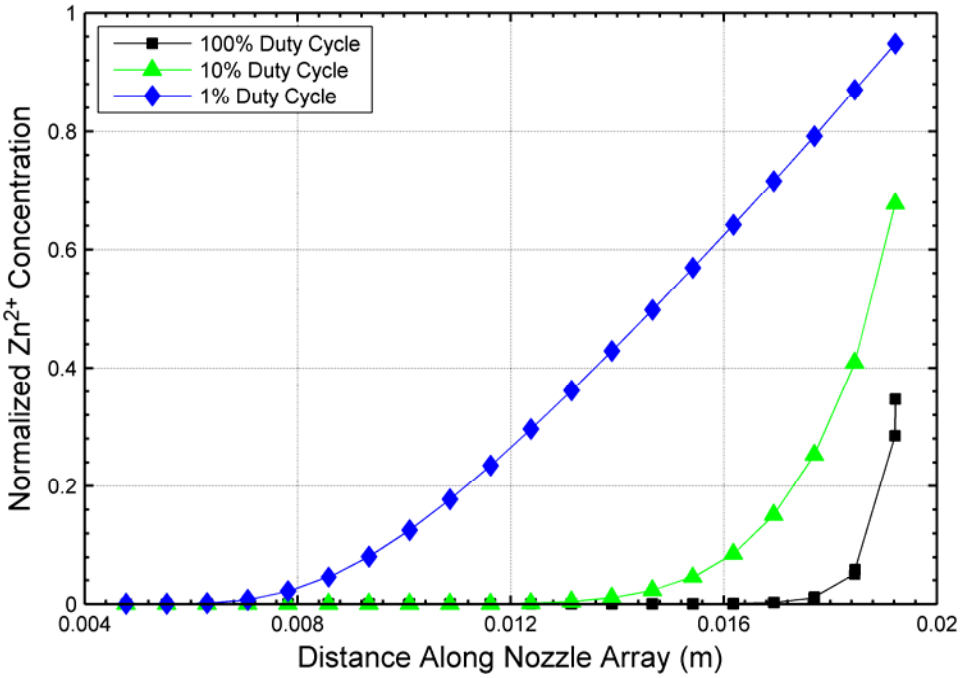

Figure B.5 Simulated results of Zn^{2+} concentration at each of the 20 nozzle orifices along the nozzle array for changing duty cycle.

B.1.2.2 Effect of Electrode Location

While reducing the duty cycle increases residence time and improves analyte charging, it decreases throughput and still fails to produce complete analyte charging. To circumnavigate this problem, instead of increasing the advection time, the diffusion time can also be decreased. By moving the electrode location from the surface of the piezoelectric element to the walls of each nozzle, the diffusion distance the ions must travel from the surface to the bulk is greatly reduced. This results in a much faster diffusion time scale, smaller than the residence time of the analyte. Figure B.6 compares the concentration contours for electrode locations for the AMUSE device operated at 50% duty cycle. Moving the electrode to the nozzle surface provides a dramatic increase in the concentration of cations ejected into a flowing solution, Figure B.7. This in turn

provides a greater opportunity for adduct formation with the analyte and improved charging and ionization.

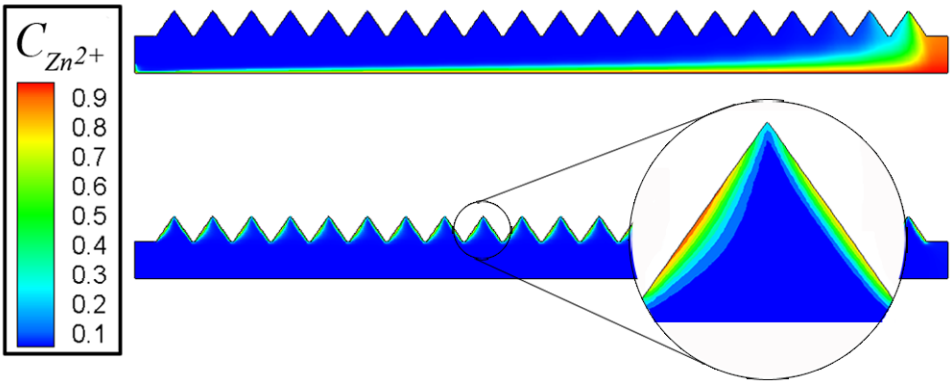

Figure B.6 Simulated results of Zn^{2+} concentration throughout the fluid reservoir for an electrode at the piezoelectric transducer top surface (top) and at the pyramidal nozzle surfaces (bottom). Both results are for 50% duty cycle operation.

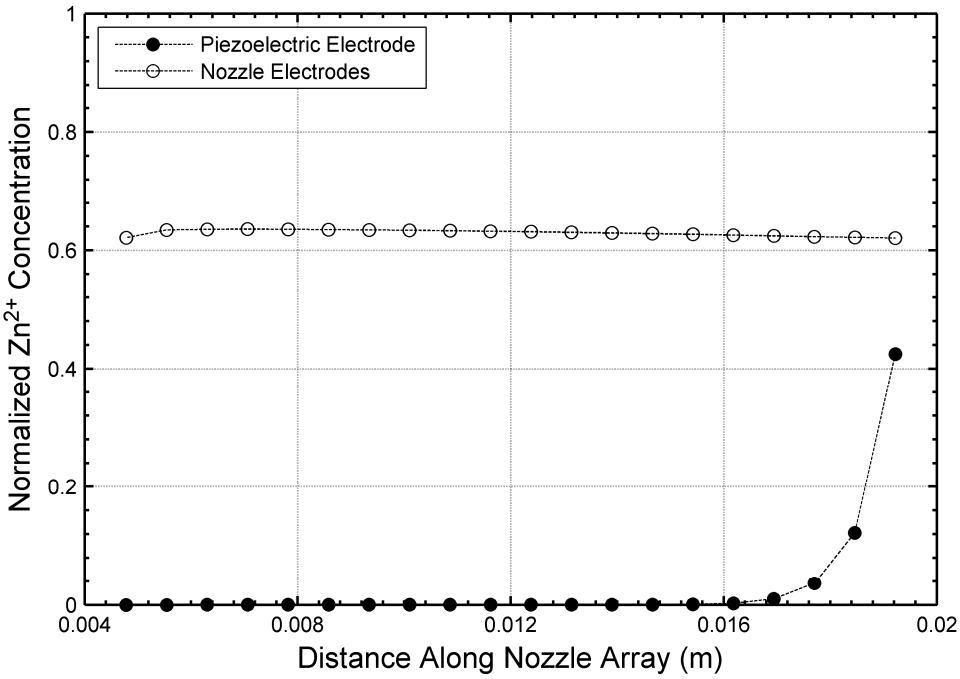

Figure B.7 Simulated results of Zn^{2+} concentration at each of the 20 nozzle orifices along the nozzle array for electrode locations at the piezoelectric element and the nozzle surface.

To compare variations in both parameters (duty cycle and electrode location), an ionization "efficiency" parameter is defined. Since the adduct formation is not modeled, a reasonable metric for ionization "efficiency" is the total concentration of ions generated and made available for analyte charging. Specifically, for the foregoing discussion, the ionization "efficiency" of zinc ion production is defined as the rate of zinc cations exiting the device (encompassed into ejected droplets) normalized by the total mass flow rate:

$$\varepsilon = \frac{\dot{m}_{Zn^{2+}}^{exit}}{\dot{m}_{total}} \tag{B.4}$$

This value is computed and compared for various duty cycles, as well as for both electrode locations. Figure B.8 plots the ionization "efficiency" as function of a single dimensionless parameter, the Peclet number, which expresses the effects of both the duty

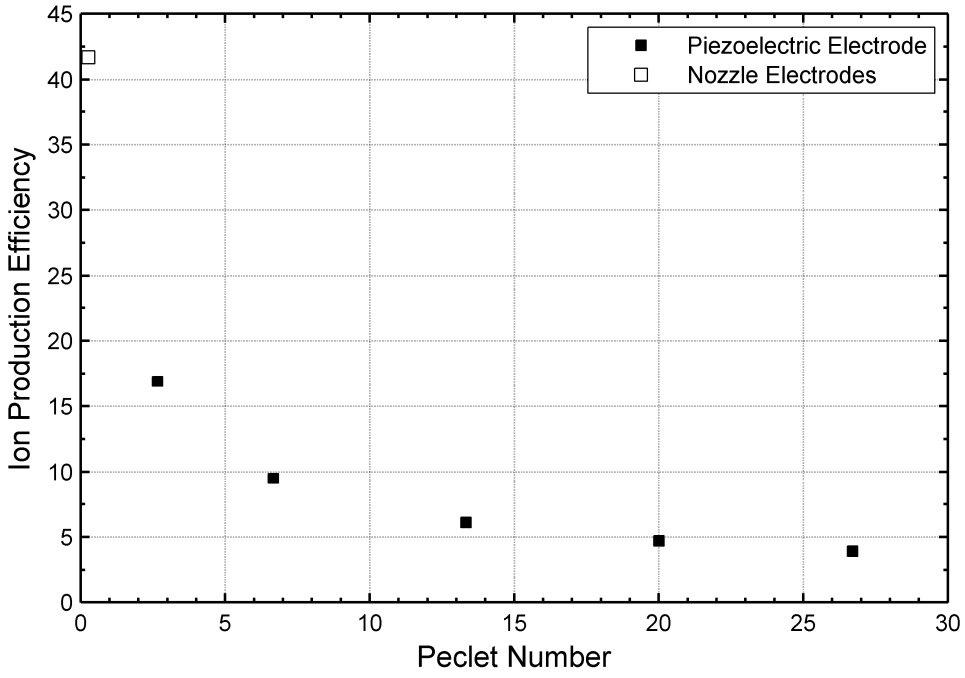

Figure B.8 Ionization "efficiency" for all simulated cases as a function of the Peclet number, Eq. B.5.

cycle reduction and charging electrode location in a generalized fashion. The Peclet number is defined as the ratio of relevant diffusion and advection time scales:

$$Pe = \frac{t_{diff}}{t_{adv}} = \frac{\delta^2 / D}{L/u} = \frac{u\delta^2}{DL} \tag{B.5}$$

Figure B.8 summarizes the results and shows that for all cases considered, i.e., with variable duty cycle and the charging electrode placed on the piezoelectric transducer, the Peclet number is always greater than unity ($Pe > 1$). From Equation B.5, these flow conditions are characterized by longer diffusion times relative to advection, $t_{diff} > t_{adv}$. As the duty cycle (and throughput) is decreased and the advection time approaches the diffusion time, the ionization "efficiency" increases steadily. The only exception is a case when the electrodes are placed on the nozzle surface (given by clear symbols in Figure B.8), which results in the advection time longer than the diffusion time yielding $Pe < 1$. This leads to a dramatic increase in the ionization "efficiency" without a sacrifice in the device throughput.

APPENDIX C

FLUENT CODE IMPLEMENTATION

An overview of the governing equations for the multiphase hydrodynamics problem, including the governing electrical equations of EHD and their inclusion into the FLUENT[128] CFD package, is covered in Chapter 3. As discussed in Chapter 3, the FLUENT framework for modeling hydrodynamics does not include the electric field and charge transport equations. Therefore, these additional equations and boundary conditions are incorporated through the FLUENT's built-in user-defined scalars (UDS) and user-define functions (UDF), coded in C/C++ language. These equations and boundary conditions are described in Chapter 3; here, a more detailed description of the exact implementation of these user-defined extensions is discussed.

C.1 Electrohydrodynamics Implementation

The electrohydrodynamics equations, formulated in Chapter 3, must be coded into FLUENT using the generic transient advection-diffusion transport equation (Equation 3.14). For the proper incorporation of the electrohydrodynamic equations and boundary conditions, a number of UDSs and user-defined memory (UDM) slots must be defined. Initially, UDSs for the electric potential, liquid volume fraction, positive charge density, negative charge density, and permittivity are used (Tables C.1 and C.2), as well as 23 UDM slots (Table C.3). The electric potential (Equation 3.3) and charge transport (Equation 3.5) equations must be cast in the form of the transport equation (Eq. 3.14) as described in Table C.2. The volume fraction and permittivity are only defined as UDSs for access to FLUENT's internally calculated gradients for use in other coded macros, i.e.

Table C.1 User-defined scalars (UDSs).

UDS_0	ϕ	Electric potential
UDS_1	α_2	Volume fraction of the liquid
UDS_2	q_+	Positive charge density
UDS_3	q_-	Negative charge density
UDS_4	$\varepsilon_r\varepsilon_o$	Permittivity

Table C.2 User-defined scalar (UDS) implementation.

	Transient	***Advective***	***Diffusive***	***Source***	***Domain***
$\theta_0 = \phi$	$\partial\theta_0/\partial t = 0$	$\vec{u}_0 = 0$	$\Gamma_{\theta_0} = \varepsilon_r\varepsilon_o$	$S_{\theta_0} = q_{net}$	Both
$\theta_1 = \alpha_2$	-	-	-	-	Both
$\theta_2 = q_+$	Default	$\vec{V}_2 = \vec{u} + \mu_{em}^+\vec{E}$	$\Gamma_{\theta_2} = 0$	$S_{\theta_2} = 0$	Liquid only
$\theta_3 = q_-$	Default	$\vec{V}_3 = \vec{u} + \mu_{em}^-\vec{E}$	$\Gamma_{\theta_3} = 0$	$S_{\theta_3} = 0$	Liquid only
$\theta_4 = \varepsilon_r\varepsilon_o$	-	-	-	-	Both

normal Maxwell stress, Equation 3.22 (gradient of volume fraction) and dielectric force, Equation 3.10 (gradient of permittivity).

The following user-defined functions are necessary for the implementation of electrohydrodynamics. The user-defined code contains the following FLUENT macros:

1. An initialization macro that initializes the fluid domain and charge density levels. The nozzle is initially filled with water of a given charge density; therefore, volume fraction of 1 and positive and negative bulk charge densities of q_o are "patched" on the cells in the nozzle.
2. A boundary profile macro, used to define the sinusoidal pressure distribution along the curved inlet boundary, representing the periodic acoustic waves produced by the piezoelectric transducer operated ~1MHz.
3. Two boundary profile macros defining different electric field configurations. Specifically, for simulations in which a periodic (AC) electric field is applied, the

potential along the curved inlet boundary is defined as a sinusoidal potential with a specified phase shift relative to the sinusoidal pressure signal. Also, for simulations investigating pulsed electric fields, the macro defines the magnitude, starting point, and pulse width of the potential pulse.

4. A diffusivity defining macro that sets the diffusivity coefficient (permittivity) for the Poisson equation (Eq. 3.3). The fluid permittivity is defined as a volume-fraction-weighted average of the two fluids for cells between phases $\left(0 < \alpha_i < 1\right)$.
5. Two adjust macros that store (1) the electric potential and volume fraction gradients into user-defined memory (UDM) slots for access by other macros, e.g. $\vec{E} = -\nabla\phi$ and (2) the volume fraction and gradients into a user-defined scalar for use in other macros. Additional fluid properties, such as ion mobility, density, permittivity, and other useful parameters are stored in UDMs for further use in macros. A list of the UDMs used can be seen in Table C.3.
6. Two source term macros that define the x- and r-components of the Coulombic and dielectric forces in the momentum equation (Eq. 3.10).
7. A source term macro that defines the source term in the Poisson equation (Eq. 3.3).
8. Two advective-flux macros that define the flux term in the UDS transport equation (Eq. 3.14). Here, the velocity, $\vec{u}$, from Equation 3.14 is redefined as $\vec{V} = \vec{u} + \mu_{em}\vec{E}$, which incorporates the fluid velocity and charge migration.
9. Two executable macros that (1) maintain electroneutrality when a droplet is ejected, by electrochemically "reducing" excess charge in the fluid bulk (nozzle) and (2) measure the total net charge on ejected droplets.

Table C.3 User-defined memory (UDM) variables.

UDM_0	$\partial\phi/\partial x$	x-component of potential gradient
UDM_1	$\partial\phi/\partial r$	r-component of potential gradient
UDM_2	$\lvert\nabla\phi\rvert$	Potential gradient magnitude
UDM_3	$\partial\alpha/\partial x$	x-component of volume fraction gradient
UDM_4	$\partial\alpha/\partial r$	r-component of volume fraction gradient
UDM_5	$\lvert\nabla\alpha\rvert$	Volume fraction gradient magnitude
UDM_6	$F_{diel,x}$	x-component of the dielectric force
UDM_7	$F_{Coul,x}$	x-component of the Coulombic force
UDM_8	F_x	Total electric force x-component
UDM_9	$F_{diel,r}$	r-component of the dielectric force
UDM_10	$F_{Coul,r}$	r-component of the Coulombic force
UDM_11	F_r	Total electric force r-component
UDM_12	$\varepsilon_r\varepsilon_o$	Permittivity
UDM_13	μ_{em}	Ion electric mobility
UDM_14	ρ	Density
UDM_15	q_{net}	Net charge density
UDM_16	$q_+\rho\vec{u}$	Positive charge flux at inlet
UDM_17	$q_-\rho\vec{u}$	Negative charge flux at inlet
UDM_18	$\rho\vec{u}$	Advective flux component
UDM_19	$\rho\mu_{em}^{+}\vec{E}$	Positive charge migration flux component
UDM_20	$-\rho\mu_{em}^{-}\vec{E}$	Negative charge migration flux component
UDM_21	$\rho\vec{V}^{+}=\rho\left(\vec{u}+\mu_{em}^{+}\vec{E}\right)$	Total positive charge flux
UDM_22	$\rho\vec{V}^{-}=\rho\left(\vec{u}-\mu_{em}^{-}\vec{E}\right)$	Total negative charge flux

FLUENT solves the governing equations (Equations 3.1-3.3, 3.5) sequentially using a two-dimensional, double-precision, pressure-based segregated solver. For each time-step, FLUENT first executes the user-defined profiles and initialization outside the solution iteration loop. Upon entering the iteration loop, FLUENT completes the following steps until convergence is achieved:

1. Compute the user-defined adjust functions, updating values for fluid properties, electric potential gradients, volume fractions, etc.
2. Current values of the electric potential distribution are used to calculate the Coulombic and dielectric forces. These forces and the current pressure are input into the momentum equations to solve for the velocity field.
3. After solving the updated momentum equations, the velocity field may not satisfy continuity. Therefore, FLUENT utilizes the Pressure-Implicit with Splitting of Operators (PISO) pressure-velocity coupling scheme, based on the SIMPLE family of algorithms (described in Chapter 3) to obtain corrections for the pressure and velocity fields and face mass fluxes.
4. The volume-of-fluid formulation is then used to update the location of the interface between the liquid and gas.
5. The Poisson equation is solved to update the potential distribution using the current positive and negative charge density distributions.
6. The positive and negative charge transport equations are solved to update the charge density distributions using the current flow field and potential distribution.
7. The fluid properties are updated and convergence is checked. If convergence is not achieved, the loop repeats again; if convergence is achieved, the whole process sequence moves to the next time-step and the iterations begin again.

For the proper convergence of all governing equations a time step of 1×10^{-9} s is used and the under-relaxation factors are all set to 1, except for momentum, which is set to 0.7, and the positive and negative charge transport equations, which are set to 0.2. These under-relaxation factors allow convergence of each time-step in approximately 50

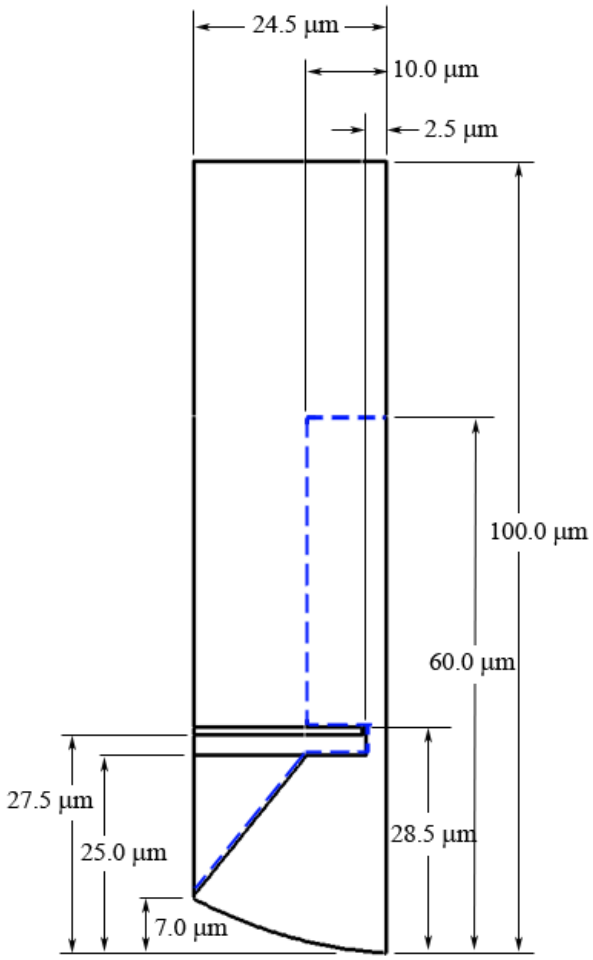

Figure C.1 Two-dimensional (2D), axisymmetric simulation domains of droplet ejection in the presence of an electric field for the "full" domain for DC electric field analysis (solid black lines) and the "truncated" domain for AC electric field analysis (dashed blue lines).

iterations. The following criteria are used as indicators of convergence: (1) a decrease in the residuals of approximately four orders of magnitude and/or (2) less than a 2% difference in residuals between successive iterations.

C.1.1 Simulation Domain

The simulation domain shown in Figure C.1 is described in detail in Chapter 3. A schematic of the axisymmetric domain and its dimensions are provided here.

APPENDIX D

ADDITIONAL MASS SPECTRA FROM AMUSE

D.1 AMUSE-Air Amplifier-FT-ICR

Mass spectra of the peptide/proteins bradykinin (4 μM), and BNP-32 (2.8 μM) were obtained using an FT-ICR mass spectrometer. Analytes were added in micromolar concentrations to an aqueous solvent containing 0.1% (v/v) formic acid (pH 2.66). Analyte ionization for these mass spectra was enhanced by applying a small (~100-250 V_{DC}) potential to the inner piezoelectric transducer electrode.

Figure D.1 displays the mass spectrum for a 4 μM sample of bradykinin (1060.2 Da). Bradykinin is peptide in the kinin group of proteins, consisting of 9 amino acids. Unlike angiotensin I, bradykinin is a physiologically active peptide.[190]

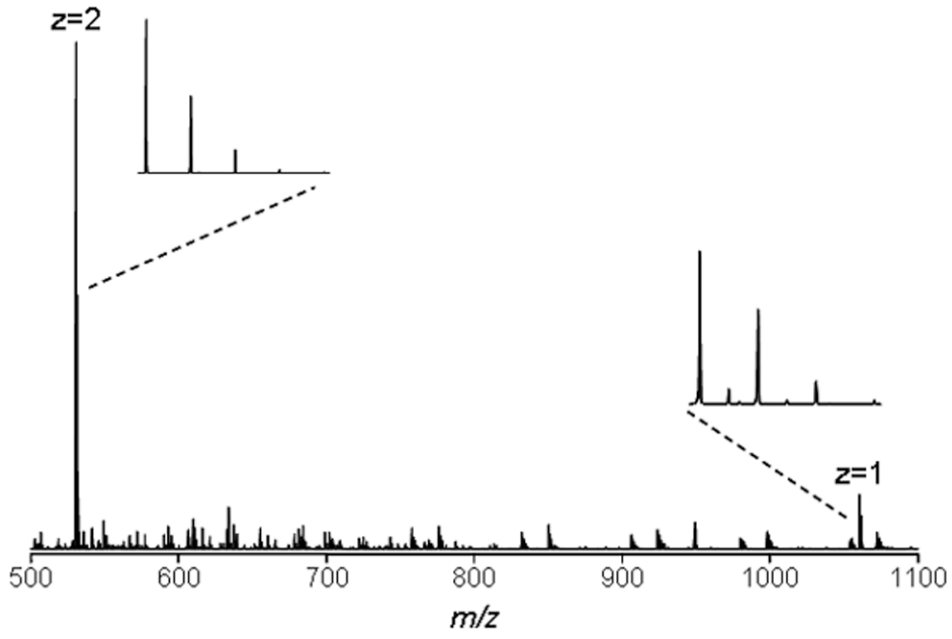

Figure D.1 Mass spectrum from a FT-ICR mass analyzer for 4 μM bradykinin in 99.9:0.1 (vol/vol) water/formic acid ionized by AMUSE.

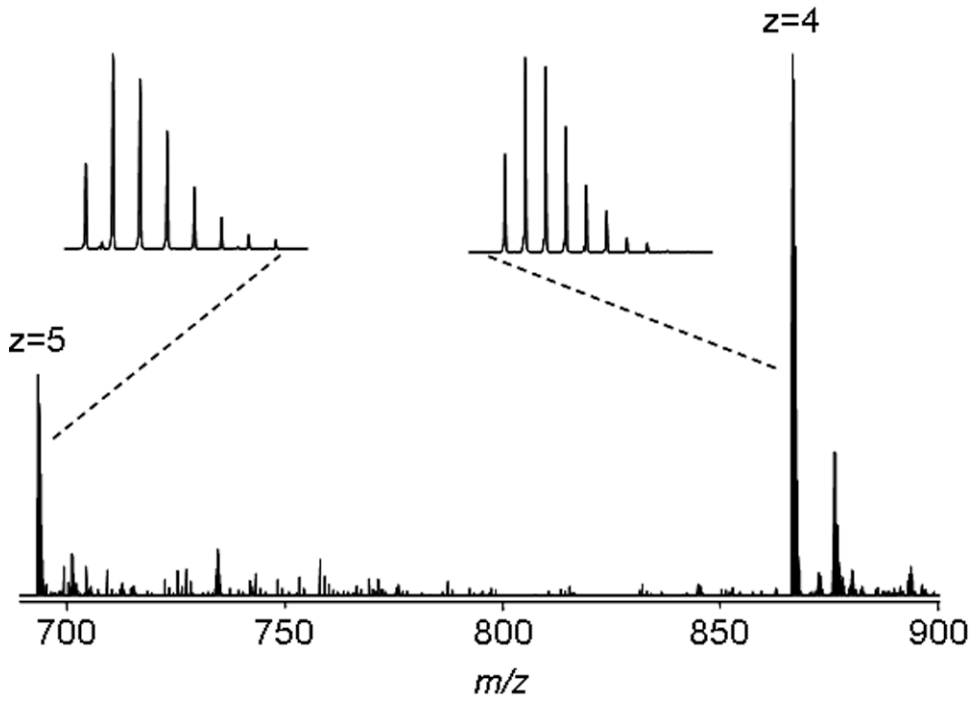

Figure D.2 Mass spectrum from a FT-ICR mass analyzer for 2.8 μM BNP-32 in 99.9:0.1 (vol/vol) water/formic acid ionized by AMUSE.

Figure D.2 displays the mass spectrum for 2.8 μM sample of BNP-32 (3464.1 Da). Brain natriuretic peptide, or BNP, is a 32 amino acid peptide containing the 17 amino acid ring structure found in all natriuretic peptides.[191] Although named brain natriuretic peptide, the main source of BNP is found in the cardiac ventricle, not in the brain. BNP is important to cardiovascular processes corresponding to volume expansion and pressure overload.[192]

D.2 AMUSE-Air Amplifier-MicrOTOF

A similar coupled configuration of the AMUSE ion source with a transport and desolvation assisting air amplifier is used with a micrOTOF mass spectrometer. Angiotensin III and reserpine were measured and analyzed in this configuration.

Figure D.3 displays the mass spectrum of 50 μM sample of angiotensin III (931.1 Da) in an aqueous solvent containing 400 μM of cupric chloride ($CuCl_2$). Angiotensin III is a peptide derivative of angiotensin II. Angiotensin III adducts are formed with both hydrogen and copper cations. Figure D.3 shows the doubly charged molecules to be much more abundant than the singly charged molecules (a single copper cation provides a +2 charge state). Reserpine contamination is also present from previous studies (m/z 609.3).

Figure C.4 displays the mass spectrum of a 3 μM sample of reserpine (608.68 Da) added to an aqueous solvent containing 0.1% (v/v) acetic acid (pH 3.25). Reserpine is a common tuning compound and is used in Chapter 5 for the investigation of MS response as function of charge separating electric field. Reserpine is a small antihypertensive and antipsychotic pharmaceutical molecule for treating high blood pressure and mental disorders displaying severe agitation.

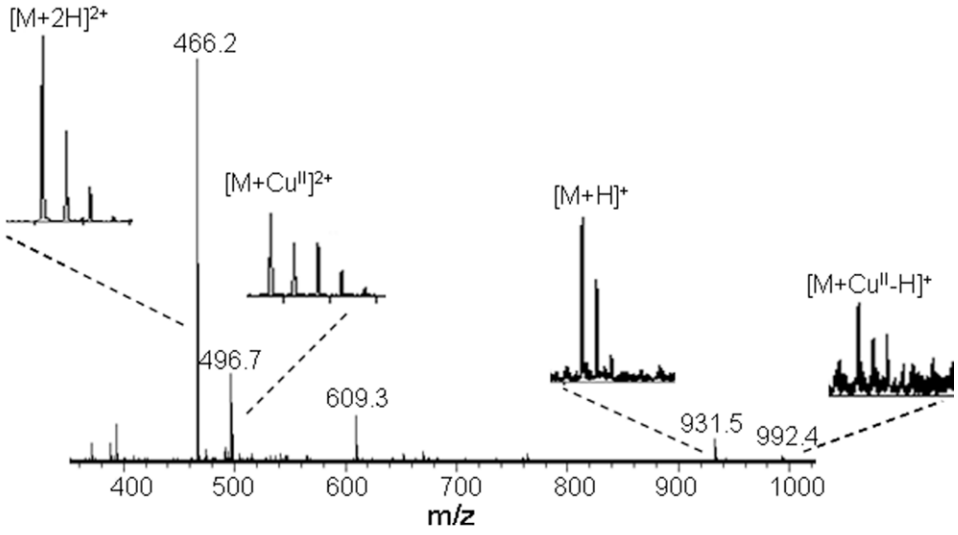

Figure D.3 Mass spectrum from a micrOTOF mass analyzer for 50 μM angiotensin III and 400 μM cupric chloride ($CuCl_2$) water ionized by AMUSE with a 1000 V_{DC} applied to the piezoelectric transducer electrode and the external wire electrode grounded.

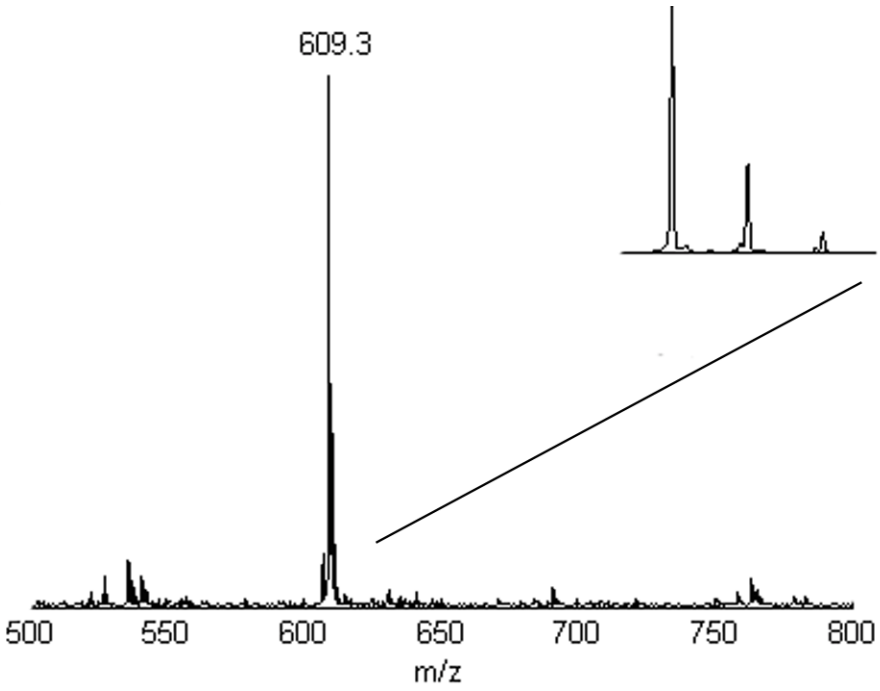

Figure D.4 Mass spectrum from a micrOTOF mass analyzer for 3 μM reserpine in 99.9:0.1 (vol/vol) water/acetic acid ionized by AMUSE.

REFERENCES

[1] Watson, J.T.,Sparkman, O.D., *Introduction to Mass Spectrometry: Instrumentation, Applications and Strategies for Data Interpretation*, 4th ed. (Wiley, West Sussex, England, 2007).

[2] Aebersold, R.,Goodlett, D.R., "Mass Spectrometry in Proteomics," Chemical Reviews. **101** (2), pp. 269-296 (2001).

[3] Aebersold, R.,Mann, M., "Mass spectrometry-based proteomics," Nature. **422** (6928), pp. 198-207 (2003).

[4] Proceedings of the HUPO 2005 Conference, "Washington, D.C.," pp. (February 2005).

[5] Whitehouse, C.M.,Dreyer, R.N.,Yamashita, M.,Fenn, J.B., "Electrospray interface for liquid chromatographs and mass spectrometers," Analytical Chemistry. **57** (3), pp. 675-679 (1985).

[6] Karas, M.,Hillenkamp, F., "Laser desorption ionization of proteins with molecular masses exceeding 10,000 daltons," Analytical Chemistry. **60** (20), pp. 2299-2301 (2002).

[7] Dole, M.,Mack, L.L.,Hines, R.L.,Mobley, R.C.,Ferguson, L.D.,Alice, M.B., "Molecular Beams of Macroions," The Journal of Chemical Physics. **49** (5), pp. 2240-2249 (1968).

[8] Fenn, J.B.,Mann, M.,Meng, C.K.,Wong, S.F.,Whitehouse, C.M., "Electrospray Ionization for Mass Spectrometry of Large Biomolecules," Science. **246** (4926), pp. 64-71 (1989).

[9] Yamashita, M.,Fenn, J.B., "Electrospray ion source. Another variation on the free-jet theme," Journal of Physical Chemistry. **88** (20), pp. 4451-4459 (1984).

[10] Cech, N.B.,Enke, C.G., "Practical implications of some recent studies in electrospray ionization fundamentals," Mass Spectrometry Reviews. **20** (6), pp. 362-387 (2001).

[11] Gabelica, V.,Pauw, E.D., "Internal energy and fragmentation of ions produced in electrospray sources," Mass Spectrometry Reviews. **24** (4), pp. 566-587 (2005).

[12] Gaskell, S.J., "Electrospray: Principles and Practice," Journal of Mass Spectrometry. **32** (7), pp. 677-688 (1997).

[13] Iribarne, J.V.,Thomson, B.A., "On the evaporation of small ions from charged droplets," The Journal of Chemical Physics. **64** (6), pp. 2287-2294 (1976).

[14] Tomer, K.B., "Separations Combined with Mass Spectrometry," Chemical Reviews. **101** (2), pp. 297-328 (2001).

[15] Bakhoum, S.F.W.,Agnes, G.R., "Study of Chemistry in Droplets with Net Charge before and after Coulomb Explosion: Ion-Induced Nucleation in Solution and Implications for Ion Production in an Electrospray," Analytical Chemistry. **77** (10), pp. 3189-3197 (2005).

[16] Blades, A.T.,Ikonomou, M.G.,Kebarle, P., "Mechanism of electrospray mass spectrometry. Electrospray as an electrolysis cell," Analytical Chemistry. **63** (19), pp. 2109-2114 (1991).

[17] Fernandez de la Mora, J.,Van Berkel, G.J.,Enke, C.G.,Cole, R.B.,Martinez-Sanchez, M.,Fenn, J.B., "Electrochemical processes in electrospray ionization mass spectrometry," Journal of Mass Spectrometry. **35** (8), pp. 939-952 (2000).

[18] Van Berkel, G.J.,Zhou, F., "Characterization of an Electrospray Ion Source as a Controlled-Current Electrolytic Cell," Analytical Chemistry. **67** (17), pp. 2916-2923 (1995).

[19] Marginean, I.,Parvin, L.,Heffernan, L.,Vertes, A., "Flexing the Electrified Meniscus: The Birth of a Jet in Electrosprays," Analytical Chemistry. **76** (14), pp. 4202-4207 (2004).

[20] Rayleigh, L.J.W.S., "On the equilibrium of liquid conducting masses charged with electricity," Philosophical Magazine. **14**, pp. 184-186 (1882).

[21] Kebarle, P.,Tang, L., "From ions in solution to ions in the gas phase - the mechanism of electrospray mass spectrometry," Analytical Chemistry. **65** (22), pp. 972A-986A (1993).

[22] Cole, R.B., "Some tenets pertaining to electrospray ionization mass spectrometry," Journal of Mass Spectrometry. **35** (7), pp. 763-772 (2000).

[23] Beaudry, F.,Vachon, P., "Electrospray ionization suppression, a physical or a chemical phenomenon?," Biomedical Chromatography. **20** (2), pp. 200-205 (2006).

[24] Cappiello, A.,Famiglini, G.,Palma, P.,Pierini, E.,Termopoli, V.,Trufelli, H., "Overcoming Matrix Effects in Liquid Chromatographyâˆ’Mass Spectrometry," Analytical Chemistry. **80** (23), pp. 9343-9348 (2008).

[25] Chowdhury, S.K.,Chait, B.T., "Method for the electrospray ionization of highly conductive aqueous solutions," Analytical Chemistry. **63** (15), pp. 1660-1664 (1991).

[26] Chowdhury, S.K.,Katta, V.,Chait, B.T., "Probing conformational changes in proteins by mass spectrometry," Journal of the American Chemical Society. **112** (24), pp. 9012-9013 (1990).

[27] Bruins, A.P.,Covey, T.R.,Henion, J.D., "Ion spray interface for combined liquid chromatography/atmospheric pressure ionization mass spectrometry," Analytical Chemistry. **59** (22), pp. 2642-2646 (1987).

[28] Henion, J.D.,Covey, T.R.,Bruins, A.P., "Ion spray apparatus and method," U.S. Patent # 4,861,988 (1989).

[29] Banks, J.F.,Quinn, J.P.,Whitehouse, C.M., "LC/ESI-MS Determination of Proteins Using Conventional Liquid Chromatography and Ultrasonically Assisted Electrospray," Analytical Chemistry. **66** (21), pp. 3688-3695 (1994).

[30] Banks, J.F.,Shen, S.,Whitehouse, C.M.,Fenn, J.B., "Ultrasonically assisted electrospray ionization for LC/MS determination of nucleosides from a transfer RNA digest," Analytical Chemistry. **66** (3), pp. 406-414 (1994).

[31] Berggren, W.T.,Westphall, M.S.,Smith, L.M., "Single-Pulse Nanoelectrospray Ionization," Analytical Chemistry. **74** (14), pp. 3443-3448 (2002).

[32] Shiea, J.,Chang, D.Y.,Lin, C.H.,Jiang, S.J., "Generating Multiply Charged Protein Ions by Ultrasonic Nebulization/Multiple Channel-Electrospray Ionization Mass Spectrometry," Analytical Chemistry. **73** (20), pp. 4983-4987 (2001).

[33] Emmett, M.R.,Caprioli, R.M., "Micro-electrospray mass spectrometry: ultra-high-sensitivity analysis of peptides and proteins," Journal of the American Society for Mass Spectrometry. **5** (7), pp. 605-613 (1994).

[34] Wilm, M.,Mann, M., "Analytical Properties of the Nanoelectrospray Ion Source," Analytical Chemistry. **68** (1), pp. 1-8 (1996).

[35] Wilm, M.S.,Mann, M., "Electrospray and Taylor-Cone theory, Dole's beam of macromolecules at last?," International Journal of Mass Spectrometry and Ion Processes. **136** (2-3), pp. 167-180 (1994).

[36] Valaskovic, G.A.,McLafferty, F.W., "Long-Lived Metallized Tips for Nanoliter Electrospray Mass Spectrometry," Journal of the American Society for Mass Spectrometry. **7** (12), pp. 1270-1272 (1996).

[37] Fang, L.,Demee, M.,Cournoyer, J.,Sierra, T.,Young, C.,Yan, B., "Parallel high-throughput accurate mass measurement using a nine-channel multiplexed electrospray liquid chromatography ultraviolet time-of-flight mass spectrometry system," Rapid Communications in Mass Spectrometry. **17** (13), pp. 1425-1432 (2003).

[38] Rulison, A.J.,Flagan, R.C., "Scale-up of electrospray atomization using linear arrays of Taylor cones," Review of Scientific Instruments. **64** (3), pp. 683-686 (1993).

[39] Schneider, B.B.,Douglas, D.J.,Chen, D.D.Y., "Multiple sprayer system for high-throughput electrospray ionization mass spectrometry," Rapid Communications in Mass Spectrometry. **16** (20), pp. 1982-1990 (2002).

[40] Lazar, I.M.,Grym, J.,Foret, F., "Microfabricated devices: A new sample introduction approach to mass spectrometry," Mass Spectrometry Reviews. **25** (4), pp. 573-594 (2006).

[41] Limbach, P.A.,Meng, Z., "Integrating micromachined devices with modern mass spectrometry," The Analyst. **127** (6), pp. 693-700 (2002).

[42] Bings, N.H.,Wang, C.,Skinner, C.D.,Colyer, C.L.,Thibault, P.,Harrison, D.J., "Microfluidic Devices Connected to Fused-Silica Capillaries with Minimal Dead Volume," Analytical Chemistry. **71** (15), pp. 3292-3296 (1999).

[43] Ivanov, A.R.,Zang, L.,Karger, B.L., "Low-Attomole Electrospray Ionization MS and MS/MS Analysis of Protein Tryptic Digests Using 20um-i.d. Polystyrene-Divinylbenzene Monolithic Capillary Columns," Analytical Chemistry. **75** (20), pp. 5306-5316 (2003).

[44] Lazar, I.M.,Ramsey, R.S.,Ramsey, J.M., "On-Chip Proteolytic Digestion and Analysis Using "Wrong-Way-Round" Electrospray Time-of-Flight Mass Spectrometry," Analytical Chemistry. **73** (8), pp. 1733-1739 (2001).

[45] Li, J.,Kelly, J.F.,Chernushevich, I.,Harrison, D.J.,Thibault, P., "Separation and Identification of Peptides from Gel-Isolated Membrane Proteins Using a Microfabricated Device for Combined Capillary Electrophoresis/Nanoelectrospray Mass Spectrometry," Analytical Chemistry. **72** (3), pp. 599-609 (2000).

[46] Li, J.,Thibault, P.,Bings, N.H.,Skinner, C.D.,Wang, C.,Colyer, C.,Harrison, J., "Integration of Microfabricated Devices to Capillary Electrophoresis-Electrospray Mass Spectrometry Using a Low Dead Volume Connection: Application to Rapid Analyses of Proteolytic Digests," Analytical Chemistry. **71** (15), pp. 3036-3045 (1999).

[47] Meng, Z.,Qi, S.,Soper, S.A.,Limbach, P.A., "Interfacing a Polymer-Based Micromachined Device to a Nanoelectrospray Ionization Fourier Transform Ion Cyclotron Resonance Mass Spectrometer," Analytical Chemistry. **73** (6), pp. 1286-1291 (2001).

[48] Zhang, B.,Foret, F.,Karger, B.L., "High-Throughput Microfabricated CE/ESI-MS: Automated Sampling from a Microwell Plate," Analytical Chemistry. **73** (11), pp. 2675-2681 (2001).

[49] Zhang, B.,Liu, H.,Karger, B.L.,Foret, F., "Microfabricated Devices for Capillary Electrophoresis-Electrospray Mass Spectrometry," Analytical Chemistry. **71** (15), pp. 3258-3264 (1999).

[50] Bedair, M.F.,Oleschuk, R.D., "Fabrication of Porous Polymer Monoliths in Polymeric Microfluidic Chips as an Electrospray Emitter for Direct Coupling to Mass Spectrometry," Analytical Chemistry. **78** (4), pp. 1130-1138 (2006).

[51] Dayon, L.,Abonnenc, M.,Prudent, M.,Lion, N.,Girault, H.H., "Multitrack electrospray chips," Journal of Mass Spectrometry. **41** (11), pp. 1484-1490 (2006).

[52] Kim, W.,Guo, M.,Yang, P.,Wang, D., "Microfabricated monolithic multinozzle emitters for nanoelectrospray mass spectrometry," Analytical Chemistry. **79** (10), pp. 3703-3707 (2007).

[53] Le Gac, S.,Arscott, S.,Cren-Olivé, C.,Rolando, C., "Two-dimensional microfabricated sources for nanoelectrospray," Journal of Mass Spectrometry. **38** (12), pp. 1259-1264 (2003).

[54] Le Gac, S.,Rolando, C.,Arscott, S., "An Open Design Microfabricated Nib-Like Nanoelectrospray Emitter Tip on a Conducting Silicon Substrate for the Application of the Ionization Voltage," Journal of the American Society for Mass Spectrometry. **17** (1), pp. 75-80 (2006).

[55] Ramsey, R.S.,Ramsey, J.M., "Generating Electrospray from Microchip Devices Using Electroosmotic Pumping," Analytical Chemistry. **69** (6), pp. 1174-1178 (1997).

[56] Xue, Q.,Foret, F.,Dunayevskiy, Y.M.,Zavracky, P.M.,McGruer, N.E.,Karger, B.L., "Multichannel Microchip Electrospray Mass Spectrometry," Analytical Chemistry. **69** (3), pp. 426-430 (1997).

[57] Yang, Y.,Kameoka, J.,Wachs, T.,Henion, J.D.,Craighead, H.G., "Quantitative Mass Spectrometric Determination of Methylphenidate Concentration in Urine Using an Electrospray Ionization Source Integrated with a Polymer Microchip," Analytical Chemistry. **76** (9), pp. 2568-2574 (2004).

[58] Corkery, L.J.,Pang, H.,Schneider, B.B.,Covey, T.R.,Siu, K.W.M., "Automated nanospray using chip-based emitters for the quantitative analysis of pharmaceutical compounds," Journal of the American Society for Mass Spectrometry. **16** (3), pp. 363-369 (2005).

[59] Corso, T.N.,Van Pelt, C.K.,Zhang, S.,Prosser, S.J.,Schultz, G.A. *Integrated microchip-based nanoelectrospray device for high-throughput mass spectrometry*. in *Biomedical Instrumentation Based on Micro- and Nanotechnology*. San Jose, CA, USA: SPIE. **4265**, pp. 81-90 (2001).

[60] Licklider, L.,Wang, X.Q.,Desai, A.,Tai, Y.C.,Lee, T.D., "A Micromachined Chip-Based Electrospray Source for Mass Spectrometry," Analytical Chemistry. **72** (2), pp. 367-375 (2000).

[61] Schultz, G.A.,Corso, T.N.,Prosser, S.J.,Zhang, S., "A Fully Integrated Monolithic Microchip Electrospray Device for Mass Spectrometry," Analytical Chemistry. **72** (17), pp. 4058-4063 (2000).

[62] Sjödahl, J.,Melin, J.,Griss, P.,Emmer, Å.,Stemme, G.,Roeraade, J., "Characterization of micromachined hollow tips for two-dimensional nanoelectrospray mass spectrometry," Rapid Communications in Mass Spectrometry. **17** (4), pp. 337-341 (2003).

[63] Tang, K.,Lin, Y.,Matson, D.W.,Kim, T.,Smith, R.D., "Generation of Multiple Electrosprays Using Microfabricated Emitter Arrays for Improved Mass Spectrometric Sensitivity," Analytical Chemistry. **73** (8), pp. 1658-1663 (2001).

[64] Zamfir, A.D.,Lion, N.,Vukelic, Z.,Bindila, L.,Rossier, J.,Girault, H.H.,Peter-Katalinic, J., "Thin chip microsprayer system coupled to quadrupole time-of-flight mass spectrometer for glycoconjugate analysis," Lab on a Chip. **5** (3), pp. 298-307 (2005).

[65] Zhang, S.,Van Pelt, C.K.,Henion, J.D., "Automated chip-based nanoelectrospray-mass spectrometry for rapid identification of proteins separated by two-dimensional gel electrophoresis," ELECTROPHORESIS. **24** (21), pp. 3620-3632 (2003).

[66] Fedorov, A.G.,Degertekin, F.L., "Electrospray Systems and Methods," U.S. Patent # 7,208,727 (2007).

[67] Meacham, J.M., *A Micromachined Ultrasonic Droplet Generator: Design, Fabrication, Visualization, and Modeling,* Georgia Institute of Technology, Doctoral Dissertation (2006).

[68] Meacham, J.M.,Ejimofor, C.,Kumar, S.,Degertekin, F.L.,Fedorov, A.G., "Micromachined ultrasonic droplet generator based on a liquid horn structure," Review of Scientific Instruments. **75** (5), pp. 1347-1352 (2004).

[69] Meacham, J.M.,Varady, M.J.,Degertekin, F.L.,Fedorov, A.G., "Droplet formation and ejection from a micromachined ultrasonic droplet generator: Visualization and scaling," Physics of Fluids. **17** (10), pp. 100605-8 (2005).

[70] ANSYS Inc., ANSYS Release 9.0, (ANSYS, Inc., Canonsburg, PA, 2004)

[71] Zarnitsyn, V.G.,Meacham, J.M.,Varady, M.J.,Hao, C.,Degertekin, F.L.,Fedorov, A.G., "Electrosonic ejector microarray for drug and gene delivery," Biomedical Microdevices. **10**, pp. 299-308 (2008).

[72] Aderogba, S.,Meacham, J.M.,Degertekin, F.L.,Fedorov, A.G.,Fernandez, F.M., "Nanoelectrospray ion generation for high-throughput mass spectrometry using a micromachined ultrasonic ejector array," Applied Physics Letters. **86** (20), pp. 203110-3 (2005).

[73] Hampton, C.Y.,Forbes, T.P.,Varady, M.J.,Meacham, J.M.,Fedorov, A.G.,Degertekin, F.L.,Fernandez, F.M., "Analytical Performance of a Venturi-Assisted Array of Micromachined Ultrasonic Electrosprays Coupled to Ion Trap Mass Spectrometry for the Analysis of Peptides and Proteins," Analytical Chemistry. **79** (21), pp. 8154-8161 (2007).

[74] Hampton, C.Y., *Applications and Fundamental Characterization of Open Air and Acoustic-Driven Ionization Methods for Mass Spectrometry,* Georgia Institute of Technology, Doctoral Dissertation (2009).

[75] Hampton, C.Y.,Silvestri, C.J.,Forbes, T.P.,Varady, M.J.,Meacham, J.M.,Fedorov, A.G.,Degertekin, F.L.,Fernández, F.M., "Comparison of the Internal Energy Deposition of Venturi-Assisted Electrospray Ionization and a Venturi-Assisted Array of Micromachined UltraSonic Electrosprays (AMUSE)," Journal of the American Society for Mass Spectrometry. **19** (9), pp. 1320-1329 (2008).

[76] Advion BioSciences Inc., Advion TriVersa Nanomate, http://www.advion.com (Advion BioScience, Inc., Ithaca, NY, 2006)

[77] Foret, F.,Kusý, P., "Microfluidics for multiplexed MS analysis," ELECTROPHORESIS. **27** (24), pp. 4877-4887 (2006).

[78] Nepomuceno, A.I.,Muddiman, D.C.,Bergen, H.R.,Craighead, J.R.,Burke, M.J.,Caskey, P.E.,Allan, J.A., "Dual Electrospray Ionization Source for Confident Generation of Accurate Mass Tags Using Liquid Chromatography Fourier Transform Ion Cyclotron Resonance Mass Spectrometry," Analytical Chemistry. **75** (14), pp. 3411-3418 (2003).

[79] Satomi, Y.,Kudo, Y.,Sasaki, K.,Hase, T.,Takao, T., "Accurate mass measurement in nano-electrospray ionization mass spectrometry by alternate switching of high voltage between sample and reference sprayers," Rapid Communications in Mass Spectrometry. **19** (4), pp. 540-546 (2005).

[80] Dethy, J.-M.,Ackermann, B.L.,Delatour, C.,Henion, J.D.,Schultz, G.A., "Demonstration of Direct Bioanalysis of Drugs in Plasma Using Nanoelectrospray Infusion from a Silicon Chip Coupled with Tandem Mass Spectrometry," Analytical Chemistry. **75** (4), pp. 805-811 (2003).

[81] Liu, H.,Felten, C.,Xue, Q.,Zhang, B.,Jedrzejewski, P.,Karger, B.L.,Foret, F., "Development of Multichannel Devices with an Array of Electrospray Tips for High-Throughput Mass Spectrometry," Analytical Chemistry. **72** (14), pp. 3303-3310 (2000).

[82] Xu, R.,Wang, T.,Isbell, J.,Cai, Z.,Sykes, C.,Brailsford, A.,Kassel, D.B., "High-Throughput Mass-Directed Parallel Purification Incorporating a Multiplexed Single Quadrupole Mass Spectrometer," Analytical Chemistry. **74** (13), pp. 3055-3062 (2002).

[83] Deng, W.,Klemic, J.F.,Li, X.,Reed, M.A.,Gomez, A., "Increase of electrospray throughput using multiplexed microfabricated sources for the scalable generation of monodisperse droplets," Journal of Aerosol Science. **37** (6), pp. 696-714 (2006).

[84] Beauchemin, D., "Inductively Coupled Plasma Mass Spectrometry," Analytical Chemistry. **78** (12), pp. 4111-4136 (2006).

[85] Fujii, K.,Nakano, T.,Kawamura, T.,Usui, F.,Bando, Y.,Wang, R.,Nishimura, T., "Multidimensional Protein Profiling Technology and Its Application to Human Plasma Proteome," Journal of Proteome Research. **3** (4), pp. 712-718 (2004).

[86] Kosaka, T.,Yoneyama-Takazawa, T.,Kubota, K.,Matsuoka, T.,Sato, I.,Sasaki, T.,Tanaka, Y., "Protein identification by peptide mass fingerprinting and peptide sequence tagging with alternating scans of nano-liquid chromatography/infrared multiphoton dissociation Fourier transform ion cyclotron resonance mass spectrometry," Journal of Mass Spectrometry. **38** (12), pp. 1281-1287 (2003).

[87] Le Bihan, T.,Pinto, D.,Figeys, D., "Nanoflow Gradient Generator Coupled with μ-LC-ESI-MS/MS for Protein Identification," Analytical Chemistry. **73** (6), pp. 1307-1315 (2001).

[88] Miao, X.-S.,Metcalfe, C.D., "Determination of pharmaceuticals in aqueous samples using positive and negative voltage switching microbore liquid chromatography/electrospray ionization tandem mass spectrometry," Journal of Mass Spectrometry. **38** (1), pp. 27-34 (2003).

[89] Qi, L.,Danielson, N.D., "Quantitative determination of pharmaceuticals using nano-electrospray ionization mass spectrometry after reversed phase mini-solid phase extraction," Journal of Pharmaceutical and Biomedical Analysis. **37** (2), pp. 225-230 (2005).

[90] Rochat, B.,Bolay, S.,Pascual, A.,Calandra, T.,Marchetti, O., "Liquid chromatography-mass spectrometry method for quantification of caspofungin in clinical plasma samples," Journal of Mass Spectrometry. **42** (4), pp. 440-449 (2007).

[91] Stokvis, E.,Ouwehand, M.,Nan, L.G.A.H.,Kemper, E.M.,Tellingen, O.v.,Rosing, H.,Beijnen, J.H., "A simple and sensitive assay for the quantitative analysis of paclitaxel in human and mouse plasma and brain tumor tissue using coupled liquid chromatography and tandem mass spectrometry," Journal of Mass Spectrometry. **39** (12), pp. 1506-1512 (2004).

[92] Tretyakova, N.Y.,Chiang, S.-Y.,Walker, V.E.,Swenberg, J.A., "Quantitative analysis of 1,3-butadiene-induced DNA adducts in vivo and in vitro using liquid chromatography electrospray ionization tandem mass spectrometry," Journal of Mass Spectrometry. **33** (4), pp. 363-376 (1998).

[93] Vainchtein, L.D.,Rosing, H.,Mirejovsky, D.,Huynh, V.,Lenaz, L.,Hillebrand, M.J.X.,Schellens, J.H.M.,Beijnen, J.H., "Quantitative analysis of EO9 (apaziquone) and its metabolite EO5a in human plasma by high-performance liquid chromatography under basic conditions coupled to electrospray tandem mass spectrometry," Journal of Mass Spectrometry. **41** (10), pp. 1268-1276 (2006).

[94] Wang, W.,Guo, T.,Rudnick, P.A.,Song, T.,Li, J.,Zhuang, Z.,Zheng, W.,DeVoe, D.L.,Lee, C.S.,Balgley, B.M., "Membrane Proteome Analysis of Microdissected Ovarian Tumor

Tissues Using Capillary Isoelectric Focusing/Reversed-Phase Liquid Chromatography-Tandem MS," Analytical Chemistry. **79** (3), pp. 1002-1009 (2007).

[95] Yin, H.,Killeen, K.,Brennen, R.,Sobek, D.,Werlich, M.,vandeGoor, T., "Microfluidic Chip for Peptide Analysis with an Integrated HPLC Column, Sample Enrichment Column, and Nanoelectrospray Tip," Analytical Chemistry. **77** (2), pp. 527-533 (2005).

[96] Forbes, T.P.,Dixon, R.B.,Muddiman, D.C.,Degertekin, F.L.,Fedorov, A.G., "Characterization of Charge Separation in the Array of Micromachined UltraSonic Electrospray (AMUSE) Ion Source for Mass Spectrometry," Journal of the American Society for Mass Spectrometry. **20** (9), pp. 1684-1687 (2009).

[97] Hall, N.A.,Guldiken, R.,McLean, J.,Degertekin, F.L. *Modeling and design of CMUTs using higher order vibration modes [capacitive micromachined ultrasonic transducers]*. in *Ultrasonics Symposium, 2004 IEEE*. **1**, pp. 260-263 (2004).

[98] Knight, J.,McLean, J.,Degertekin, F.L., "Low temperature fabrication of immersion capacitive micromachined ultrasonic transducers on silicon and dielectric substrates," Ultrasonics, Ferroelectrics and Frequency Control, IEEE Transactions on. **51** (10), pp. 1324-1333 (2004).

[99] Forbes, T.P.,Degertekin, F.L.,Fedorov, A.G., "Multiplexed operation of a micromachined ultrasonic droplet ejector array," Review of Scientific Instruments. **78** (10), pp. 104101-6 (2007).

[100] Kino, G.S., *Acoustic Waves: Devices, Imaging, and Analog Signal Processing* (Prentice-Hall, Englewood Cliffs, NJ, 1987).

[101] Li, Y.,Pozniak, B.P.,Cole, R.B., "Mapping of Potential Gradients within the Electrospray Emitter," Analytical Chemistry. **75** (24), pp. 6987-6994 (2003).

[102] Van Berkel, G.J.,Asano, K.G.,Granger, M.C., "Controlling Analyte Electrochemistry in an Electrospray Ion Source with a Three-Electrode Emitter Cell," Analytical Chemistry. **76** (5), pp. 1493-1499 (2004).

[103] Jackson, G.S.,Enke, C.G., "Electrical Equivalence of Electrospray Ionization with Conducting and Nonconducting Needles," Analytical Chemistry. **71** (17), pp. 3777-3784 (1999).

[104] Iribarne, J.V.,Dziedzic, P.J.,Thomson, B.A., "Atmospheric pressure ion evaporation-mass spectrometry," International Journal or Mass Spectrometry and Ion Physics. **50** (3), pp. 331-347 (1983).

[105] Thomson, B.A.,Iribarne, J.V., "Field induced ion evaporation from liquid surfaces at atmospheric pressure," The Journal of Chemical Physics. **71** (11), pp. 4451-4463 (1979).

[106] Zeleny, J., "Instability of Electrified Liquid Surfaces," Physical Review. **10** (1), pp. 1 (1917).

[107] Taylor, G., "Disintegration of Water Drops in an Electric Field," Proceedings of the Royal Society of London. Series A, Mathematical and Physical Sciences. **280** (1382), pp. 383-397 (1964).

[108] Gañán-Calvo, A.M.,Dávila, J.,Barrero, A., "Current and droplet size in the electrospraying of liquids. Scaling laws," Journal of Aerosol Science. **28** (2), pp. 249-275 (1997).

[109] Hartman, R.P.A.,Brunner, D.J.,Camelot, D.M.A.,Marijnissen, J.C.M.,Scarlett, B., "Electrohydrodynamic atomization in the cone-jet mode physical modeling of the liquid cone and jet," Journal of Aerosol Science. **30** (7), pp. 823-849 (1999).

[110] Marginean, I.,Nemes, P.,Parvin, L.,Vertes, A., "How much charge is there on a pulsating Taylor cone?," Applied Physics Letters. **89** (6), pp. 064104-3 (2006).

[111] Nemes, P.,Marginean, I.,Vertes, A., "Spraying Mode Effect on Droplet Formation and Ion Chemistry in Electrosprays," Analytical Chemistry. **79** (8), pp. 3105-3116 (2007).

[112] Parvin, L.,Galicia, M.C.,Gauntt, J.M.,Carney, L.M.,Nguyen, A.B.,Park, E.,Heffernan, L.,Vertes, A., "Electrospray Diagnostics by Fourier Analysis of Current Oscillations and Fast Imaging," Analytical Chemistry. **77** (13), pp. 3908-3915 (2005).

[113] Collins, R.T.,Jones, J.J.,Harris, M.T.,Basaran, O.A., "Electrohydrodynamic tip streaming and emission of charged drops from liquid cones," Nature Physics. **4** (2), pp. 149-154 (2008).

[114] Hayati, I.,Bailey, A.,Tadros, T.F., "Investigations into the mechanism of electrohydrodynamic spraying of liquids : II. Mechanism of stable jet formation and electrical forces acting on a liquid cone," Journal of Colloid and Interface Science. **117** (1), pp. 222-230 (1987).

[115] Hirt, C.W., "Electro-hydrodynamics of semi-conductive fluids: with applications to electro-spraying," Flow Science Technical Note. **#70** (FSI-04-TN70), pp. (2004).

[116] Lastow, O.,Balachandran, W., "Numerical simulation of electrohydrodynamic (EHD) atomization," Journal of Electrostatics. **64** (12), pp. 850-859 (2006).

[117] Melcher, J.R.,Taylor, G.I., "Electrohydrodynamics: a review of the role of interfacial shear stress," Annual Review of Fluid Mechanics. **1**, pp. 111-146 (1969).

[118] Notz, P.K.,Basaran, O.A., "Dynamics of Drop Formation in an Electric Field," Journal of Colloid and Interface Science. **213** (1), pp. 218-237 (1999).

[119] Saville, D.A., "Electrohydrodynamics: The Taylor-Melcher Leaky Dielectric Model," Annual Review of Fluid Mechanics. **29** (1), pp. 27-64 (1997).

[120] Sen, A.K.,Darabi, J.,Knapp, D.R.,Liu, J., "Modeling and characterization of a carbon fiber emitter for electrospray ionization," Journal of Micromechanics and Microengineering. **16** (3), pp. 620 (2006).

[121] Zeng, J.,Sobek, D.,Korsmeyer, T., "Electro-hydrodynamic modeling of electrospray ionization: CAD for a μfluidic device - mass spectrometer interface," Transducers '03. 12th International Conference on Solid-State Sensors, Actuators and Microsystems. Digest of Technical Papers. **2**, pp. 1275-1278 (2003).

[122] Barengol'ts, S.,Litvinov, E.,Suvorov, V.,Uimanov, I., "Numerical modeling of the electrohydrodynamic and thermal instability of a conducting liquid surface in a strong electric field," Technical Physics Letters. **27** (5), pp. 370-372 (2001).

[123] Suvorov, V.G., "Numerical analysis of liquid metal flow in the presence of an electric field: application to liquid metal ion source," Surface and Interface Analysis. **36** (5-6), pp. 421-425 (2004).

[124] Suvorov, V.G.,Litvinov, E.A., "Dynamic Taylor cone formation on liquid metal surface: numerical modelling," Journal of Physics D: Applied Physics. (11), pp. 1245 (2000).

[125] Suvorov, V.G.,Zubarev, N.M., "Formation of the Taylor cone on the surface of liquid metal in the presence of an electric field," Journal of Physics D: Applied Physics. (2), pp. 289 (2004).

[126] Castellanos, A., *Electrohydrodynamics*, International Centre for Mechanical Sciences: Course and Lectures - No. 380 (Springer Wien, New York, 1998).

[127] Forbes, T.P.,Degertekin, F.L.,Fedorov, A.G., "Electrohydrodynamics of Charge Separation in Droplet-Based Ion Sources with Time-Varying Electrical and Mechanical Actuation," Journal of the American Society for Mass Spectrometry. doi: 10.1016/j.jasms.2009.12.022 (2009).

[128] Fluent, Fluent version 6.3, (Fluent, Lebanon, NH, 2006)

[129] Landau, L.D.,Lifshitz, E.M.,Pitaevskii, L.P., *Electrodynamics of Continuous Media*, 2nd ed. (Elsevier Butterworth-Heinemann, Amsterdam, 2004).

[130] Eggers, J., "Nonlinear dynamics and breakup of free-surface flows," Reviews of Modern Physics. **69** (3), pp. 865 (1997).

[131] Harvie, D.J.E.,Fletcher, D.F., "A new volume of fluid advection algorithm: the defined donating region scheme," International Journal for Numerical Methods in Fluids. **35** (2), pp. 151-172 (2001).

[132] Hirt, C.W.,Nichols, B.D., "Volume of fluid (VOF) method for the dynamics of free boundaries," Journal of Computational Physics. **39** (1), pp. 201-225 (1981).

[133] Rider, W.J.,Kothe, D.B., "Reconstructing Volume Tracking," Journal of Computational Physics. **141** (2), pp. 112-152 (1998).

[134] Rudman, M., "Volume-Tracking Methods for Interfacial Flow Calculations " International Journal for Numerical Methods in Fluids. **24** (7), pp. 671-691 (1997).

[135] Rudman, M., "A volume-tracking method for incompressible multifluid flows with large density variations," International Journal for Numerical Methods in Fluids. **28** (2), pp. 357-378 (1998).

[136] Noh, W.F.,Woodward, P., "SLIC (Simple Line Interface Calculations)," Lecture Notes Phys. **59**, pp. 330-340 (1976).

[137] Ubbink, O., *Numerical Prediction of Two Fluid Systems with Sharp Interfaces,* Imperial College of Science, Technology and Medicine, Ph.D. thesis (1997).

[138] Rusche, H., *Computational fluid dynamics of dispersed two-phase flows at high phase fractions,* Imperial College of Science, Technology and Medicine, Ph.D. thesis (2002).

[139] Youngs, D.L., *Time-Dependent Multi-Material Flow with Large Fluid Distortion*, Numerical Methods for Fluid Dynamics (Academic Press, London, 1982).

[140] Brackbill, J.U.,Kothe, D.B.,Zemach, C., "A continuum method for modeling surface tension," Journal of Computational Physics. **100** (2), pp. 335-354 (1992).

[141] Baliga, B.R.,Patankar, S.V., "A control volume finite-element method for two-dimensional fluid flow and heat transfer," Numerical Heat Transfer Part A. Applications. **6** (3), pp. 245 - 261 (1983).

[142] Ferziger, J.H.,Peric, M., *Computational Methods for Fluid Dynamics*, 2nd ed. (Springer, Berlin, 1999).

[143] Patankar, S.V., *Numerical heat transfer and fluid flow*, (Hemisphere Publishing Corporation, Washington, 1980).

[144] Griffiths, D.J., *Introduction to Electrodynamics*, 3rd ed. (Prentice Hall, New Jersey, 1999).

[145] Hayt, W.H.,Buck, J.A., *Engineering Electromagnetics*, 6th ed. (McGraw Hill, Boston, 2001).

[146] Shtern, V.,Barrero, A., "Striking features of fluid flows in taylor cones related to electrosprays," Journal of Aerosol Science. **25** (6), pp. 1049-1063 (1994).

[147] Dixon, R.B.,Muddiman, D.C.,Hawkridge, A.M.,Fedorov, A.G., "Probing the Mechanisms of an Air Amplifier Using a LTQ-FT-ICR-MS and Fluorescence Spectroscopy," Journal of the American Society for Mass Spectrometry. **18** (11), pp. 1909-1913 (2007).

[148] Becker, E.,Hiller, W.J.,Kowalewski, T.A., "Experimental and theoretical investigation of large-amplitude oscillations of liquid droplets," Journal of Fluid Mechanics. **231**, pp. 189-210 (1991).

[149] Rayleigh, L.J.W.S., "On the capillary phenomena of jets," Proceedings of the Royal Society of London. **29**, pp. 71-97 (1879).

[150] Rayleigh, L.J.W.S., "Further observations upon liquid jets, in continuation of those recorded in the Royal Society's 'Proceedings' for March and May 1879," Proceedings of the Royal Society of London. **34**, pp. 130-145 (1882).

[151] Rayleigh, L.J.W.S., "Some applications of photography," Nature. **44**, pp. 249-254 (1891).

[152] National Instruments, LabVIEW version 7.0, (National Instruments, Austin TX, 2006)

[153] Zhang, X.,Basaran, O.A., "Dynamics of drop formation from a capillary in the presence of an electric field," Journal of Fluid Mechanics. **326**, pp. 239-263 (1996).

[154] Marginean, I.,Nemes, P.,Vertes, A., "Order-Chaos-Order Transitions in Electrosprays: The Electrified Dripping Faucet," Physical Review Letters. **97**, pp. 064502 (2006).

[155] Marginean, I.,Nemes, P.,Vertes, A., "Astable regime in electrosprays," Physical Review E. **76** (2), pp. 026320 (2007).

[156] Fernandez de la Mora, J., "The Fluid Dynamics of Taylor Cones," Annual Review of Fluid Mechanics. **39**, pp. 217-243 (2007).

[157] Fernandez de la Mora, J.,Loscertales, I.G., "The current emitted by highly conducting Taylor cones," Journal of Fluid Mechanics. **260**, pp. 155-184 (1994).

[158] Fernandez de la Mora, J.,Navascues, J.,Fernandez, F.,Rosell-Llompart, J., "Generation of submicron monodisperse aerosols in electrosprays," Journal of Aerosol Science. **21** (special issue), pp. S673-S676 (1990).

[159] Smith, D.P.H., "The Electrohydrodynamic Atomization of Liquids," IEEE Transactions on Industry Applications. **IA-22** (3), pp. 527-535 (1986).

[160] IEEE-DEIS-EHD Technical Committee, "Recommended International Standard for Dimensionless Parameters Used in Electrohydrodynamics," IEEE Transactions on Dielectrics and Electrical Insulation. **10** (1), pp. 3-6 (2003).

[161] Fenn, J.B., "Ion formation from charged droplets: roles of geometry, energy, and time," Journal of the American Society for Mass Spectrometry. **4** (7), pp. 524-535 (1993).

[162] Loftus, P., The Buzz: Targeting Cancer With Bee Venom, (The Wall Street Journal, 2009)

[163] Margoliash, E., "Primary Structure and Evolution of Cytochrome C," Proceedings of the National Academy of Sciences. **50** (4), pp. 672–679 (1963).

[164] Olson, S.,Oeckler, R.,Li, X.,Du, L.,Traganos, F.,Zhao, X.,Burke-Wolin, T., "Angiotensin II stimulates nitric oxide production in pulmonary artery endothelium via the type 2 receptor " American Journal of Physiology - Lung Cellular and Molecular Physiology. **287**, pp. L559-L568 (2004).

[165] Iavarone, A.T.,Jurchen, J.C.,Williams, E.R., "Effects of Solvent on the Maximum Charge State and Charge State Distribution of Protein Ions Produced by Electrospray Ionization," Journal of the American Society for Mass Spectrometry. **11**, pp. 976-985 (2000).

[166] Iavarone, A.T.,Jurchen, J.C.,Williams, E.R., "Supercharged Protein and Peptide Ions Formed by Electrospray Ionization," Analytical Chemistry. **73**, pp. 1455-1460 (2001).

[167] Iavarone, A.T.,Williams, E.R., "Supercharging in electrospray ionization: effects on signal and charge," International Journal of Mass Spectrometry. **219**, pp. 63-72 (2002).

[168] Iavarone, A.T.,Williams, E.R., "Mechanism of Charging and Supercharging Molecules in Electrospray Ionization," Journal of the American Chemical Society. **125**, pp. 2319-2327 (2003).

[169] Oberacher, H., "On the use of different mass spectrometric techniques for characterization of sequence variability in genomic DNA," Analytical and Bioanalytical Chemistry. **391** (1), pp. 135-149 (2008).

[170] van den Heuvel, R.H.H.,Gato, S.,Versluis, C.,Pascal Gerbaux,Kleanthous, C.,Heck, A.J.R., "Real-time monitoring of enzymatic DNA hydrolysis by electrospray ionization mass spectrometry," Nucleic Acids Research. **33** (10), pp. e96 (2005).

[171] Gupta, R.,Beck, J.L.,Ralph, S.F.,Sheil, M.M.,Aldrich-Wright, J.R., "Comparison of the Binding Stoichiometries of Positively Charged DNA-Binding Drugs Using Posivite and Negative Electrospray Ionization Mass Spectrometry," Journal of the American Society for Mass Spectrometry. **15**, pp. 1382-1391 (2004).

[172] Collette, C.,De Pauw, E., "Calibration of the Internal Energy Distribution of Ions Produced by Electrospray," Rapid Communications in Mass Spectrometry. **12**, pp. 165-170 (1998).

[173] Metz, T.O.,Pagea, J.S.,Bakera, E.S.,Tanga, K.,Dinga, J.,Shena, Y.,Smith, R.D., "High-resolution separations and improved ion production and transmission in metabolomics," Trends in Analytical Chemistry. **27** (3), pp. 205-214 (2008).

[174] Tang, K.,Page, J.S.,Smith, R.D., "Charge Competition and the Linear Dynamic Range of Detection in Electrospray Ionization Mass Spectrometry," Journal of the American Society for Mass Spectrometry. **15** (10), pp. 1416-1423 (2004).

[175] He, Q.,Pang, C.,Tai, Y.-C.,Lee, T.D., "Ion Liquid Chromatography on-a-chip with beads-packed parylene column," Proceedings of the 17th IEEE International Conference for MEMS. pp. 212-215 (2004).

[176] Le Gac, S.,Carlier, J.,Camart, J.-C.,Cren-Olivé, C.,Rolando, C., "Monoliths for microfluidic devices in proteomics," Journal of Chromatography B. **808** (1), pp. 3-14 (2004).

[177] Shih, C.-Y.,Chen, Y.,Tai, Y.-C., "Parylene-strengthened thermal isolation technology for microfluidic system-on-chip applications," Sensors and Actuators A: Physical. **126** (1), pp. 270-276 (2006).

[178] Xie, J.,Miao, Y.,Shih, J.,Tai, Y.-C.,Lee, T.D., "Microfluidic platform for liquid chromatography-tandem mass spectrometry analyses of complex peptide mixtures," Analytical Chemistry. **77**, pp. 6947-6953 (2005).

[179] Mery, E.,Ricoul, F.,Sarrut, N.,Constantin, O.,Delapierre, G.,Garin, J.,Vinet, F., "A silicon microfluidic chip integrating an ordered micropillar array separation column and a nano-electrospray emitter for LC/MS analysis of peptides," Sensors and Actuators B: Chemical. **134** (2), pp. 438-446 (2008).

[180] Lazar, I.M.,Trisiripisal, P.,Sarvaiya, H.A., "Microfluidic liquid chromatography system for proteomic applications and biomarker screening," Analytical Chemistry. **78**, pp. 5513-5524 (2006).

[181] Mellors, J.S.,Gorbounov, V.,Ramsey, R.S.,Ramsey, J.M., "Fully Integrated Glass Microfluidic Device for Performing High-Efficiency Capillary Electrophoresis and Electrospray Ionization Mass Spectrometry," Analytical Chemistry. **80** (18), pp. 6881-6887 (2008).

[182] Brennen, R.A.,Yin, H.,Killeen, K.P., "Microfluidic gradient formation for nanoflow chip LC," Analytical Chemistry. **79** (24), pp. 9302-9309 (2007).

[183] Ghitun, M.,Bonneil, E.,Fortier, M.-H.,Yin, H.,Killeen, K.,Thibault, P., "Integrated microfluidic devices with enhanced separation performance: Application to phosphoproteome analyses of differentiated cell model systems," Journal of Separation Science. **29** (11), pp. 1539-1549 (2006).

[184] Yin, H.,Killeen, K., "The fundamental aspects and applications of Agilent HPLC-Chip," Journal of Separation Science. **30** (10), pp. 1427-1434 (2007).

[185] Yin, H.,Killeen, K.,Brennen, R.,Sobek, D.,Werlich, M.,Goor, T.v.d., "Microfluidic chip for peptide analysis with an integrated HPLC column, sample enrichment column, and nanoelectrospray tip," Analytical Chemistry. **77** (527-533), pp. (2005).

[186] Fedorov, A.G., "Confining/Focusing Vortex Flow Transmission Structure, Mass Spectrometry Systems, and Methods of Transmitting Particles, Doplets, and Ions," U.S. Patent Application 11/895,532 (2007).

[187] Senturia, S.D., *Microsystem Design*, (Kluwer Academic Publishers, Boston, 2001).

[188] APC International Ltd., Material properties of lead zirconate titanate (PZT-8) material 880, www.americanpiezo.com (APC International, Ltd., 2006)

[189] Bard, A.J.,Faulkner, L.R., *Electrochemical Methods: Fundamentals and Applications*, 2nd ed. (Wiley, India, 2004).

[190] Rhaleb, N.E.,Drapeau, G.,Dion, S.,Jukic, D.,Rouissi, N.,Regoli, D., "Structure-activity studies on bradykinin and related peptides: agonists.," British Journal of Pharmacology. **99** (3), pp. 445-448 (1990).

[191] Cardarelli, R.,Lumicao, T.G., "B-type Natriuretic Peptide: A Review of Its Diagnostic, Prognostic, and Therapeutic Monitoring Value in Heart Failure for Primary Care Physicians " The Journal of the American Board of Family Practice. **16**, pp. 327-333 (2003).

[192] Cheung, B.M.Y.,Kumana, C.R., "Natriuretic Peptides—Relevance in Cardiovascular Disease " The Journal of the AMerican Medical Association. **280** (23), pp. 1983-1984 (1998).